Neutron Skin Measurement of ^{208}Pb and ^{48}Ca Using Parity Violating Electron Scattering

Sachinthani Amali Premathilake
B.S. in Physics, University of Peradeniya, Sri Lanka, 2015

A Dissertation Presented to the Faculty of the
University of Virginia in Candidacy for he Degree of Doctor of
Philosophy

Department of Physics

University of Virginia
April, 2023

Approved by:

Prof. Kent Paschke (Advisor)

Prof. Donal Day (Committee Member)

Prof. Nilanga Liyanage (Committee Member)

Prof. Shane Davis (GSAS Representative)

ABSTRACT

Parity-violating electron scattering experiments (PVES) provides a clean probe of neutron densities that is model independent and free from strong interaction uncertainties in interpretation. The PREX-2 and CREX experiments were run in 2019 and 2020 at Jefferson laboratory measured the nucleon skin thickness, the difference between the r.m.s. neutron radius R_n and the r.m.s. proton radius R_p, of ^{208}Pb and ^{48}Ca via parity violating electroweak asymmetry in the elastic scattering of longitudinally polarized electrons. PREX-2 experiment was performed with 950 MeV electrons scattered at a 5° angle with $Q^2 = 0.00616 \pm 0.00004$ (GeV/c)^2, while CREX used 2182 MeV electrons at the same angle with $Q^2 = 0.0297 \pm 0.0002$ (GeV/c)^2. For PREX-2 the measured asymmetry was $A_{PV} = 550 \pm 16$ (stat.) $\pm$ (syst.) ppb, which corresponds to $R_{skin} = 0.278 \pm 0.078$ (exp.) $\pm$ 0.012 (theo.) fm. The CREX asymmetry was $A_{PV} = 2668 \pm 106$ (stat.) $\pm$ 40 (syst.) ppb, which corresponds to $R_{skin} = 0.121 \pm 0.026$ (exp.) ± 0.024 (model) fm. One of the crucial systematic uncertainty that PREX-2 and CREX were sensitive to was the non-parity violating asymmetries that resulted from the helicity correlated false asymmetries in the polarized electron beam. There was a lot of work put towards understanding and suppressing the asymmetries arising from these effects. The parity violating asymmetry measurement required a very precise determination of the electron beam polarization. To accurately determine the beam polarization, a Compton polarimeter was used during both PREX-2 and CREX. A careful alignment of the laser to the Fabry-Perot cavity, data analysis and systematic control was employed to get a precise beam polarization result for the experiments. The PREX-2 measurement has broad implications for increasing our knowledge about neutron star structure and the equation of state of nuclear matter. The combined PREX and CREX results will have implications for future energy density functional calculations and the theory of nuclear structure.

ACKNOWLEDGEMENTS

I would like to take this opportunity to express my gratitude to the individuals who have contributed to the successful completion of this thesis. Without their support, encouragement, and guidance, this accomplishment would not have been possible. I am deeply grateful for those who have played a pivotal role in my academic journey and helped me achieve my goals.

First, I would like to express my sincere appreciation to my advisor, Prof. Kent Paschke, for his invaluable guidance and support throughout my PhD life. Kent's guidance has been really helpful, and his encouragement and feedback have been a constant source of motivation. I cannot thank Kent enough for his patience and understanding during challenging times. I am honored to have had the opportunity to work under Kent's guidance and call him my PhD advisor.

I would like to thank Caryn Palatchi, Dave Gaskell, Ciprian Gal and Juan Carlos for their support and guidance. They taught me a lot of things, and I'm forever grateful. I would also like to thank my colleague Allison for her support. Another big thank you to the PREX and CREX collaborators for their support.

I would like to thank my mom and dad, who have always encouraged me to pursue my dreams and provided me with the gift of education. Without them, I would not be where I am today, and I will always remember their love and support as I move forward in life. I express my deepest gratitude to my husband Randika, whose love and support have been the backbone of my PhD journey. His encouragement, sacrifices, and understanding have been invaluable, and I am truly blessed to have him in my life. I would like to thank my brother Viraj, who has been an incredible influence on my life and academic pursuits. I would also like to thank my sister Darshika, baby Vihnya and baby Nathalie for being such an amazing and special part of my life.

Thanks to all of my Pera friends, Charlottesville friends and Newport News friends who have been an important part of my academic journey. I am forever grateful for Jayendrika for her friendship and unwavering support. I will always cherish the memories we have created together. I would like to extend my heartfelt gratitude to my friends Sachith, Anushika, and Kapila, who helped me adjust to life in the USA when I first arrived.

TABLE OF CONTENTS

LIST OF TABLES

LIST OF FIGURES

CHAPTER 1

THEORY AND MOTIVATION

The Lead Radius Experiment-2 (PREX-2) and the Calcium Radius Experiment (CREX) are high precision parity violating electron scattering experiments that aim to measure the parity violating asymmetry to better than parts per million (ppm) precision. A longitudinally polarized electrons are scattered off of neutron rich ^{208}Pb and ^{48}Ca targets, to measure the weak form factor, weak charge and neutron distribution, and finally to extract the neutron skin thickness of the target nucleus.

1.1 ELECTROWEAK SCATTERING

1.1.1 INTRODUCTION TO ELECTROWEAK THEORY

A new branch of physics developed in the 20^{th} century called particle physics focused on understanding the fundamental particles which constitute the universe. Experiments by Rutherford discovered the “proton” [1] and James Chadwick discovered evidence of a second nucleon which had almost the same mass as the proton but electrically neutral and named it the “neutron” [2]. These discoveries showed that the atomic nuclei were composed of two primary nucleons, the positively charged proton and the electrically neutral neutron.

After the discovery of different “neutrinos”, “baryons” and “mesons” scientists came up with a model to classify these altogether and named it the “Standard Model of Particle Physics”. At present, this provides the theoretical framework which describes elementary particles and their interactions. The main three groups in the the Standard Model are quarks and leptons and gauge bosons. There are four fundamental forces which act on the matter. They are: electromagnetic force, weak force, strong force and gravitational force. Figure 1 summarizes the elementary particles of the Standard Model.

In the 60’s, Glashow, Weinberg and Salam, formulated a way to unify the electric and weak interactions into “electroweak” interaction. The existence of charged massive weak bosons ($W^{\pm}$), a neutral massive weak boson (Z^0) and a neutral massless boson of the electromagnetic interaction (γ) comes out of this theory and showed these produced by spontaneous symmetry breaking. The masses of the W and Z bosons were related through the ”Weak-mixing angle” (Weinberg angle), θ_W,

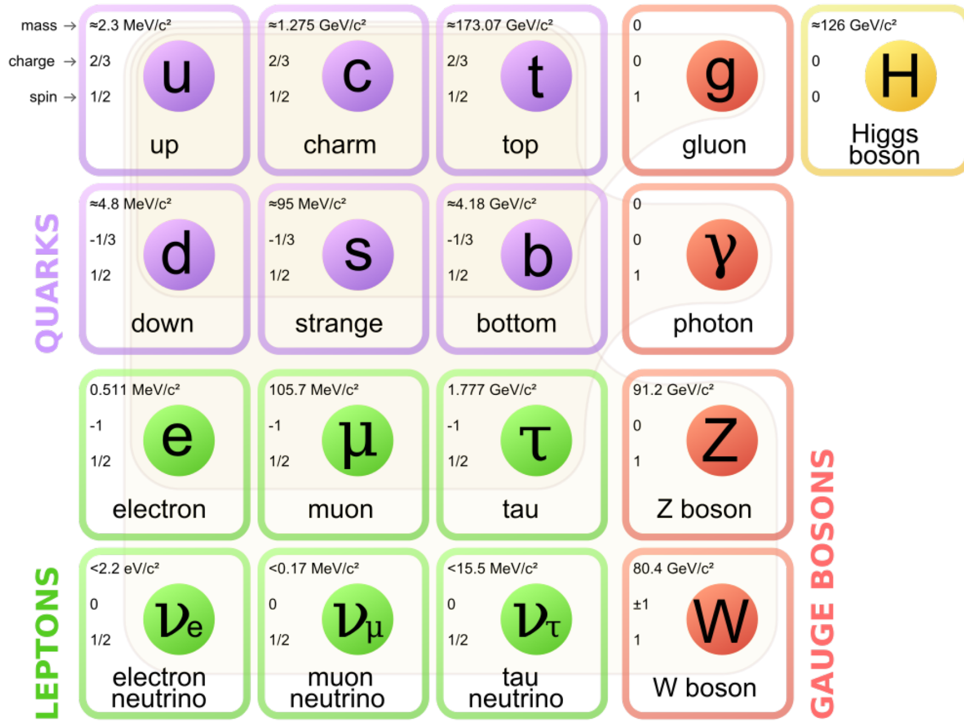

FIG. 1: An illustration of the particles included in the Standard Model [3].

$$M_Z = \frac{M_W}{\cos\theta_W}. \tag{1}$$

In electroweak unification, the electric and weak fields arise from a set of four massless gauge fields: W^-, W^+, W^0 form an isotriplet and B^0 an isosinglet. The two neutral states W^0 and B^0 mix via the "Weak-mixing angle" θ_W to form the photon and Z_0 bosons [4],

$$\begin{pmatrix} \gamma \\ Z^0 \end{pmatrix} = \begin{pmatrix} \cos\theta_W & \sin\theta_W \\ -\sin\theta_W & \cos\theta_W \end{pmatrix} \begin{pmatrix} B^0 \\ W^0 \end{pmatrix}. \tag{2}$$

During the mixing, the weak Z^0 boson acquires mass while the γ boson remains massless. The mechanism through which the three weak bosons acquire mass through spontaneous electroweak symmetry breaking, is the Higgs mechanism. The weak force interacts with the Higgs field, and mediating particles acquire mass, whereas the electromagnetic force does not interact with the Higgs field leaving the photon massless [5]. The Higgs mechanism was experimentally verified with the discovery of the Higgs boson at the LHC at CERN in 2012

[6].

In 1958, Bludman suggested existence of weak neutral current. In 1973, the Gargamelle bubble chamber experiment showed the existence of the neutral Z^0. The weak force mediator masses were calculated to be [4],

$$M_W = 82 \ \pm \ 2 \ GeV/c^2, \qquad M_Z = 92 \ \pm \ 2 \ GeV/c^2. \tag{3}$$

1.1.2 PARITY VIOLATION IN THE WEAK INTERACTION

Parity is a discrete transformation under which a physical system flips the sign of its spatial coordinates. When parity operator, P, acts on the spatial wave function of a system, $\psi(\vec{r})$, it alters the sign of its coordinates as,

$$\mathbf{P}\psi(\vec{r}) = \psi(-\vec{r}). \tag{4}$$

When the parity operator is applied to for the second time, it returns to the original wave function,

$$\mathbf{P}^2\psi(\vec{r}) = \mathbf{P}\psi(-\vec{r}) = \psi(\vec{r}). \tag{5}$$

$p = \pm 1$ is the eigenvalues of $\mathbf{P}$, with +1 corresponding to parity conservation and -1 corresponding to parity nonconservation.

Mathematically, the helicity (h) of a particle is the projection of its spin vector$(\vec{s})$ into the direction of its momentum $(\vec{p})$,

$$h = \vec{s} \cdot \hat{p}. \tag{6}$$

Under parity operation, the helicity of a particle gets flipped because it alters the direction of the particle's momentum $(\vec{p})$ and leaves its spin $(\vec{s})$ unchanged, as shown in Fig. 2.

In 1915, Emmy Noether showed that there is always a conserved quantity for every symmetry in nature [8]. At that time physicist assume parity was conserved in all physical processes and a universal symmetry. Then in 1950's τ - θ puzzle came, τ and θ were identified as two particles, which were identical in every way but had completely separate decay modes. Lee and Yang addressed this problem suggesting τ and θ were the same particle with parity just not conserved in one of the decay channels [9].

In 1956 Madame Wu carried out cobolt-60 experiment, the idea behind the experiment was to test whether nuclear beta decay, which happens via the weak interaction, violates or

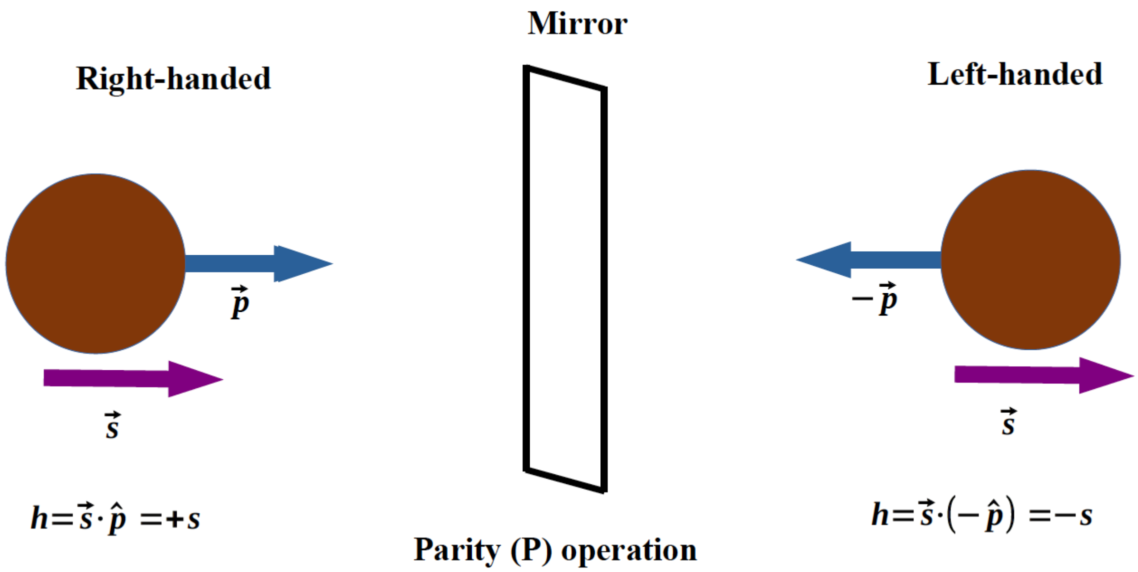

FIG. 2: Helicity reversal under parity operation [7].

conserves parity symmetry. Cobolt-60 nuclei were polarized with the nuclear spins aligned parallel to the magnetic field of a solenoid and the cobolt-60 nuclei under went betadecay via the weak interaction as,

$$ {}^{60}_{27}Co \rightarrow {}^{60}_{28}Ni + e^{-} + \bar{\nu}_e + 2\gamma. \tag{7}$$

Wu recorded the direction of the emitted electrons. It was discovered that most particles were emitted in the direction opposite to the direction of the magnetic field as shown in Fig. 3. This experiment established parity violation in the weak interaction.

1.1.3 ELECTROMAGNETIC SCATTERING AND FORM FACTOR

Let's look at a simple process where an electron with a momentum $\vec{p_i}$ scatters off a target nucleus at rest in the lab. The differential scattering cross-section is related to the scattering amplitude,

$$\frac{d\sigma}{d\Omega} \propto |\mathcal{M}_{fi}|^2, \tag{8}$$

where,

$$\mathcal{M}_{fi} =< \phi_f|V(\vec{r})|\phi_i > . \tag{9}$$

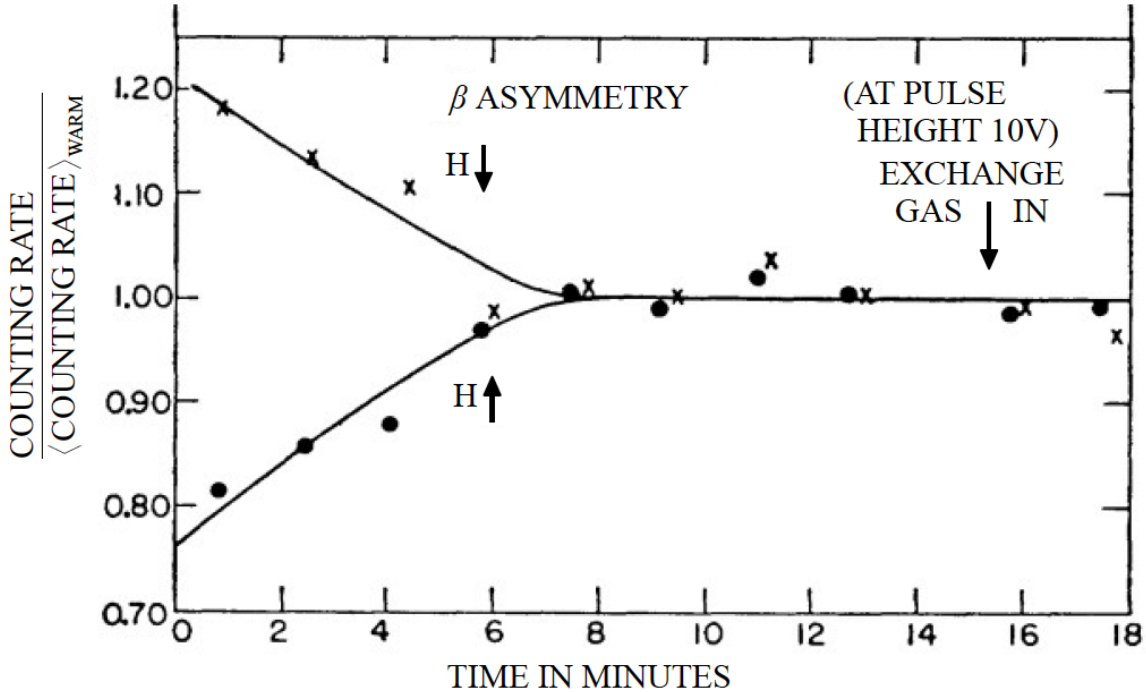

FIG. 3: The first experimental proof of parity-violation [10].

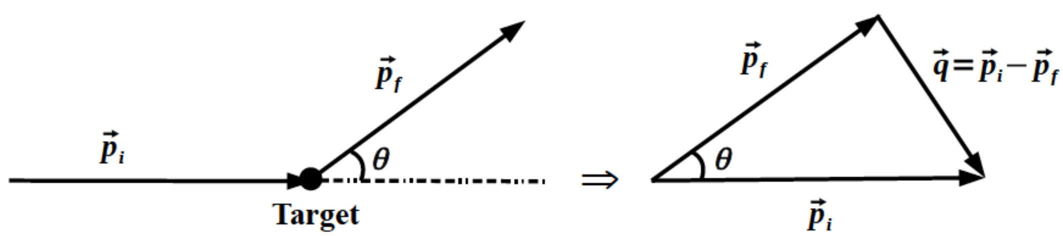

FIG. 4: Schematic of a electromagnetic scattering process.

ϕ_i and ϕ_f are the wave functions for the incoming and outgoing electrons respectively and $V(\vec{r})$ is the Coulomb potential for a charge density,

$$V(\vec{r}) = \frac{-Ze^2}{4\pi\epsilon_0}\int \frac{\rho(\vec{r'})}{|\vec{r}-\vec{r'}|}d^3\vec{r'}, \tag{10}$$

with $\vec{R} = |\vec{r}-\vec{r'}|$. Eq. 9 can written as,

$$\mathcal{M}_{fi} = \frac{-Ze^2}{4\pi\epsilon_0}\int \frac{e^{i\frac{\vec{q}.\vec{R}}{\hbar}}}{\vec{R}}d^3\vec{R}\left[\int e^{i\frac{\vec{q}.\vec{r'}}{\hbar}}\rho(\vec{r'})d^3\vec{r'}\right]. \tag{11}$$

The quantity inside the brackets is the Fourier transform of the charge distribution and is referred to as a form factor. This encodes geometric information about nuclear structure,

$$F(q) = \int e^{i\frac{\vec{q}.\vec{r'}}{\hbar}}\rho(\vec{r'})d^3\vec{r'}. \tag{12}$$

For spin-zero target nuclei the form factor F(q) is purely electromagnetic. For small momentum transfer, $F(q) \approx 1$ and Eq. 11 reduces to the Mott scattering amplitude. Then Eq. 8 can be written as,

$$\frac{d\sigma}{d\Omega} = \left(\frac{d\sigma}{d\Omega}\right)_{Mott}|F(q)|^2. \tag{13}$$

This equation shows the relationship between scattering cross section, an experimentally observable quantity, and a quantity containing information about the geometry of the scattering nucleus.

1.1.4 WEAK NEUTRAL CURRENT

The mediator of neutral weak interaction is Z^0 vector boson. The vertex factor for neutral weak interaction can be written as [4],

$$\frac{-ig_z}{2}\gamma^\mu(C_V^f - C_A^f\gamma^5), \tag{14}$$

where g_z is the neutral coupling constant, and coefficient c_V^f and c_A^f are weak neutral current vector and axial-vector couplings that depend on the type of quark or lepton (f) involved, and γ^μ are the Dirac matrices. g_z can written as,

$$g_z = \frac{g_{em}}{\sin\theta_W\cos\theta_W}, \tag{15}$$

where $g_{em} = \sqrt{4\pi\alpha_{em}}$, is the electromagnetic coupling constant and θ_W is the weak mixing angle [4]. Table 1 shows the values of c_V and c_A for the electron and light quarks in the Glashow-Weinberg-Salam model.

The weak neutral current for a given electron (e) can be written as,

$$J^\mu(e) = \bar{u}(e)\boldsymbol{\nu}u(e) = \bar{u}(e)\left[\frac{-ig_z}{2}\gamma^\mu(C_V^f - C_A^f\gamma^5)\right], \tag{16}$$

f	C_V	C_A
e^-	$-\frac{1}{2} + 2\ sin^2\theta_W$	$-\frac{1}{2}$
u	$\frac{1}{2}$ - $\frac{4}{3}$ $\sin^2\theta_W$	$\frac{1}{2}$
d, s	$-\frac{1}{2} + \frac{2}{3}\sin^2\theta_W$	$-\frac{1}{2}$

TABLE 1: Neutral vector and axial vector couplings in the GWS model for the electron and light quarks [4].

where u(e) and $\bar{u}(e)$ are initial and final electron spinors. Here γ^μ is odd under parity and $\gamma^\mu\gamma^5$ is even under parity, sum of these two terms leads to violation of parity in weak interactions.

The coupling of electron to $W^\pm$ is,

$$\frac{-ig_w}{2\sqrt{2}}\gamma^\mu(1-\gamma^5), \tag{17}$$

where, $g_w = \frac{g_{em}}{\sin\theta_W}$. These interactions are said to violate parity and because the terms come with equal strength, the parity violation is said to be "maximal".

1.1.5 ELECTRON SCATTERING FROM A WEAK POTENTIAL

The weak interaction has vector and axial vector components. When an electron scatters from a spin zero nucleus, the potential can be written as [11],

$$\hat{V}(r) = V(r) + \gamma^5 A(r), \tag{18}$$

where V(r) is the vector potential for Coulomb interaction and A(r) is the axial-vector potential coming from the weak neutral current. A(r) can be written as a function of the weak charge density $\rho_W(r)$

$$A(r) = \frac{G_F}{2^{\frac{3}{2}}}\rho_W(r), \tag{19}$$

where G_F is the Fermi constant. For a target nucleus with N neutrons and Z protons, the weak charge density integrates to the total weak charge of the nucleus [11],

$$\int d^3r\rho_W(r) = -N + (1-4\sin^2\theta_W)Z. \tag{20}$$

The empirical value of the weak mixing angle is $\sin^2\theta_W \approx 0.23$, and the factor governing the proton component of weak charge is 1 - $4\sin^2\theta_W \approx 0.08$. Then, $\rho_W(r)$ approximates the neutron density $\rho_n(r)$ normalized to neutron number N. Therefore, the neutron density of the nucleus largely determines the weak charge density and this quantity is a good proxy for neutron density measurements.

Electron wave function ψ for right-handed (+) and left-handed (-) electrons can be express as,

$$\psi_\pm = \frac{1}{2}(1 \pm \gamma^5)\psi, \tag{21}$$

with the potential,

$$V_\pm(r) = V(r) \pm A(r). \tag{22}$$

From this, positive helicity states (right-handed electrons) scatter from a potential $V(r) + A(r)$, while negative helicity states (left-handed electrons) scatter from a potential $V(r) - A(r)$ [11]. Thus, parity-violating asymmetry arises from the scattering of opposite helicity states, of longitudinally polarized electrons, from the two different potentials.

1.1.6 PARITY VIOLATING ASYMMETRY

PREX and CREX are parity violating electron scattering experiments where a polarized beam of electrons is scattered from an unpolarized nuclear target, here ^{208}Pb and ^{48}Ca. Here we can observe both electromagnetic and weak interaction. The electromagnetic interaction between the electric charge of the electron beam and the target nucleus protons, is mediated through the exchange of the γ boson. The weak interaction, between the weak charge of the beam electrons and that of the target nucleus, is mediated through the Z^0 boson exchange.

The key observable of this formulation is the parity violating asymmetry A_{PV}. The asymmetry is the normalized difference between scattering cross sections for incident electrons with left and right handed helicity states and A_{PV} can be written as,

$$A_{PV} = \frac{\sigma_R - \sigma_L}{\sigma_R + \sigma_L}, \tag{23}$$

where $\sigma_{R(L)}$ is the differential scattering cross-section for right(left) handed incident electrons. $\sigma_{R(L)}$ can be written as,

$$\sigma_{R(L)} = \frac{d\sigma_{R(L)}}{d\Omega} \propto (\mathcal{M}_\gamma + \mathcal{M}_Z^{R(L)})^2, \tag{24}$$

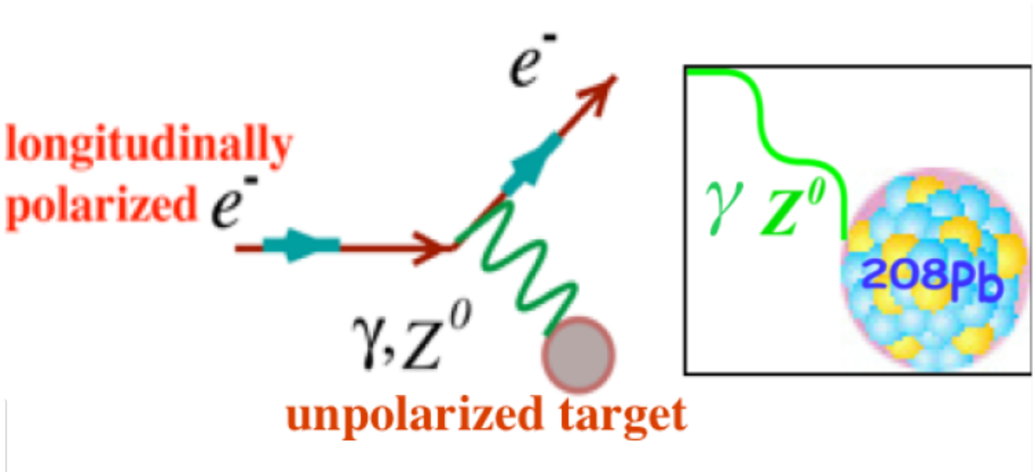

FIG. 5: Electron scattering off ^{208}Pb target nucleus with Z-boson and photon mediators [12].

where $\mathcal{M}_Z$ and $\mathcal{M}_\gamma$ are the weak and electromagnetic amplitudes, respectively. Using Eq. 22 and Eq. 23,

$$A_{PV} \approx \frac{(\mathcal{M}_\gamma + \mathcal{M}_Z)^2 - (\mathcal{M}_\gamma - \mathcal{M}_Z)^2}{(\mathcal{M}_\gamma + \mathcal{M}_Z)^2 + (\mathcal{M}_\gamma - \mathcal{M}_Z)^2}. \tag{25}$$

Since $\mathcal{M}_\mathcal{Z} \ll \mathcal{M}_\gamma$ Eq. 24 reduces to,

$$A_{PV} \approx \frac{2\mathcal{M}_\gamma^* \mathcal{M}_Z}{\mathcal{M}_\gamma^2}. \tag{26}$$

Using Born approximation we can write A_{PV} as,

$$A_{PV} = \frac{G_F Q^2}{4\pi\alpha\sqrt{2}} \left[1 - 4\sin^2\theta_W - \frac{F_n(Q^2)}{F_p(Q^2)} \right], \tag{27}$$

where G_F is the Fermi coupling constant, $\alpha$is the fine structure constant, θ_W is the weak mixing angle and Q^2 is the four-momentum transfer in the process, and $F_{n(p)}(Q^2)$ are the nuclear form factors for the neutron(proton). Since the Born approximation is not valid for the heavy nucleus, Coulomb distortion effects must be accounted for the calculation for ^{208}Pb.

It's clear that parity violating asymmetry relates to the neutron and proton form factors, thus A_{PV} probes the neutron density at choice of Q^2. The form factor is the Fourier transform of the associated density distribution,

$$F_{n(p)}(Q^2) = \int j_0(qr)\rho_{n(p)}(r)d^3r. \tag{28}$$

The mean square radius of the neutron(proton) distribution is related to the form factor by,

$$\langle R^2_{n(p)} \rangle \propto \left. \frac{dF_{n(p)})(Q^2)}{dQ^2} \right|_{Q^2=0}. \tag{29}$$

Due to the small weak charge of the proton and non-existent electric charge of the neutron, weak form factor primarily couples to the neutron distribution and the electric charge form factor entirely couples to the proton distribution. Therefore, parity violating electron scattering provides a model independent probe of neutron density measurements. This was first proposed by Donnelly, Dubach, and Sick in 1989 and suggested that parity violating electron scattering can measure neutron densities in nuclei [13].

1.2 NUCLEAR STRUCTURE AND EQUATION OF STATE

1.2.1 CONCEPT OF NEUTRON SKIN

For stable light nuclei ($Z < 20$), the ratio $\frac{N}{Z}$ is approximately 1, as we go higher in Z, the nucleus tends to have a larger $\frac{N}{Z}(> 1)$ fractions to remain stable (see Fig. 6). This is to compensate for increased electromagnetic repulsion between the larger number of protons. Therefore, for large or complex nuclei, there is a difference between the neutron and proton distribution. Figure 7 shows the neutron and proton density distributions in a ^{208}Pb nucleus.

It is predicted the central region of a complex nucleus is composed of a more symmetrical mixture of protons and neutrons, and there is an outer region composed purely of neutrons, so radii occupied by neutrons in the nucleus extends beyond the radii occupied by protons. This has never been precisely measured. Excess neutrons in heavy nuclei are predicted to form a "neutron skin".

The thickness of the neutron skin is then the difference between the RMS neutron radius R_n ($\sqrt{\langle r_n^2 \rangle}$) and the RMS proton radius R_p ($\sqrt{\langle r_p^2 \rangle}$),

$$\triangle r_{np} = \sqrt{\langle r_n^2 \rangle} - \sqrt{\langle r_p^2 \rangle}. \tag{30}$$

According to Eq. 27, the measured parity violating asymmetry in polarized electron scattering directly relates to the ratio of neutron and proton form factor distributions at

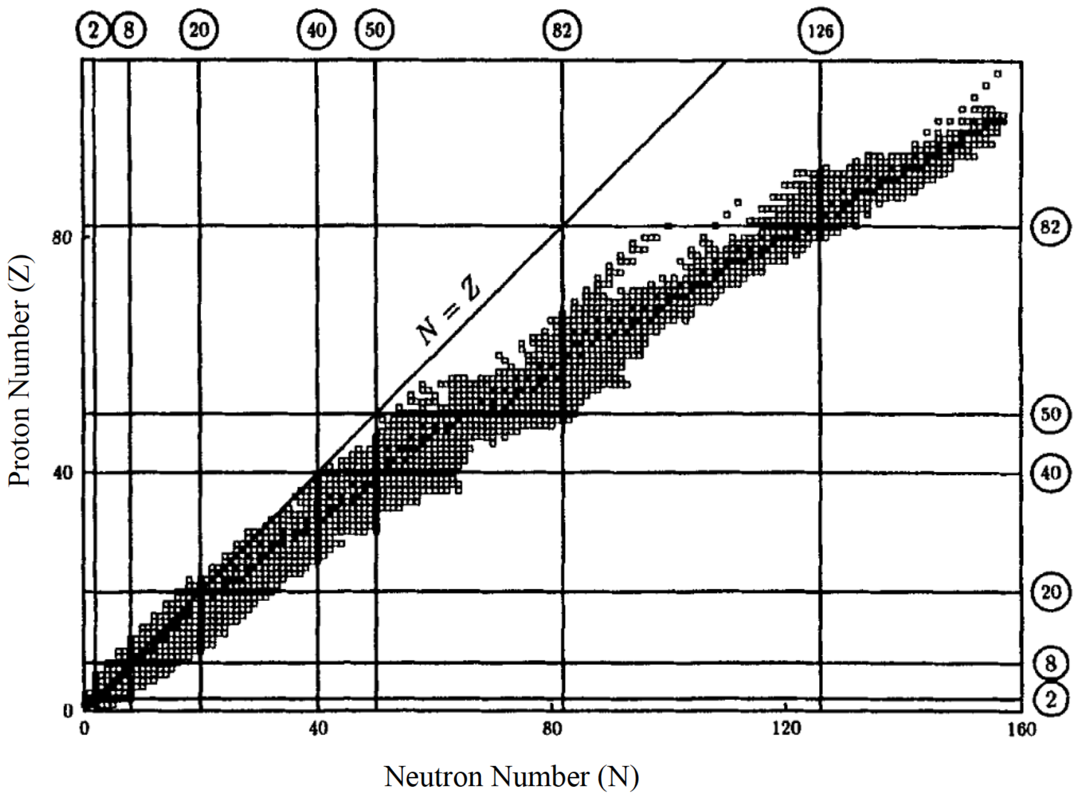

FIG. 6: The nuclear landscape: distribution of nuclei as a function of proton and neutron numbers [14].

particular Q^2[1] Theoretically, $\triangle r_{np}$ (R_{skin}) and A_{PV} has a linear relationship for carefully selected Q^2[2] over existing nuclear structure models as shown in Fig. 8. Every existing model that predicts weak charge density and an electric charge density demonstrate that neutron skin thickness and the parity-violating asymmetry are dependent parameters. Therefore, parity violating asymmetry provides a clean measure of the neutron skin thickness.

The structure of nuclei is determined by the interactions of the protons and neutrons. Every atomic nucleus is composed of Z number of protons and N number of neutrons and nuclear mass number is A = Z + N. Just few year after the discovery of the neutron, Bethe and Weizs$\ddot{a}$cker formulated the liquid drop model (LDM) [15]. This model assumes a hard edge sphere of constant density, with volume V $\sim$ A and radius R $\sim$ $A^{1/3}$. The key determinant of whether a nucleus is stable or not is its binding energy. Theoretically

[1] The four momentum transfer squared Q^2 is the momentum transferred from the electron to the target nucleus

[2] In the regions alongside the first diffracted cross section minimum there are places A_{PV} is highly sensitive to the neutron radius.

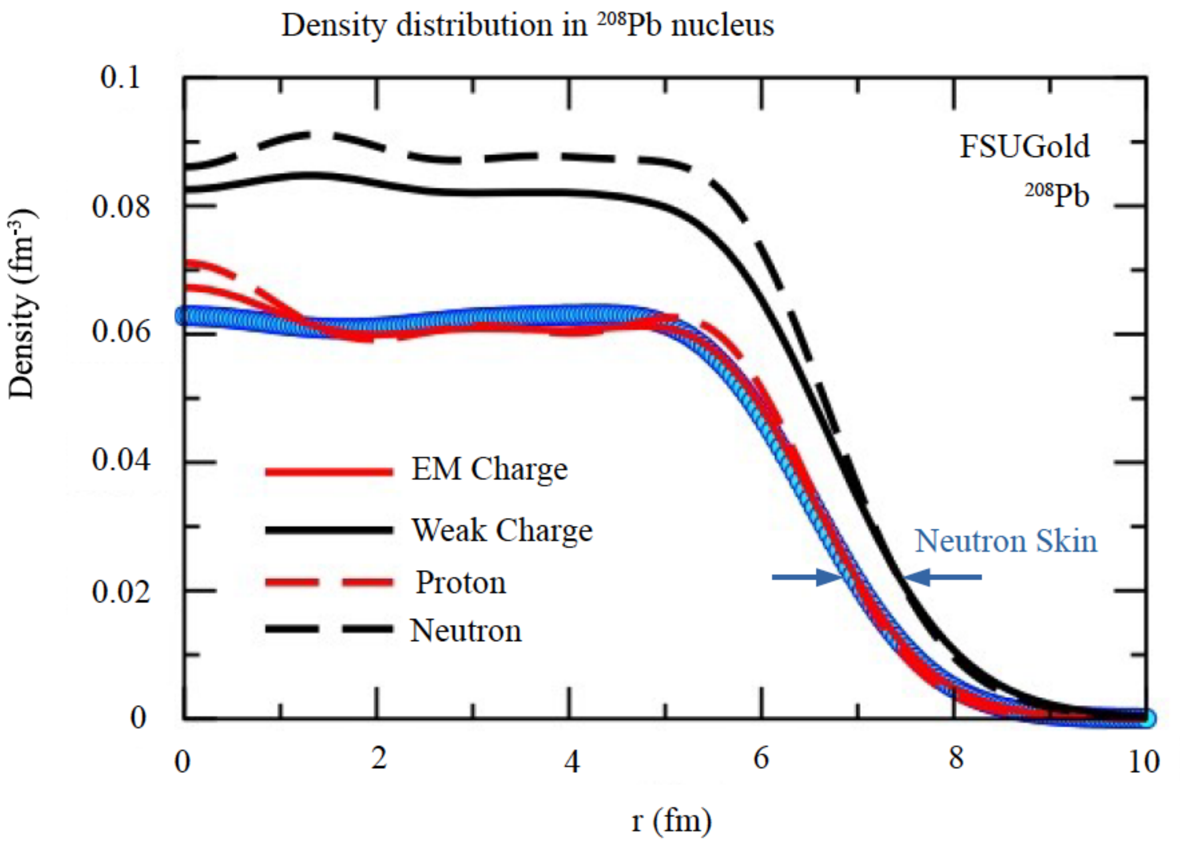

FIG. 7: Neutron and proton distributions in ^{208}Pb as predicted by FSUGold.The dashed lines are the proton (red) and neutron (black) density distributions, solid lines are the electromagnetic charge (red) and weak-charge (black) distributions. The blue circles represent the experimental charge distribution [15].

binding energy is the energy to disassemble a nucleus into its constituent nucleons. In the LDM the nuclear binding energy (neglecting paring effects) is expressed as simpler version of Semi-Emperical Mass formula [17],

$$B(Z,N) = a_V A - a_S A^{2/3} - a_C \frac{Z(Z-1)}{A^{1/3}} - a_A \frac{(N-Z)^2}{A} + \delta(A,Z),$$
$$\delta(A,Z) = \begin{cases} +\delta_0, & \text{Z, N even} \\ 0 & \text{A odd} \\ -\delta_0 & \text{Z, N odd (A even)} \end{cases} \tag{31}$$

Here, a_V is the volume term, a_S is the counteracting surface tension energy, a_C is the

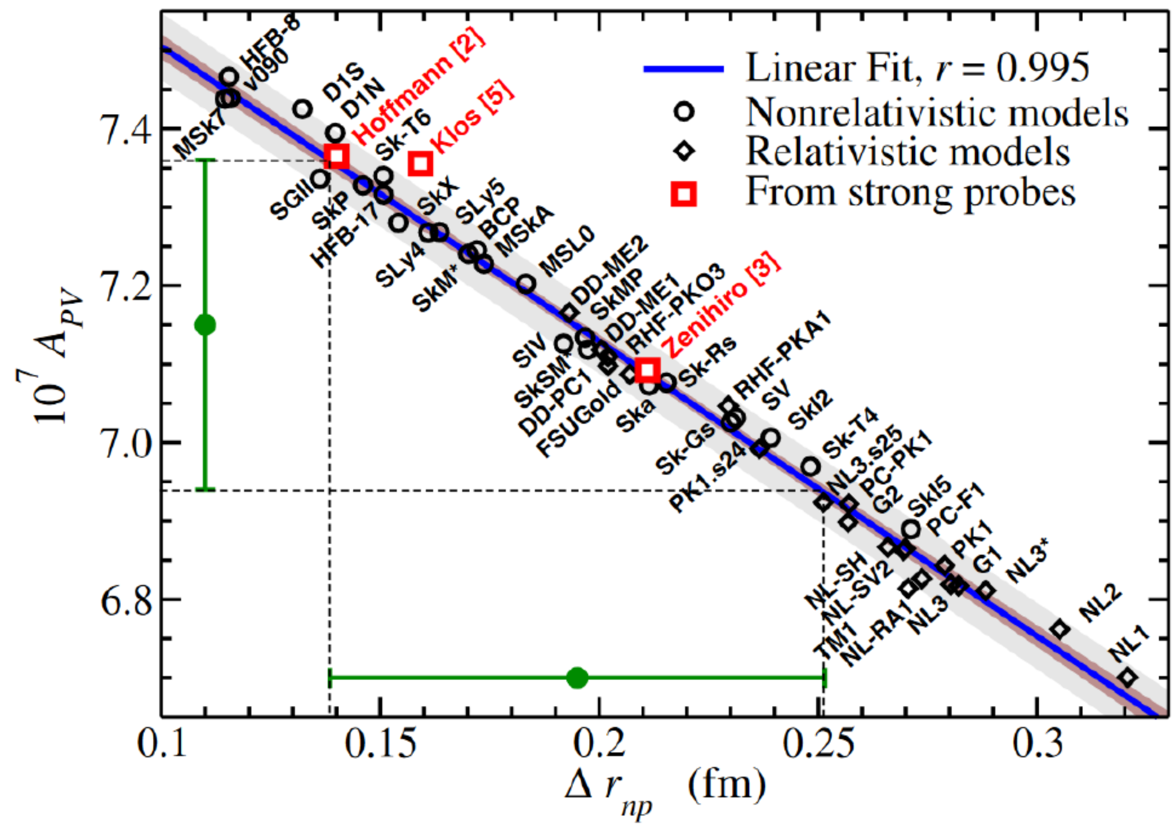

FIG. 8: Parity violating asymmetry for ^{208}Pb at the kinematics of PREX against the neutron skin of ^{208}Pb. In red are three reported measurements of $\triangle r_{np}$ from hadronic probes. In green is a hypothetical measurement of $A_{PV} = 715$ ppb, with 3% precision and its corresponding neutron skin thickness [16].

Coulomb repulsion term, a_A is the asymmetry term correction from the Pauli exclusion principle and δ is the pairing term caused by the spin coupling effect. In heavy nuclei, more neutrons than protons are needed to balance the repulsion between protons. Due to the Pauli exclusion principle, the energy of these extra neutrons will be higher than the rest nucleons, therefore an asymmetry term is introduced.

The different coefficients of this model should determined empirically and it's challenging to apply this to all nuclear matter. For example the asymmetry energy term can only be measured on nuclei which have more neutrons than protons. Therefore it is customary to define the general parameters that characterize the Equation of State of nuclear matter (EOS) which gives a theoretical description. ^{208}Pb is the heaviest stable nucleus and has 44 excess neutrons, so the PREX-2 will have significant implications for the asymmetry energy term.

The EOS parameterize the structure of nuclear matter. It describes the state of a nuclear system in terms of proton (ρ_p) and neutron (ρ_n) densities, under ideal thermodynamic properties such as temperature and pressure. EOS has both well known terms and barely constrained terms such as symmetry energy (energy penalty for breaking N=Z symmetry). If we think about a nucleus as the radius reaches the edge of the nucleus, the density falls off as shown in Fig. 7. Therefore the symmetry energy as a function of density has a key role in determining the thickness of the neutron skin.

The density of stable nucleus is $\rho = \rho_p + \rho_n$. The slope of the symmetry energy at saturation density (ρ_0) is defined as L,

$$L(\rho) = \frac{dS}{d\rho}\bigg|_{\rho_0}. \tag{32}$$

The saturation density of nuclei is estimated by theoretical models is $\rho_0 = 0.15\ \mathrm{fm}^{-3}$ [18]. To first order we can define the nuclear EOS as energy of symmetric nuclear matter and breaking of the symmetry, α^2 [19],

$$\epsilon(\rho, \alpha) = \epsilon(\rho, 0) + S(\rho)\alpha^2, \tag{33}$$

where $\alpha = (\rho_n - \rho_p)/\rho$ and $S(\rho)$ is the symmetry energy. Given that symmetric nuclear matter saturates and it's pressure vanishes at saturation, the slope of the symmetry energy L is closely related to the pressure of pure neutron matter (P_{PNM}) at saturation density. That is,

$$P_{PNM}(\rho_0) \approx \frac{1}{3} L\rho_0. \tag{34}$$

Quantitatively, mean-field predictions show a clear correlation between neutron skin of a heavy nucleus and L the density slope of the symmetry energy as shown in Fig. 9. As shown in Fig. 10 different models have very different symmetry energies and neutron radius measurement calibrates the EOS of neutron rich matter directly, and guides models needed for heavy nuclei via L, the slope of the symmetry energy at saturation density. So the measurement of neutron skin thickness could constrain the slope of the symmetry energy without model dependence and it would be helpful in understanding the symmetry energy and the EOS.

1.3 PVES EXPERIMENTS

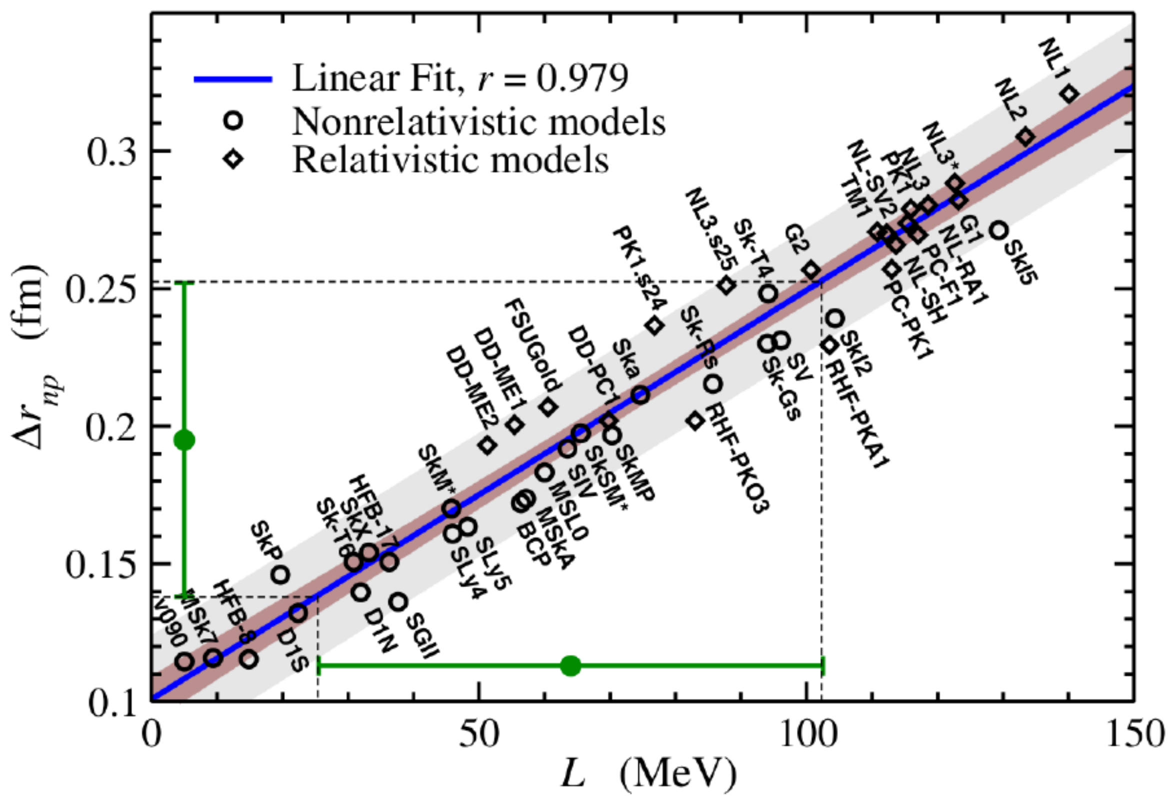

FIG. 9: Correlation between ^{208}Pb neutron skin thickness against slope of the symmetry energy (L) [16]

In parity violating electron scattering experiments (PVES), a longitudinally polarized electron beam is incident on an unpolarized target. Then change the sign of the longitudinal polarization mimicking a parity transformation, and measure the fractional rate difference between right and left helicity states. An interference between the electromagnetic and weak amplitudes, gives rise to a parity violating asymmetry (Fig. 11 and Fig. 12).

The first parity violating electron scattering (PVES) experiment is the E122 at SLAC in the late 1970s, which served as a blueprint for parity electron scattering experiments. Since this was supposed to measure relatively small size asymmetry it needed stringent control over systematic corrections related to beam quality. An experimental blueprint for the E122 experiment is shown in Fig. 13.

Several other experiments followed E122 and measured A_{PV} with better precision over time. Different experiments had different purposes, but the same PVES technique was used in every experiment.

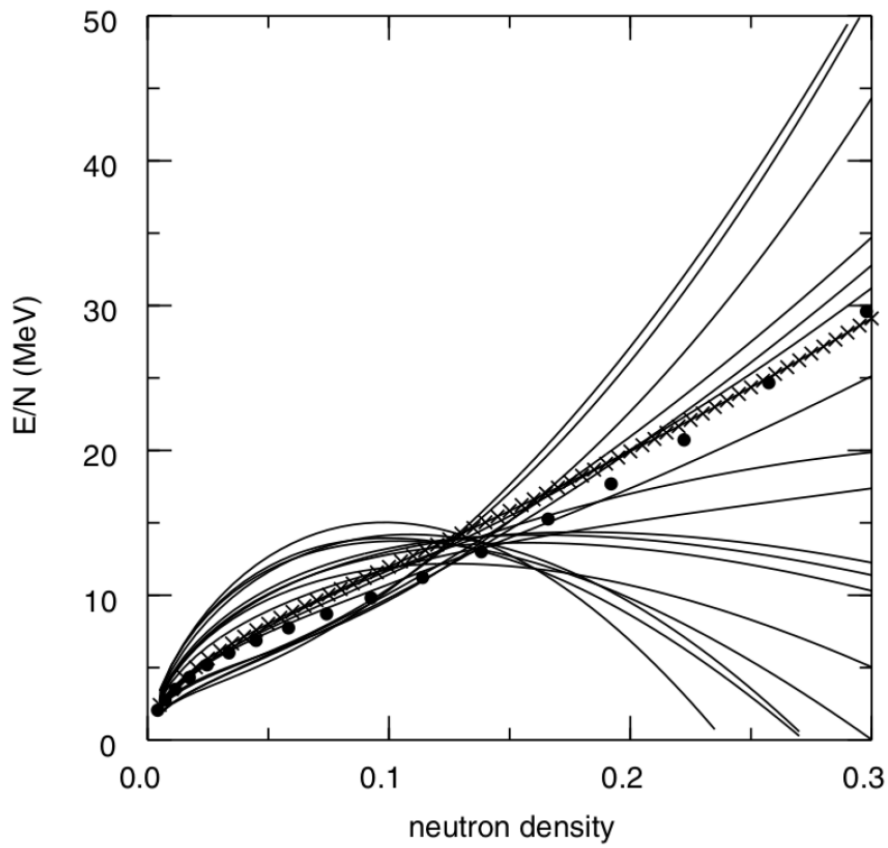

FIG. 10: A variety of models predicting the symmetry energy E/N vs. the neutron density [12].

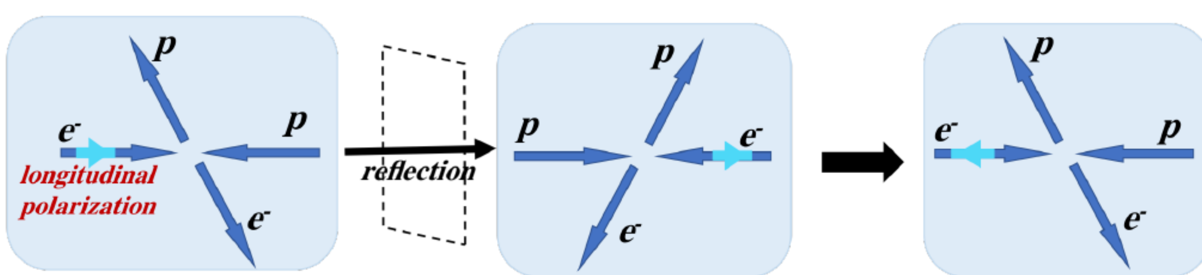

FIG. 11: Illustration of how the helicity correlated scattering symmetry corresponds to parity violation [12].

A series of PVES experiments have been conducted at JLab since the late 1990s. JLab

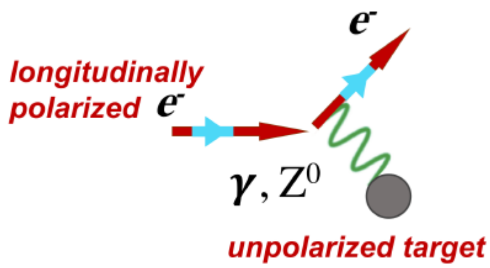

(a)

$$\sigma \propto \left|M_\gamma + M_{weak}\right|^2 \sim |M_\gamma|^2$$
$$+\, M_\gamma (M_{weak})^* + (M_\gamma)^* M_{weak} + |M_{weak}|^2$$

(b)

FIG. 12: Interference between weak and electromagnetic amplitudes, gives rise to parity violating asymmetry [12].

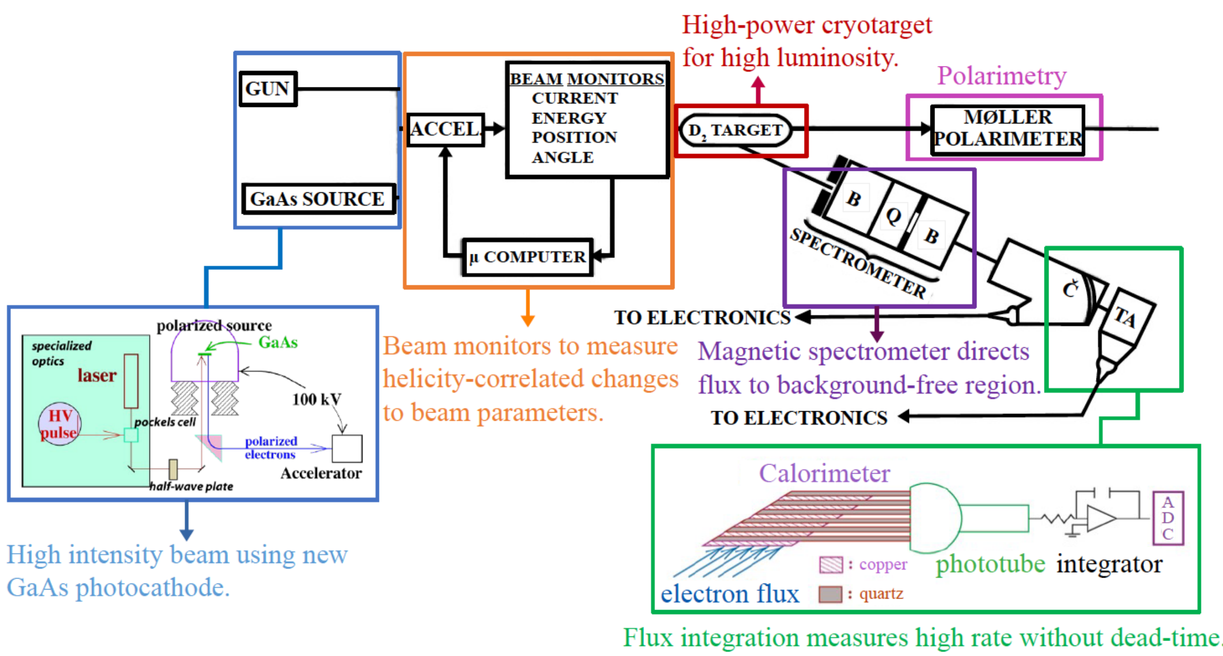

FIG. 13: E122 experiment blueprint at SLAC [7].

is pioneering PVES because of it's high quality CEBAF beam. Table. 2 shows past PVeS experiments completed at JLab, along with their observations.

1.4 MOTIVATIONS

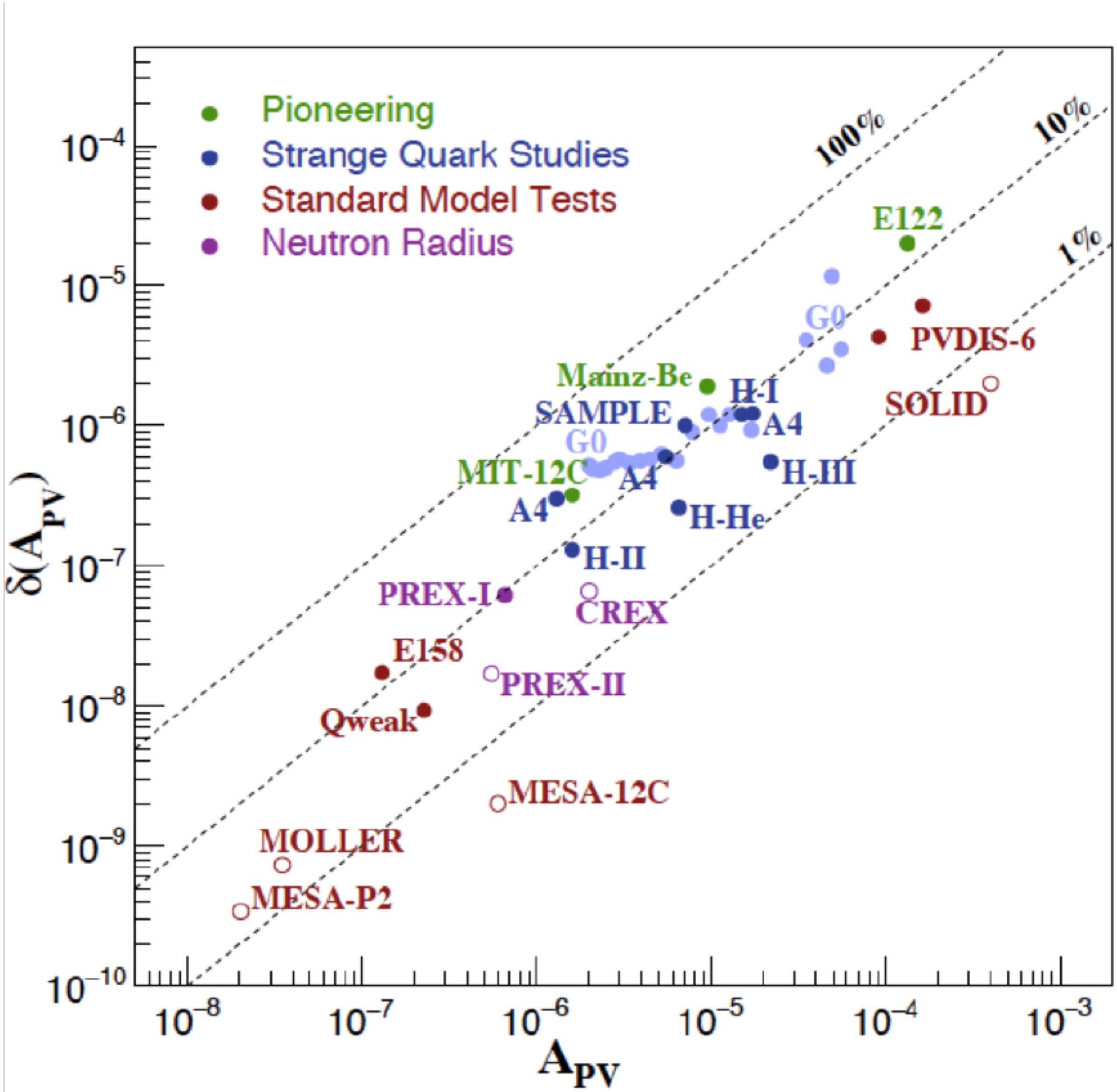

FIG. 14: Precision of various PVES experiments: x-axis shows measured or predicted asymmetry and y-axis shows the uncertainty on A_{PV} [12].

1.4.1 TARGET CHOICE

It's better to use a nucleus with a thick skin to measure neutron skin thickness as the skin is tiny. Thicker skin means more excess neutrons. The best candidates are doubly magic because they suppress the inelastic levels which are difficult experimentally and also they

	Experiment	Measurement
Hall A	HAPPeX	"strange" quark contributions to electro-magnetic structure of proton and neutron
	PVDIS	"weak" quark coupling parameters
	PREX-1	neutron radius of 208Pb
Hall C	G0	measured contribution of strange quarks to charge and magnetization distributions of the nucleon
	Qweak	weak charge of proton through PVES at very low Q2

TABLE 2: Past PVES experiments at JLab

are more amendable for nuclear structure calculations. When a nucleon shell is fully filled and the next higher energy shell is empty, it's referred to as a nucleon with magic number. These are stable because it's hard to separate out a nucleon from that closed shell. Nuclei whose numbers of protons and neutrons are both magic are called doubly magic nuclei, and are more stable.

PREX-2 and CREX uses ^{208}Pb and ^{48}Ca respectively as the target nucleus. These are the only readily available, stable, spin-0, doubly magic, and neutron-rich nuclei. ^{208}Pb has 44 excess neutrons and ^{48}Ca has 8 excess neutrons. Because both nuclei are spin-0 we don't need to worry about the target polarization. Since ^{208}Pb is doubly magic the first exited state of ^{208}Pb has relatively high excitation energy of 2.615 MeV and, similarly the first excited state of ^{48}Ca is 3.831 MeV. These relatively large first excited state energy is useful for experimental apparatus because spectrometers can accept nearly all elastically scattered events and reject almost all inelastic events. A_{PV} from inelastic scattering is unknown.

PREX-2 is important to nuclear structure theory as well as nuclear astrophysics and CREX results will test macroscopic models. ^{48}Ca is much lighter nuclei than ^{208}Pb and it's governed by a different realm of nuclear theory. ^{208}Pb can be modeled using a mean-field approach in the realm of density functional theory where individual interactions between nucleons are used to constrain an overall functional used to parameterize a mean field for the nuclear system [20]. ^{48}Ca lies in the medium region of the nuclear landscape, as shown in Fig. 15. ^{48}Ca is accessible from ab-initio methods where it allows direct comparison to Chiral Effective Field Theory (EFT) calculations, which is very sensitive to three-nucleon forces [21]. Since ^{48}Ca is large enough to apply the DFT methods, the neutron skin thickness measurement of ^{48}Ca will provide a critical bridge between ab-initio approaches and nuclear

DFT.

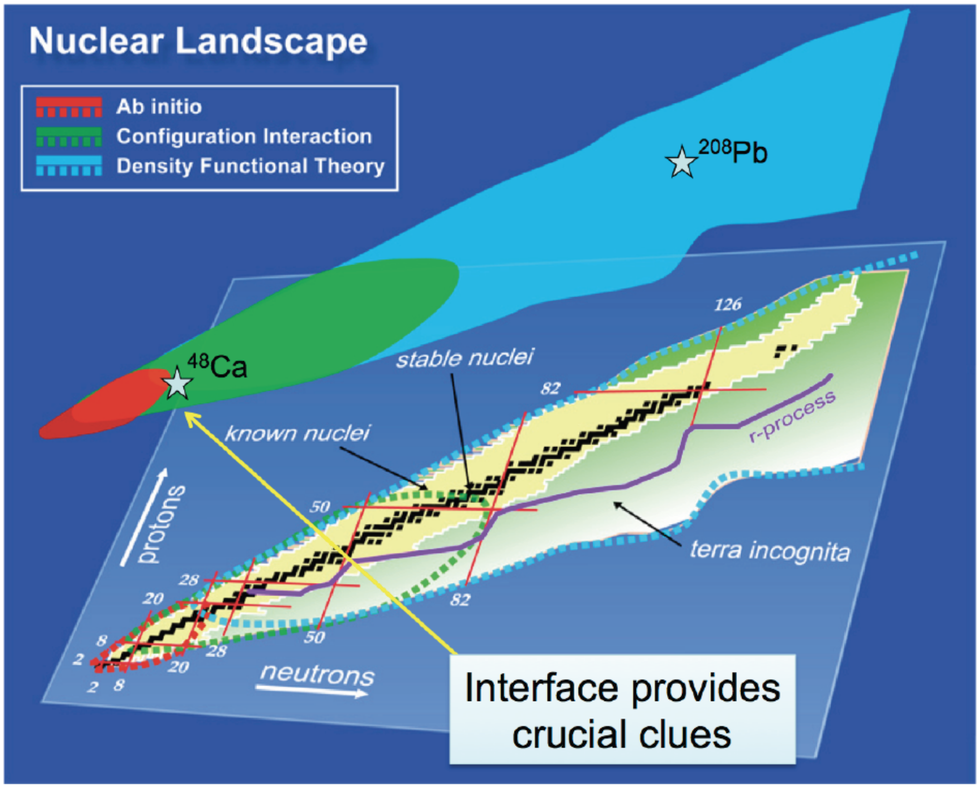

FIG. 15: Nuclear landscape in a (Z, N) plane [22].

1.4.2 KINEMATICS

For the experiment we must think about how to configure mechanics to get the maximum precision on the measured neutron radius R_n with minimum running time, therefore choice of kinematics is important. Parity violating asymmetry is larger at higher beam energy and larger scattering angle, but scattering rate is larger at smaller beam energy and scattering angle as shown in Fig. 16. Also, calculations show sensitivity of A_{PV} w.r.t. neutron radius is varying along beam energy. Therefore, all of these thing should be considered when choosing kinematics. The metric for choosing kinematics is called the Figure Of Merit (FOM),

$$FOM = R \times A^2 \times \epsilon^2. \tag{35}$$

Here, R is the detected scattering rate, A is the expected parity violating asymmetry which is calculated from mean field theory models, and ϵ is the sensitivity to neutron radius. This

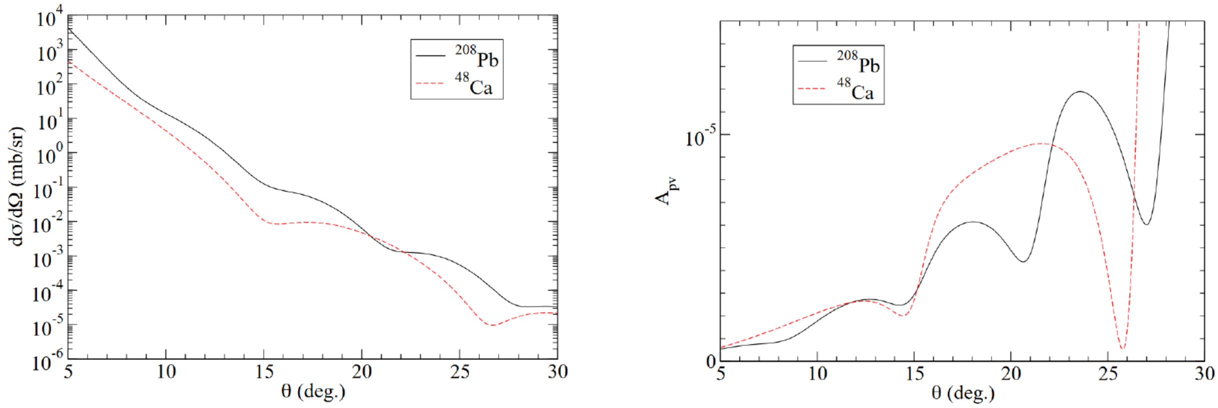

FIG. 16: Left: Cross section dependence on scattering angle for both ^{208}Pb and ^{48}Ca at 855 MeV. Right: A_{PV} dependence on scattering angle for both ^{208}Pb and ^{48}Ca at 855 MeV [23].

is calculated as $\epsilon = \frac{dA}{A} = (A_1 - A)/A$, where A is computed from Mean Field Theory calculation and A_1 is the asymmetry from the Mean Field Theory calculation such that the neutron radius is increased by 1%.

The statistical uncertainty of the neutron radius measurement is,

$$\delta R_n^{(stat)} \propto \sqrt{\frac{1}{(FOM)}}. \tag{36}$$

For the experiment kinematics should be selected to maximize FOM.

The PREX-2 proposed FOM was maximized[3]at $\theta_{PREX} = 5^\circ$ and E_{PREX} =0.95 GeV [24], while the CREX proposed for scattering kinematics of $\theta_{CREX} = 5^\circ$ and $E_{CREX} = 2.1$ GeV [22].

1.4.3 UNCERTAINTY BUDGET

The goal of PREX-2 is to achieve the 1% precision in the ^{208}Pb neutron radius, which requires the precision of A_{PV} measurement better than 3% [16]. CREX proposed a precision of 0.02 fm (0.6%) in the ^{48}Ca neutron radius, which correspond to a 4% uncertainty in A_{PV}.

To reduce statistical uncertainty of the experiment many scattered electrons should be collected.

[3]These were not the exact optimization, but took into account realistic limitations in available beam energy and the need to build a common apparatus at the same scattering angle.

$$\delta A = \sqrt{\sigma_{stat}^2 + \sigma_{sys}^2} \qquad \sigma_{stat} = \frac{1}{P\sqrt{N}}, \tag{37}$$

where N is the total number of scattered electrons and P is the beam polarization.

1.4.4 BEAM POLARIZATION EFFECTS

Parity violating asymmetry calculations are done assuming a perfect longitudinally polarized beam but in reality beam polarization at the target is not 100%. There are methods to accurately monitor the polarization of the electron beam through out the experiment and those will be discussed later in this thesis. To account for the effects of polarization, we scale the measured asymmetry by the measured polarization,

$$A_{PV} = \frac{A_{meas}}{P} \tag{38}$$

Since higher asymmetry comes with higher beam polarization, accelerator is configured to get the maximum beam polarization for the experiment.

Transverse Beam Polarization

The transverse asymmetry comes from a nonzero component of beam polarization in a direction transverse to the beam direction and is given by,

$$A_T = \frac{\sigma^{\uparrow} - \sigma^{\downarrow}}{\sigma^{\uparrow} + \sigma^{\downarrow}} \tag{39}$$

Where $\sigma^{\downarrow(\uparrow)}$ is the elastic scattering cross-section for spins transverse to the direction of electron beam motion. A_T is parity conserving, thus this effect produces a source of false asymmetry and we need to correct that. For PREX-2 and CREX, the detector package has two detectors per spectrometer arm which are optimized for greater sensitivity to this transverse asymmetry.

1.4.5 NEUTRON SKIN CALCULATION

Although there is a high degree of correlation between model predictions for A_{PV} and neutron skin thickness for ^{208}Pb and ^{48}Ca, it is illustrative to build a formalism to get the neutron skin thickness from the measured asymmetry.

The weak charge density of ^{208}Pb, $\rho_W(r)$, can be approximated in 2 parameter Fermi function (similar to charge density) as [25],

$$\rho_W(r) = \frac{\rho_0}{1 + exp[(r - R)/a]}, \tag{40}$$

where ρ_0 is then weak charge normalization factor, R is the weak charge radius parameter, and a is the surface thickness parameter. RMS weak radius, R_W, of a nucleus is,

$$R_W^2 = \frac{1}{Q_W} \int r^2 \rho_W(r) d^3r, \tag{41}$$

where Q_W is the weak charge of the nucleus. The weak charge density, when integrated over volume gives the total weak charge,

$$Q_W = \int d^3r \rho_W(r) = Zq_p + Nq_n, \tag{42}$$

where q_n = -0.9878 is the radiatively corrected weak charge of the neutron, q_p = 0.0721 is the radiatively corrected weak charge of the proton. Then, Q_W = -118.55 is the weak charge of the ^{208}Pb nucleus.

The charge radius of any nucleus can be expressed as [25],

$$R_{ch}^2 = R_p^2 + \langle r_p^2 \rangle + \frac{N}{Z} \langle r_n^2 \rangle + \frac{3}{4M^2} + \langle r^2 \rangle_{s0}, \tag{43}$$

where R_p is the proton radius of the nucleus, $\langle r_p^2 \rangle$ = 0.769 fm^2, is the mean-square charge radius of a single proton, $\langle r_n^2 \rangle$ = -0.116 fm^2 is the mean square charge radius of a single neutron, $\langle r^2 \rangle_{so}$ = -0.028 fm^2 is the contribution of spin orbit currents to R_{ch}, and M is the nucleon mass. Then Eq. 43 becomes,

$$R_{ch}^2 = R_p^2 + 0.5956 \text{ fm}^2 \tag{44}$$

The point neutron RMS radius R_n is related to the weak radius R_W as [25]

$$R_n^2 = \frac{Q_W}{q_n N} R_W^2 - \frac{q_p Z}{q_n N} R_{ch}^2 - \langle r_p^2 \rangle - \frac{Z}{N} \langle r_n^2 \rangle + \frac{Z+N}{q_n N} \langle r_s^2 \rangle, \tag{45}$$

where $\langle r_s^2 \rangle$ is the square of the nucleon strangeness radius. Then using the experimentally measured R_{ch} = 5.503 fm, R_n^2 can be obtained with a small correction $\langle r_s^2 \rangle$ as,

$$R_n^2 = 0.9525 R_W^2 - 1.671 \langle r_s^2 \rangle + 0.7450 \text{ fm}^2. \tag{46}$$

The strangeness radius of the nucleon can be constrained by experimental data, and it is known to be $\langle r_s^2 \rangle$ = 0.02 ± 0.04 fm^2. Then for ^{208}Pb neutron RMS radius is [25],

$$R_{n208}^2 = 0.9525 R_{W(208)}^2 + 0.7875 \text{ fm}^2. \tag{47}$$

Using the same argument with, and $R_{ch} = 3.47$ fm for ^{48}Ca,

$$R_{n48}^2 = 0.9525 R_{W(48)}^2 - 0.0193 \text{ fm}^2. \tag{48}$$

In this way, one can calculate the neutron skin, $R_{skin} = R_n$ - R_p in ^{208}Pb and ^{48}Ca with R_W determined through measurement of A_{PV}.

1.4.6 NEUTRON STARS

Neutron stars are comprised of baryons (protons, neutrons) and leptons (electrons, muons) and outside of black holes they are the densest celestial bodies known. Neutron stars are typically held together by both nuclear forces and gravity against the Fermi pressure, and the high pressure due to gravity is so strong that it can over comes even electron degeneracy pressure, crushing together electrons and protons into neutrons. By exploring different neutron star properties we can place constraints on nuclear physics and different neutron density measurements have implications for nuclear structure and neutron-rich matter in astrophysics.

Although ^{208}Pb and a neutron star has 18 orders magnitude difference in their size (fm vs. km), both share the same EOS, therefore ^{208}Pb can function as a terrestrial laboratory to study the physical properties of neutrons stars. In a neutron star, symmetry pressure pushes against gravity, whereas symmetry pressure pushes against surface tension in nuclei. Neutron skin thickness and the size of a neutron star are connected, through the density dependence of the symmetry energy L. The larger the neutron skin thickness, the larger the symmetry energy slope L, and larger the pressure, and therefore the larger the radius of a neutron star, for a given mass.

The correlation within a specific nuclear structure model between neutron star radius R_{NS} and L is shown in Fig. 17. Once the L value is fixed by an experimental measurement of the neutron skin thickness in ^{208}Pb, one can calculate the radius of a neutron star.

Another property of neutrons stars is their deformability Λ, a measure of the neutron star's tendency to form mass quadrupoles under gravitational forces [15] and can be written as,

$$\Lambda \propto \left(\frac{R_{NS}}{M_{NS}} \right)^5, \tag{49}$$

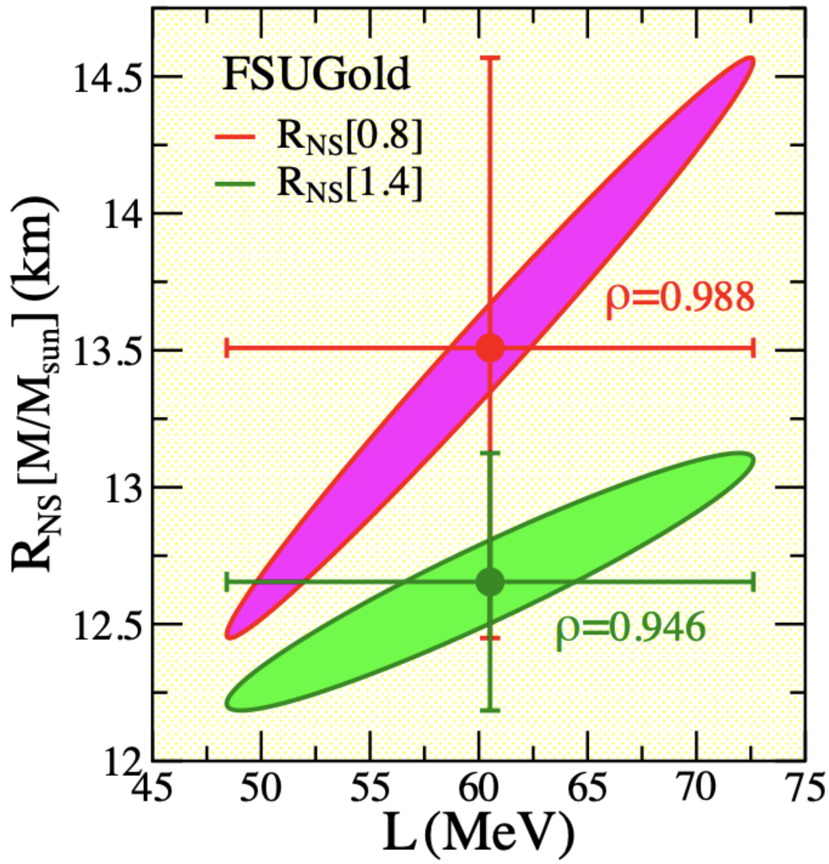

FIG. 17: Covariance ellipses displaying the correlation between the slope of the symmetry energy L and stellar radii for a $0.8M_\odot$ and a $1.4M_\odot$ neutron star, as predicted by the relativistic density functional FSUGold [15].

where M_{NS} is the neutron star mass. LIGO's 2017 detection of a binary neutron star merger set an upper bound on the deformability, and PREX-2 also can constrain this property.

1.4.7 PREX-1

PREX-1 ran in 2010, measured the parity-violating asymmetry in the elastic scattering of electrons off ^{208}Pb at 1.0 GeV and at a 5° scattering angle. It was the first electroweak observation that the weak charge density is more extended than the electric charge density, establishing there is indeed a weak skin around a heavy nucleus.

PREX-1 measured the parity violating asymmetry in ^{208}Pb to be,

$$A_{PV} = 0.657 \pm 0.060(stat) \pm 0.014(sys) \text{ ppm}. \tag{50}$$

The corresponding neutron skin thickness was found to be,

$$R_n - R_p = 0.33^{+0.16}_{-0.18}\ \text{fm}. \tag{51}$$

PREX-1 demonstrated successful control of systematic errors, and achieved systematic error goals, but it was statistics limited and only 15% of the planned statistics were taken because of various experimental difficulties. PREX-2 increased the precision of the parity violating asymmetry measurement and also on neutron skin thickness. The CREX experiment follows the same design as the PREX experiments, but it put constraints on a different realm of nuclear theory.

CHAPTER 2

PREX-2 AND CREX EXPERIMENTAL SETUP

2.1 JEFFERSON LABORATORY

PREX-2 and CREX were run at the Thomas Jefferson National Accelerator facility (JLab) in Newport News, VA, which is a medium energy electron scattering laboratory designed to conduct research for understanding subatomic particles such as quarks and gluons. This is one of the facilities which can conduct parity-violation experiments. The main feature of this lab is the Continuous Electron Beam Accelerator Facility(CEBAF). The facility has three major components: injector, accelerator and four experimental halls. We conducted PREX-2 and CREX in Hall A. PREX-2 was run between June and September 2019 while CREX was run from December 2019 to September 2020. CREX took a longer than expected time because it was interrupted for four months (From March to July 2020) due to the COVID19 pandemic. A sketch of the CEBAF is shown in figure 18.

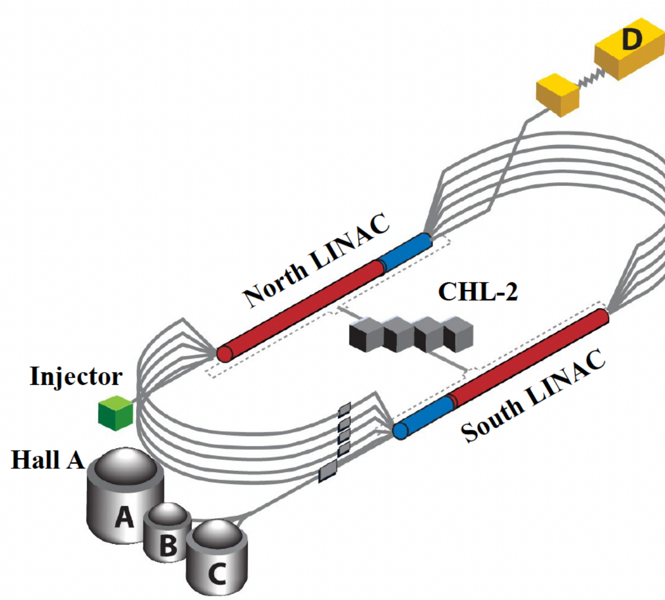

FIG. 18: Sketch of JLab accelerator site and four experimental halls: A, B, C, and D [26]

The electron beam is generated at the injector where it is accelerated from 130keV to 5MeV before entering the first pass. Each linear accelerator (LINAC), uses superconductors to provides necessary electron beam acceleration to reach desired energy and these consists of twenty five cryo-cooled, superconducting radio-frequency (SRF) modules. After the 12 GeV upgrade, the CEBAF is capable of delivering up to 12 GeV electrons to some halls and can deliver up to 200 μA of beam to all four halls simultaneously. The lasers for the halls operate in pulsed mode, out of phase with each other, with the Hall A laser running at 499 MHz bunch pulse timing [27].

2.2 POLARIZED ELECTRON SOURCE

The polarized electrons delivered to the experimental halls originate at the Jefferson Lab polarized electron source (Injector). The polarized source setup is shown in Fig. 19. The set of lasers passing through optical elements, used to convert linearly polarized light in to circularly polarized light. Injector mainly consists of set of lasers, attenuators, insertable half-wave plate (IHWP), RTP Pockels cell, rotatable half-wave plate (RHWP), and photocathode. These components are collectively capable of delivering the parity quality beam (PQB) required by PREX-2 and CREX.

2.2.1 RTP POCKELS CELL (PC)

The right and left handed longitudinally polarized electrons come from right and left circularly polarized light. It starts with linearly polarized photons from a laser source that are then converted to circular polarization with a Pockels cell electro-optic device.

Pockels cell converts the linearly polarized light into circularly polarized light, and it also provides the fast helicity reversal needed for the experiment. The PC's helicity-control mechanisms and electronics are described in the Chapter 3.

2.2.2 INSERTABLE HALFWAVE PLATE (IHWP)

In the injector there is a remotely controllable half wave plate upsteram of the Pockels cell that can be used to insert or retract from the beam line. The main use of the IHWP is to reverse the incident laser polarization by 90 degrees before entering the Pockels cell. This is one of the slow helicity reversal methods. Change in the size of measured asymmetry with respect to the IHWP change indicates there is a helicity correlated systematic contamination. During these experiments, IHWP changed by timescales ranging from 6 to 8 hours. Using

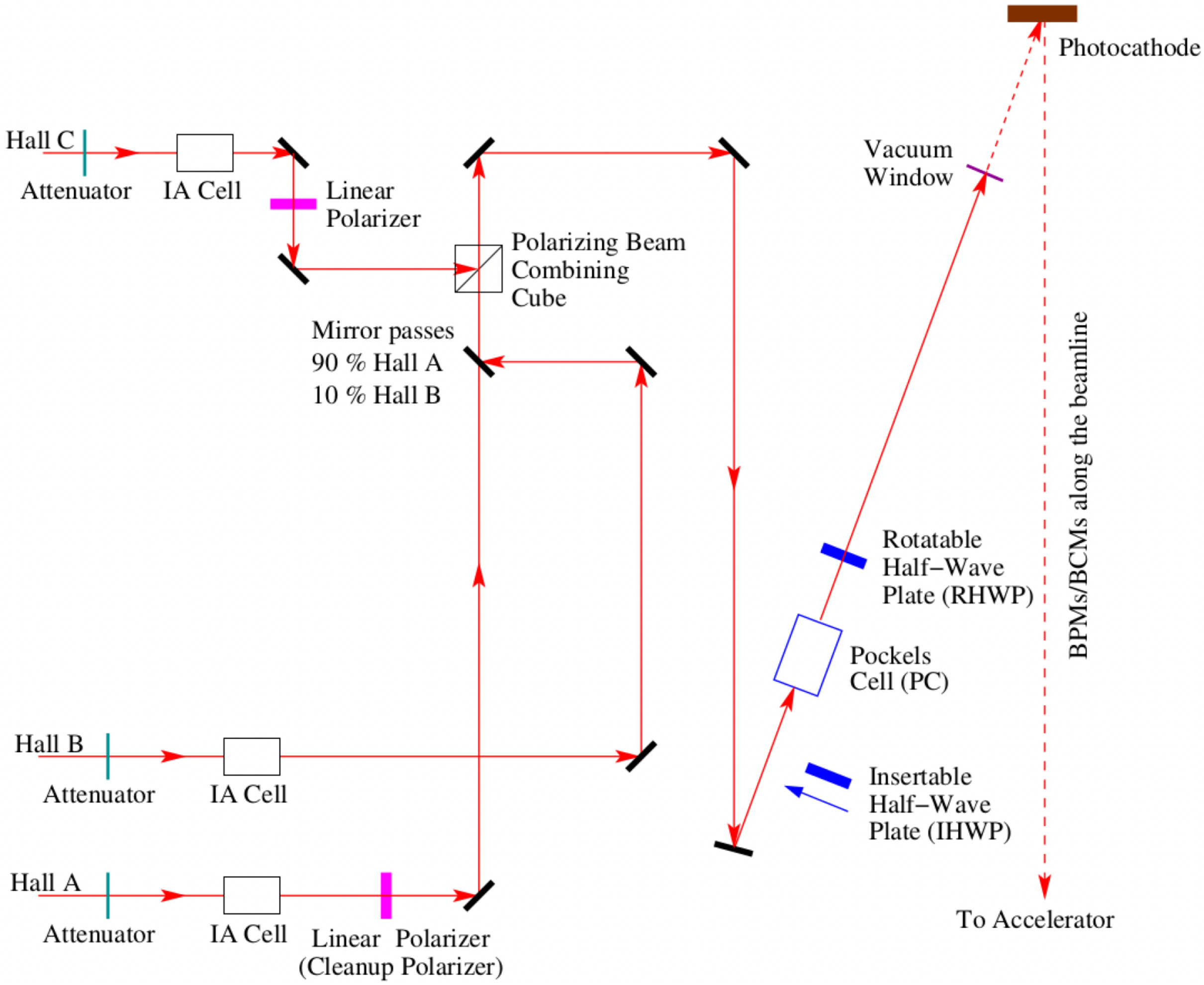

FIG. 19: Layout of the polarized electron source [12].

IHWP we can cancel out the helicity correlated systematic uncertainty, by taking an equally statistically weighted, and sign-corrected, average of the two IHWP state data sets.

2.2.3 PHOTOCATHODE

The laser light exiting the Pockels cell then hits the surface of a strained super-lattice Gallium Arsenide (GaAs) photocathode, where the circularly polarized photons generate the longitudinally polarized electron beam for injection into the accelerator. The photocathode is composed of GaAs, a semiconducting material with a band gap of about 1.4 eV to 1.6 eV, near IR laser light is enough to excite electrons in GaAs from valance band up to the conduction band where they are ejected from the material by the photoelectric effect.

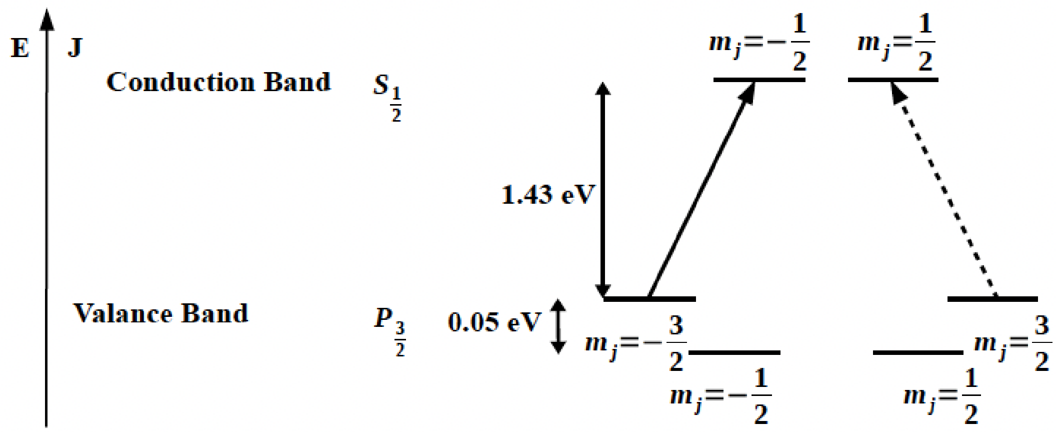

FIG. 20: Photo-emission process in a strained GaAs photocathode [7].

2.2.4 INJECTOR SPIN MANIPULATION

The so-called "double Wien filter" is the second method of slow helicity reversal, located downstream of the photocathode. It consists of two orthogonal spin manipulators separated by two solenoid magnets. Here the electron beam helicity is reversed relative to both the electronic helicity control signals and the voltage applied to the Pockels cell, hence the effect should only be seen in the sign of the polarization, and therefore the scattering asymmetry. The beam polarization is oriented vertically by the first solenoid and the vertical Wien filter. Then the beam polarization is rotated by 90 degrees by the second solenoid. The horizontal Wien filter is used to optimize the degree of longitudinal polarization in to the experimental hall. Combination of IHWP system and the double Wien system improves cancellation of helicity-correlated systematic errors. This is done by averaging the asymmetries measured during a pair of opposite Wien states that have roughly equal amounts of data. During PREX-2 the Wien settings changed roughly every two to three weeks, while during CREX it is changed only twice [28].

2.3 ACCELERATOR

JLab's CEBAF accelerator is composed of two super conducting radio frequency (SRF) parallel linear accelerators (north and south LINAC). Each LINAC has 25 helium-cooled cryogenic modules and each module is made of 8 superconducting niobium cavities. Electrons from the injector are kept circulating around LINACs until the desired energy is reached and then extracted into the experimental halls using radio frequency extractors and septum

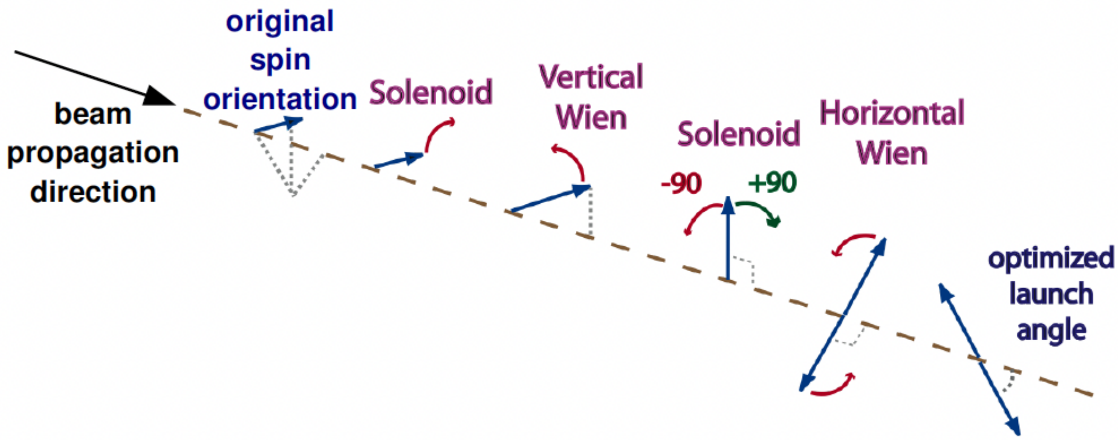

FIG. 21: A diagram of the double Wien filter concept in the injector [28].

magnets.

2.4 HALL A BEAMLINE

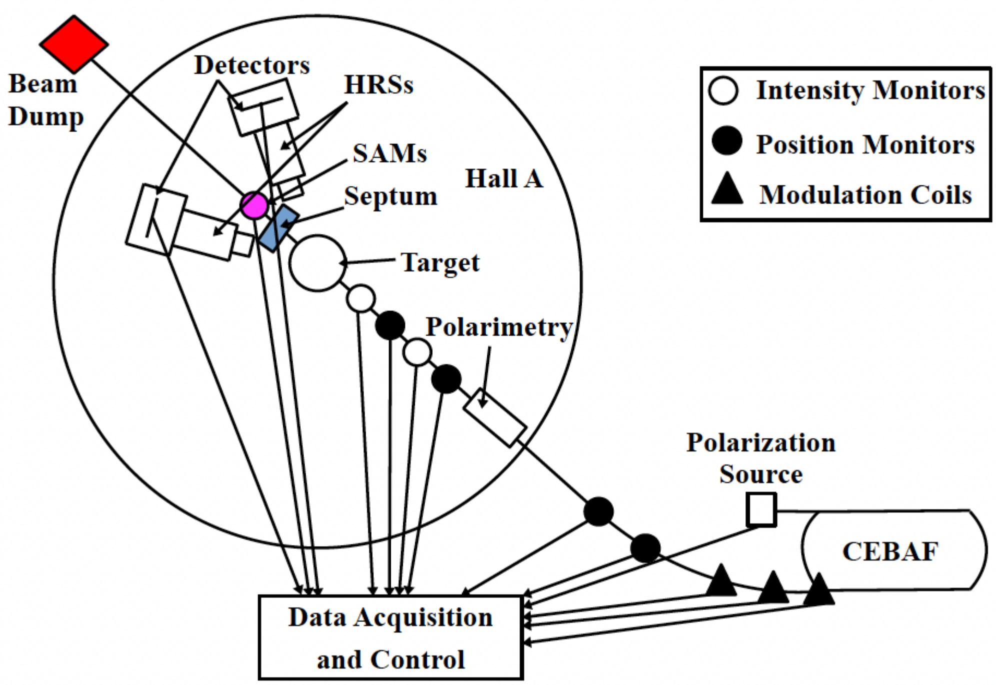

FIG. 22: A diagram of the Hall A beamline. [7]

After acceleration in CEBAF, the beam is coming into the beam switch yard (BSY), where the electron beam is separated for distribution in to the halls. The Hall A beamline begins at the BSY and ends at the beam dump in Hall A. The beamline is mounted 10 feet above the floor and the floor, wall, and roof of the Hall Are made of concrete. The beam is transported through different components such as beam position monitors, beam current monitors, the beam modulation system, polarimeters, and target scattering chambers.

2.4.1 BEAM POSITION MONITORS (BPM)

Several beam position monitors are placed along the Hall A beamline to track the beam position and to calculate helicity correlated position differences. Usually BPMs are placed after beam elements such as steering magnets, quads or other focusing beam elements.

BPMs are wire stripline monitors composed of four antennas, X_P, X_M, Y_P and Y_M, placed symmetrically around the beam pipe, with X and Y referring to the horizontal and vertical directions and P and M referring to the plus and minus sides of these axes. Each of these antennas provide a signal proportional to the beam position and beam intensity. The signal from each antenna is sampled and integrated, and the resulting signal is sent to the integrating DAQ where they are measured as voltages in the ADCs[1].

The antennas are either oriented along the horizontal-vertical axes or they are oriented at ± 45 degrees. The antennas are rotated 45 degrees with respect to the horizontal-vertical X-Y plane to avoid synchrotron radiation. In asymmetry analysis, the output from these stripline antennas are used to calculate the beam position as,

$$X = k\frac{X_P - X_M}{X_P + X_M} \qquad Y = k\frac{Y_P - Y_M}{Y_P + Y_M} \tag{52}$$

where k = 18.76 mm is a calibration constant [12]. Those that are oriented along ± 45 are rotated in analysis so that bpmX corresponds to horizontal and bpmY corresponds to vertical.

$$X_H = \frac{x - y}{\sqrt{2}} \qquad Y_H = \frac{x + y}{\sqrt{2}} \tag{53}$$

[1] Analog signal to digital signal converters

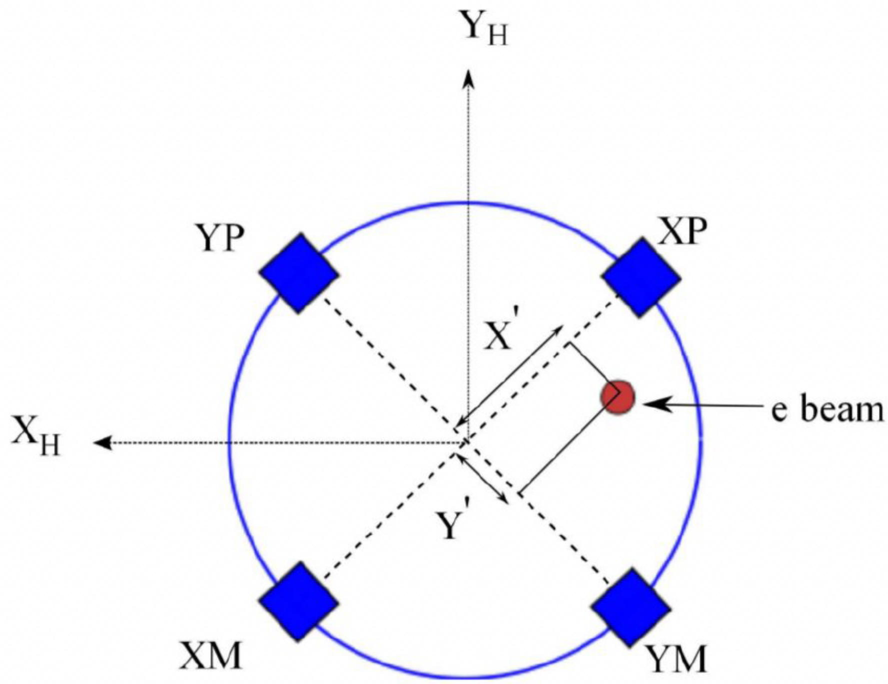

FIG. 23: Schematic diagram of a four wire-antennae of a stripline BPM, rotated by 45 degrees from experimental hall horizontal-vertical direction [29].

For PREX-2 and CREX a special set of magnets were used to lock the beam position on the target, the beam position lock is achieved using BPM4a and BPM4e. We also used these two BPMs to measure the helicity-correlated position and angle differences on the target. Hall A arc BPMs, BPM11 and BPM12, are the most sensitive to the beam dispersion and because of that those are used to measure beam energy.

BPMs located within the Compton polarimeter's chicane are used when tuning the beam delivery to the hall and for analyzing the Compton polarimetry data. BPMs located within the injector are used when setting up the polarized source to minimize helicity correlated asymmetries in the injector.

2.4.2 BEAM CHARGE MONITORS (BCM)

PREX-2 and CREX used Beam Charge Monitors (BCMs) to track how much current was being delivered to the hall and to measure and correct helicity-correlated charge asymmetries. Figure 24 shows a schematic diagram of Hall A BCM system. Three types of BCMs are used for the experiment: UNSER, upstream beam current monitor (US BCM) and downstream

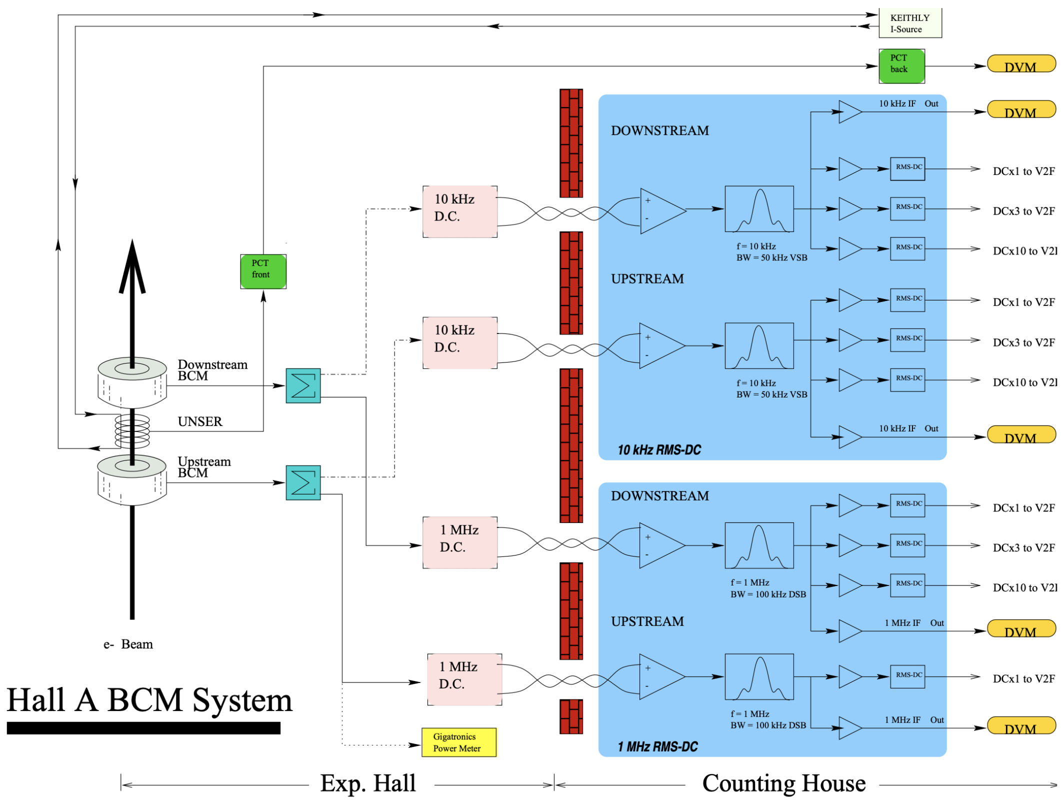

FIG. 24: Schematic of the Hall A beam current measurement system [30].

beam current monitor (DS BCM).

The UNSER bcm is a parametric current transformer, which is relatively noisy and unstable on minute timescale, making it unreliable to measure the beam current continuously. However it's highly linear and stable on short time scales, so it can be used to calibrate other BCMs. UNSER is calibrated by passing a known current through a wire inside the beam pipe and other BCMs' pedestals are measured with respect to the UNSER using dedicated current ramp runs [30].

The US BCM and DS BCM are resonant radio-frequency (RF) cavities made of stainless steel cylindrical waveguides which are tuned to the frequency of the beam, which is 1.497 GHz. Each of these cavities outputs a voltage signal proportional to the beam intensity, output signals are then split into two, one converted to 10 kHz and the other to 1 MHz [30]. We only use the 1 MHz channels during PREX-2 and CREX. These BCMs, when properly calibrated, provided a continuous current monitor for each helicity state for the experiment. In addition, BCMs located in the injector are also fed into the parity DAQ and are used for injector source setup and studies.

2.4.3 BEAM MODULATION (DITHERING)

PREX-2 and CREX used a beam modulation system that is designed to change the beam's position, angle and energy on target, to quantify the response of beam monitors and main detectors to these changes. These responses are used to make corrections to the measured asymmetry to reduce contamination from helicity correlated false beam asymmetries.

The beam modulation system has six magnetic coils to modulate the trajectory in x and y directions. These coils were placed on the Hall A beamline upstream of the dispersive arc. The energy modulation was performed via a vernier input on a cavity in the accelerator's south LINAC. Beam modulation cycle was run every 10 min and last approximately 1 minute. Each completed cycle is referred to as a super cycle and has complete modulation of the seven coils in sequence. A schematic diagram of the various coils along the beamline is shown in Fig. 25

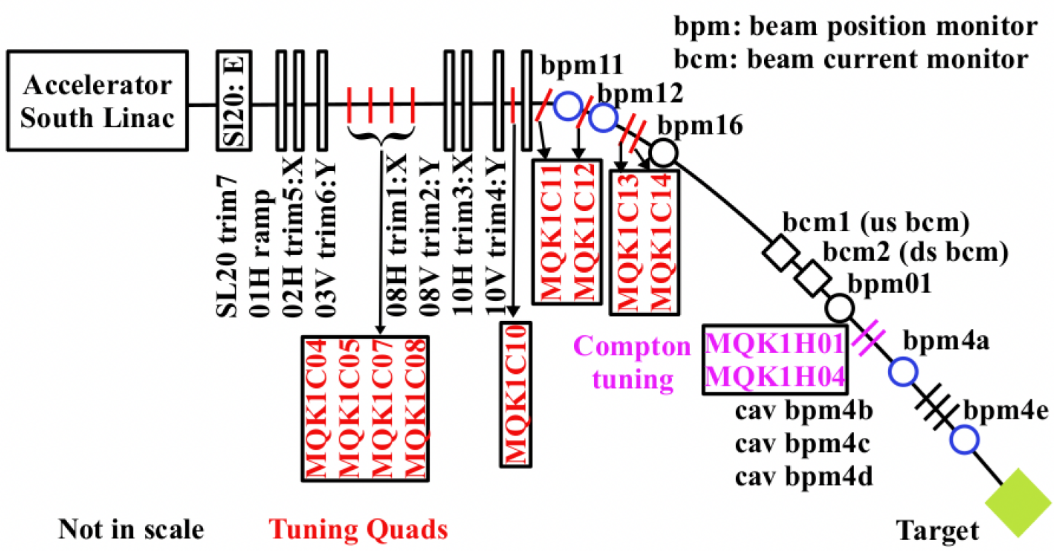

FIG. 25: Schematic view of the dithering coils. Trim1, trim3, and trim5 modulate the beam horizontally, trim2, trim4, and trim6 modulate the beam vertically, and trim7 modulates the beam energy [7].

2.4.4 POLARIMETERS

Beam polarization is one of the systematic corrections for the experiment and must be estimated precisely. The experimental asymmetries are scaled by the measured beam polarization to obtain the physics asymmetries.

During PREX-2 and CREX, the beam polarization was measured by three different polarimeters: Mott, Moller and Compton. The Moller and Compton polarimeters sat in Hall A while the Mott polarimeter, was on the injector beamline.

Mott Polarimeter

The Mott polarimeter is located at the 5 MeV region of the accelerator. This measured the beam polarization by scanning the horizontal wien field to maximize transverse polarization onto a gold foil target and scattering the 5 MeV longitudinally polarized electrons off the target. Backscattered electrons were measured along horizontal and vertical directions by four detectors and asymmetry from the scattering is then compared to a theoretical analyzing power to calculate polarization [31].

The Mott beam polarization measurements were invasive, and were performed during beam studies by the accelerator group. PREX-2 and CREX did not use the results of the Mott polarimeter in the extraction of the final beam polarization. The Mott measurement is primarily used to orient the beam polarization into the horizontal plane, and as a cross check on the magnitude of the laser polarization.

Moller Polarimeter

The Moller polarimeter is a Hall A standard polarimeter located between the raster coils and the target BPMs. To measure beam polarization, Moller polarimeter uses a magnetically polarized thin iron foil target to perform Moller scattering ($e^- + e^- \rightarrow e^- + e^-$) of the incident beam with the polarized electrons in the iron and measure the asymmetry in the scattered electrons. Moller polarimeters can make measurements over a wide range of beam energies but must be operated at low currents ($\sim$1μA) to avoid target depolarization and radiation load in the hall. Since it is required to direct beam onto the separate Moller target apparatus, these measurements are invasive so dedicated Moller runs must be taken. Schematic of Moller polarimeter is shown in Fig. 26.

The Moller target is placed inside a solenoidal magnetic field, and the field polarizes target foil along the beam line. At the target, elastic Moller scattering off the atomic electrons occurs and the scattering cross section contains a spin and helicity dependence. The measured Moller asymmetry is given by,

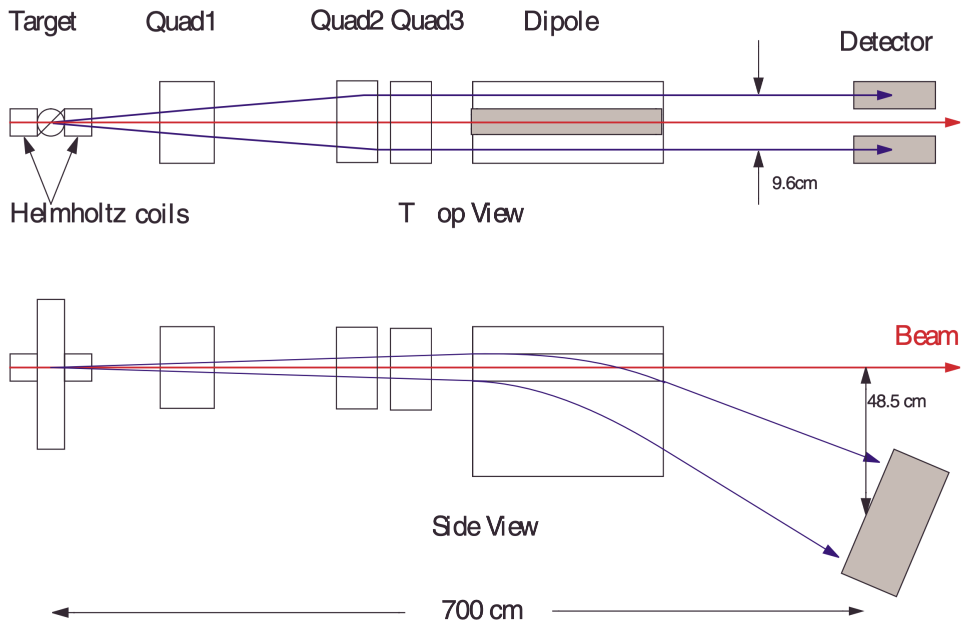

FIG. 26: Schematic of the Hall A Moller polarimeter top and side view [32]

$$A_{Moller} = < A_{ZZ} > \times P_e \times P_t, \tag{54}$$

where P_e is the beam polarization, P_t is the target polarization, and $<A_{ZZ}>$ is the system's sensitivity to changes in beam and target polarization on scattering cross sections (average analyzing power), which is obtained from simulation [33]. The P_t is obtained from calculation given the precise foil location and magnetic field size and direction. The limiting source of systematic uncertainty for the Moller measurement was the foil polarization and the extrapolation from low current to high current that experiments actually runs at.

The Moller measurements require a special setup for its transport magnets (quads and dipoles) [34], hence several hours of setup was needed to enter the Moller run configuration and to return to normal running condition. During PREX-2 and CREX Moller measurements were performed every one to two weeks, and each measurement takes approximately one to two shifts (8-16 hours).

Compton Polarimetr

The Hall A Compton polarimeter use Compton scattering of the polarized electrons with a circularly polarized photon beam to measure the electron beam polarization. This was located towards the beamline entrance of the hall, and consisted of a magnetic chicane, a photon source, a photon detector, and an electron detector. During Compton operations, the electron beam is steered downward about 30 cm from the primary beamline in a magnetic chicane into a resonant optical cavity where a circularly polarized green laser is locked in to the cavity. The electron beam then hits the laser resulting in Compton scattering and scattered photons are detected by a photon detector. This signal is used to calculate an asymmetry in the photon detector from which we can get the electron beam polarization. The unscattered electron beam is then diverted out of the chicane and continues along into Hall A for the main experiment, hence The Compton can run non invasively to the experiment.

The Compton polarimeter theory, experimental setup and analysis will be discussed in Chapter 4 and Chapter 5.

2.4.5 RASTER AND HARP SCANS

The intrinsic beam spot size is very crucial for the experiment because target health depends on that. Too large a spot size can introduce extra noise in the main detector signal while too small a spot size may lead to target melting, therefore beam spot size should be optimized. For both PREX-2 and CREX the intrinsic spot size was kept on the order of $100 \times 100\ \mu m^2$ before the target. To measure the spot size, array of conductive wires were passed through the beam which is called as a "harp scan". This was done at the beginning of the experiment or if there is any change in the beam properties upstream of the target.

During PREX-2 and CREX, a system called "raster" was necessary to prevent thermal damages to the target due to beam heating. This was used to distribute the beam profile systematically over the target face in a repeating square or rectangular pattern. It is crucial to use a proper raster size, if the raster is too large, the spectrometer optical calibration becomes difficult, if the raster is too small, the target could be damaged by high beam intensity. For the ^{208}Pb target, the raster was set at 4 mm $\times$ 6 mm and for the ^{48}Ca target, it was set at 2 mm $\times$ 2 mm. Also, for the ^{208}Pb target the raster pattern is synchronized with the helicity pattern to eliminate noise arising from target non-uniformity. The raster system has two magnetic coils located several meters upstream of the target, to steer the beam vertically and horizontally.

The raster size and pattern are checked using low current runs called spot++. The size of the raster is verified using the counting mode scintillator detectors in the spectrometer focal plane(see Section 2.6.3). The raster current is measured as a function of time to get the detector rates for each rastered position on the target. The raster size is determined by running the rastered beam on a carbon hole target, the known size of the hole could be compared to the size of the raster. Figure 27 shows a typical spot++ run on a carbon hole target.

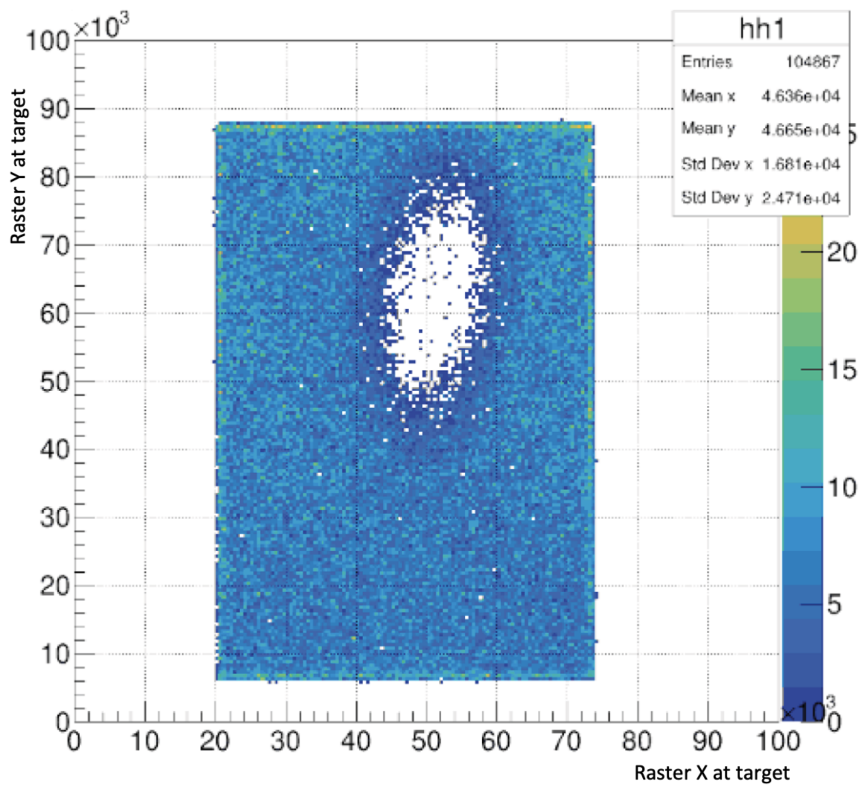

FIG. 27: Raster map on the carbon hole target. This plot use uncalibrated raster units, to perform the calibration the size of the hole is compared to the size of the raster.

2.4.6 SMALL ANGLE MONITORS (SAMS)

Small Angle Monitors (SAMs) are placed downstream of the target to measure the rate of charged particles emerging from the target at small (∼0.5 degrees) angles during the experiment. The SAMs are located approximately 7 m downstream of the target, and positioned symmetrically around the beamline. The SAMs consist of 8 quartz detectors with light guides and photo-multiplier tubes. The layout of the SAMs can be seen in Fig. 28.

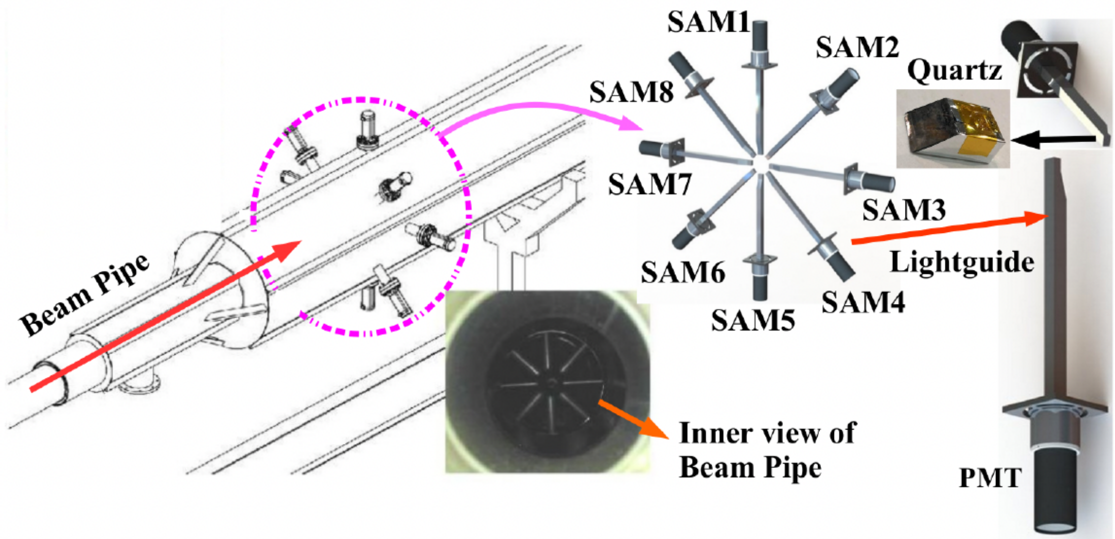

FIG. 28: Schematic of the SAMs in the downstream beamline [7].

SAMs symmetric design helps to monitor helicity correlated beam position and angle differences and these are sensitive to changes in beam position, angle, energy and quality of the target. SAMs are a good diagnostic tool to monitor and help correct for beam related false asymmetries.

2.4.7 TARGET SYSTEM

The PREX-2 and CREX targets were inside a sealed aluminum scattering chamber which had two copper target ladders. One ladder can slide in and out of the beam horizontally, and the other can slides at an angle of 45 degrees. A CAD drawing of the chamber is shown in Fig. 29.

The primary horizontal ladder (the “cold” ladder) contained total of 16 targets, ten ^{208}Pb PREX-2 production targets, one ^{48}Ca CREX production target, one ^{40}Ca target, two natural Pb targets, one carbon foil target, and one carbon foil target with a 2 mm diameter hole. During PREX-2, running slot for the ^{48}Ca target was kept empty. For normal running this ladder was cooled by liquid helium, and the temperature would be between 17 K and 26 K.

The other 45 degree ladder (the “warm” ladder) contained five targets which were used

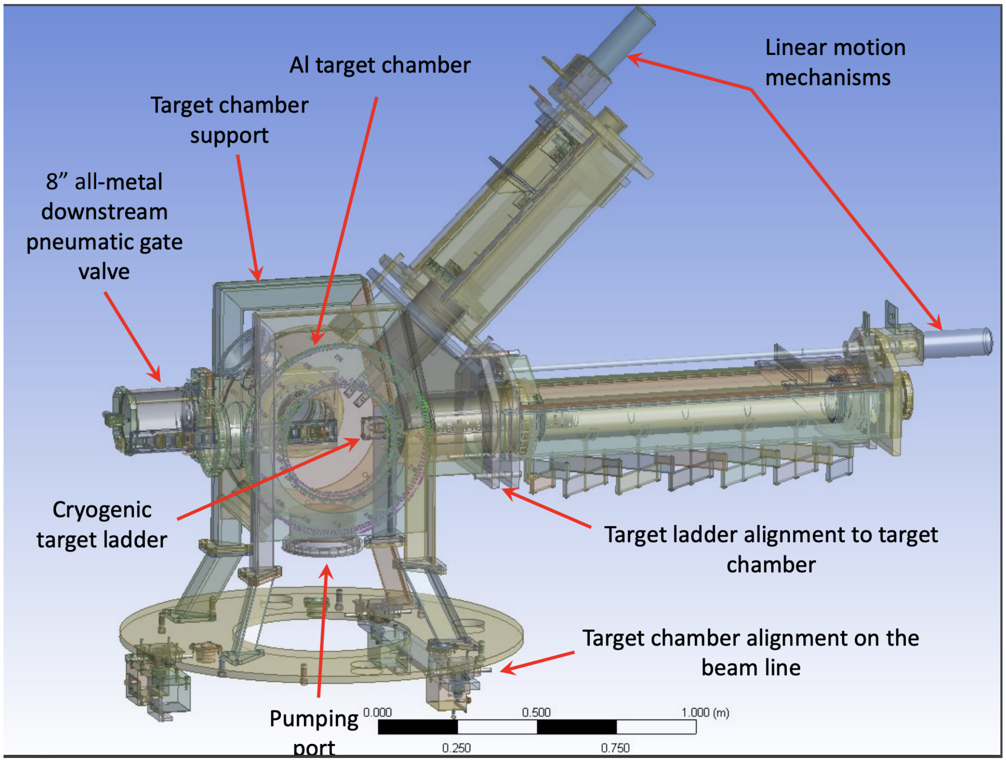

FIG. 29: PREX-2 and CREX scattering chamber [35].

for spectrometer optics calibration. This ladder had one natural Pb target, one tungsten target, one carbon foil target, one carbon hole target, and one cell of water. This ladder was kept at room temperature.

The PREX-2 production targets have a 0.553 mm thick 90-95% isotopically pure ^{208}Pb foil sandwiched between two 0.25 mm thick diamond foil layers. The ^{208}Pb target is sandwiched between diamond foil to keep the Pb foil below its melting point to prevent it from potential damage, but the diamond eventually degrades due to beam damage. Degradation of diamond causes non-uniformity in the lead target thickness and ultimately leads to target melting. Degraded ^{208}Pb targets would result in excess noise in the detector and increased radiation in the hall. Because of that, 10 production targets were installed and degraded target can be switched with a fresh Pb target. PREX-2 used seven production targets before the end of the experiment.

One indicator of target degradation is a sudden increase in the measured main detector asymmetry widths, also it will increase power deposition in the upstream collimator (Section 2.4.8) and increases radiation levels inside the hall and causes an increase in Compton background rates. Figure 31 shows a melted Pb target and how detector widths increases

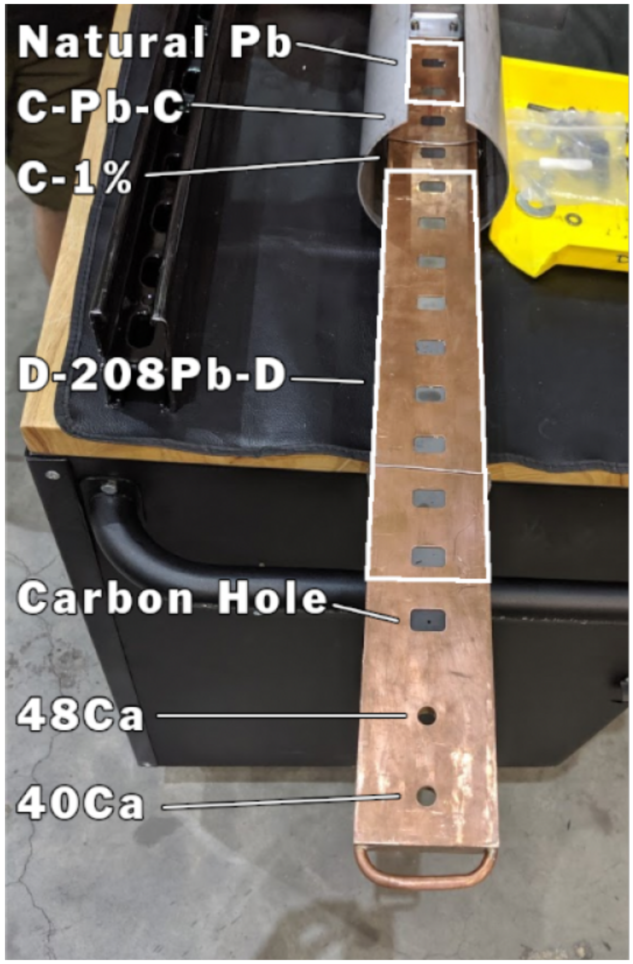

FIG. 30: Schematic of the cold ladder [36].

when it's degraded. Target degradation is measured using spot++ runs. The raster current distribution on target can be plotted and any nonuniform distribution indicates target degradation which is shown in Fig. 32.

The CREX target is a single 6 mm thick piece of 95% pure isotropic ^{48}Ca, composed of 95.99% ^{48}Ca, 3.84% ^{40}Ca, and a small fraction of other isotopes. Ca doesn't undergo target degradation like Pb so only one target was sufficient for the entire experiment. But unfortunately due to beam mis-steering incident which occurred on January 18th, 2020 the original ^{48}Ca target was melted. The remainder of the experiment was conducted using an alternate ^{48}Ca target, which had been constructed for earlier tests. The new Ca target is a stack of three separate pucks each with roughly 12.7 mm diameter. A photograph of the damaged Ca target is shown in Fig. 33.

2.4.8 COLLIMATOR SYSTEM

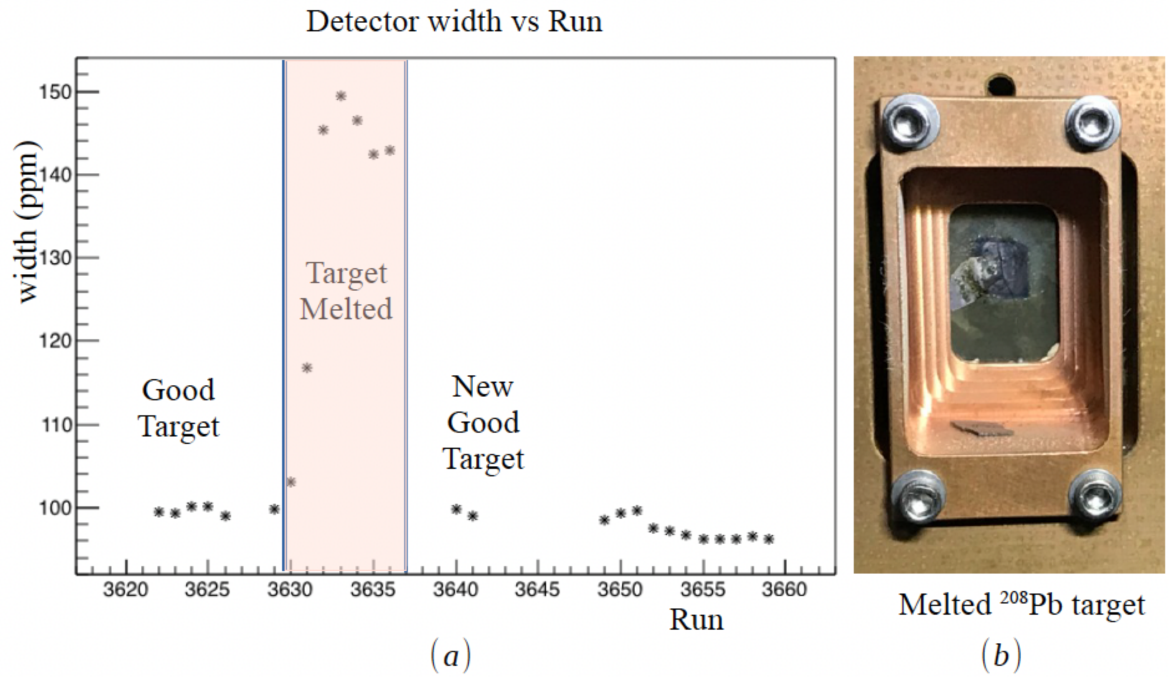

FIG. 31: Target degradation in production running. (a) detector width of measured asymmetry versus run number (b) A photograph of a melted ^{208}Pb target [7].

The purpose of the PREX-2 collimator system is to optimize the "High Resolution Spectrometer" (HRS) acceptance for the figure of merit and to mitigate radiation. One collimator system is located between the scattering chamber and the septum magnet and other collimator is at the entrance of the first quadrupole magnet Q1 (see Fig. 36).

The beamline collimator (between scattering chamber and the septum magnet) is approximately 80 cm downstream from the target. It is designed to reduce the radiation coming from low angle scattered beam that have a scattering angle too large to reach the dump, but too narrow an angle to reach the HRSs. This is made out of a copper-tungsten alloy and is aligned with the central beam axis. It is 10 cm in diameter, 10.5 cm in length and consists of a spiraling water channel for cooling. The collimator allows the scatters that are less than 0.78 degrees and absorbs rest of the scatters, protecting Hall A components downstream of the target.

The collimators at the Q1 entrances are made of lead and used as the HRS acceptance defining collimators for the experiments. The left and right collimators are symmetric with respect to the beamline to maximize systematic error cancellations. A photograph of these

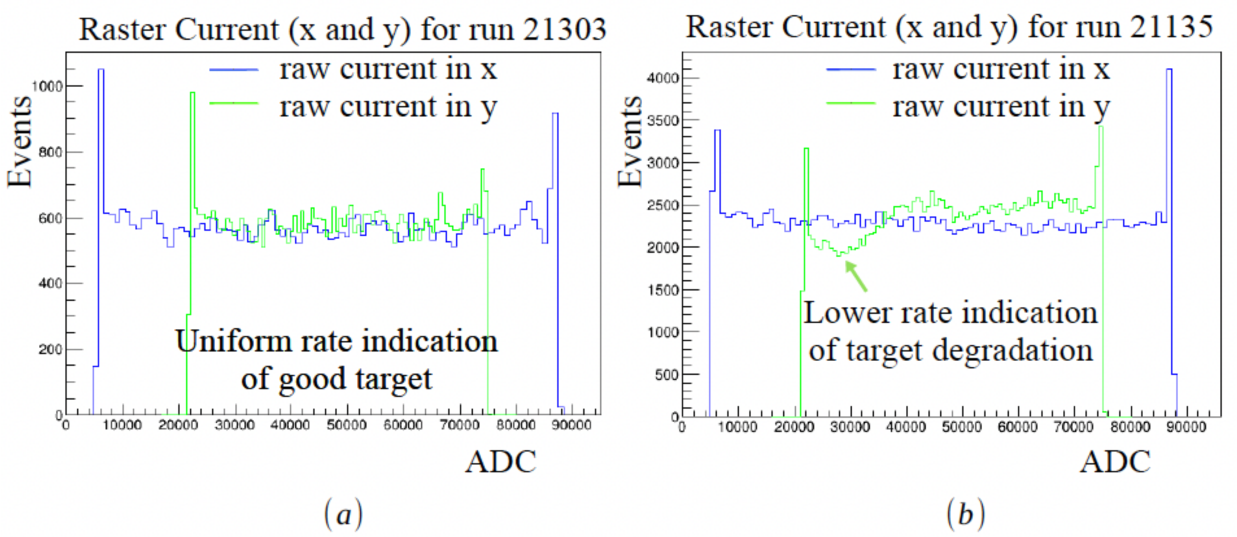

FIG. 32: Counting mode raster checks (a) Raster map of one of the ^{208}Pb targets when it was fresh. (b) Raster map on one of the degraded ^{208}Pb targets [7].

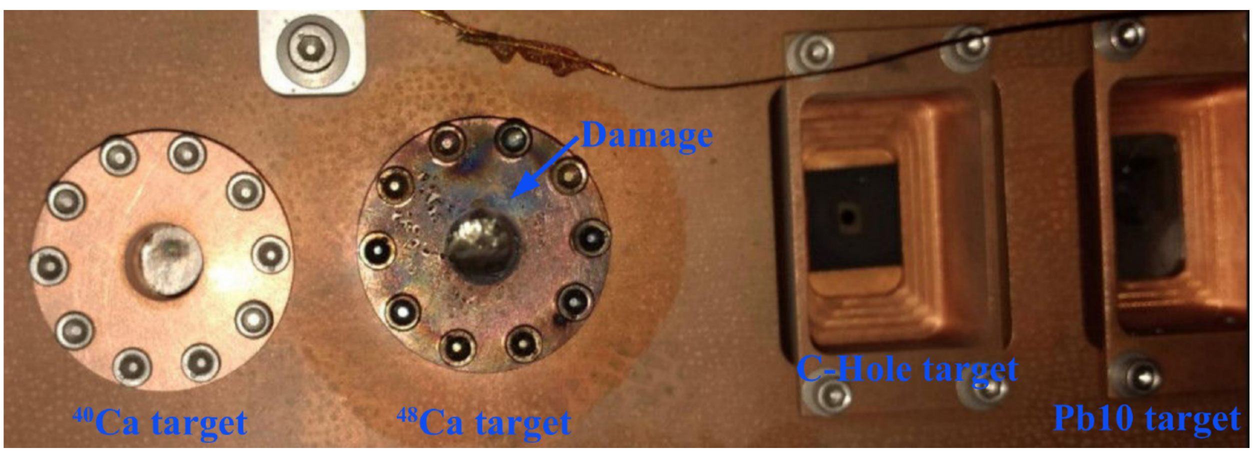

FIG. 33: Photograph of damaged original ^{48}Ca target [37].

collimators is shown in Fig. 34.

2.4.9 SEPTUM MAGNET

The septum is used to overcome the physical constraints of the HRS's. The minimum angle the spectrometers can be rotated with respect to the beamline is 12.5 degrees, but

FIG. 34: Photograph of the Q1 magnet entrances, with the acceptance defining collimators, painted blue [7].

PREX-2 and CREX central acceptance scattering angle is ∼5 degrees. The septum magnets bend elastically scattered electrons at ∼5 degrees, into the HRSs (after the beamline collimator).

The septum is located between the target scattering chamber and the first quadrupole of the HRSs. Figure 35 shows a CAD view of the septum and beamline collimator used in PREX-2 and CREX. The septum is composed of two non-superconducting magnetic dipoles with three coils each, which induce magnetic fields up and down, which bend the forward moving scattering electrons left or right into the spectrometers. The unscattered and scattered electrons at much smaller angles pass through the central beamline to the beam dump.

2.5 HIGH RESOLUTION SPECTROMETER

PREX-2 and CREX use the standard Hall A HRS system which has two identical HRSs

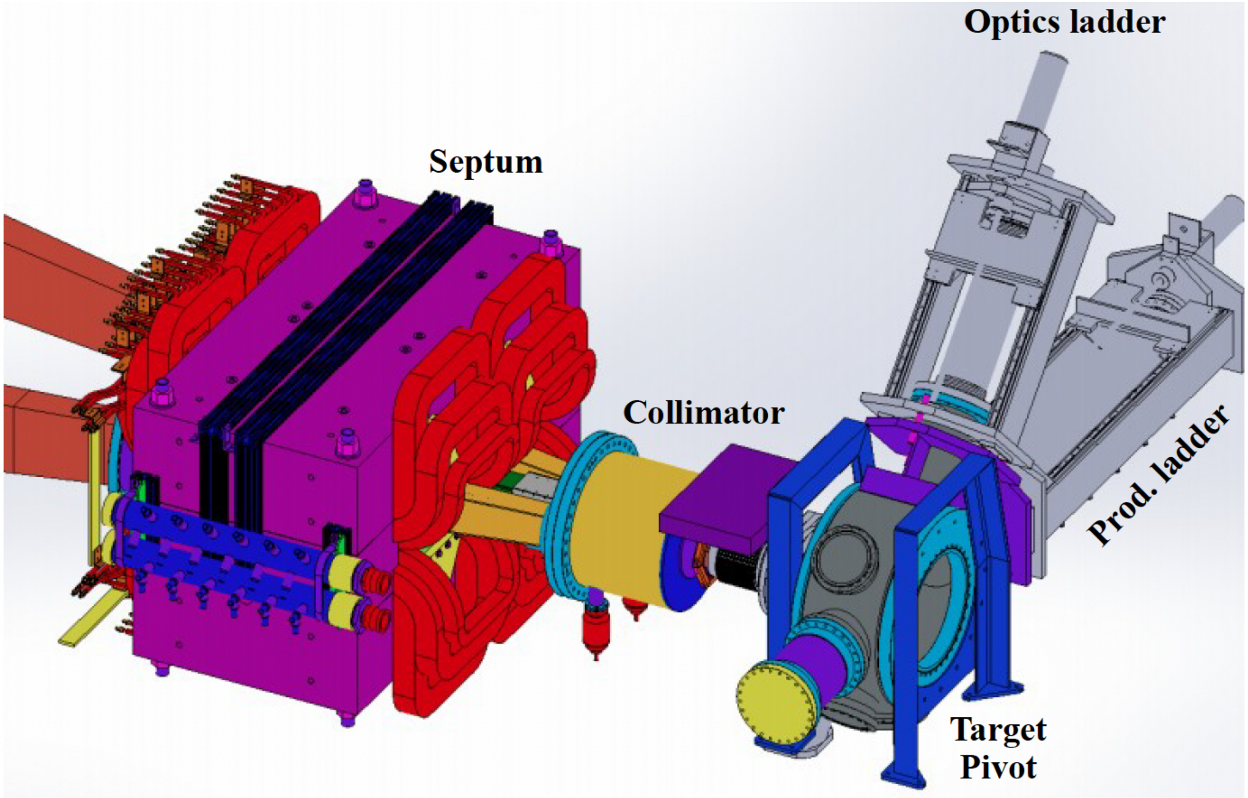

FIG. 35: CAD view of the septum magnet and beamline collimator used for PREX-2 and CREX [7].

positioned symmetrically on opposite sides of the beamline. There are a series of magnets, two quadrupoles, large dipole magnet and another quadrupole magnet to focus and guide the beam into the spectrometer. A schematic of magnet system is shown in Fig. 36. Each magnet is tuned during the commissioning of both PREX-2 and CREX to provide good resolution and focusing of the elastic events onto the main quartz detectors.

2.6 MAIN DETECTORS

The PREX-2 and CREX main detectors and counting mode detectors are placed inside a concrete shielding hut at the top of both HRSs. In each HRS the detector package has integrating quartz detectors (main detectors and auxiliary A_T detectors), Gas Electron Multiplier (GEM) chamber tracking system and standard Hall A Vertical Drift Chamber (VDC) tracking system with scintillators. To protect the detector system from ionizing radiation backgrounds, the detector systems, data acquisition systems and high voltage controls are

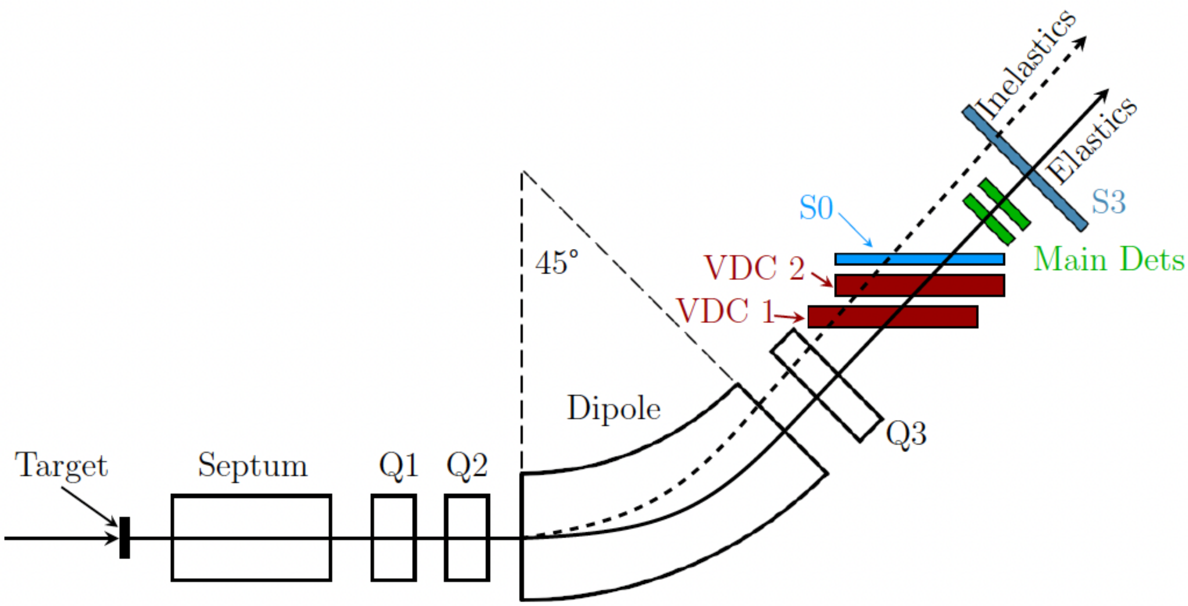

FIG. 36: A diagram of the HRS optics for PREX-2 and CREX [7].

housed within the shielding hut. Photograph of detector package is shown in Fig. 37.

2.6.1 INTEGRATING DETECTORS

Both PREX-2 and CREX had four main detectors, with two in each spectrometer arm, which is primarily dedicated to the integration mode physics asymmetry measurements. The two detectors in each arm are placed one upstream and one downstream. Each individual quartz detector uses a single piece of fused quartz that is 5 mm thick, 3.5 cm wide, and 16 cm long. A photomultiplier tube (PMT) was attached to each detector which would detect the Cerenkov light from particles travels across the quartz.

Each detector package had two background monitoring A_T detectors, downstream of the main detectors. A_T detectors are used for monitor any parity-conserving asymmetry backgrounds from residual transverse polarization of the electron beam or any other possible false asymmetry backgrounds. A_T detectors are identical in design to the main detectors.

2.6.2 VERTICAL DRIFT CHAMBERS

Hall A detector package had two identical vertical drift chambers (VDCs) in both spectrometer arms. Particle tracking is done by using VDCs located about 3.5 m downstream of

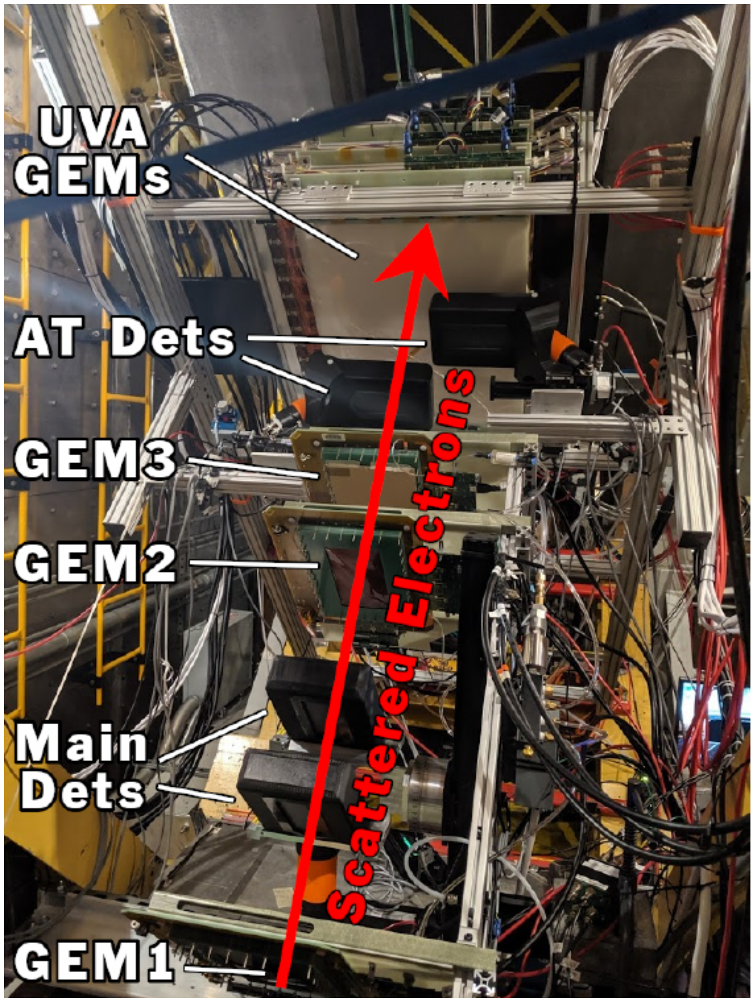

FIG. 37: The detector package used during PREX-2 and CREX [36].

the Q3. Each VDC has several planar grids of thin high voltage signal wires. The chamber is filled with a mix of argon and ethane gas such that when a charged particle passing through the gas, it ionizes along the track. These tracks are used to identify the position and angle of incoming electrons [30].

2.6.3 SCINTILLATORS

PREX-2 and CREX used two plastic scintillators in each HRS to produce event triggers while running the counting mode DAQ. The first detector called "S0" is placed between the second VDC and the main detectors in each arm. The second detector, which is an array of scintillators, called "S3" is placed downstream of the entire detector package (see Fig. 36). These scintillators are always turned off when the counting mode DAQ is not in use.

2.7 DATA ACQUISITION

The PREX-2 and CREX experiments had implemented two independent Data Acquisition (DAQ) systems for integration and counting modes. The integrating DAQ (parity DAQ) was used for the main physics asymmetry measurement and the counting mode DAQ was used for particle tracking, Q^2 measurements, background studies, and other HRS optics calibrations.

2.7.1 INTEGRATING MODE DAQ

Parity experiments such as PREX-2 and CREX have very high scattering rates and it's impossible to count individual hits on the detector. Because of this, integration method is required. The parity DAQ, integrates the detected signal over a helicity window, and saved the integrated signals for each helicity window as a single event. This DAQ could handle extremely high scattering rates with minimal DAQ dead time hence used for the physics asymmetry measurement.

PREX-2 and CREX parity DAQ consists of four VME crates (signal processing modules): Counting House(CH), Left HRS (LHRS), Right HRS (RHRS) and Injector crate. The signals from various beam monitors and detector signals are sent to these different crates. The DAQ systems are all controlled by a central Linux workstation in the Hall A counting house which runs the CODA Run Control (RC) system. VME crates send data over JLab's Ethernet network to the RC system. The Event Transfer (ET) system provides central access to data events for multiple clients in real time. The ET system is used for controlling beam charge asymmetry feedback and for monitoring the data in real time. A schematic of the DAQ systems is shown in Fig. 38.

The helicity frequency is controlled using the helicity control board in the injector, where the helicity patterns are created pseudo-randomly and fed into the Pockels cell. The helicity signal that is sent to the Pockels cell is not sent to the other crates directly, but is instead delayed by 8 helicity windows for 120 Hz and 16 windows for 240 Hz helicity frequency. The delayed and randomized helicity signal can eliminate false asymmetries arise from electronic pickup from reporting of the helicity signal to the DAQ. The timing scheme of the DAQ was executed by the HAPPEX timing board (HAPTB) and this is triggered by the Macro Pulse Signal (MPS). Each MPS window consists of T_{Settle} and T_{Stable} time. The leading edge of T_{Stable} triggers the parity DAQ to begin data acquisition. T_{Settle} is the amount of time during which the beam polarization state is unacceptable (time to go from one helicity state

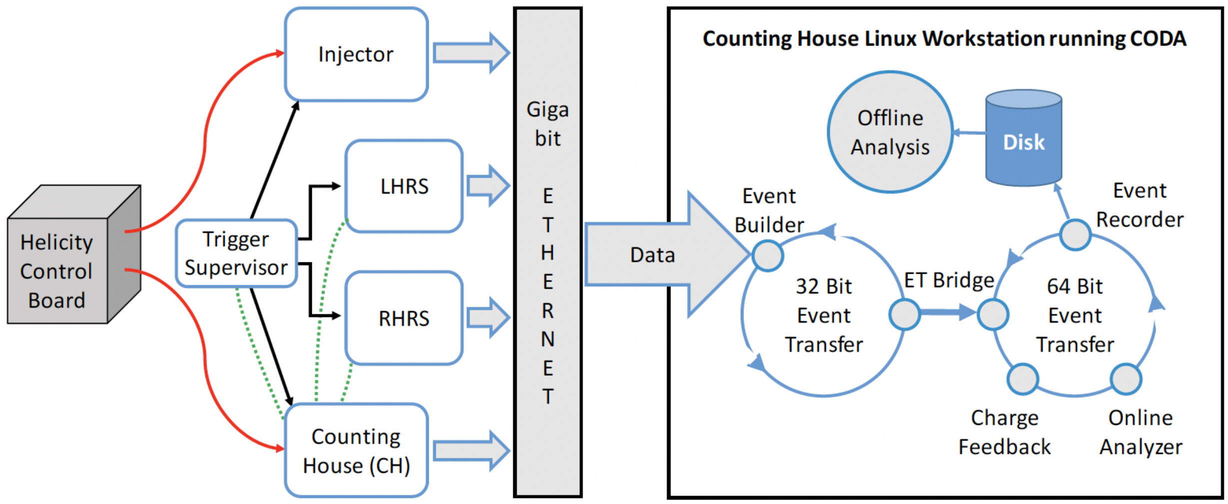

FIG. 38: The basic layout of the PREX-2 and CREX CODA system [37].

to the other).

The helicity signal determines the polarity of the Pockels cell high voltage. The first window of a helicity pattern (multiplet) was generated using a pseudo-random algorithm. Helicity patterns can be quartet (+ - - + or - + + -) or octet (+ - - + - + + - or - + + - + - - +), "+" and "-" are the sign of the voltages applied to the Pockels cell. These multiplets are formed at multiples of 60 Hz to cancel out 60 Hz noise of the power line. PREX-2 was initially run at 120 Hz quartet pattern mode, halfway through running, it was changed to 240 Hz octet mode. CREX was run at 120 Hz quartet mode.

The data taken by the parity DAQ is analyzed using "Just Another Parity ANalyzer (JAPAN)" package developed for PREX-2 and CREX.

2.7.2 COUNTING MODE DAQ

The counting DAQ is a Hall A standard data acquisition system which were located in each detector hut. With the two scintillators S0 and S3, logical AND and OR combinations were used to produce event triggers for the counting DAQ. The counting DAQ is normally operated at lower beam currents to avoid DAQ deadtime. The counting DAQ uses the standard Hall A "Podd" analyzer for data analysis.

2.8 EPICS

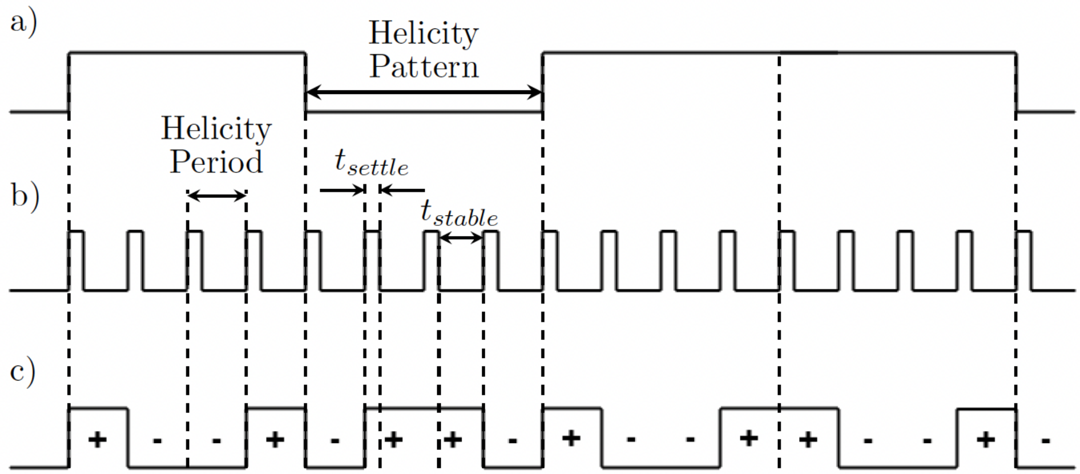

FIG. 39: Quartet helicity pattern timing a) helicity pattern signal, b) Macro-Pulse Signal and c) helicity sign [36].

To get real time information about the monitors that we used in the experiment, a special system was used, called EPICS (Experimental Physics and Industrial Control System). EPICS was developed at Argonne National Laboratory and is implemented at JLab for most accelerator and experimental systems.

PREX-2 and CREX use EPICS to track relevant beam quantities and spectrometer and detector information. EPICS gives real-time information on critical experimental quantities. Specified parameters were read from EPICS into the integrating data stream at approximately one minute time intervals.

CHAPTER 3

PARITY QUALITY BEAM FOR PREX-2 AND CREX

3.1 INTRODUCTION

The polarized electrons delivered to the experimental halls originate at the Jefferson lab polarized electron source. Here, circularly polarized photons from a laser source hits a strained GaAsP photocathode to make photoelectrons. The electron polarization state is determined by the laser light's polarization state. Then these electrons are accelerated in the accelerator and transport into the experimental halls.

The laser polarization is controlled by optical components on the source laser table. The laser circular polarization is generated using an electro-optical device, called a Pockels Cell (PC). The Pockels cell is used in $\lambda/4-$wave configuration, switching between right and left circular polarizations. The PC crystal varies its birefringence in linear response to an applied electric field, creating right and left helicity laser light.

Monitoring the beam current, position, angle, and energy is critical for both PREX-2 and CREX. These two experiments compare the left and the right helicity electrons and measure changes in scattering rates, therefore any change in the polarized beam, correlated with the helicity reversal, is a potential false asymmetry. In order to get a precise parity violating asymmetry, beam false asymmetries should kept at a minimum.

3.1.1 FALSE ASYMMETRY

As previously stated, any change in the polarized beam correlated with the helicity reversal is a potential source for systematic uncertainty. This includes intensity changes, position changes, spot size changes and energy changes. For a precise comparison between two helicity states, the beam on the target must be very symmetric in other words, intensity, position and spot size must be identical for the two helicity states.

As shown in Fig. 40, an intensity asymmetry in the electron beam can arise from a polarization asymmetry in the laser beam when incident on a polarizing element (such as a photocathode). A position difference in the electron beam can arise from a polarization gradient in the Pockels cell. This is a 1^{st} moment effect producing a shift in central laser beam position. A spot size asymmetry can arise from a 2^{nd} moment in polarization gradient, which can broaden or narrow the beam distribution.

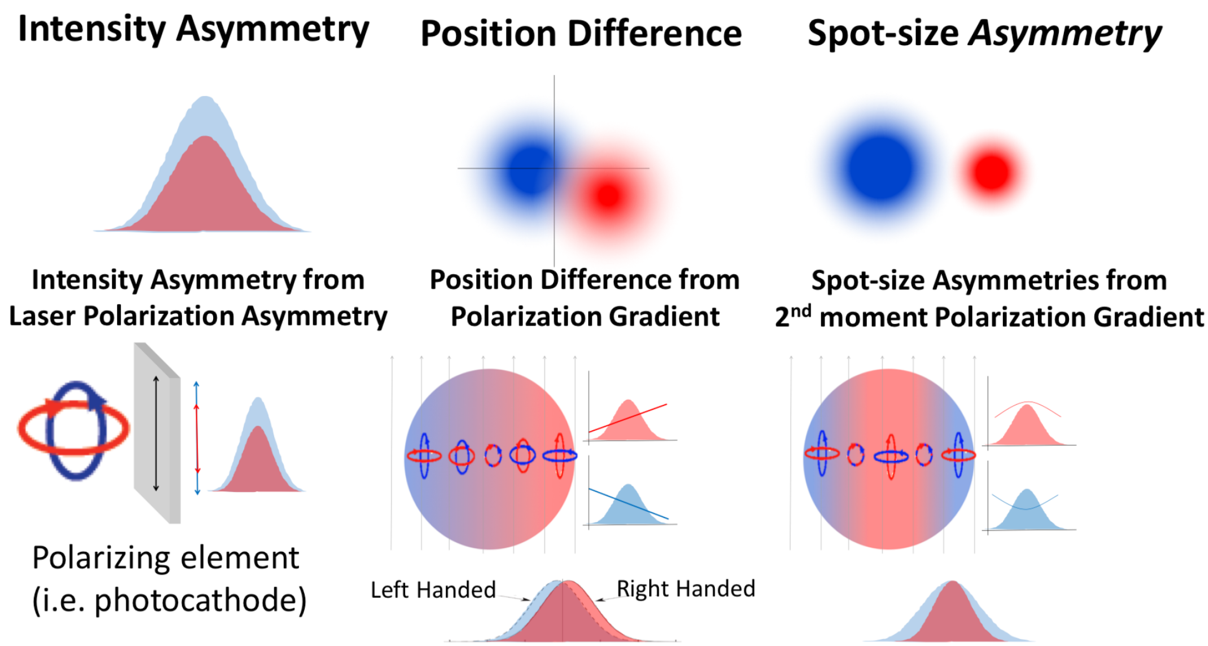

FIG. 40: Origin of analyzing power dependent beam asymmetries. The red and blue ellipses represent polarization ellipses for the opposing right and left circularly polarized states, with residual linear polarization in opposite perpendicular or parallel directions relative to the analyzing power of the photocathode. [38].

3.1.2 POLARIZED ELECTRON SOURCE (INJECTOR) SETUP

The schematic of the polarized electron source (injector) setup at Jefferson lab is shown in Fig. 41. Some of the components in the setup are discussed in Section 2.2. JLab injector setup has four different lasers, one for each experimental hall. The source studies, were performed with only the Hall A laser.

In the laser setup, first we have an Intensity Attenuator (IA) which is consisted of a Pockels cell between two linear polarizers, configured to use as a variable electro-optic shutter. The Hall A laser passed through a linear polarizer to ensure that the laser light polarization was either horizontal or vertical. An insertable half-wave plate (IHWP) was placed immediately upstream of the Pockels cell, and its function was to reverse the incoming horizontal

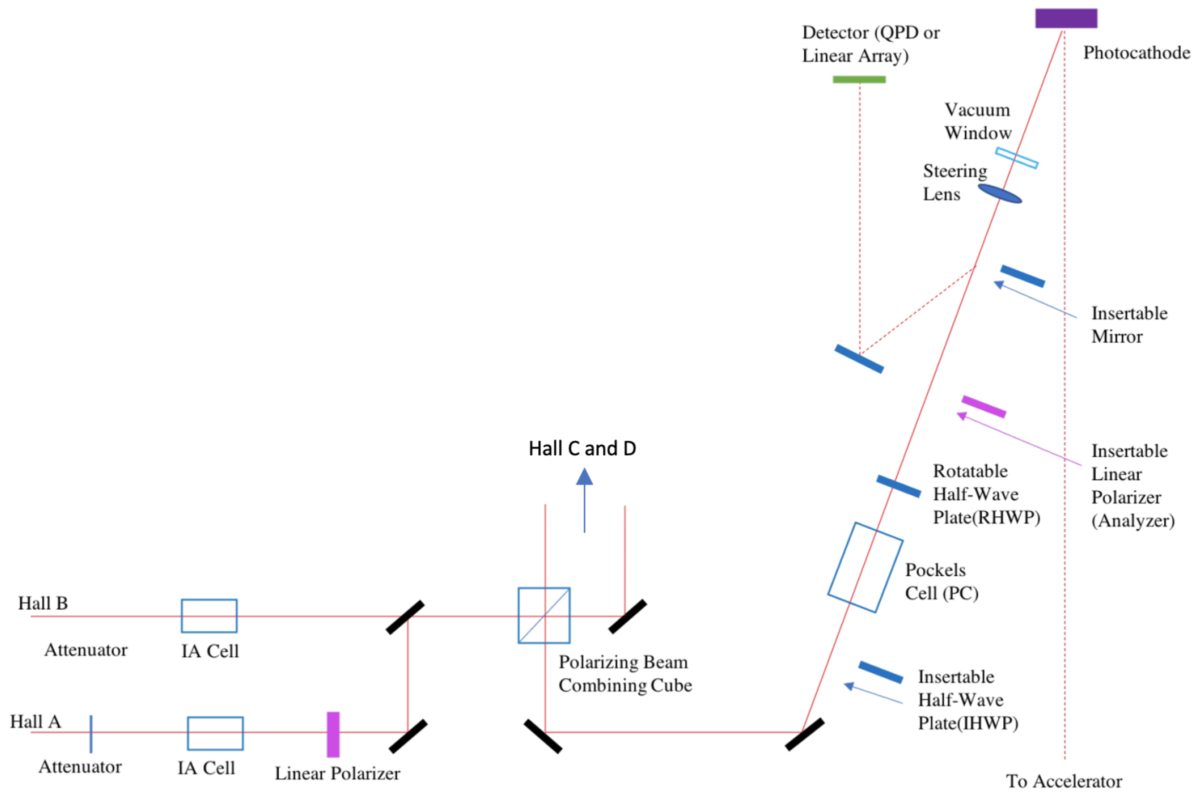

FIG. 41: The schematic of the injector setup at JLab.

polarization to vertical. This was changing the laser circular polarization sign without changing the PC voltages. This is one of the slow-helicity reversal methods. Then the laser light is directed to the PC. The Pockels Cell (PC) was used to convert linearly polarized light into circularly polarized light. A rotatable half-wave plate (RHWP), immediately downstream of the PC was used to rotate the polarization axis of the residual linear polarization.

The insertable linear polarizer (analyzer), the quad-photodiode (QPD) detector and the linear-array photodiode (LAPD) detector were only used during the laser table studies. The insertable mirror directed the laser light onto the QPD or LAPD detector. The QPD was a four quadrant photodiode which was used to measure the laser beam intensity and position difference. The LAPD was an array of 16 photodiodes, that was used to measure the laser beam intensity, position and spot-size simultaneously on the laser table. The linear polarizer can amplify effects of residual polarization because it transmitted 100% of linearly polarized laser light along one axis and 0% along the complementary axis. This can be used to understand the the effects of photocathode. The photocathode's analyzing power is $\sim$

6%.

3.2 HELICITY CORRELATED BEAM ASYMMETRIES

When operated in $\lambda/4$-configuration, the Pockels cell alternates between acting as a quarter wave plate with its fast axis along +45° and a quarter wave plate with its fast axis along -45°, switching incident linearly polarized light into alternating right and left circular polarization states. The resultant right and left circular polarization states of the PC may not be perfectly circular, it may have slight ellipticity. This ellipticity may not be symmetric and different for right and left polarization. The phase shift introduced by the PC on the laser light can be expressed as,

$$\delta^R = -(\frac{\pi}{2} + \alpha) - \Delta \qquad \delta^L = +(\frac{\pi}{2} + \alpha) - \Delta, \tag{55}$$

where $\delta^{R(L)}$ refers to the phase shift associated with the right (left) helicity light. The α is a component of linear polarization which is symmetric in both polarization states. The Δ is an asymmetric component between the polarization states, which results in a residual linear polarization along complementary axes between the two helicity states, as shown in Fig. 42.

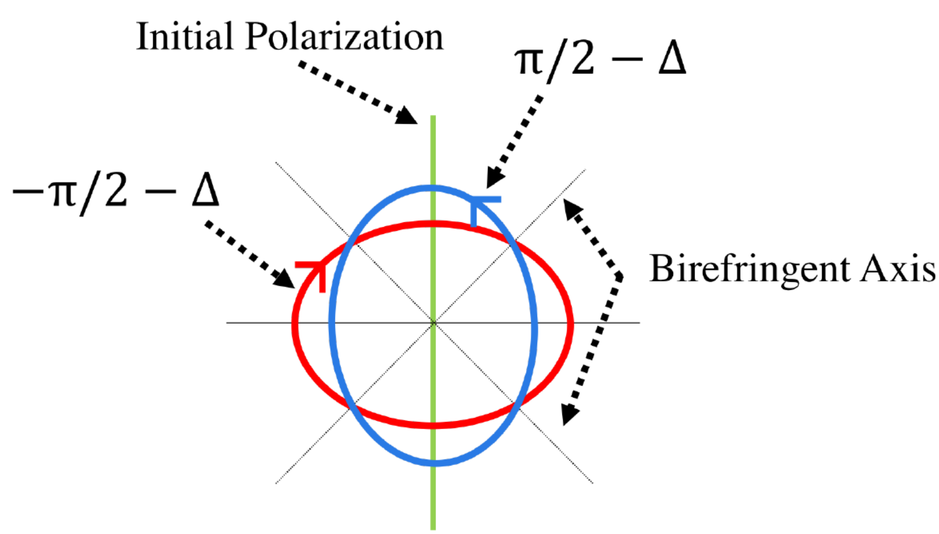

FIG. 42: Red and blue ellipses illustrate the polarization state of the right and left helicity states after initially vertically polarized light passes through the Pockels cell. Δ-phase is asymmetric, and results in residual linear polarization along complementary axis between the two helicity states light.

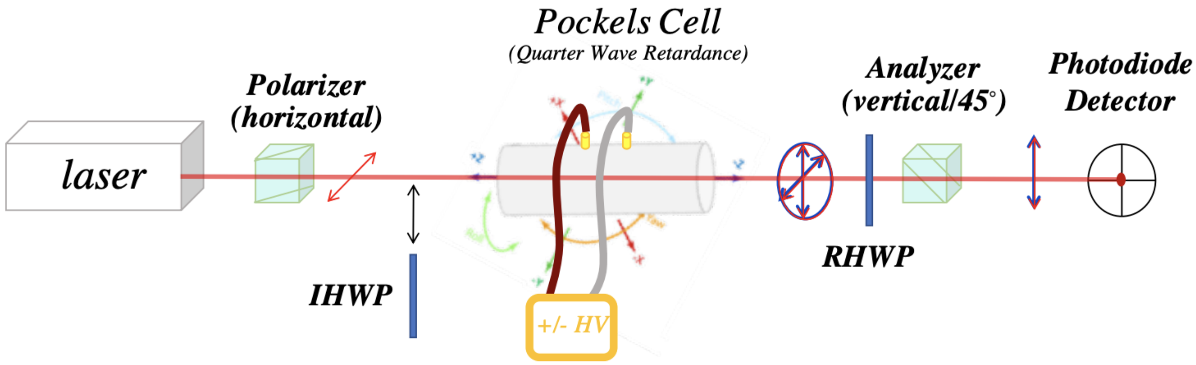

FIG. 43: Laser table configuration with HWP, RHWP and analyzer.

When performing diagnostic tests on the laser table, we used a polarizer with 100% analyzing power as the polarizing element, as shown in Fig. 43. If an analyzer, with transmission coefficients T_x and T_y along axis x and y, is placed downstream of the PC, the transmission through the polarizing element for each polarization state can be described as [38],

$$T^{R(L)} = \frac{T}{2}(1 + \epsilon/T \sin(2(n - \psi)) \cos\delta^{R(L)}), \tag{56}$$

where, T = $(T_x+T_y)/2$, ϵ = T_x - T_y, defines the analyzing power of the polarizing element, η is the effective fast-axis of the Pockels cell crystal relative to the horizontal axis and ψ is the angle subtended between the analyzing direction x and the horizontal axis.

The differences in the phase shift introduced by the PC in the two helicity states creates an intensity asymmetry in the charge of the electron beam. This helicity correlated beam intensity asymmetry (HCBA), can be expressed as,

$$A_I = \frac{T^R - T^L}{T^R + T^L} \approx \frac{\epsilon}{T}\sin(2(\eta - \psi))\frac{1}{2}(\cos\delta^R - \cos\delta^L) \approx -\frac{\epsilon}{T}\sin(2(\eta - \psi))\Delta, \tag{57}$$

where, we have used the approximation $cos\delta^R$ - $cos\delta^L \approx \delta^R + \delta^L = -2\Delta$ [39]. $\frac{\epsilon}{T}$ is often referred to as the "analyzing power". Note that the symmetric phase shift, α, cancels and only the asymmetric phase shift, Δ, appears in the equation above.

If a rotating half wave plate (RHWP) and an additional retardation plate downstream of the PC is inserted between the Pockels cell and the analyzer, the helicity correlated beam asymmetry of Eq. 57 becomes [38],

$$A_q = -\frac{\epsilon}{T}[\beta\sin(2\rho - 2\psi) + \gamma\sin(2\theta - 2\psi) + \Delta_{S1}\cos(4\theta - 2\psi) + \Delta_{S2}\sin(4\theta - 2\psi)], \tag{58}$$

where, θ is the RHWP angle, ψ is the analyzing direction, β is the phase shift from the additional retardation plate and ρ is the orientation of the additional retardation plate. γ is due to the RHWP's deviation from being a perfect $\lambda/2$-plate, and Δ is asymmetric phase shift which can arise either in S1[1] and S2. For the electron beam, this additional retardation plate is analogous to vacuum windows and the 100% analyzer analogous to photocathode with smaller analyzing power(<6%).

The IHWP insertion before the PC rotates the polarization axis of the linear laser light incident on the PC by 90°.

3.2.1 PITA EFFECT

The Δ-phase can be derived by considering the total phase shift,

$$\Delta \approx -\frac{\pi}{2|V_{\lambda/4}|}V_{\Delta}, \tag{59}$$

where, $V_{\lambda/4}$ is the quarter wave voltage[2] of the PC. V_{Δ} is called a PITA (Phase Induced Transmission Asymmetry)-voltage, which controls the Δ-phase. Then, the electron beam charge asymmetry (A_q) is given by [40] [12],

$$A_q \approx \frac{\epsilon}{T}(\sin(2(n-\psi))\frac{\pi}{2|V_{\lambda/4|}}V_{\Delta} - \Delta_0), \tag{60}$$

where, Δ_0 is an offset phase shift introduced by residual birefringence of the PC and optics downstream of it. If the fast axis of the crystal is along 45° ($\eta = 45°$), this reduces to,

$$A_q \approx \frac{\epsilon}{T}(\cos(2\psi)\frac{\pi}{2|V_{\lambda/4|}}V_{\Delta} - \Delta_0). \tag{61}$$

For 100% analyzer ($\epsilon/T = 1$) along S1 ($\psi = 0°$, $90°$) on the laser table, this reduces to,

$$A_I \approx -\Delta \approx \frac{\pi}{2|V_{\lambda/4|}}V_{\Delta} - \Delta_0. \tag{62}$$

The PITA equation characterizes the sensitivity of a given optical system and the analyzer to any residual linear polarization present in the laser light. The sensitivity of A_q to V_{Δ} is

[1] The Stokes parameters S1 and S2, respectively define the degree of linear polarization along horizontal and vertical axes and degree of linear polarization along the diagonal ±45° axes.

[2] quarter wave voltage is the voltage required for quarter-wave phase retardation of the laser light of wavelength λ, to generate right and left circularly polarized light. For the RTP PC, for 780 nm wavelength, $V_{\lambda/4}$ is $\sim$ 1500 V [12].

called the PITA-slope. To determine the ideal voltage at which to run the PC, as well as the sensitivity of A_q to changes in the voltage, a "PITA scan" is performed in which A_q is measured as a function of V_{PC}. PITA voltage can control polarization asymmetries along the S1 direction and can zero out intensity asymmetries introduced by Δ_0 with PC voltage. An example of PITA scan is shown in Fig. 44.

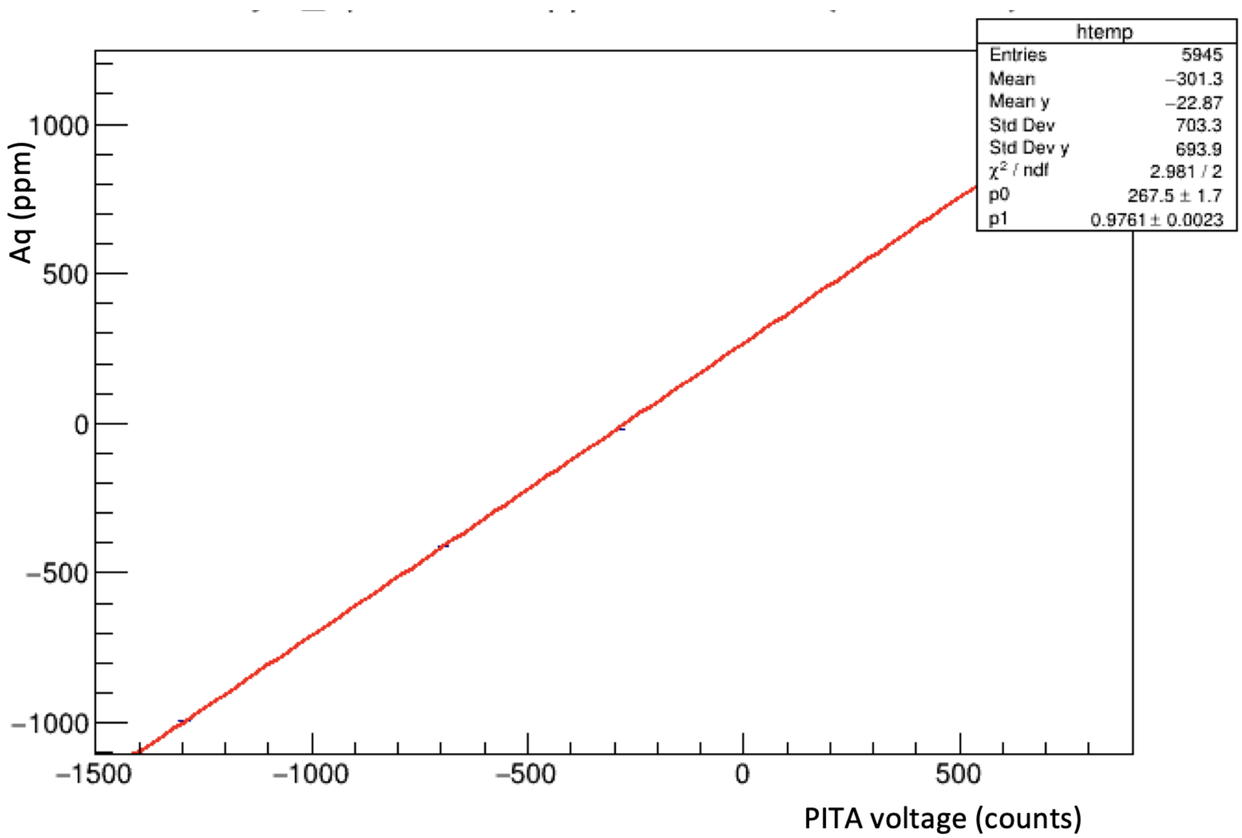

FIG. 44: A typical PITA scan plot. The helicity correlated beam intensity asymmetry (A_q) is plotted on the y-axis, and PITA offset voltages are plotted on the x-axis (1V is 16.384 counts).

3.2.2 INTENSITY ASYMMETRY-S2

In addition to polarization asymmetry along S1 (horizontal or vertical), there can also be polarization asymmetry along S2 (diagonal axis). In RTP PC, the relative roll between two crystals give rise to S2 polarization asymmetry. As stated before, a birefringence with fast/slow axis along $\pm 45^\circ$ along the RTP, gives rise to an asymmetry along S1 which can be corrected with Pockels cell PITA voltage. If there is a birefringence with a fast/slow axes along x/y (see Fig. 49), this gives rise to an asymmetry along S2 which cannot be corrected with Pockels cell voltage. If one of the crystals in the PC has its y/z axes slightly rotated relative to the other crystal, it is effectively acting as an additional birefringent element. When aligning RTP PC, the relative roll between the crystals have to be used to minimize this polarization asymmetry along the S2. Figure 45 shows A_q as measured by the photodiode after passing through RTP PC and polarizer oriented along 45°, on the y-axis and relative roll angle between the two crystals in the RTP cell, on the x-axis.

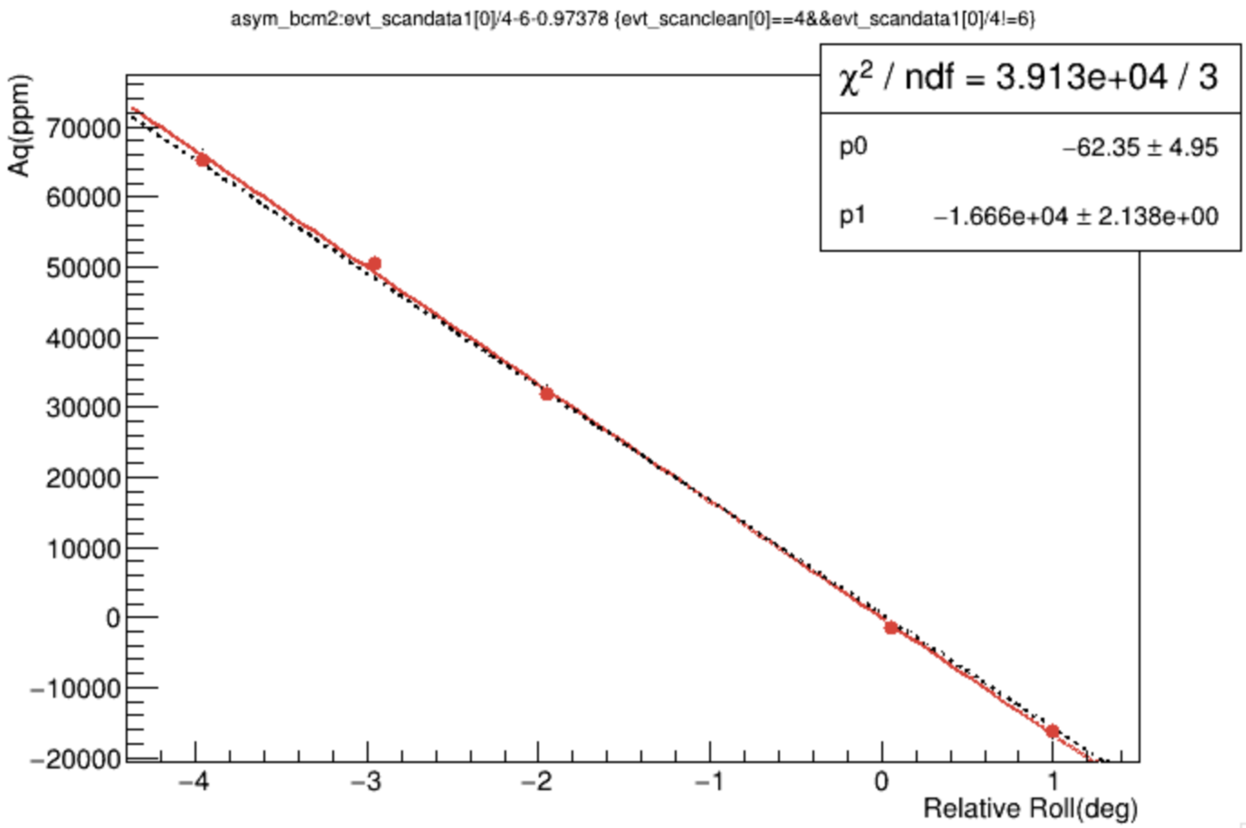

FIG. 45: Relative Roll and Aq dependence in S2.

3.2.3 POSITION DIFFERENCES

If a Gaussian beam encounters a gradient in transmission, it undergoes a shift in the beam central position. In the same way a polarization asymmetry gradient in the Pockels cell, when analyzed, gives rise to an intensity asymmetry gradient which creates position differences between right and left polarization states. The position difference can be expressed as [38],

$$D_x = x^R - x^L = -\frac{\epsilon}{T}\frac{\frac{d\Delta}{dx}w^2}{2}\cos(2\psi), \tag{63}$$

where, $\frac{d\Delta}{dx}$ is the Δ-phase polarization gradient, and w is the beam waist at the Pockels cell. This type of position difference is called as, "analyzing-like" since the position difference is proportional to the analyzing power ϵ/T.

Having a modest laser beam spot-size in the crystal can minimize the gradient experienced by the beam distribution and reduce position differences. We cannot reduce the spot size too much or else thermal gradients will create additional birefringence non-uniformities.

In RTP PC, the largest birefringence gradients come from the intrinsic refractive index non-uniformities. To control these position difference, a PC design with ability to control electric field gradients was used. To counteract the crystal intrinsic non-uniformity, we used grounded side panels to induce fringe-electric fields. By controlling the electric field gradients for each helicity state, in both of the crystals, the asymmetric position motion of the light can be suppressed [38].

These gradients can control another type of position difference called, "steering-like" position difference. Steering is a helicity correlated change in angle of the outgoing laser beam through the Pockels cell, which is independent of the the analyzing power. We used the electric field gradient to induce steering to precisely control the helicity correlated position differences.

3.2.4 RHWP SCANS

For the Pockels cell alignment we use a rotating half wave plate (RHWP). Helicity correlated beam asymmetry coming from a RHWP and an additional retardation plate downstream of the RHWP is described in Eq. 58. When aligning the PC, it's important to minimize the 4θ term in this Equation. We can also minimize the birefringence coming from the vacuum windows on the offset term by rotating the photocathode direction such that $\psi = \rho$. The 2θ term corresponds to an imperfect RHWP and can be reduced by using a RHWP very well matched to the laser wavelength. RHWP scans can be used to understand position differences and steering.

An example of a RHWP scans[3] with the electron beam is shown in Fig. 46. Here, voltage offsets were used to induce a steering offset and we can see offsets terms D_x and D_y have

[3] For a detailed description of RHWP scans refer [28]

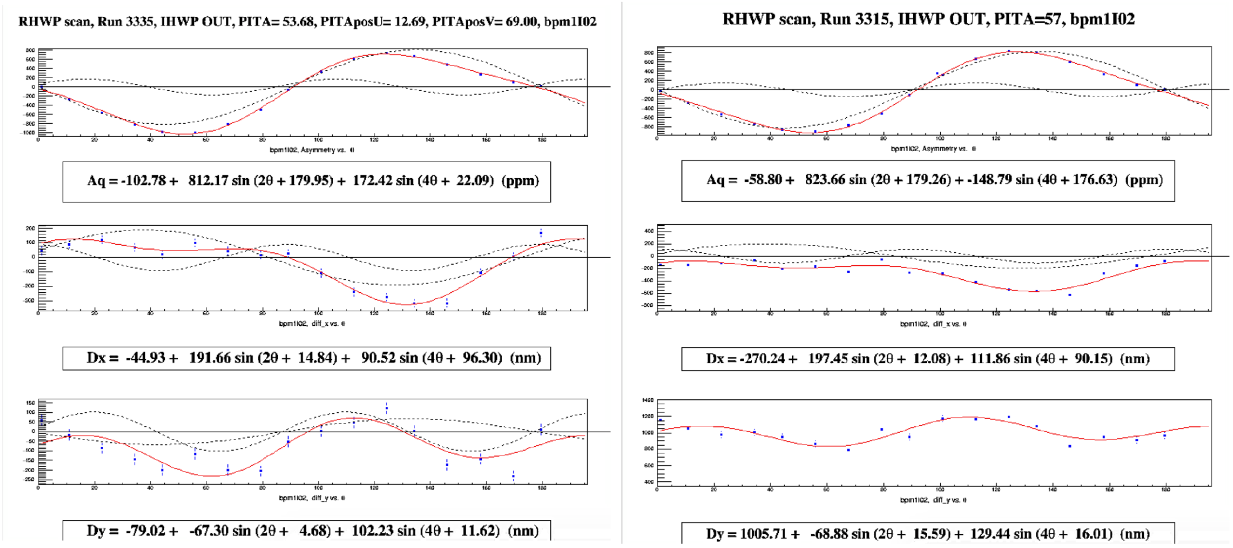

(a) (b)

FIG. 46: RTP RHWP scans with electron beam. a) Scan with a steering offsets have been reduced by adjusting voltages b) Scan with a large steering offset.

been reduced significantly.

3.3 RTP POCKELS CELL

For PREX-2 and CREX experiments a new Pockels cell called RTP[4] (Rubidium Titanyl Phosphate) was used. The old PC KD*P (potassium dideuterium phosphate), cell suffer from piezo-electric ringing when high voltage is suddenly applied to switch polarization states. That resulted a lengthy transition and settle time[5]. The transition time was further delayed by an effect believed to change accumulation on the Pockels cell crystal due to finite surface conductivity. Therefore, a new fast switching PC was tested. This RTP PC was designed for the future MOLLER experiment but it was tested prior to PREX-2 and used for both PREX-2 and CREX. The comparison between RTP and KD* transition times are shown in Fig. 47.

All crystals have some degree of non uniformities that could produce helicity dependent laser beam motion. To counteract this and minimize helicity correlated beam asymmetries,

[4]This PC was developed by Caryn Palatchi

[5]Transition time is the time to switch from one helicity state to the other helicity state and this is a dead time for data collecting

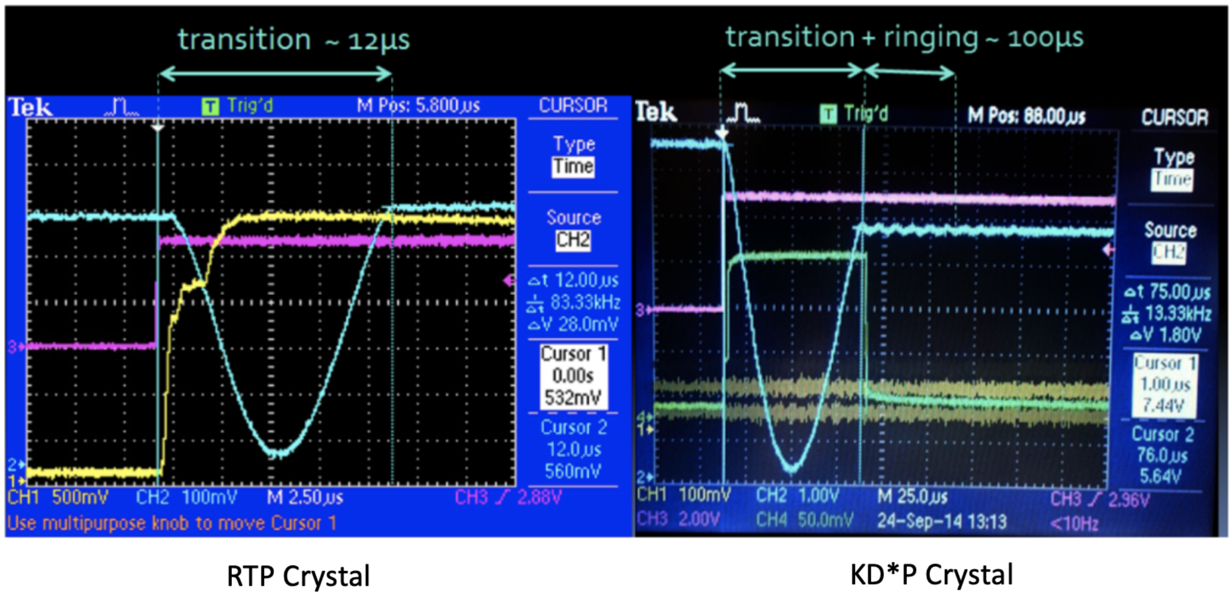

FIG. 47: Transition time for RTP and KD*P crystals.

a new design of the RTP Pockels cell was required. The new RTP PC was designed to control the electric field gradients and by that, suppress helicity correlated beam motion. RTP crystals have a high intrinsic birefringence. To avoid severe wavelength dependence and temperature dependent effects, two crystals are used in RTP Pockels cells with their fast and slow axes in opposite orientations. The RTP crystals dimensions are 12x12x10 mm. The commercial PC design have a common grounded plate and two high voltage (HV) plate on top of each crystals. For the new design, crystals have each electrode independently controlled. Grounded side-panels were added near the sides of each crystal and added 4 HV plates. The commercial design and the new design is shown in Fig. 48. The new design has four voltages for each helicty state, two voltages per crystal. The voltage of each electrode is of opposite sign for the opposing helicity state, hence there are eight independent voltages used in total.

As shown in Fig. 49, the voltage settings control the electric field gradient along the z-axis of each crystal and they control the steering along the z-axis for each crystal. The two crystals were oriented such that, the first crystal's electric field gradient controls the steering along -45° and the second crystal's electric field gradient controls the steering along +45°.

The voltage shift in each crystal which induces steering is referred to as α-position voltage, because it controls the alpha phase gradient. The first crystal, with its z-axis along U,

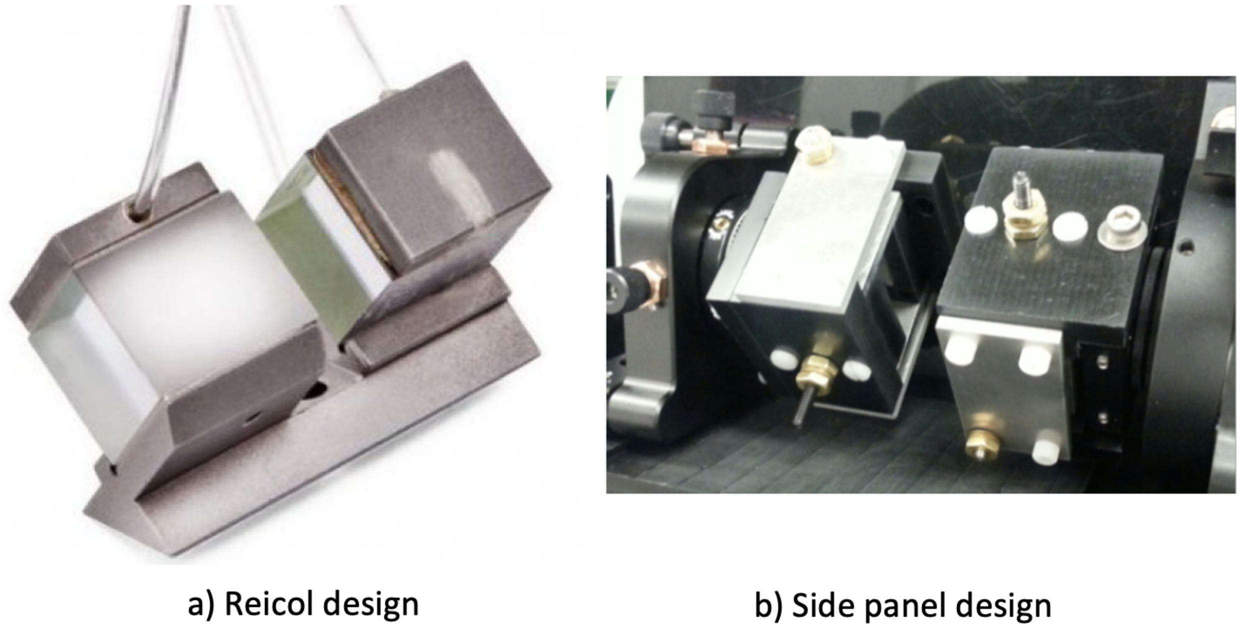

FIG. 48: The RTP Pockels cell design [41] a) Commercial design, b) New side panel design.

controls the steering along the U-direction with "α-position-U" voltage, $V_{\alpha pos,u}$ and the second crystal with z-axis along V, controls the steering along the V-direction with "α-position-V" voltage, $V_{\alpha pos,v}$. More about the design and voltage sequence of the new RTP PC can be found in this paper [38].

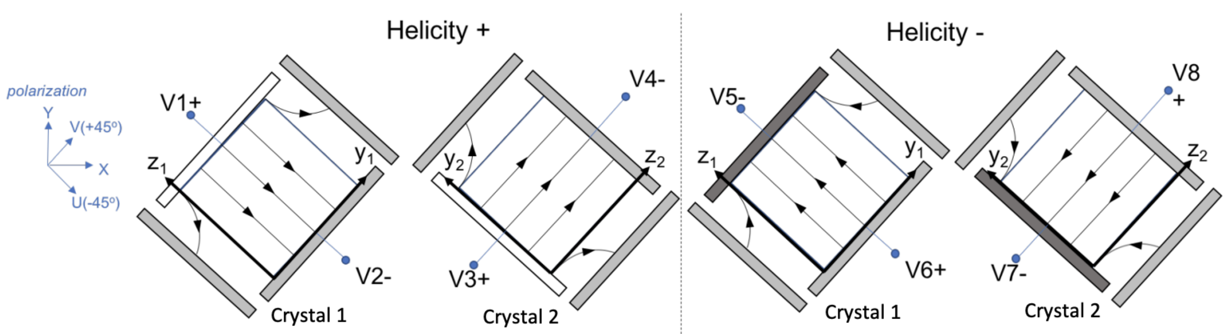

FIG. 49: Defining axes of RTP cell and configuration of 8 HVs [38].

The RTP cell mount was designed such that it can control the relative pitch, yaw, roll, horizontal and vertical translation between the two crystals. Also, it can control overall pitch, yaw and roll, horizontal and vertical translation of the two crystals.

Each of the RTP 8 high voltages were driven by a HV driver which is composed of an optocoupler system. The system has 2 optodiodes in parallel, which reverse conduct when light is applies via LEDs. Upon switching the helicity state, the current flow through one set of LEDs cease and the current flow through another set begins. The circuit for this optodiode configuration is shown in Fig. 50.

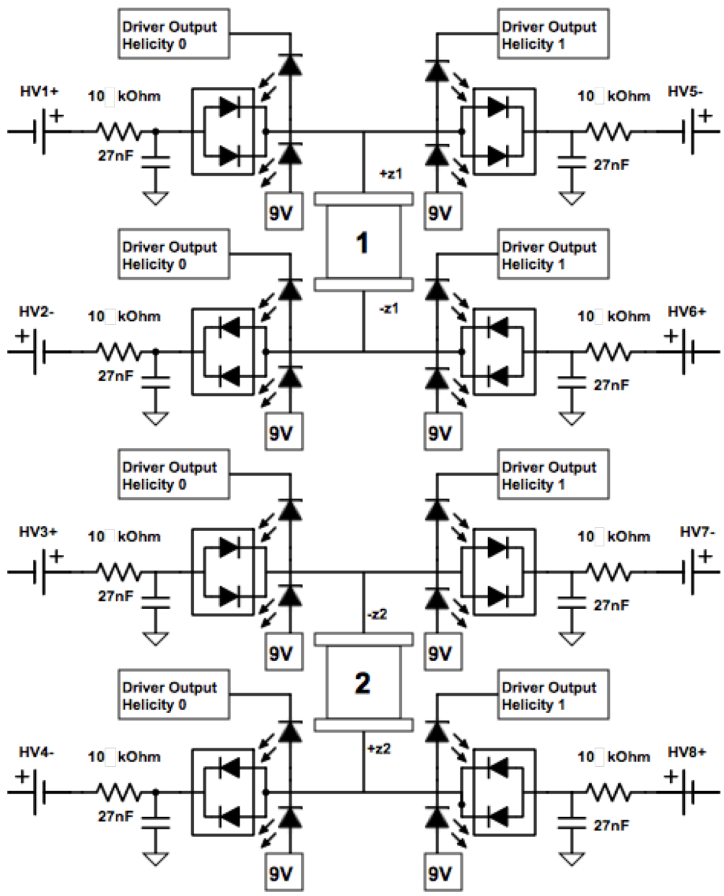

FIG. 50: Schematic of the 8HV driver configuration with optodriver.

The full design of the RTP crystal is shown in Fig. 51.

3.4 RTP PC CHARACTERIZATION

The RTP Pockels cell was first characterized on the UVA laser table and then on the JLab injector laser table. The intensity asymmetry, position difference, spot size asymmetries were studied here.

As discussed earlier, a linear polarizer (analyzer) was installed immediately after the PC

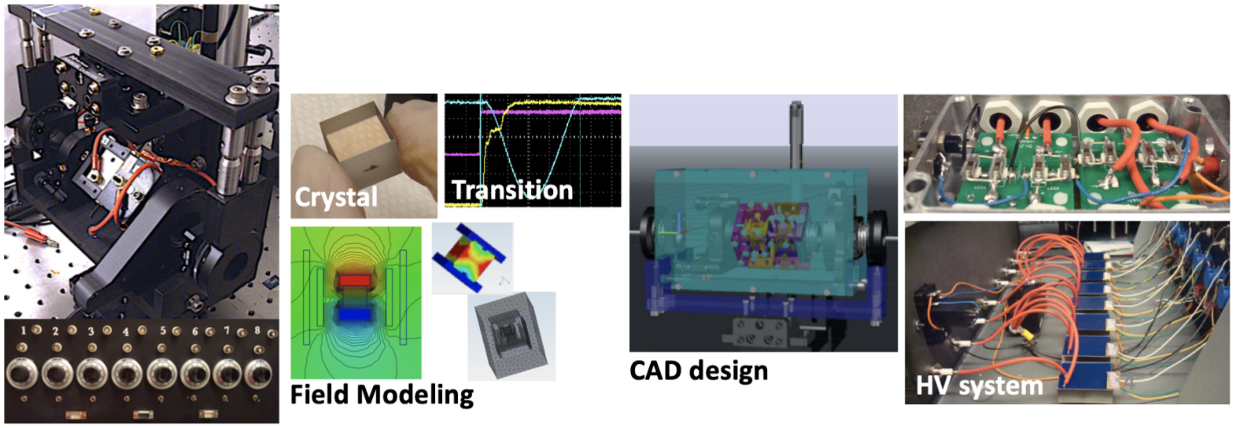

FIG. 51: The RTP cell design [42].

to provide the analyzing power in the system to mimic the photocathode. The Pockels cell was mounted on motorized stages which could be moved horizontally or vertically. We could measure the RTP sensitivity to position by doing translation scan with the cell. In the laser setup, horizontally polarized light was incident on the RTP Pockels cell, and using the analyzer, transmitted light could be analyzed with a quadphotodiode as shown in Fig. 43.

The Pockels cell is scanned by translation stages horizontally along X and vertically along Y, and the intensity asymmetry dependence on the cell position was measured. Figure 52 shows the translation scan with intensity asymmetry A_q in S1 (after polarized beam passes through vertical analyzer) as a function of Pockels cell transverse position in the X/Y plane perpendicular to the beam propagation axis. In this figure, you can see the A_q with respect to position shows the birefringence gradient and these gradients are intrinsic to the RTP system, and give rise to analyzing-like position differences and cannot zeroed out with the translation of the PC. This scan result motivated the new cell design.

To understand the cell sensitivity to the angle, the cell angle scanned over several pitch/yaw positions in a grid (the same laser setup was used for this measurement). The intensity asymmetry A_q dependence on cell angle is shown is Fig. 53.

Another study to understand how analyzing-like position differences depend on the PC angle was performed with the qpd detector. The results of scanning pitch and yaw are show in Fig. 54. From the scans we saw, yaw couples primarily to the position difference in x, and pitch couples primarily to the position difference in y. This measurement showed that the PC angle adjustments can minimize analyzing-like position differences caused by birefringence.

The characterization of the steering ability of the RTP pc was done at the JLab laser table.

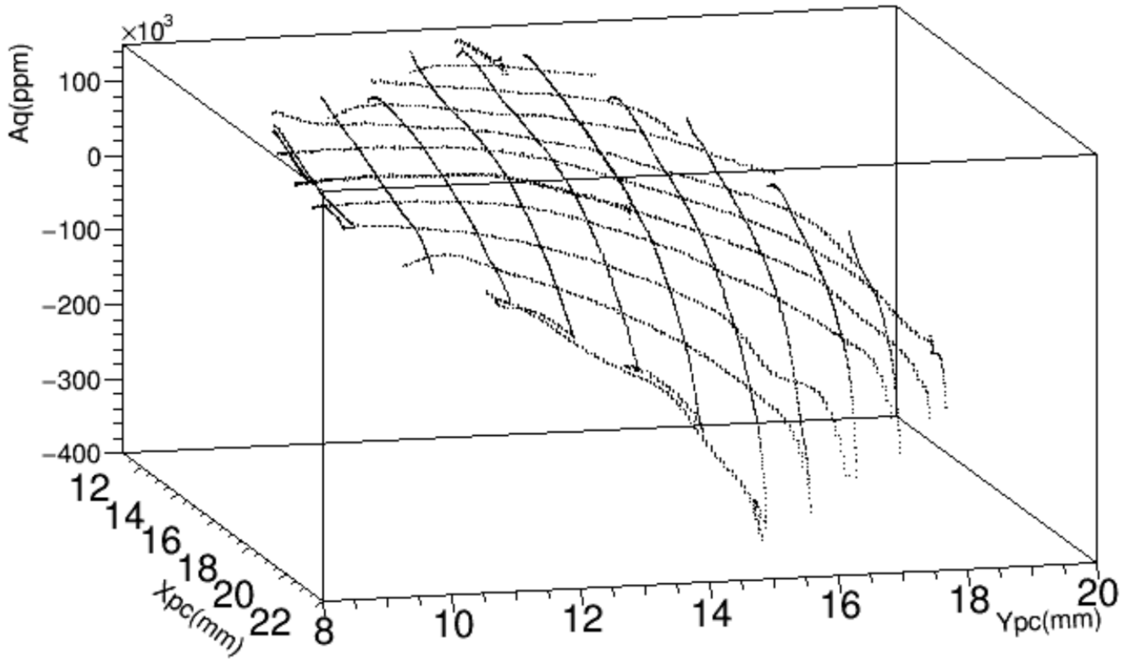

FIG. 52: RTP PC translations scan [38].

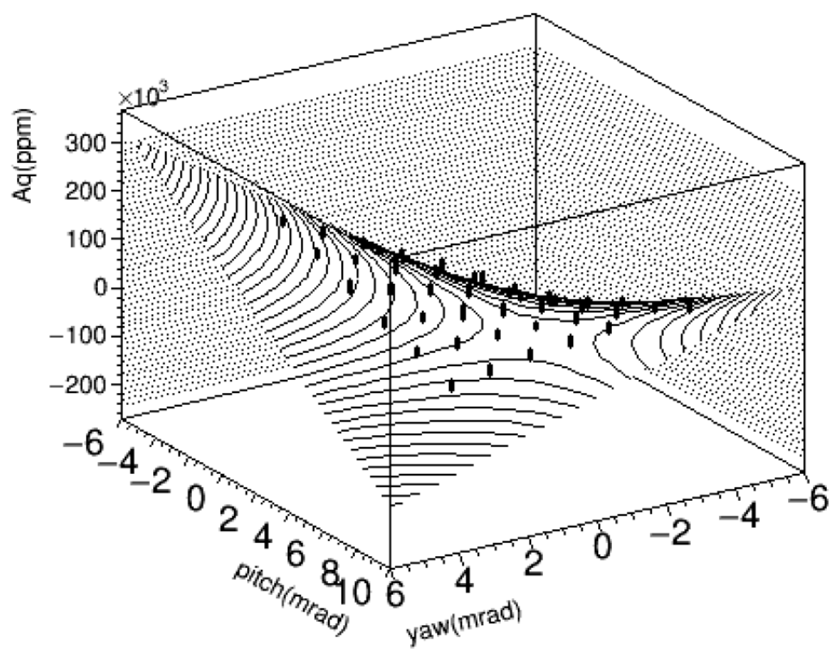

FIG. 53: RTP PC angle scan [43].

The study was performed with horizontal input polarization before the cell, no analyzer downstream of the cell, and qpd detector to measure the beam position differences. As we

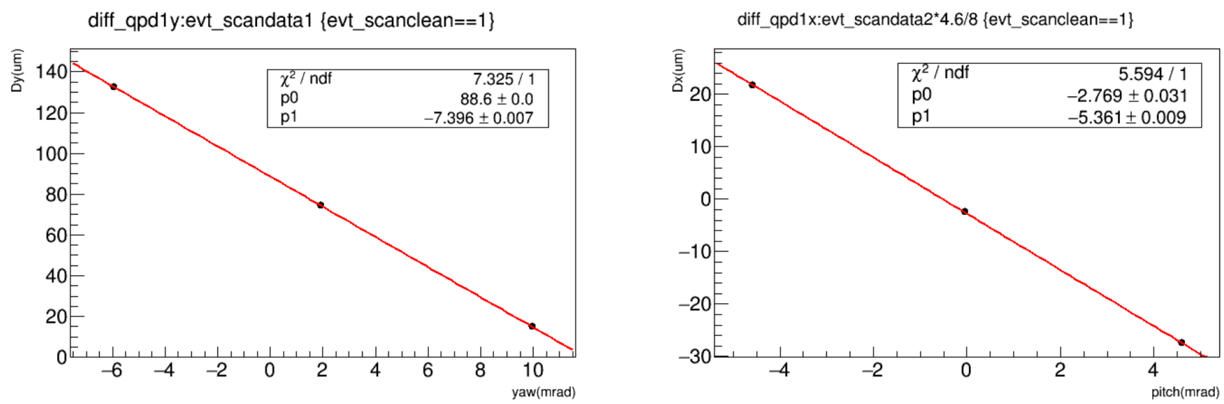

FIG. 54: D_x and D_y dependence on the RTP PC angle.Data points are fit with a saddle function [44].

discussed earlier, the RTP cell was designed such that it can control helicity correlated beam steering with the the electric field gradient along the z-axis of each crystal. The first crystal has its z-axis along U (-45° direction) and it controls the steering along the U-direction with alpha-position-U voltage ($V_{\alpha pos,u}$). The second crystal has its z-axis along V($+45^\circ$ direction) and it controls the steering along the V-direction with alpha-position-V voltage ($V_{\alpha pos,v}$).

We did different voltage scans to understand the U and V voltage dependence on the measured position differences. The Fig. 55 shows alpha-position-U voltage scan at JLab. We saw the laser steering dependence on applied voltage was linear, and it is sufficient to control and zero out any position differences intrinsic to the crystal system.

To measure the spot size asymmetries for RTP, a linear-array photodiode (LAPD) detector was used. The linear array consists of 16 photodiodes (but used 6-8 photodiodes for measurements), 1.22 mm x 1.84 mm in size, separated by 0.25 mm.

The linear array measures the spot-size of the laser in an arithmetic or Gaussian method (as described in [28]). In the arithmetic method, the mean beam position $\bar{x}$, and the beam spot size σ are calculated from weighted sums of the intensities of the individual pads as,

$$\bar{x} = \frac{\sum_i I(x_i)x_i}{\sum_i I(x_i)}, \tag{64}$$

$$\sigma = \frac{\sum_i I(x_i)(x_i - \bar{x})^2}{\sum_I I(x_i)}, \tag{65}$$

where, x_i and $I(x_i)$ are the beam position and intensity on the i^{th} element of the array. In

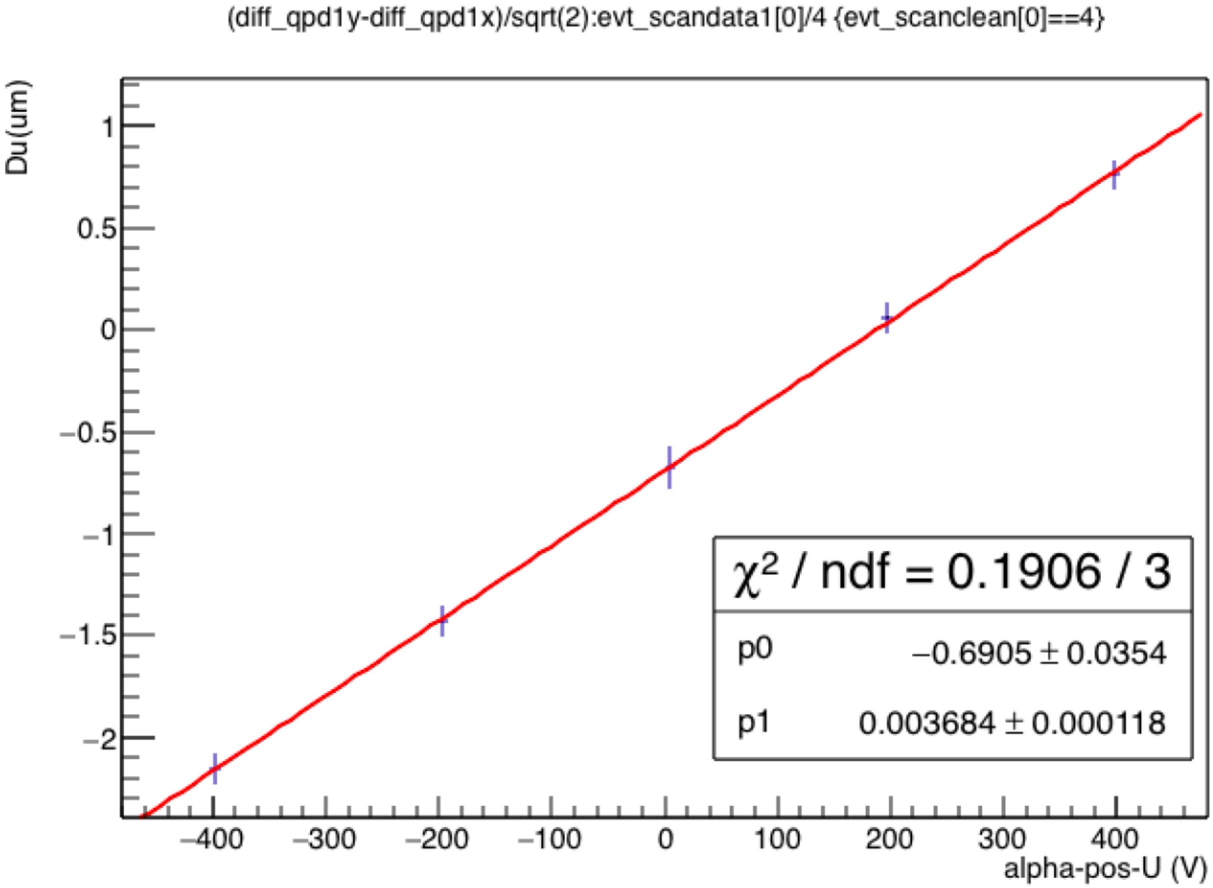

FIG. 55: Alpha-position-U voltage scan [45].

the Gaussian method, the beam intensity across all the pads are fit to a Gaussian, to extract the centroid position and width as the standard deviation.

We collected a series of measurements with the array oriented along X, Y, +45°, 45° for no analyser, S1 and S2, and fully characterized the spot size asymmetry. To infer the spot-size asymmetry that would be created on the electron beam, we scaled S1 and S2 spot-size asymmetries down by the analyzing power of the cathode and scaled the no-analyzer spot-size asymmetry by the ratio of the throw distances $\frac{D_{cathode}}{D_{LAPD}}$. With the laser table measurements, the spot size asymmetry was bounded to be $5 \times 10^{-6} - 3 \times 10^{-5}$, which was acceptable for PREX-2 CREX.

3.4.1 TEMPERATURE SENSITIVITY

Operating the RTP PC, on the laser table with 100% analyzing power, we observed slow fluctuation in A_q by $\sim \pm 30{,}000$ ppm over the course of several hours as shown in Fig. 56, and we believe this fluctuation is related to the temperature difference between the crystals. The RTP crystals were aligned in which the fast axis of one crystal perpendicular to the fast axis of the other crystal to cancel the birefringence, in a so called "thermal compensation design". Even though the thermal compensation design does a great deal to mitigate temperature effects on the Pockels cell performance, some small thermal fluctuations are still observed. For our RTP crystals at 780 nm, we estimate the charge asymmetry from a temperature difference between the crystals to be $\sim$ 670 ppm/mK.

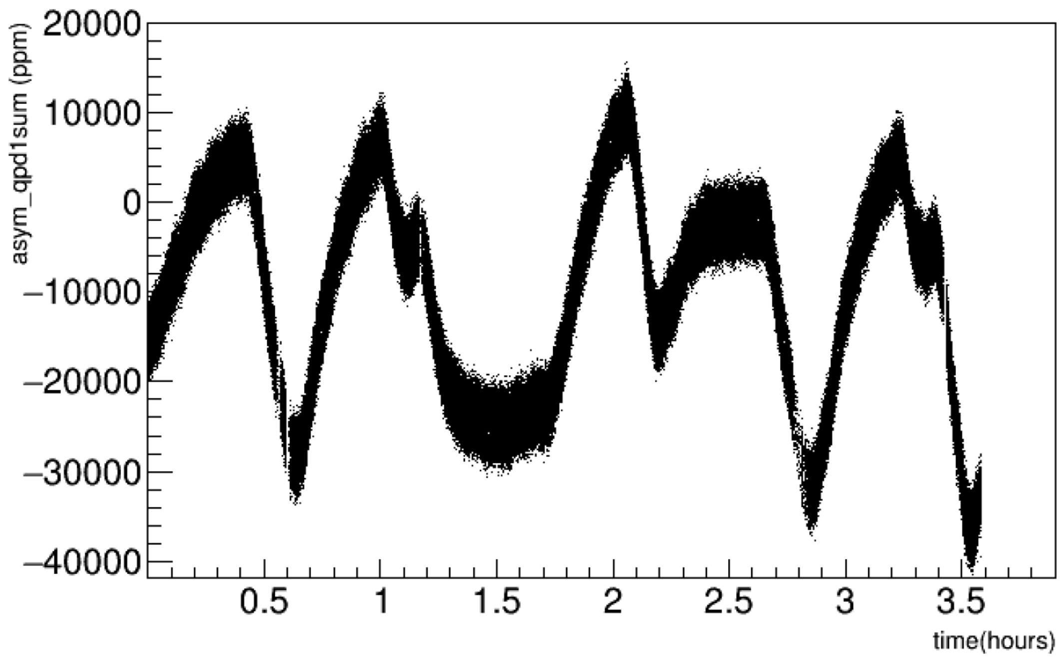

FIG. 56: Aq fluctuations, analyzed in S1 [46].

It is difficult to control the temperature difference between the crystals at the milli-Kelvin level, but we can use PITA voltage to correct this intensity asymmetry. The temperature induced birefringence is well within the PITA-voltage induced birefringence adjustment range. When running the experiment we corrected the temperature fluctuation with a PITA-voltage feedback loop.

PITA Feedback

On the laser table we directly measure the polarization asymmetry by inserting a 100% polarizer which analyzes along S1, and converting a polarization asymmetry into an intensity asymmetry measurable by a photodiode. With the electron beam, the photocathode serves as a partial polarizer with a small analyzing power, which analyzes along an axis determined by the RHWP, and converting a polarization asymmetry into a charge asymmetry measurable by BCMs and BPMs.

The active charge feedback system is used to correct the Pockels cell high voltage to minimize the charge asymmetry. During the experiment, the charge asymmetry is measured by the BCMs in the Hall. During one feedback cycle, the JAPAN feedback online analyzer, analyzes data collected by the parity DAQ and measure the charge asymmetry for the cycle. To determine the sensitivity of charge asymmetry to changes in the voltage, a PITA scan is performed before the experiment and slopes are fed in to the JAPAN. Then, the feedback analyzer calculates the Pockels cell high voltage correction based on the measured asymmetry and "PITA" slope. The feedback system transmitted these voltages to the Pockels cell high voltage electronics via the EPICS interface. The flowchart for the active feedback system is shown in Fig. 57. The feedback system actively performed this process concurrently with data taking, to drive charge asymmetry close to zero.

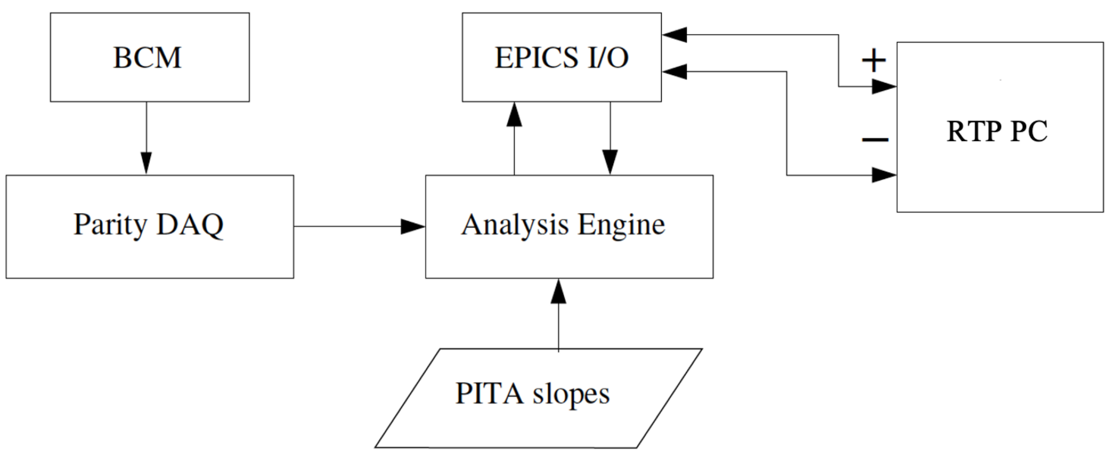

FIG. 57: The active feedback flowchart.

In order for feedback to work well, we have to carefully select the RHWP angle and the feedback interval. With the RTP cell, we can zero out any charge asymmetry offset term (2θ term) with RTP relative roll and position differences can be minimized using alpha-position-U/V voltage. Therefore, we are free to choose any RHWP angle. But in order to use PC voltages to correct A_q, we need to have some degrees of analyzing power along S1 to get a significant PITA slope. For running, we selected a RHWP angle near S2 so that the analyzing power was small along S1 but large enough that we could correct A_q with reasonably low PITA voltages.

The feedback interval is the length of time, which the charge asymmetry is measured before applying a correction with PITA voltage. The feedback interval must be long enough to obtain a good statistical accuracy on A_q, otherwise we'd just be falsely correcting electronics noise. Also, the feedback interval must be short enough that the central value of A_q doesn't change too much over the interval, otherwise A_q will drift faster than you correct it and feedback will fail to converge. The charge asymmetry should converge fairly quickly as RMS/N, where N is the number of feedback intervals [40]. After careful consideration the feedback cycle length was chosen as 7.5 seconds and BCM analog upstream was used as the feedback monitor during two experiments.

3.5 RTP PC ALIGNMENT PROCEDURE

First we checked the laser spot size at the cell, it had a waist of $2\sigma \sim 1$ mm (at the photocathode spot size is about ~ 3 mm). Then roughly center the RTP crystal on the laser beam. We align the back reflections to incoming beam as closely as possible using PC pitch and yaw. Next using a spinning linear polarizer between PC and a power meter attached to an oscilloscope, approximately minimize the degree of linear polarization for both helicity states using PC voltages, pitch, yaw and roll. Then insert the IHWP and maximize DOCP for both IHWP states.

Then using the analyzer, we minimize, A_q in S1 with PITA voltage and A_q in S2 with relative roll. Next we zero out the steering effects using alpha-phase gradients (with no analyzer). Finally, we try to reduce the birefringence gradient effects in S1, the analyzing-like position differences, using the Pockels cell pitch and yaw angle. Helicity correlated spot size asymmetries were measured with a linear array photodiode, by orienting the photodiode array in horizontal, vertical, and $\pm 45^{\circ}$ directions (slight translational adjustments may reduce spot size asymmetries). All of these were laser table alignments.

Then we rotate the photocathode to suppress the polarization effects appearing in the A_q offset terms in the RHWP scans. The photocathode orientation was adjusted and a RHWP scan was done at each of the orientations, until the A_q offset is small. This will minimize photocathode sensitivity to linear polarization produced by birefringence in the vacuum window. Figure 58 shows the RHWP scans before and after the cathode rotation and you can see cathode rotation suppressed the A_q offset term.

Then at RHWP angle set to S1, we minimize A_q in S1 with PITA voltage. Then,

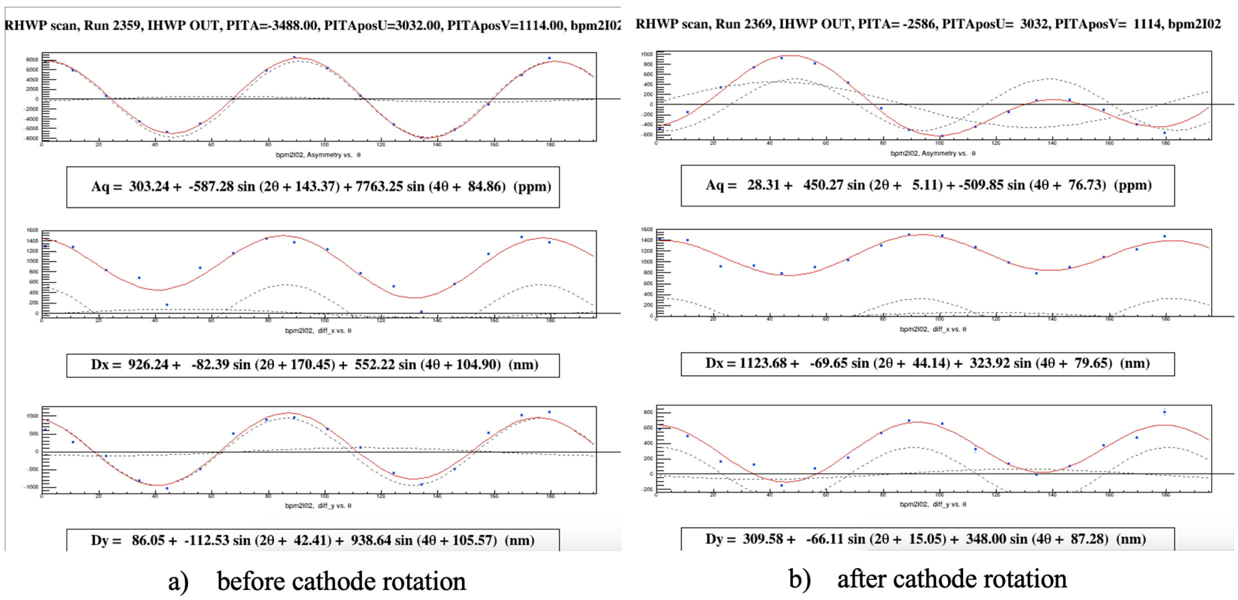

FIG. 58: RHWP scans for cathode rotation befor PREX-2.

at RHWP angle near S2, where PITA slope is small, we perform PITA-voltage feedback and approximately minimize A_q. Next we set alpha-position-U and alpha-position-V to minimize position differences in the injector. We also examine the position differences further downstream in the injector beam-line, to make sure the position differences remain small and there is no significant clipping on apertures.

3.6 RTP PC ALIGNMENT WITH THE ELECTRON BEAM

RTP cell was installed in the Jefferson lab laser table prior to running PREX-2 and CREX. First the cell was optimized on the injector laser table. Then we tested the PC alignment with the electron beam.

First thing we checked was the RTP charge feedback system with PC PITA voltages. We used a BPM in the 130 keV region of the injector and the feedback was performed in 7.5 second intervals at two different RHWP settings. First with the RHWP angle set to align the Pockels cell S1 polarization direction along the analyzing axis of the photocathode, maximizing the sensitivity of A_q to PITA voltage and temperature fluctuation. Next the RHWP angle at $\sim$ S2 that reduced the sensitivity to PITA voltage and temperature fluctuations by a factor of $10\times$. Figure 59 shows the feedback plots for S1 and $\sim$S2 angles set by the RHWP.

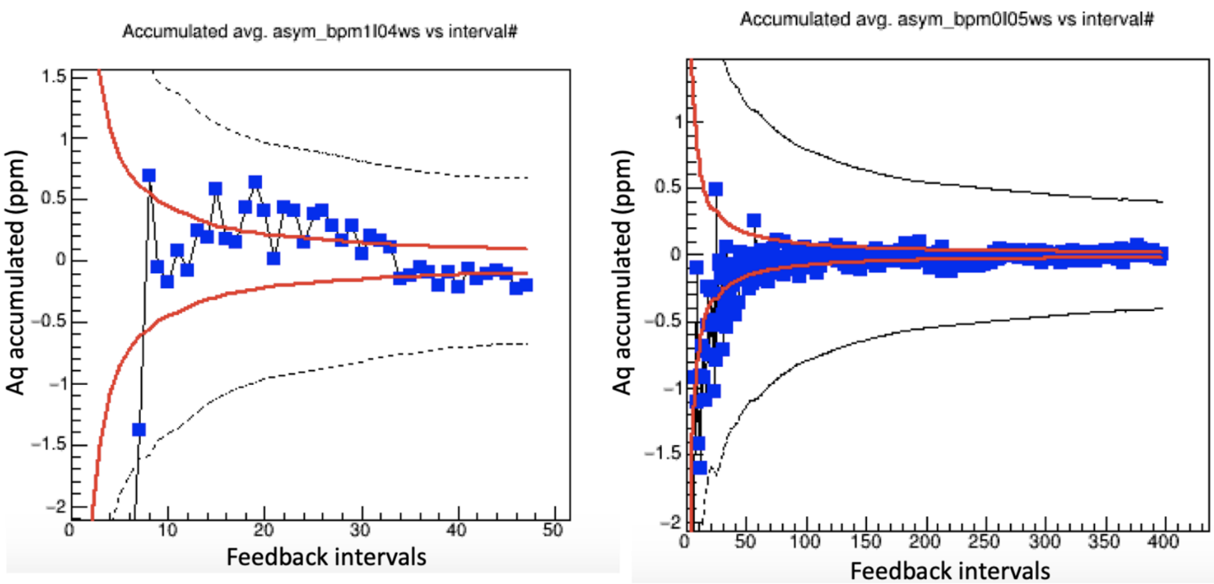

a) Aq feedback at S1 b) Aq feedback near S2

FIG. 59: The charge feedback for RTP. a) feedback at S1, b) feedback near S2. Red curve is RMS/N scaling and black dotted curve is RMS/$\sqrt{N}$ scaling

The statistical limit for the rate of convergence of A_q is between RMS/N (Red curve) and RMS/$\sqrt{N}$ (black dotted curve), where N is the number of intervals. In both measurements, the charge asymmetry converged faster than RMS/$\sqrt{N}$ and nearly as fast as RMS/N. This shows that the RTP Pockels cell can successfully control charge asymmetry in the electron beam.

Then we tested position feedback. Position difference feedback was performed using the RTP steering control voltages $V_{\alpha pos,U}$ and $V_{\alpha pos,V}$ to minimize the measured position differences on a BPM in the 130 keV region of the injector.

Just like a PITA scan, a scan was performed to get the sensitivities of $V_{\alpha pos,U}$ and $V_{\alpha pos,V}$ to D_x and D_y position differences and slopes of these scans were fed to the feedback analyzer. Feedback was performed every 2 minutes, after sufficient precision was obtained on the position difference measurement to make meaningful corrections. Figure 60 shows the position differences convergence with position feedback.

We were able to achieve very small position differences (<30 nm), in the first 10 BPMs in the 130 keV injector region with the position feedback.

In addition to these feedback, for PREX-2 and CREX we performed hall C IA feedback to minimize hall C charge asymmetry, which was needed for their experiment.

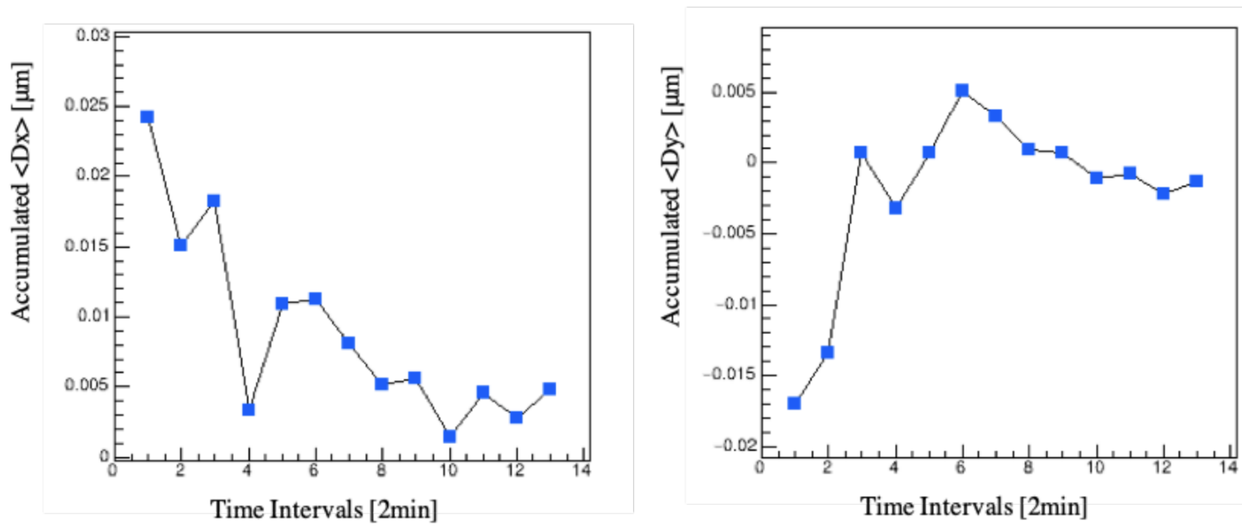

FIG. 60: RTP position feedback using $V_{\alpha pos,U}$ and $V_{\alpha pos,V}$ voltages.

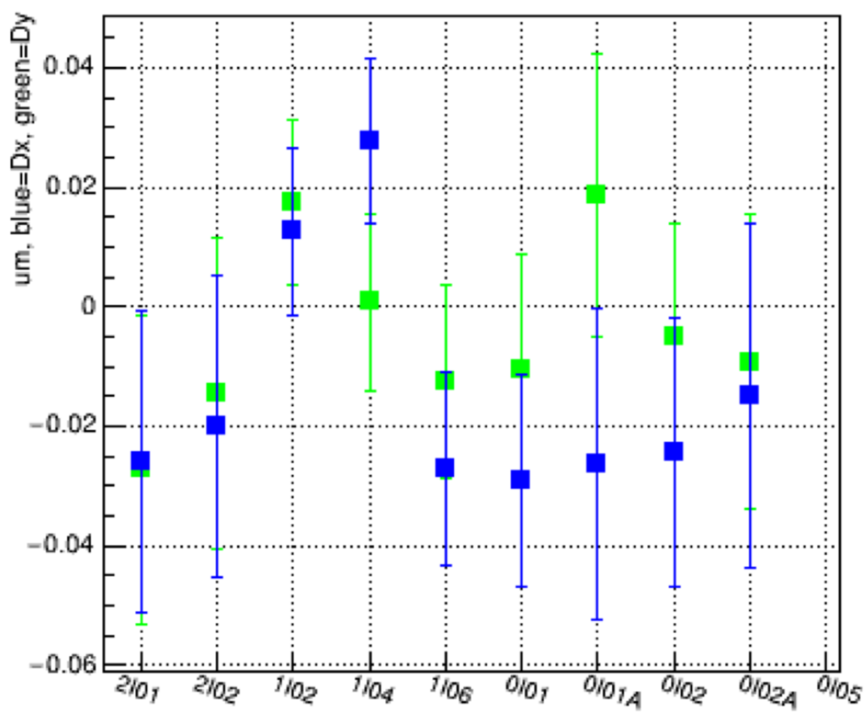

FIG. 61: RTP position feedback using $V_{\alpha pos,U}$ and $V_{\alpha pos,V}$ voltages for first 10 BPMs in the injector.

3.6.1 ELECTRON BEAM TRANSPORT THROUGH THE ACCELERATOR

We saw the new RTP Pockels cell can provide parity quality beam for PREX-2 and CREX from the injector studies. Although the position differences are small in the injector region it is important to maintain small helicity correlated asymmetries through out the accelerator and in the hall. If beam optics deviates from the design it will be hard to maintain small position differences for the experiment. Two important considerations for optimal electron beam transport are, clean apertures and adiabatic damping.

Beam losses due to clipping on apertures in the injector is an important factor to consider in achieving parity quality beam. Apertures couple position differences into charge asymmetries and couple spot-size asymmetries into position differences. Therefore, good optical transport throughout the injector and accelerator is crucial.

If the electron beam is aligned well with the optics, acceleration can reduce position differences from injector to Hall by[6]$\sim$ factor of 10. This position difference suppression is achieved through adiabatic damping. This is a relativistic effect in which the transverse phase space is reduced as the beam accelerates. This ensure the reduction of the helicity correlated position asymmetry by a factor of $\sqrt{P_{final}/P_{gun}}$, where P is the electron beam momentum at the photogun and at the experiment hall. In practice, it is difficult to achieve the desired adiabatic damping because correlations in the phase space project small changes in to large position differences in one direction of phase space. For PREX-2 and CREX, small helicity-correlated position differences were achieved via primarily feedback applied using the RTP Pockels cell.

3.7 PREX-2 AND CREX PARITY QUALITY BEAM RESULTS

When the two experiments were running, the charge asymmetry feedback was run concurrently with the data taking. The RTP position feedback was only performed in the injector before the experiment to appropriately set the injector position differences. As slow helicity reversals, IHWP was changed every $\sim$ 6-8 hours, and for PREX-2 the wien was changed three times and for CREX wien was changed 2 times.

Figure 62 shows a plot of sign corrected A_q over the course of the PREX-2 experiment[7]. Weighting by the detector statistical error and accounting for slow reversal cancellations gives an average A_q of 20 ppb for PREX-2. Figure 63 shows the A_q for the CREX and the average is 90 ppb.

We used occasional alpha-phase voltage adjustment on the crystal to control the position

[6] HAPPEX-II experiment had this suppression of position differences.

[7] The data collected in one IHWP state is called a “slug”

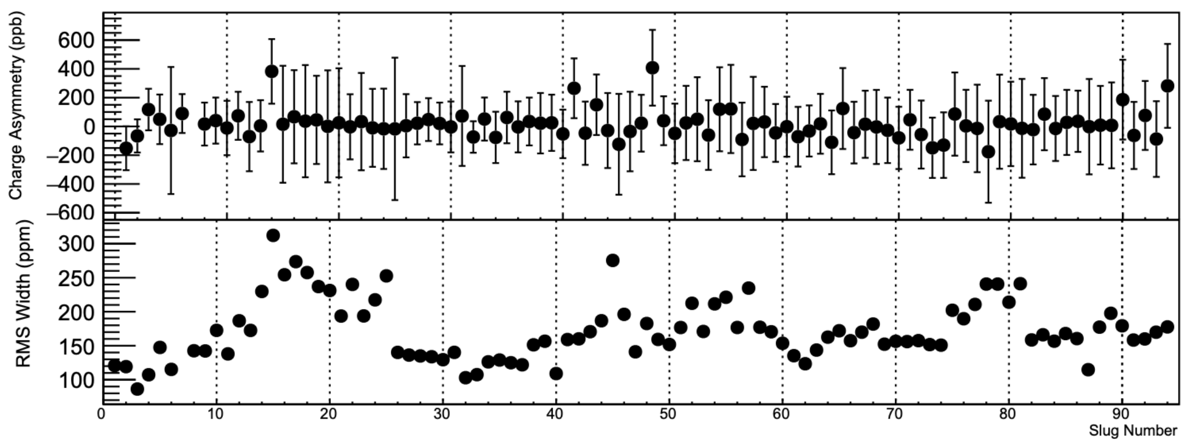

FIG. 62: Charge asymmetry during PREX-2.

differences on the target, over the course of the experiment. The goal was to make the position difference, on average, down to a nm. For both experiments we made initial adjustment and waited to see how well slow reversals cancelled on average and then towards the end, made successive adjustments to drive the average accumulated position difference towards 0. The Fig. 64 shows the position differences of BPM4e during PREX-2 experiment.

The average helicity correlated beam results for PREX-2 and CREX will be discussed in Chapter 6.

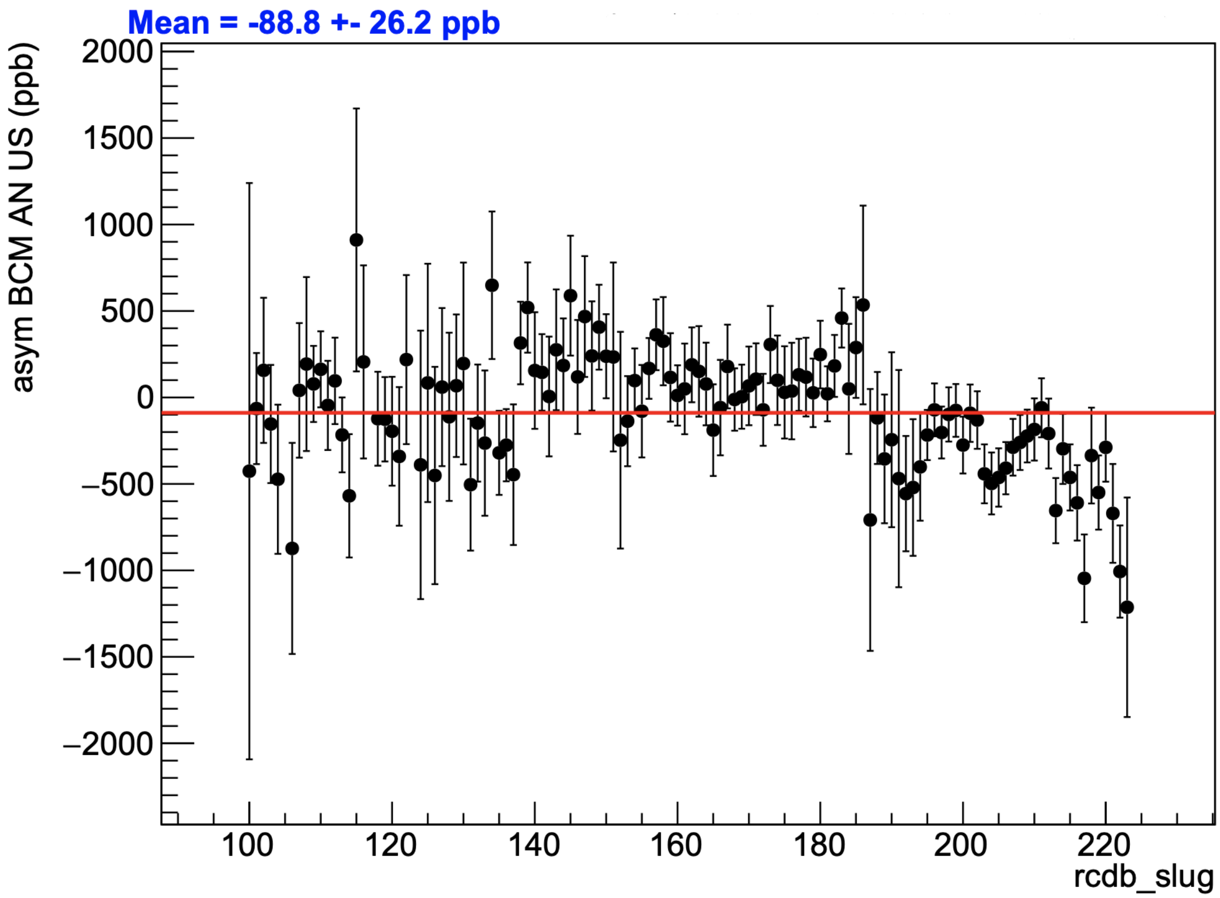

FIG. 63: Charge asymmetry during CREX.

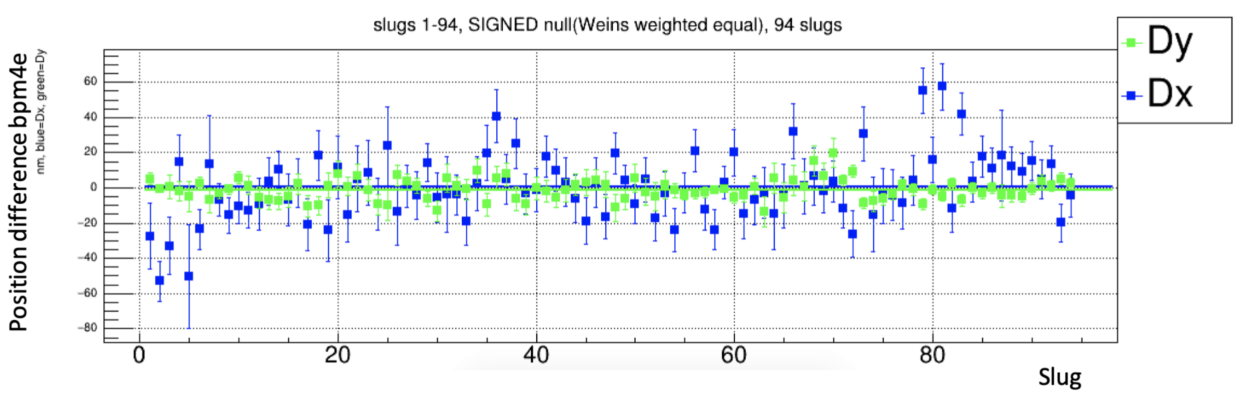

FIG. 64: Position difference of BPM4e during CREX.

CHAPTER 4

COMPTON POLARIMETRY

The Hall A Compton polarimeter is used to measure the polarization of the electron beam with high precision. This polarimeter was first installed in Hall A in 1999 and since then it has been used to measure polarization for various experiments. The Compton polarimeter uses backscattered Compton photons to measure beam polarization.

4.1 COMPTON SCATTERING KINEMATICS

Compton scattering was first explained by Arthur Holly Compton in 1923 and earned the 1927 Nobel Prize in Physics for this discovery. He observed a shift in the wavelength of hard x-rays and γ-rays scattering from graphite, and this shift could only be explained by the particle-like behavior of photons [47]. In 1954, Lipps and Tolhoek developed a formulation for polarized Compton scattering, giving a foundation for the use of Compton scattering in polarimetry [48].

Compton scattering is the process of an electron and photon scattering off each other in the reaction $e^{-}\gamma \rightarrow e^{-}\gamma$, as shown in Fig. 65.

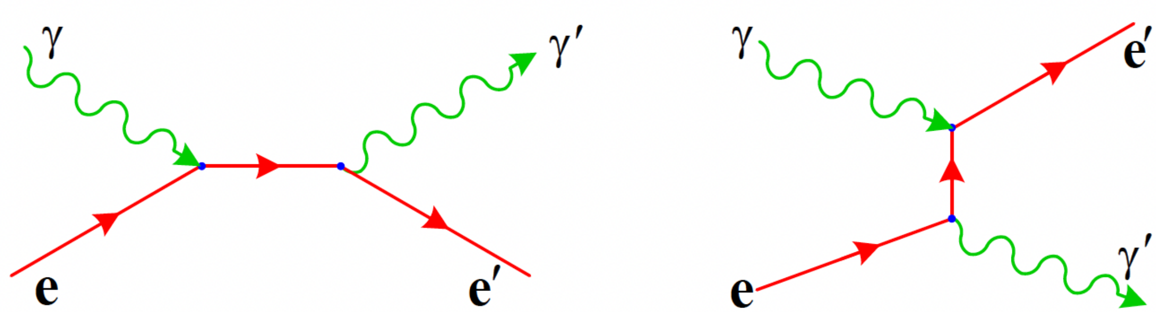

FIG. 65: Feynman diagrams for Compton scattering [49].

The Compton scattering kinematics in the laboratory frame are shown in Fig. 66. The incident electron has energy E and four-momentum p, and the incident photon has energy

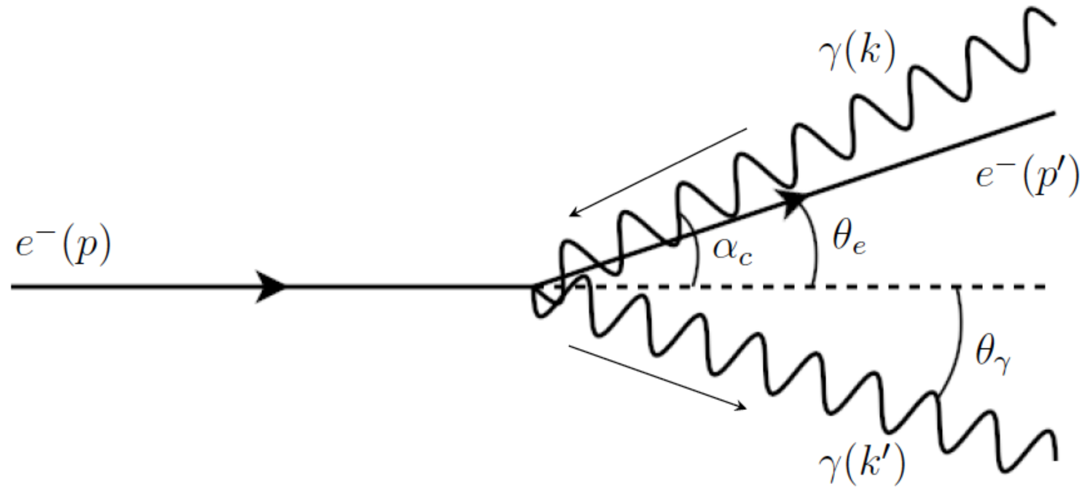

FIG. 66: Diagram of relevant Compton angles for kinematics. Angles are not to scale [49].

k. In the Hall A Compton polarimeter, the electron beam passes through the resonant laser with λ = 532 nm and photon energy k = 2.33 eV, with a slight crossing angle of $\alpha_c \sim$ 23 mrad. After scattering, the electron has a new energy and four-momentum, E' and p' respectively, with a scattering angle of θ_e. The scattered photon has energy k' and scattering angle θ_γ. The initial and final state of the electron and photon can be describe as follows,

$$p^\mu = (E, 0, 0, p), \tag{66}$$

$$k^\mu = (k, -k\sin(\alpha_c), 0, -k\sin(\alpha_c) \tag{67}$$

$$p'^\mu = (E', p'\sin(\theta_e), 0, p'\cos(\theta_e)), \tag{68}$$

$$k'^\mu = (k', k'\sin(\theta_\gamma), 0, k'\cos(\theta_\gamma)), \tag{69}$$

By applying conservation of energy and conservation of momentum we derive the scattered photon energy. Then, in the limit of a zero angle crossing (small α_c) of the laser and electron beam, and using p = $\sqrt{E^2 + m_e^2}$, the relation between the scattered photon energy and photon scattering angle can be derived as [50],

$$k' = \frac{4kaE^2}{m_e^2 + a\theta_\gamma^2 E^2}, \tag{70}$$

where,

$$a \equiv \frac{1}{1 + \frac{4kE}{m_e^2}}, \tag{71}$$

A plot of the scattered photon energy as a function of scattering angle for PREX-2 and CREX kinematics is given in Fig. 68. The maximum scattered photon energy, k'_{max} occurs when $\theta_\gamma = 0$. k'_{max} is called as "Compton edge" energy and corresponds to a Compton photon being backscattered at a full 180 degrees.

For PREX-2, 950 MeV beam electrons with 532 nm laser light corresponds to 31.2 MeV Compton edge and for CREX, 2182.5 MeV beam electrons corresponds to Compton edge of 157.7 MeV.

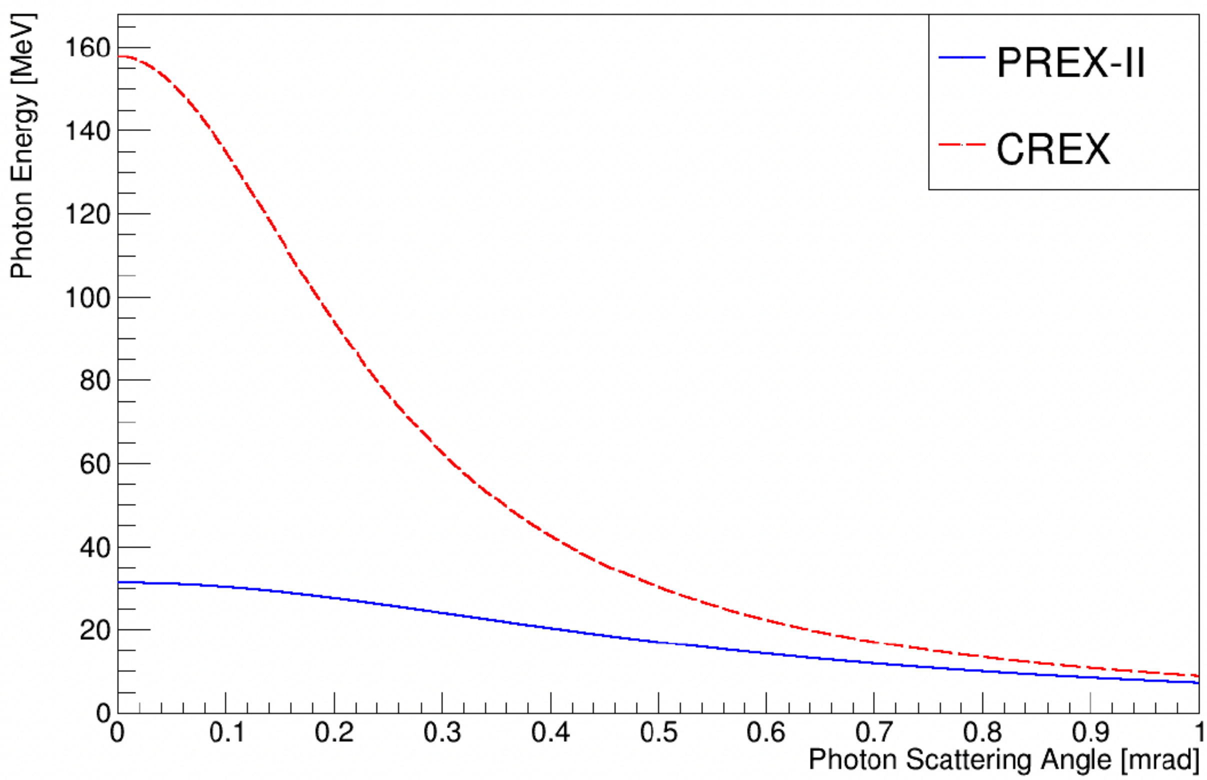

FIG. 67: Compton scattered photon energy k' plotted as a function of photon scattering angle θ_γ for the PREX-2 and CREX.

4.2 COMPTON CROSS SECTION AND ASYMMETRY

A cross section is a prediction of a probability of a particle being scattered by another particle. It is always measured by the effective surface area seen by the incident particles.

The differential cross-section for unpolarized Compton scattering, in the case of zero crossing angle is given by,

$$\frac{d^2\sigma_0}{d\rho d\phi} = r_0^2 a \left[\frac{\rho^2(1-a)^2}{1-\rho(1-a)} + 1 + \left(\frac{1-\rho(1+a)}{1-\rho(1-a)} \right)^2 \right], \tag{72}$$

where $\mathrm{r}_0 = \alpha\hbar\mathrm{c}/\mathrm{mc}^2 = 2.817 \times 10^{13}$ cm is the classical electron radius, $\rho = k'/k'_{max}$, and ϕ is the out-of-plane scattering angle [50].

Longitudinal and transverse differential cross sections are defined as,

$$\frac{d\sigma_L}{d\rho d\phi} = r_0^2 a \left[(1-\rho(1+a)) \left(1 - \frac{1}{(1-\rho(1-a))^2} \right) \right], \tag{73}$$

$$\frac{d\sigma_T}{d\rho d\phi} = r_0^2 a \left[(\rho(1-a)) \left(\frac{\sqrt{4a\rho(1-\rho)}}{1-\rho(1-a)} \right) \right]. \tag{74}$$

The complete differential cross section can be written as [51],

$$\frac{d^2\sigma}{d\rho d\phi} = \frac{d^2\sigma_0}{d\rho d\phi} \mp P_\gamma P_e \left(\cos(\psi) \frac{d^2\sigma_L}{d\rho d\phi} + \sin(\psi)\cos(\phi) \frac{d^2\sigma_T}{d\rho d\phi} \right), \tag{75}$$

where P_γ is the laser degree of circular polarization (DOCP), P_e is the electron beam polarization, and ψ is the angle of the direction of the electron spin with respect to the beam propagation axis $\vec{z}$. The "+" and "-" signs are defined by the helicity states of electrons and photons.

Transverse dependent part of Eq. 75 drops out when integrating over the azimuthal angle ϕ. Then, the differential cross section becomes

$$\frac{d\sigma}{d\rho} = \frac{d\sigma_0}{d\rho} \mp P_\gamma P_e \cos(\psi) \frac{d\sigma_L}{d\rho}, \tag{76}$$

$$\frac{d\sigma}{d\rho} = \frac{d\sigma_0}{d\rho} \left(1 \mp P_\gamma P_e \cos\psi A_c \right), \tag{77}$$

where A_c is the Compton scattering analyzing power,

$$A_c \equiv \frac{d\sigma_L/d\rho}{d\sigma_0/d\rho}. \tag{78}$$

The analyzing power A_c is at a maximum at the Compton edge (at $\rho = 1$)

$$A_c^{max} \equiv \frac{(1-a)(1+a)}{1+a^2}. \tag{79}$$

Using the longitudinal spin-dependent piece of the cross section we can build an experimentally measurable asymmetry,

$$A_{exp} = \frac{(d\sigma/d\rho)^+ - (d\sigma/d\rho)^-}{(d\sigma/d\rho)^+ + (d\sigma/d\rho)^-} = P_\gamma P_e \cos\psi A_c, \tag{80}$$

The experimental asymmetry is maximized when the electron spin is purely longitudinal ($\psi = 0$). PREX-2 and CREX were both set up to have a longitudinal beam, so we can take $\psi = 0$.

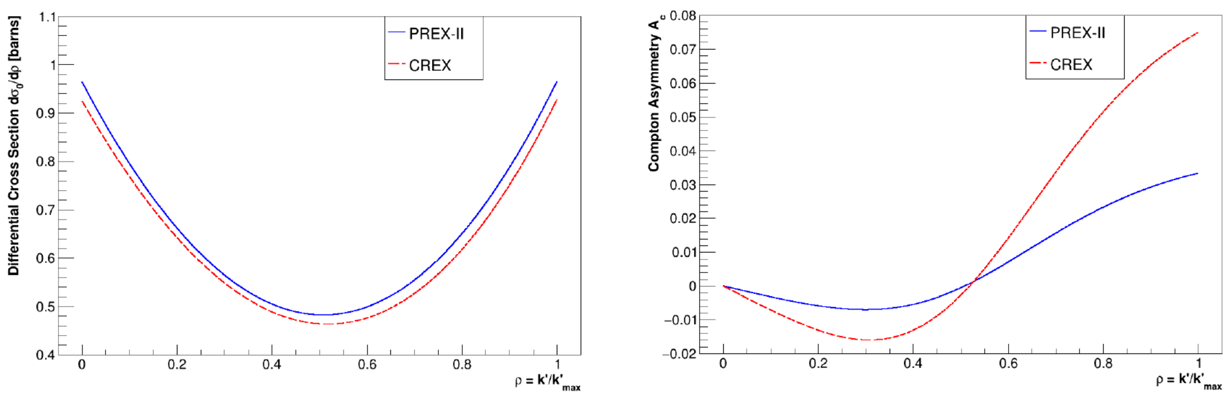

FIG. 68: The unpolarized Compton cross section (left), and theoretical analyzing power A_c (right) as a function of backscattered photon energy for the PREX-2 and CREX.

A_c is the theoretical analyzing power but for the polarization measurement we need the experimental analyzing power which is corrected for effects such as non linearity. Here, the experimental analyzing power is the measured Compton asymmetry if we had 100% polarized beam and 100% circularly polarized laser light.

4.3 COMPTON COUNTING ASYMMETRY

Compton photon asymmetry can be calculated by counting the number of scattered photons detected for each helicity state. This can be done in two different ways.

A counting asymmetry can be measured on a bin-by-bin basis. In this technique the Compton energy range is divided into i energy bins and the scattering rate is integrated over each bin i,

$$n_i^{\pm} = L \int_{\rho_i}^{\rho_{i+1}} d\rho \epsilon(\rho) \frac{d\sigma}{d\rho}(1 \pm P_\gamma P_e\ A_c(\rho)) \tag{81}$$

where L is the integrated luminosity of the incident photons and electrons at the Compton interaction point, and $\epsilon(\rho)$ is the detector response function. The measured asymmetry for the i^{th} energy bin is then given by,

$$A_{exp}^{(i)} = \frac{n_i^+ - n_i^-}{n_i^+ + n_i^-} = P_e^{(i)} P_\gamma \langle A_c \rangle^{(i)}, \tag{82}$$

where $P_e^{(i)}$ is the mean electron beam polarization for each bin i and $\langle A_c \rangle^{(i)}$ is the average theoretical analyzing power for i^{th} bin. The mean polarization is then taken from a fit to the expected asymmetry over the binned distribution $A_{exp}^{(i)}$ [52].

The second method for measuring a counting asymmetry is to calculate the asymmetry of all events over the entire Compton energy range using Eq. 81, and integrating over the energy range ρ_{min} (lower threshold energy) to 1 (Compton edge energy), asymmetry is given by,

$$A_{exp} = \frac{N^+ - N^-}{N^+ + N^-} = P_e^{(i)} P_\gamma \langle A_l \rangle, \tag{83}$$

$$\langle A_l \rangle = \frac{\int_{\rho_{min}}^{1} d\rho \epsilon(\rho) \frac{d\sigma}{d\rho}(\rho) A_c(\rho)}{\int_{\rho_{min}}^{1} d\rho \epsilon(\rho) \frac{d\sigma}{d\rho}(\rho)}, \tag{84}$$

where, $\langle A_l \rangle$ is the average analyzing power over the entire measured energy range.

4.4 COMPTON INTEGRATING ASYMMETRY

The next method to measure the asymmetry is to measure total energy deposited from the photon detector PMT for each helicity state and calculate the asymmetry from that. With this method, the energy weighted signal is,

$$S^{\pm} = L \int_{\rho_{min}}^{1} d\rho Y(\rho) \epsilon(\rho) \frac{d\sigma}{d\rho}(\rho)(1 \pm P_\gamma P_e\ A_c(\rho)), \tag{85}$$

where $Y(\rho)$ is the average detected signal for each helicity state. Here the analyzing power is,

$$\langle A_l \rangle = \frac{\int_{\rho_{min}}^{1} d\rho Y(\rho) \epsilon(\rho) \frac{d\sigma}{d\rho}(\rho) A_c(\rho)}{\int_{\rho_{min}}^{1} d\rho Y(\rho) \epsilon(\rho) \frac{d\sigma}{d\rho}(\rho)}. \tag{86}$$

For PREX-2 and CREX, this integration method was used to measure Compton asymmetry. The measured asymmetry is then given by,

$$A_{exp} = P_\gamma P_e \langle A_l \rangle = \frac{S_+ - S_-}{S_+ + S_-}. \tag{87}$$

4.5 HALL A COMPTON APPARATUS

Hall A Compton polarimeter has three main subsystems, laser system, photon detector and an electron detector. Each of the detectors is capable of independently determining the beam polarization by detecting either the Compton scattered electron or photon. But, for PREX-2 and CREX only the photon detector was used to measure the polarization.

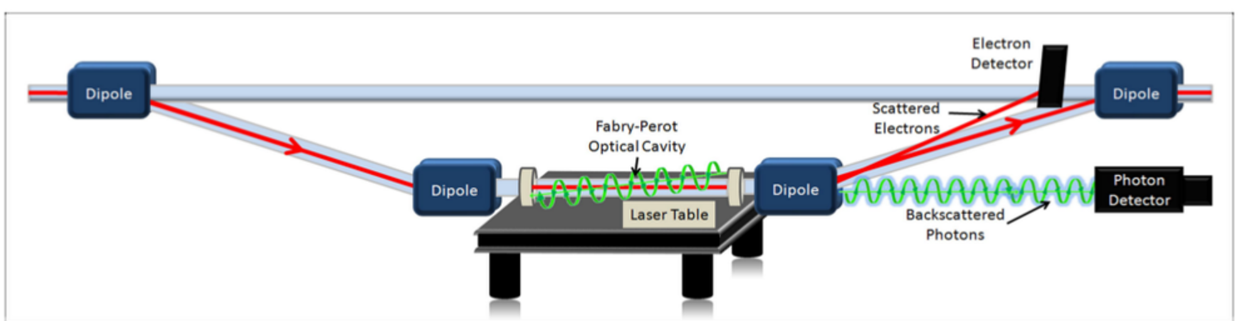

FIG. 69: Schematic of the Hall A Compton polarimeter showing magnetic chicane, laser table, and electron and photon detectors [53].

A schematic of the Hall A Compton polarimeter is given in Fig. 69. Electrons are diverted into the Compton chicane, where they undergo Compton scattering with laser photons in a high-finesse Fabry-Perot cavity. Scattered electrons are detected in a silicon microstrip electron detector and backscattered photons are detected in a GSO photon calorimeter. In next three section these systems will be discussed. The remainder of the electron beam are diverted back out of the Compton chicane, and continue to the Hall A target, allowing for a continuous polarization measurement without significantly disturbing the incident electron beam.

4.5.1 PHOTON DETECTOR

PREX-2 and CREX photon detector is a cerium-doped gadolinium orthosilicate

$(Gd_2SiO_5 : Ce$, "GSO") cylindrical crystal which is 15 cm long and has a 6 cm diameter. The detector sits approximately 6 meters downstream from the Compton interaction point. The Compton backscattered photons are unaffected by magnetic fields from the dipole magnets and pass straight through the third dipole in the chicane into the photon detector.

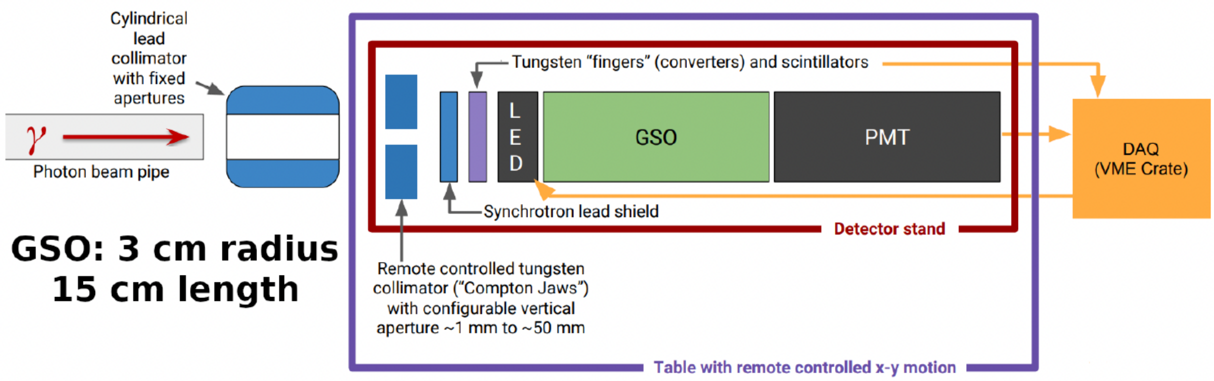

FIG. 70: Schematic of the Hall A Compton photon detector layout [36].

The Hall A Compton beamline has a collimator directly upstream of the photon detector to reduce background from non-Compton processes (bremsstrahlung background). The collimator is a 6 cm long, 2 cm in inner diameter, lead cylinder, located approximately 6 m downstream of the center of the interaction point (CIP), and the collimator's position relative to the CIP is fixed. Downstream of the collimator there is a another secondary collimator called "jaws", which consists of two pieces of tungsten metal that could be moved vertically to change the photon acceptance. The jaws collimator was not used during PREX-2 and CREX to get the full photon acceptance.

To shield the photon detector from low energy synchrotron radiation background, a thin lead disk is mounted on the downstream side of the jaws. The installed disk is 250 μm thick, and chosen to be as thin as possible to achieve acceptable background rates.

Upstream of the photon detector there are two tungsten "fingers", just behind the fingers are two small scintillators, each about 8 cm long, 1 cm wide, and 1 cm thick, attached to photomultiplier tubes. One tungsten finger is oriented horizontally, positioned 20 mm above the center of the GSO crystal; the other is oriented vertically and is positioned 20 mm towards beam left from the center of the crystal. When the tungsten fingers intercept the photon beam they create showers, which are then detected by the scintillators.

These scintilators are used to align the photon detector with photon beam. The fingers,

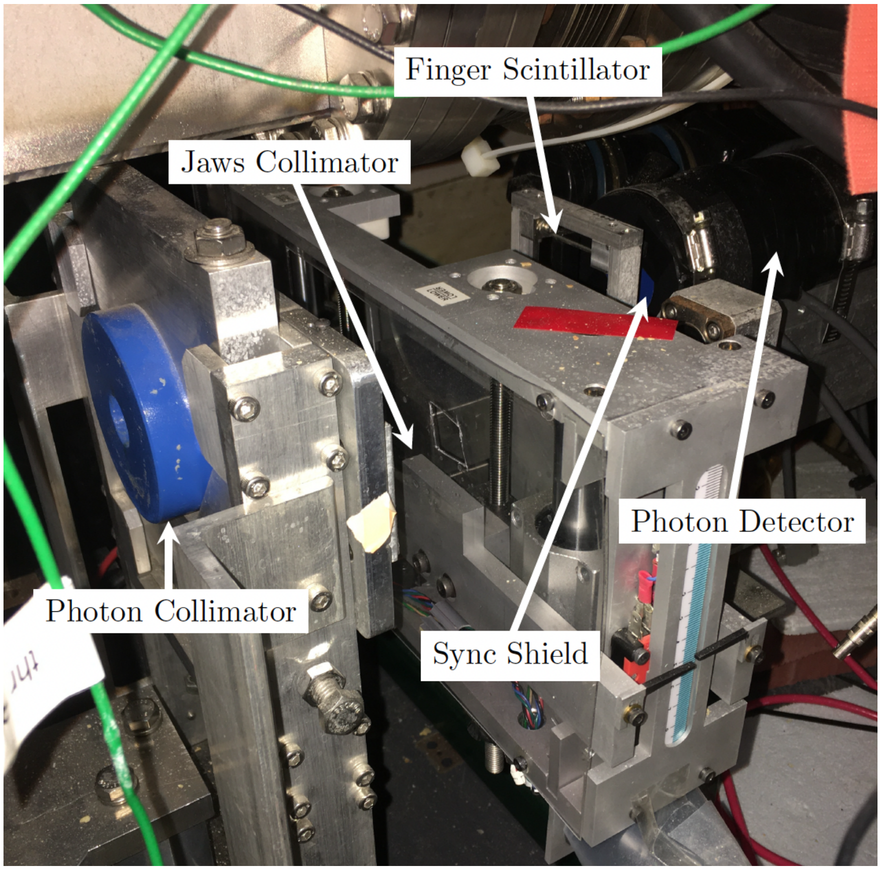

FIG. 71: Photo of the Hall A Compton photon detector components [36].

their scintillators, and the photon detector are all mounted onto the remotely-controlled photon detector table. To align the detector, the photon detector table is scanned horizontally while centered vertically, and then scanned vertically while centered horizontally. When the photon beam hits the tungsten fingers, the counting rate increases notably. By finding the table position that yielded maximum rate, the table position is calibrated to the position of the center of the Compton scattered photon distribution. The detector is then centered on this distribution by applying the calibrated offset position between the fingers and detected fingers.

The GSO crystal is coupled to a 12-stage BURLE Industries RCA 8575 PMT with a customized PMT base for readout. The two experiments each had their own PMTs, both were the same make and model but with different voltage-dividers to optimize performance for their respective expected signal levels. The PMT voltage was calibrated for both experiments such that a single Compton edge photon pulse would have a height of about 1200 raw ADC units [36].

GSO was chosen as the scintillator for the Compton polarimeter due to its high efficiency at low energies. GSO has a fast and bright signal. Also, the fast decay ($\approx$ 56 ns) time can support high rates in the detector. One of the biggest challenges with GSO is high thermal neutron capture rate. PREX-2 and CREX produced lot of thermal neutrons from the target and these neutrons get captured in the gadolinium, producing high backgrounds in the detector, which required subtracting during data analysis.

4.5.2 ELECTRON DETECTOR

The Compton asymmetry may also be measured using scattered electron. After the interaction with laser beam, the scattered electrons lose some of their energy and are bent at a larger angle than the unscattered ones and are thus separated from the primary beam. The electron detector is placed above the primary beamline on the chicane between the third and fourth chicane dipole magnets. The electron detector consists of four planes of 192 silicon microstrips. The planes are aligned such that the electron beam is normally incident, and the strips are horizontal.

The expression for electron deflection above the the primary beamline after the third dipole magnet is given by,

$$\Delta y = ecBx_{det}\left(\frac{1}{E'_{min}} - \frac{1}{E}\right), \tag{88}$$

where e is the electron charge, B is the field integral of the dipole magnet, x_{det} is the horizontal position of the electron detector measured from the third dipole, and E'_{min} is Compton edge for electrons ($E'_{min} = E - k'_{max}$). By knowing Δy from the primary beam, we can reconstruct the trajectory of the scattered electron and deduce its momentum (energy). The electron detector signal is sent to the electron detector DAQ which calculates an asymmetry through electron counts per microstrip in each plane.

The electron detector was not used during PREX-2 and only used for diagnostic measurements during CREX.

4.5.3 LASER SYSTEM

Between dipoles two and three (Fig. 69) there was a small room with the optics table. A schematic of the Compton optical setup is shown in Fig. 72.

The seed laser of this system was a diode pumped neodymium-doped yttrium aluminum garnet (Nd:YAG) laser that delivered a continuous wave (CW) IR (λ = 1064 nm) beam

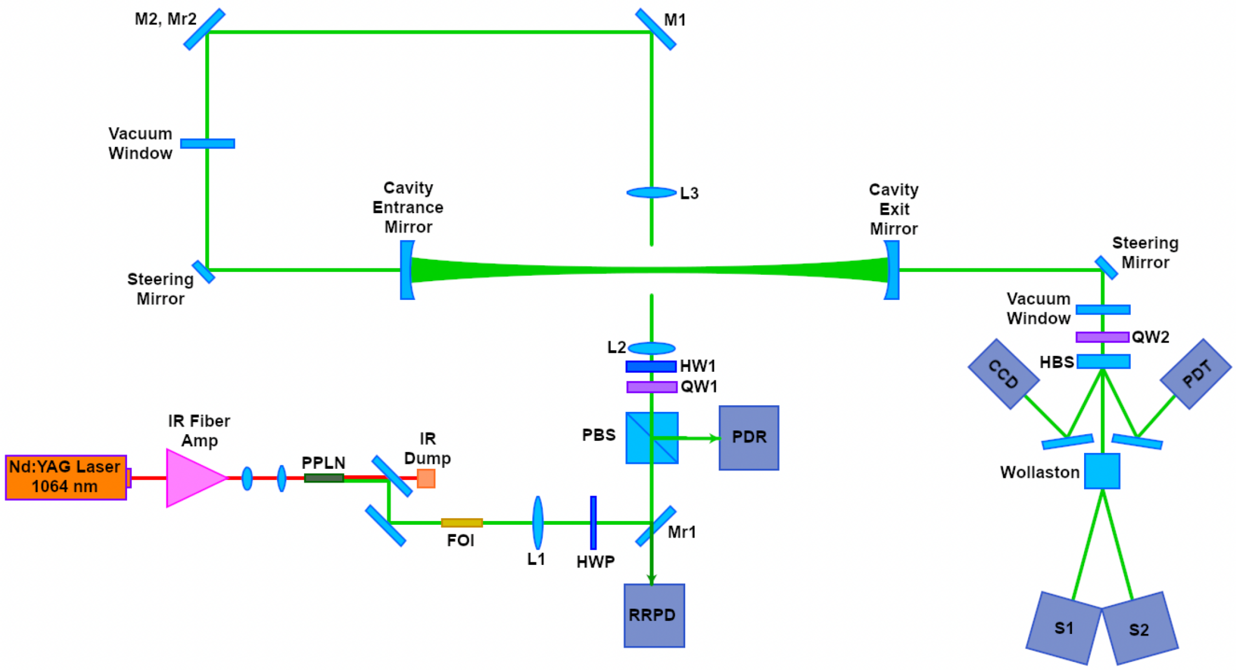

FIG. 72: Schematic of the Compton optical system with the primary components labeled.

up to 250 mW power. The seed laser was fiber coupled to IPG Photonics single mode ytterbium doped fiber laser amplifier capable of generating a CW beam up to 10 W. The fiber amplifier output was then focused into a Periodically Poled Lithium Niobate (PPLN) crystal for frequency doubling to produce green laser light (λ = 532 nm). Two dichroic mirrors were placed after the PPLN crystal to separate the green beam from the residual IR beam. The PPLN crystal was placed in an externally controlled, temperature stabilized oven. Adjusting the temperature of the PPLN crystal and the angle of the crystal with respect to the laser beam, a good green power can be achieved. Due to small thickness of the crystal, care must be taken to ensure that the beam was not clipped and passing through the center of the crystal.

There was a Faraday optical isolator (FOI) to protect the laser equipment from back-reflected light. Then the green light passed through series of transport and polarization manipulation optics. As shown in Fig. 72 L1, L2 and L3 lenses shape and focus the incident beam to the optical cavity. L2 and L3 lenses are also used to get a correct waist size at the cavity center. L1 and L2 are on fixed mounts and L3 is mounted on a remote controlled translation stage. A periscope with two motorized mirrors, M1 and M2 allow translational and rotational motion for aligning the laser beam with respect to the optical axis of the cavity formed by two cavity mirrors. The other turning mirrors are fixed at 45 degrees with respect to the incident beam.

The laser emerging from the laser head is vertically polarized. It was then sent through a half wave plate followed by a polarizing beam splitter (PBS) which acts as a variable attenuator and rotate the beam polarization. The laser beam was linearly polarized horizontally as it passed through the PBS. Then the beam polarization was changed from linear to circular using a combination of remotely controlled quarterwave plate (QW1) and a halfwave plate (HW1). With these two wavelplates we can build any arbitrary polarization state at the entrance of the cavity.

The laser was then directed through a series of partially-transmitting mirrors into the Fabry-Perot cavity. The beam arrived at the optical cavity is partially reflected and partially transmitted. The reflected beam was measured by the retro-reflected photodiode (RRPD). A reflection photodiode (PDR) attached to integrating sphere is used to maintain cavity lock using the Pound-Drever-Hall method.

At the exit of the cavity, a holographic beam splitter (HBS) splits the beam into several beams. The polarization of the transmitted laser beam was measured by a system consisting of a quarter-wave plate, a Wollaston prism and two detectors each mounted on an integrating sphere. There is a CCD camera for viewing the transmitted beam, which is used for imaging the transmitted beam on screen in counting house. A transmitted photodiode (PDT) monitored the relative power of transmitted beam and is calibrated to produce a measurement of the power stored in the cavity.

Fabry-Perot cavity

A perfect Gaussian beam can be characterized by two parameters,

$$w(z) = w_0 \sqrt{1 + \left(\frac{z}{z_R}\right)^2}, \tag{89}$$

$$R(z) = z\left[1 + \left(\frac{z_R}{z}\right)^2\right], \tag{90}$$

z is the axial distance from the beam's narrowest point (waist). w(z) is the 2σ width of the transverse intensity distribution at z and R(z) is the radius of curvature of the laser beam wavefront at z. w_0 is beam radius at the waist (see Fig. 73).

Gaussian beams have most of their power propagate in the TEM_{00} mode, therefore mode-matching the laser to the fundamental TEM_{00} mode is required. Mode-matching to an optical

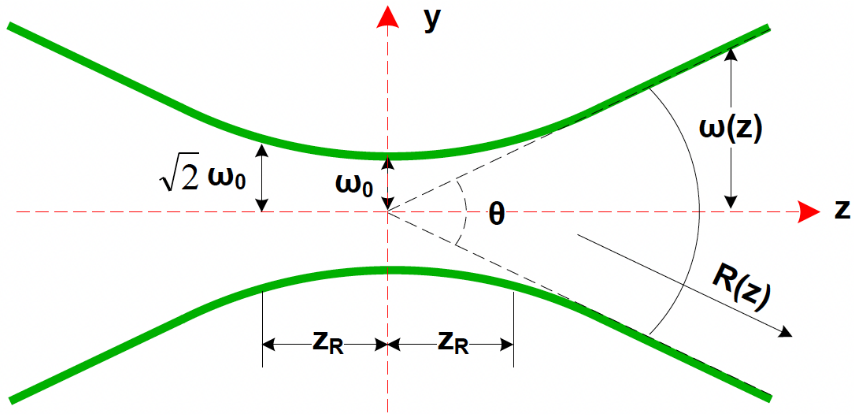

FIG. 73: A longitudinal profile of a Gaussian beam [49].

cavity is the process of shaping and aligning a laser such that its electric field distribution matches a particular resonating mode of the optical cavity. If the laser is better mode-matched to the cavity, more power will be coupled into the fundamental cavity oscillating mode and less power will be reflected backward.

There is another parameter which shows the deviation of a laser beam from the ideal Gaussian beam. This is known as the laser beam quality factor or mostly known as M^2 factor. $M^2 = 1$ describes an ideal Gaussian beam. To measure M^2 we can use this equation [49],

$$\sigma^2(z) = \sigma_0^2 + \left(\frac{M^2\lambda}{\pi\sigma_0}\right)^2 (z - z_0)^2, \tag{91}$$

where $\sigma^2(z)$ is the 4σ beam width in the x or y direction, λ is the wavelength of the laser beam, z_0 is the location of the beam waist and σ_0 is the second moment width. Beam profile measurements on the Compton laser were performed using a camera and by fitting the data M^2 can be calculated. Changing focal length and distance of lenses in the Compton optical system, a good M^2 ($M^2 < 1.1$) is achieved for both x and y directions.

In order to "lock" the cavity onto a resonance the Pound-Drever-Hall (PDH) technique is used. Due to drift and jitter in the laser, both the laser frequency and cavity resonance frequency can vary with time. Therefore we need a system that allow us to establish a frequency matching between laser and cavity. The method called feedback control was used to achieve an equality in laser and cavity resonance frequencies. Here the cavity resonance frequency is used as a reference frequency and extracts an error signal proportional to the frequency deviation of the laser from this reference signal, and then suppress that using feedback on either cavity or laser. In Hall A Compton setup, cavity mirrors are fixed but the laser is tunable. A piezo-electric transducer was attached to the laser crystal and we feed the error signal back to the laser to lock the laser to the cavity. A schematic of the locking electronics can be seen in Fig. 74.

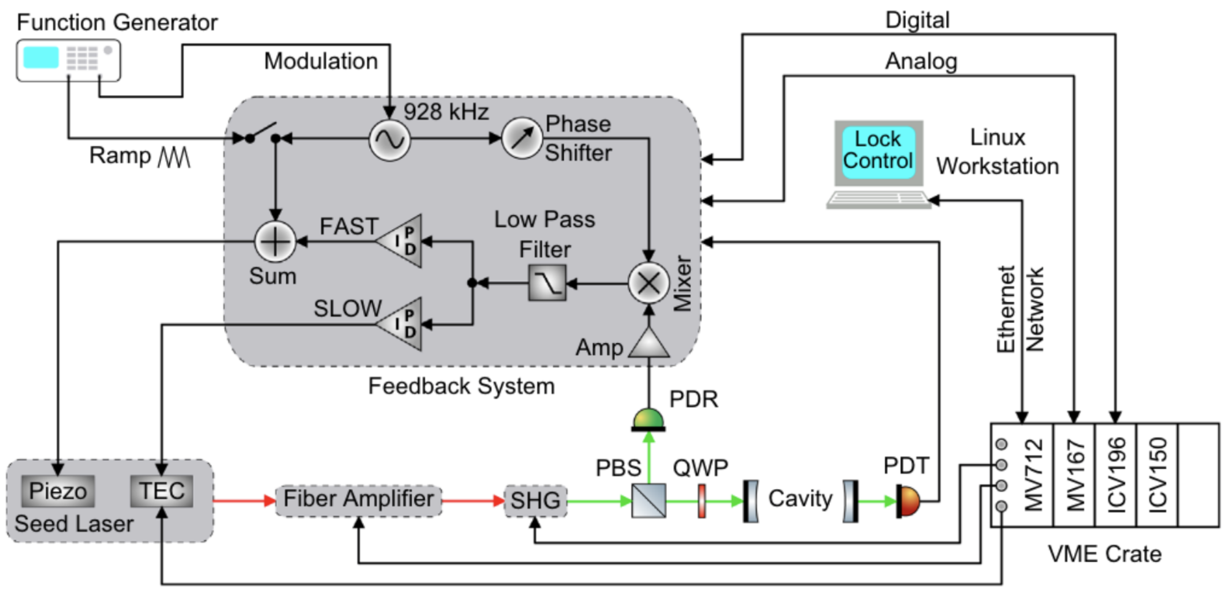

FIG. 74: A schematic of feedback control system used for Hall A Compton polarimeter [54].

Laser polarization

According to Eq. 87, knowing the degree of circular polarization (DOCP) of the laser is vital to precisely calculate the electron beam polarization. Also, the Compton asymmetry measured at the point of interaction is directly proportional to the DOCP. Therefore, a photon beam with DOCP 100% is desired.

The electric field, $E(x, y, z, t)$ of a monochromatic plane wave traveling in an isotropic media can be written as,

$$E(x, y, z, t) = (E_x\hat{x} + E_y\hat{y})e^{i(\omega t - kz)}, \tag{92}$$

where E_x and E_y are the transverse components in x and y directions, ω is the angular frequency and k is the wave vector (k $= 2\pi/\lambda$). If we consider a pair of plane waves that are orthogonal to each other it can be represented as [55] [49],

$$E(x, y, t) = \begin{pmatrix} X(t) \\ Y(t) \end{pmatrix} = \begin{pmatrix} A_x \cos(\omega t) \\ A_y \cos(\omega t - \delta) \end{pmatrix}. \tag{93}$$

Here, A_x and A_y are real amplitudes and δ is the angular phase difference between them. The evolution of Eq. 93 defines the most general polarization ellipse,

$$\frac{X^2(t)}{A_x} + \frac{Y^2(t)}{A_y} - \frac{2X(t)Y(t)}{A_x A_y} \cos\delta = \sin^2\delta. \tag{94}$$

The sign of δ defines the helicity of the ellipse. The elliptic polarization can be referred to as right-handed or left-handed, depending on the direction in which the electric field vector rotates. The helicity state h_γ is related to δ by the following relationship,

$$h_\gamma = \begin{cases} +1, \text{Left-handed} & \delta \in [0, \pi] \\ -1, \text{Right-handed} & \delta \in [-\pi, 0] \end{cases}$$

If $\delta = 0$ (π), then the polarization is linear and if $\delta = \pm\, \frac{\pi}{2}$, the polarization is circular.

In 1941 Robert Clark Jones wrote a series of three papers outlining a method for describing polarized light as a complex two component vector, and optical systems with 2×2 complex matrices. When light passes through an optical element, the polarization of the transmitted light can be described by taking the product of the Jones matrix of the optical element and the Jones vector of the incident light.

The polarization state for two orthogonal plane waves (previous case) can be represented by Jones vector J with two components,

$$\mathrm{J} = \begin{pmatrix} A_x \\ A_y e^{i\delta} \end{pmatrix}. \tag{95}$$

It is convenient to work with Jones vector of various polarization states. Table 3 gives some examples of common polarization states using Jones vectors.

In 1952 G. G. Stokes introduced a new way to describe polarization of lights with its observable quantities, such as, intensity and the orientation of the polarization ellipse [55].

$$\mathrm{P} = \begin{pmatrix} P_0 = A_x^2 + A_y^2 \\ P_1 = A_x^2 - A_y^2 \\ P_2 = 2A_x A_y \cos\delta \\ P_2 = 2A_x A_y \sin\delta \end{pmatrix} = \begin{pmatrix} I \\ I_x - I_y \\ I_{+\frac{\pi}{4}} - I_{-\frac{\pi}{4}} \\ I_L - I_R \end{pmatrix}, \tag{96}$$

Horizontal linear polarization	$\begin{pmatrix} 1 \\ 0 \end{pmatrix}$
Vertical linear polarization	$\begin{pmatrix} 0 \\ 1 \end{pmatrix}$
Right circular polarization	$\frac{1}{\sqrt{2}}\begin{pmatrix} 1 \\ -i \end{pmatrix}$
Left circular polarization	$\frac{1}{\sqrt{2}}\begin{pmatrix} 1 \\ i \end{pmatrix}$

TABLE 3: States of light polarization using Jones vectors. All vectors normalized to unity.

where, I is the beam intensity, I_x, I_y, $I_{+\frac{\pi}{4}}$ and $I_{-\frac{\pi}{4}}$ are the intensities after a linear polarizer oriented along $\hat{x}$, $\hat{y}$, $\hat{x}+\hat{y}$ and $\hat{x}-\hat{y}$ respectively. I_L and I_R are the intensities after circular left and right polarizers respectively. For a fully polarized wave,

$$P_0 = \sqrt{P_1^2 + P_2^2 + P_3^2}. \tag{97}$$

In this formalism, the left and right circular states are defined as [55],

$$\hat{L} = \begin{pmatrix} 1 \\ 0 \\ 0 \\ 1 \end{pmatrix} \qquad \hat{R} = \begin{pmatrix} 1 \\ 0 \\ 0 \\ -1 \end{pmatrix}, \tag{98}$$

The degree of linear polarization (DOLP), the degree of circular polarization (DOCP) and degree of polarization (DOP) can be defined as [55],

$$\text{DOLP} = \frac{\sqrt{P_1^2 + P_2^2}}{P_0}, \tag{99}$$

$$\text{DOCP} = \frac{P_3}{P_0}, \tag{100}$$

$$\text{DOP} = \sqrt{\text{DOLP}^2 + \text{DOCP}^2} = \frac{\sqrt{P_1^2 + P_2^2 + P_3^2}}{P_0}. \tag{101}$$

For our experiment we need to know the degree of circular polarization in the CIP very precisely. When the laser is locked, the cavity is closed under high vacuum and there is no direct way to measure the polarization inside the cavity. We can only measure the incoming power in to the cavity, reflected power and transmitted power out of the cavity and infer the polarization inside the cavity from that.

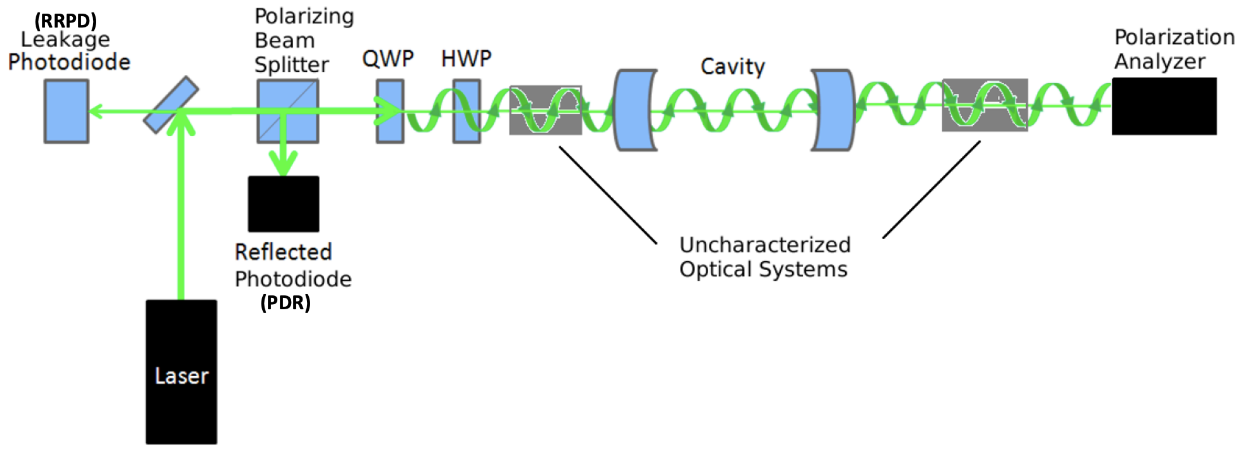

FIG. 75: Simplified schematic of optical setup for producing and measuring polarized light inside Fabry-Perot optical cavity [53].

Figure 75 shows a schematic of the optical setup for the Compton polarization. In this figure the "uncharacterized" region have turning mirrors and a vacuum window. If the entrance and exit optical system were fully characterized along with the cavity mirrors, one could determine the polarization inside the cavity by measuring the polarization characteristics of the reflected or transmitted beam. To fully characterize the system, the reflected beam and transmitted beam should be characterized in different configurations such as cavity locked, unlocked, cavity under vacuum and open to air. The challenge is complicated by the fact that the system is different when under vacuum, due to stresses on the vacuum windows, and potentially different when the cavity is locked and small amounts of birefringence in the dielectric of the cavity mirrors can compound to a significant effect.

Laser Entrance Function

The laser "entrance function", describes the laser polarization at each element along the entrance line. In entrance region the light passes twice through the same system (forward and reverse) and we can compare the changes in the polarization states between the two beams to characterize the intermediate optical system.

The entrance function of the cavity can change due to mechanical stress from tightening bolts and it can change when pulling the vacuum, therefore it's important to check things under vacuum. We should characterize the birefringence of the cavity mirrors and the cavity entrance vacuum windows, and birefringence of the cavity itself.

To build a model we used optical reversibility. This principle recognized that, in the absence of depolarization, as the path of system is reversed, the parameters for the change in polarization through each element will have their signs reversed [56]. Coupled with the reversal of circular polarization components at the back reflection at the cavity mirror, we can use this principle to characterize the entrance function.

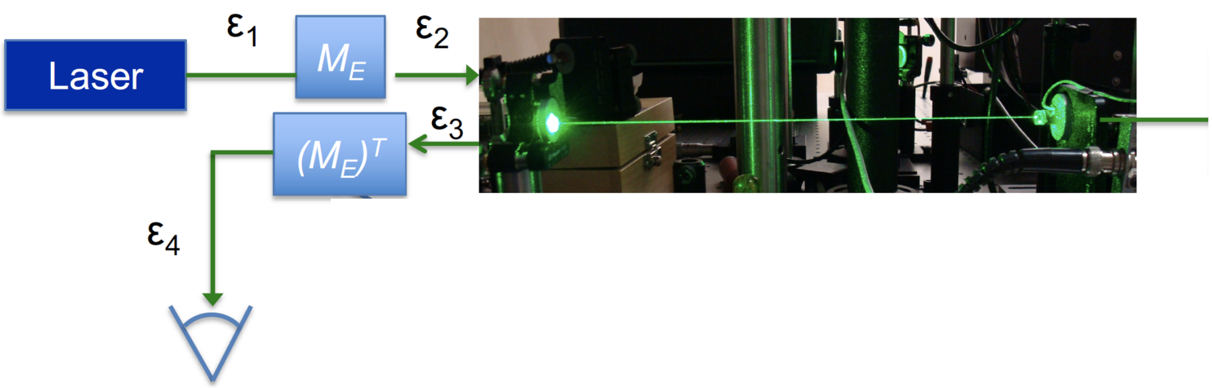

FIG. 76: Simplified schematic of optical setup for measuring polarized light inside Fabry-Perot optical cavity.

The retro reflected photodiode (RRPD) is used to build the entrance function. RRPD receives the reflected laser light from the cavity mirror while the cavity is not locked. Using the optical reversibility theorem, the light at the cavity entrance is circular if and only if the light reflected backward is linearly polarized (but rotated 90 degrees) after traversing the QWP. As illustrated in Fig. 76 the propagation of light into the Fabry Perot cavity (transfer function) can be described by matrix, $\mathrm{M_E}$, with, light propagating in opposite direction described by the transpose matrix, $(\mathrm{M_E})^{\mathrm{T}}$.

$$
\begin{aligned}
\epsilon_2 &= \mathrm{M_E}\epsilon_1 \\
\epsilon_4 &= (\mathrm{M_E})^{\mathrm{T}}\epsilon_3 \\
\epsilon_4 &= (\mathrm{M_E})^{\mathrm{T}}\mathrm{M_E}\epsilon_1,
\end{aligned}
\tag{102}
$$

where, ϵ is the polarization vector at different points. The reflected light is analyzed by a polarizer into its two linear states. The "reflected photodiode (PDR)" and the "leakage photodiode (RRPD)", illustrated in Fig. 75, measure the intensity in the vertical and horizontal polarization states respectively. The entrance function M_E can be written as,

$$M_E = [M_{\text{general}}(A, \text{gamma}, B)][M_{\text{HWP}}(\theta_{H1,H2})][M_{\text{QWP}}(\theta_{Q1,Q2})], \tag{103}$$

where, M_{general} is the Jones matrix for the composite general birefringent system to be characterized, and M_{HWP} and M_{QWP} are the Jones matrices for a quarter and half wave plate respectively. A and B are angles of rotations for the polarization and gamma describes the phase retardance. H1(Q1) and H2(Q2) are angle offsets for the HWP (QWP) angles and scale factors for the induced phase retardance respectively.

To determine the parameters of the model, a full scan of the HWP and QWP is done and the signal in the RRPD is measured as a function of the rotation angle. According to optical reversibility, the circular polarization at the cavity entrance is maximized when RRPD signal is minimized. Example of an entrance scan result is shown in Fig. 77. Using this entrance function, we can determine the laser polarization at the cavity entrance for an arbitrary input state.

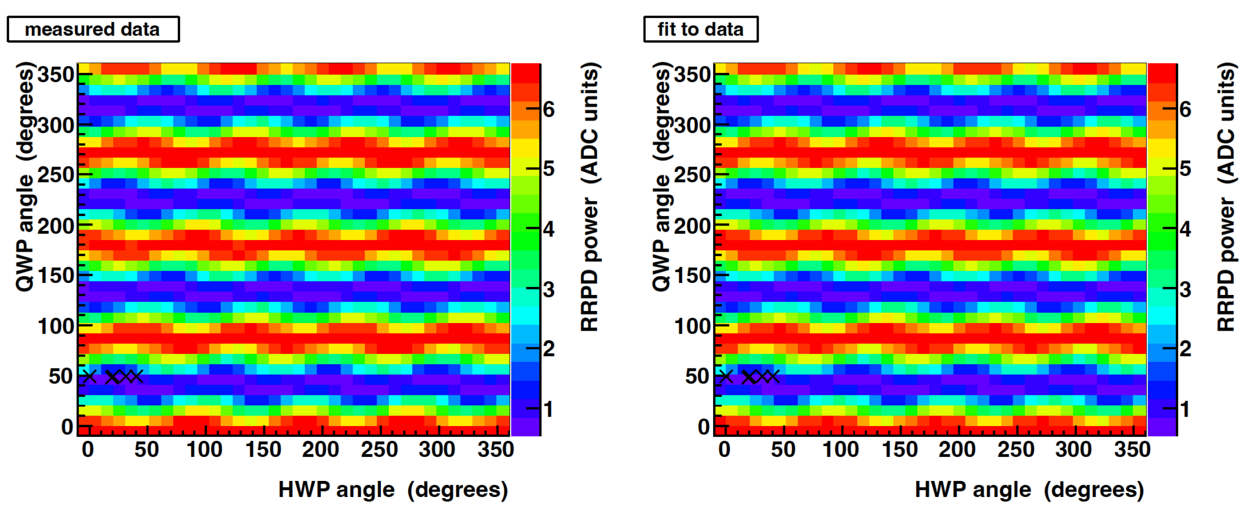

FIG. 77: RRPD signal as a function of HWP and QWP rotation angle. Left: Measured signal, Right: fit to the model of Eq. 103.

Laser Exit Scan

Previous experiments had inferred the polarization in the cavity by measuring the polarization in the exit line and using a "transfer function"[1].

The exit scan the polarization measurement was performed with cavity under vacuum with an ellipsometer; a system composed of a quarter-wave plate, holographic beam sampler (HBS), a Wollaston prism and two photodiodes (S1 and S2) as shown in Fig. 78. This system is also used for online monitoring of cavity exit polarization.

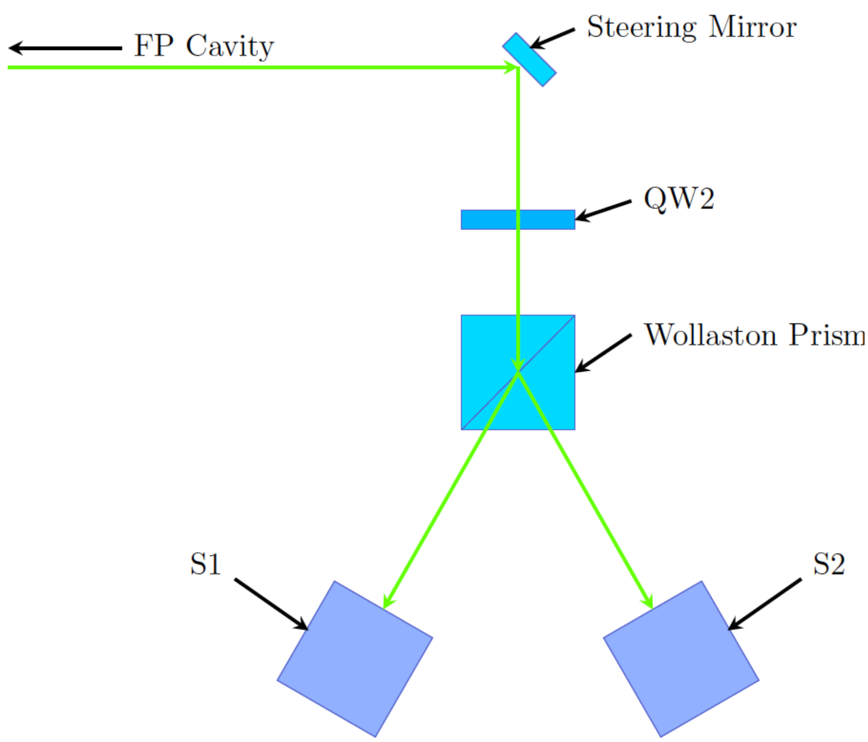

FIG. 78: A schematic of cavity exit line. [36].

When polarized light passes through the Wollaston prism it separates light into two separate linearly polarized outgoing beams with orthogonal polarization. If we denote the powers read by S_1 and S_2 as $\hat{S}_1$[2] and $\hat{S}_2$, these can written as [36],

[1]The transfer function describes the evolution of the laser polarization after the second cavity mirror as it is transported via steering mirrors and vacuum window.

[2]The polarization state ($\hat{S}$) of incident beam is characterized by a Mueller matrix composed of four Stokes parameters by $\hat{S}$ = (P0, P1, P2, P3).

$$\hat{S}_1 = \frac{1}{2}(P_0 - P_1 \cos^2 2\theta + P_2 \cos 2\theta \sin 2\theta - P_3 \sin 2\theta) \begin{pmatrix} 1 \\ 1 \\ 0 \\ 0 \end{pmatrix}, \tag{104}$$

$$\hat{S}_2 = \frac{1}{2}(P_0 + P_1 \cos^2 2\theta - P_2 \cos 2\theta \sin 2\theta + P_3 \sin 2\theta) \begin{pmatrix} 1 \\ -1 \\ 0 \\ 0 \end{pmatrix}, \tag{105}$$

where θ is the angle of rotation in the rotation matrix of the quarter wave plate. I_1 and I_2 are the intensities received by the spheres S_1 and S_2.

For an angle $\theta = \frac{\pi}{4}$, DOCP can be written as,

$$\text{DOCP} = \frac{I_1 - I_2}{I_1 + I_2} = \frac{P_3}{P_0}. \tag{106}$$

This requires a very precise alignment of the slow axis of the QWP to the horizontal axis of the Wollaston prism. It was experimentally determined with a Glan polarizer.
When the system is precisely aligned, so that $\theta = 45^\circ$, this can provide online monitoring of polarization of the cavity. This measurement helps to characterize the time-dependence of the laser cavity DOCP. Figure 79 shows total power measured by two photodiodes S_1 and S_2 versus the quarter-wave plate scan angle. The Stokes parameters P1, P2, and P3 can be extracted using this.

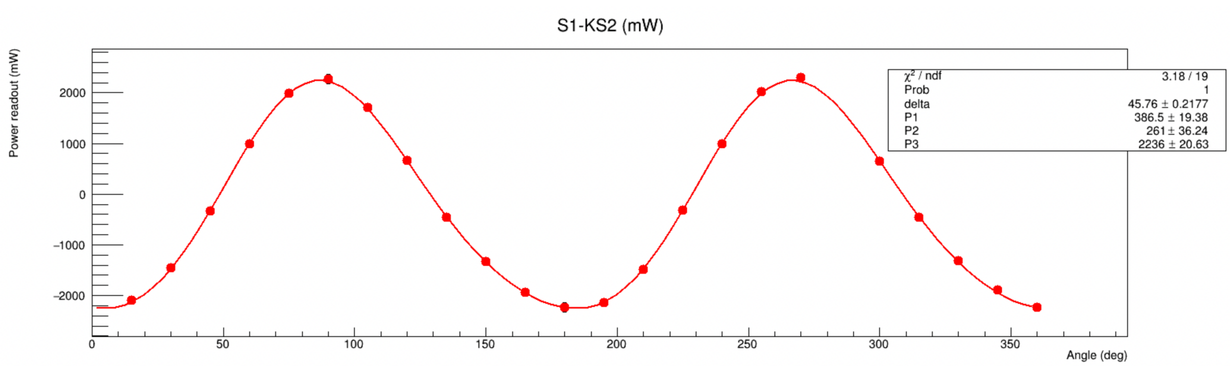

FIG. 79: Extraction of Stokes parameters from a QWP scan at the cavity exit.

This method of inferring the polarization in the cavity did not take into account effects due to birefringence of the cavity mirrors. To understand that and to characterize the DOCP in the CIP, another exit line scan was performed with cavity open to air. Using this scan, we tried to measure the cavity birefringnce. A known input polarization state is prepared before the cavity and then the polarization was measured after the second cavity mirror. To measure the polarization states after the cavity, we had a polarization station with a Glan polarizer, QWP and a photodiode. Space limitations after the second cavity mirror prevented this measurement station to be placed in line, therefore to do this measurement we had to use additional components. For Fabry-Perot cavity to lock the light should go to the PDT detector in the exit line(see Fig. 72), therefore to do this measurement we used a Non Polarizing Beam Splitter (NPBS). The NPBS could reflect 50% of incident light and transmit the other 50%. A schematic of the exit line elements is shown in Fig. 80.

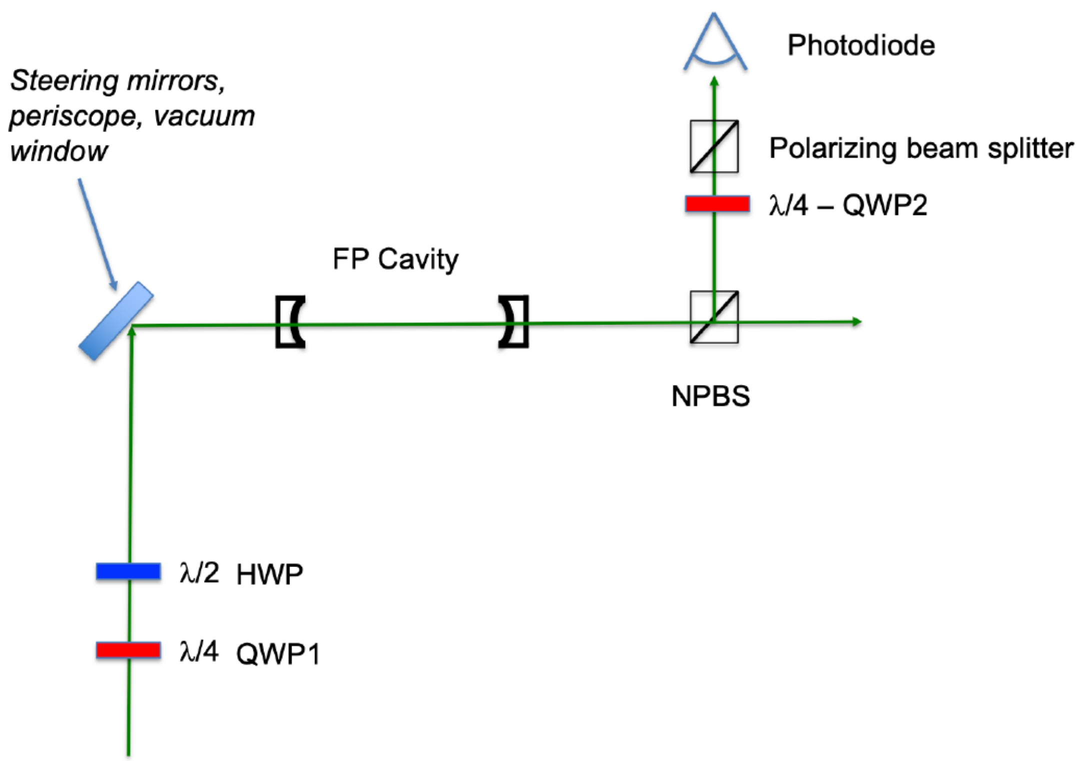

FIG. 80: Schematic of the exit line elements to measure the cavity birefringence.

Unfortunately, NPBS has a non negligible effect on the polarization, that must be characterized first. The NPBS was placed in the Compton setup as shown in Fig. 81 Using the quarter wave plate and half wave plate, known input states were created before the NPBS and reflected beam was measured. The Stokes parameters of the reflected beam were

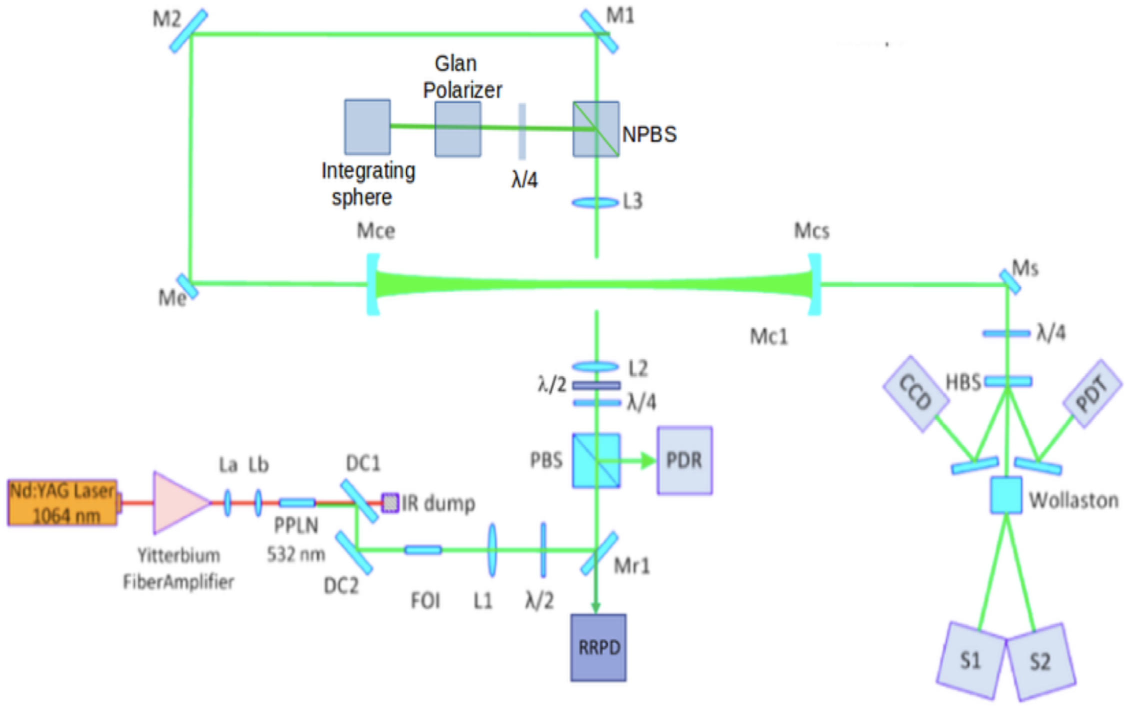

FIG. 81: A schematic of NPBS characterizing setup.

measured using the rotating quarter wave plate + fixed polarizer technique [57].

The polarization on the exit line is measured by rotating the QWP and measuring the photodiode response. The fit of the photodiode response vs QWP angle gives the Stokes parameters s0, s1, s2, and s3. Then the Stoke parameters calculated from this measurement were fit to model of a general birefringent element using knowledge of the initial laser polarization state. A three parameter Jones Matrix was used to model the NPBS,

$$M_{\mathrm{NPBS}} = R(\eta)P(\delta)R(\theta). \tag{107}$$

Here, R are rotation matrices and P represents the matrix for a plate that induces a phase shift δ.

The Fig. 82 shows the plot of the fit. Blue and orange points are the Stokes parameters from the data and Y-axis is the measurement number[3] The blue dashed curve is the result of the fit, while the orange dashed-dot curve shows the initial polarization state before the NPBS.

Mathematically, the system can be described using Jones matrix formalism,

[3]measurement number corresponds to the angles (QWP, HWP) (45, 20), (50, 20), (40, 20), (90, 92), (90, 47), (90, 69.5), (90, 24.5), (90, 48), (90, 93), (135, 20) respectively

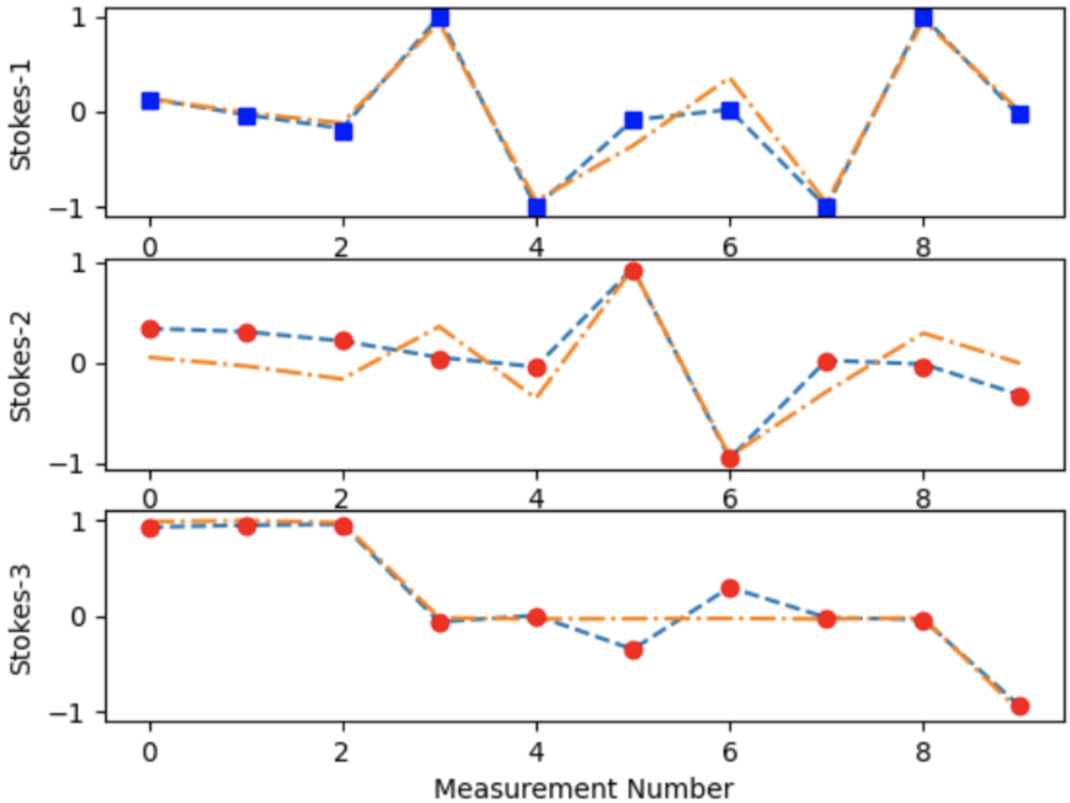

FIG. 82: A plot of Stokes parameters from the data vs measurement number (different incident polarization conditions) used to measure the NPBS birefringence. The blue dashed curve is the result of the fit, and the orange dashed-dot curve shows the initial polarization state before the NPBS.

$$\mathrm{P}_{\mathrm{final}} = \mathrm{M}_{\mathrm{cav}}\mathrm{M}_{\mathrm{NPBS}}\mathrm{P}_{\mathrm{initial}}, \tag{108}$$

$\mathrm{M}_{\mathrm{cav}}$ encodes total effect of birefringence due to cavity system and this can written in terms of two rotation matrices and a single phase retarder,

$$\mathrm{M}_{\mathrm{cav}} = R(\eta)PH(\delta)R(\theta), \tag{109}$$

where, $R(\eta)$ and $R(\theta)$ rotator matrices, and $PH(\delta)$ is the phase retarder.

Using the setup shown in Fig. 78 we can find the birefringence of the cavity. Several input polarization states were created before the cavity and using the same, rotating quarter wave plate + fixed polarizer technique we can get the birefringence of the cavity. To calculate the Jones vectors and Stokes parameters at the cavity entrance for each QWP and HWP

angle, we can use cavity open to air entrance function (M_E). Then, model the evolution of the laser polarization in the cavity using a generic birefringent element.
Then, compare to the "measured" Stokes parameters after the cavity to determine the three parameters of the matrix above. Similar to Fig. 82, the Fig. 83 shows the measured polarization after the cavity with points, and fit result with curves.

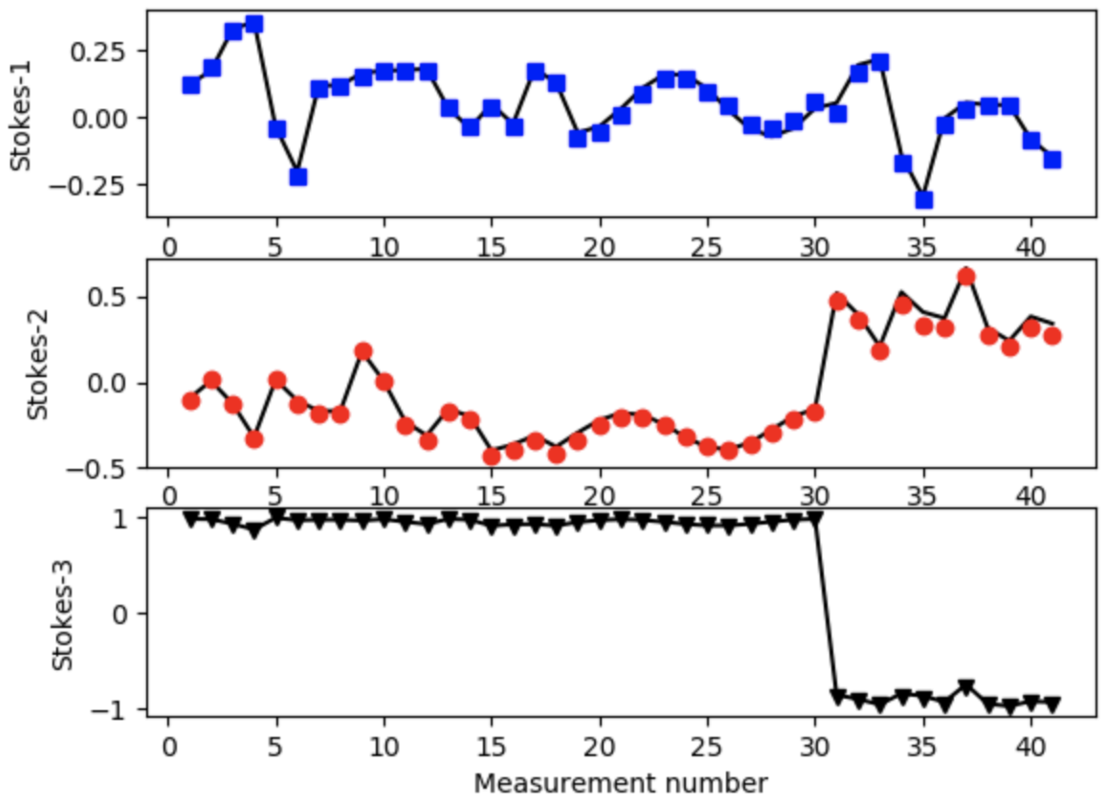

FIG. 83: A plot of Stokes parameters from the data vs measurement number used to measure the birefringence of the cavity. Points represent the measured polarization after the cavity, and the curves represent fit result.

The final step in this whole procedure is to determine the cavity polarization for the system under vacuum. This will require the entrance function for cavity under vacuum.

With cavity birefringence and entrance function, we can predict DOCP inside the cavity and determine the optimum settings circular polarization. With cavity birefringence and the entrance function we can construct an optical model of the DOCP for arbitrary QWP and HWP angles. The Fig. 84 shows DOCP inside the cavity as a function of QWP and HWP angles, for PREX-II and CREX. From the model we can get the optimum settings for circular polarization inside the cavity.

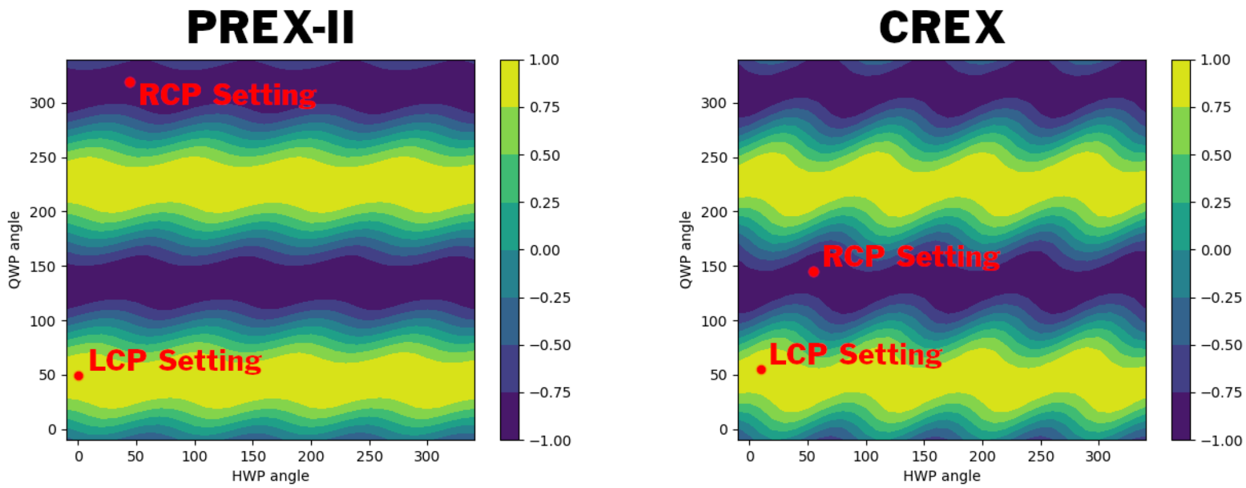

FIG. 84: DOCP inside the cavity as a function of QWP and HWP angles for PREX-II (Left) and CREX (right). The chosen values for left circular polarization (LCP) and right circular polarization (RCP) are labeled.

.

To test the model of the DOCP, Compton was run with less than 100% DOCP QWP and HWP positions for brief periods. Here, if the laser DOCP on the table is tuned too far away from either right or left circular setting, it can send too much back reflected light into the fiber amplifier, which can possibly damage it. Therefore we had to change the QWP and HWP by small angles. Here, the measured asymmetry and the predicted asymmetry from the model could be compared, and this could be used as a cross check of the laser polarization model.

The QWP and HWP configurations used for PREX-2 and CREX are listed in the Table. 4[4]. 15.5% of PREX-II Compton statistics are taken with low DOCP, and 4.3% of the CREX run is taken with low DOCP.

4.6 COMPTON DATA ACQUISITION

As discussed in sections 4.3 and 4.4, Compton photon scattering asymmetry can be measured either by counting the number of scattered photons detected for each helicity state, or by integrating the scattered photon signal for each helicity state. The Hall A Compton

[4] As discussed in Section 5.6.2 for CREX averaged over the two solutions are shown.

Experiment	QWP angle	HWP angle	Predicted laser DOCP
PREX-II	49.2°	0.2°	0.9999
	49.2°	15.2°	0.9980
	49.2°	31.2°	0.9595
	47.7°	19.1°	0.9887
CREX	39.3°	63.5°	0.9974
	39.3°	73°	0.9945
	39.3°	56°	0.9901
	50.5°	27.4°	0.9974
	43.5°	63.5°	0.9933
	37°	63.5°	0.9918

TABLE 4: Different QWP/HWP settings used during PREX-2 and CREX to cross check the laser DOCP model.

polarimeter photon detector DAQ can simultaneously perform two different types of asymmetry measurements, an integrating mode measurement and a counting mode measurement. Both integrating and counting modes were used during PREX-2 and CREX. To get the polarization, only the integrating mode asymmetry was used. However for some systematic uncertainty studies and for applying cuts to the data counting mode measurements were used.

The Compton DAQ works under the CEBAF Online Data Acquisition (CODA) framework. The DAQ has two Nuclear Instrumentation Module (NIM) crates and a VMEbus (Versa Module Europa) crate. The Compton DAQ module which performs the integration is a 200 MHz Struck SIS3320 8-channel 12-bit flash ADC (fADC). The timing signals are generated using a HAPTB (HAPPEx Timing Board). This module takes the helicity timing signal (MPS signal) , and sends the start and stop integration signals to the fADC. The timing structure for the Compton integrating DAQ is shown in Fig. 85.

The PMT signal is passed through a LeCroy 612A 12 channel PMT amplifier which amplifies the PMT signal by a factor of 10 and then sends to the fADC, where it counts sample, at a 200 MHz frequency between the “start” and “stop” control signals, which correspond to period of stable beam polarization t_{stable}. During readout period, fADC sums up the samples taken during the previous helicity window and the sum is pushed to the accumulator (Acc0) in “summed raw ADC units (sRAU)”. Using these sums we can extract

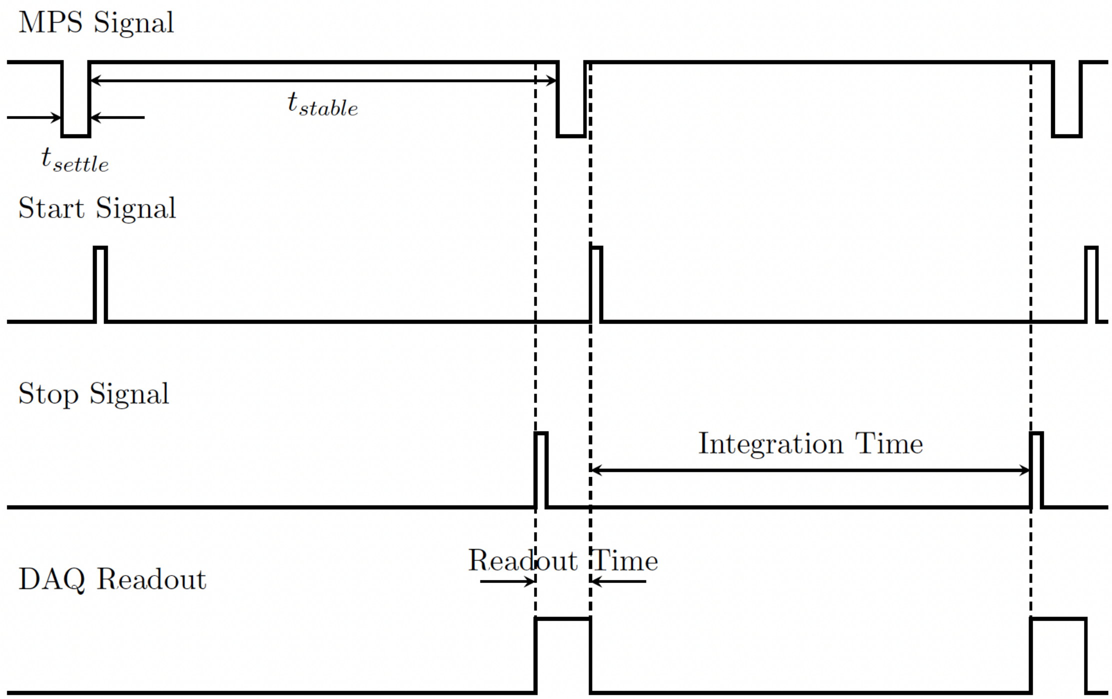

FIG. 85: Hall A Compton polarimeter integrating mode timing structure [36].

a Compton asymmetry. A DAQ map of the photon detector signal is shown in Fig. 86.

Necessary diagnostic signals, such as readback from the Hall A BCM, BPMs in the Compton beamline and the laser power photodiode output are converted to frequency signals in a VtoF converter, and read out in every helicity window.

4.6.1 AUXILIARY DETECTORS

There are several other detectors in the Compton setup that are used for beamline monitoring, detector positioning and for Compton analysis.

These include the two perpendicular finger scintillators used to center the photon detector with respect to the electron beam.

In addition to that there are four beamline scintillating detectors placed on the laser table, two upstream of the cavity and two downstream. We used rates of these background detectors to diagnose if the electron beam is centred in the chicane. If the electron beam is not centred in the chicane it can produce radiation by hitting the chicane and damage the laser electronics. The two upstream background detectors are placed approximately 80 cm upstream from the Compton interaction point, placed just to the left and right of the beam pipe. The two downstream detectors are placed approximately 80 cm downstream from the

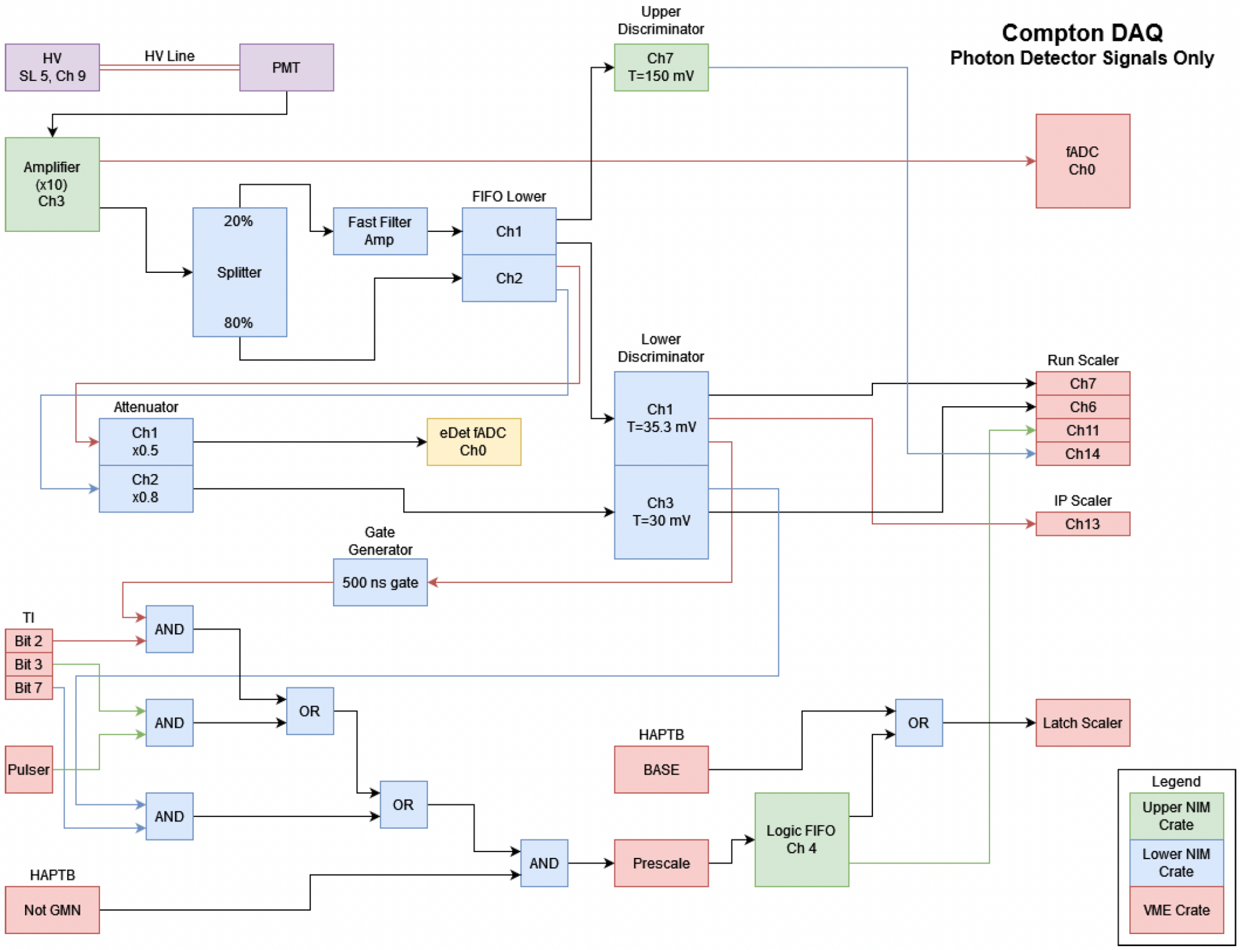

FIG. 86: A DAQ map of the photon detector signal [36].

Compton interaction point, placed just above and below of the beam pipe.

4.7 LED PULSER SETUP

To characterize photon detector non linearity, a LED pulser system was built using automatically controllable LEDs placed at the front of the photon detector. Linearity measurement is achieved by flashing two LEDs, one of constant low brightness ("delta" LED), and another LED with decrease in brightness ("variable" LED).

The LED pulser runs with a timing sequence of, both LEDs flash, "variable" LED flashes, "delta" LED flashes and both LEDs off, and PMT signal is read out by an ADC at each step of the sequence. A finite difference measurement is then made by taking the difference between the "variable" +"delta" flash and the "variable" only flash (Y(x+δ) - Y(x)), and plot it vs the "variable" alone flash yield (Y(x)). If the system is non linear this plot will have a non zero slope, and to characterize the non linearity this is fitted with a polynomial.

To do a precise a non linearity measurement we need to think about source of systematic errors incorporate with this measurement.

The first systematic is the electrical cross talk between the two LED signals. To measure this a third LED ("dark delta" LED) is placed outside the photon detector housing. This "dark delta" LED mimics electrical effects of the regular "delta" LED without giving any light to the photon detector. Doing the same finite difference measurement with this "dark delta" LED instead of the regular "delta"" LED we can get a measurement of cross talk.

When doing the linearity measurement, the "variable" LED brightness ranges from a level twice as large as a Compton event to zero within a pulser cycle. When the "variable" LED changes from its dimmest setting to its brightest setting, it is seen that the PMT gain changes for the first few pulser settings of the next cycle due to thermal effects. To minimize this effect, another LED ("load" LED) is added to run at a constant low brightness to keep the PMT under a low brightness load all the time.

4.8 MONTE CARLO SIMULATION

The energy weighted analyzing power, $\langle A_l \rangle$ as discussed in Section 4.4 is calculated by simulating Compton photons interacting with the GSO crystal using a GEANT4 based Monte Carlo simulation. Using the simulation we can understand how the different factor such as the photon collimator, the finite detector size, and the GSO crystal response affect the experimental analyzing power calculation.

The basic principle of the Monte Carlo was randomly selecting the starting kinematics of a Compton scattered photon and "shoot" it towards the detector. Geant4 uses different random number distributions to simulate the trajectory and subsequent interactions. We repeat the process a total of N times, where N is chosen to be sufficiently large to reduce the statistical error on the simulation. The simulated photons are allowed to interact with beamline components in the Compton setup. Figure 87 shows beamline components in the Compton simulation. In the simultaion, only the photons were simulated and the corresponding scattered electron was not used in this simulation

In the simulation, each event starts by first selecting a value of ρ sampled from a distribution of the differential cross section of Eq. 72. This ρ is then converted to an absolute photon energy using other kinematic variables such as a, defined in Eq. 71, and scattering angle θ_γ. The azimuthal scattering angle ϕ is sampled from a uniform distribution from 0

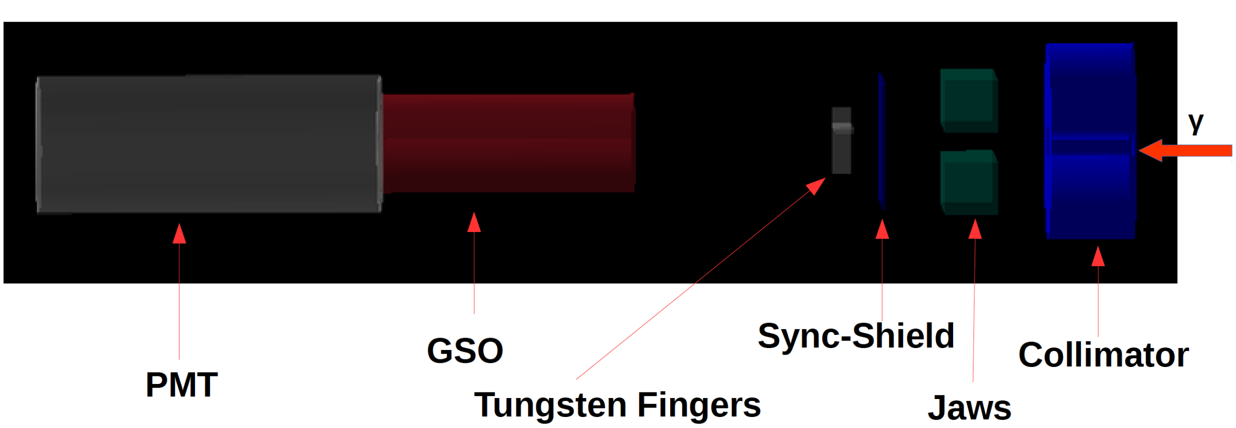

FIG. 87: A Simple schematic of the Compton beamline components in the simulation

to 2π rad. In the simulation the analyzing power is calculated numerically as,

$$\langle A_l \rangle = \frac{\Sigma_i Y(\rho_i)\epsilon(\rho_i)A_l(\rho_i)}{\Sigma_i Y(\rho_i)\epsilon(\rho_i)}. \tag{110}$$

The primary photon generated is sent through different volumes of the simulation. Components such as the 5m stainless steel beam pipe, stainless steel vacuum window, lead collimator, tungsten fingers and synchrotron shield are included in the simulation. Photons then interact with the GSO crystal itself. The Monte Carlo outputs the total energy deposited in the calorimeter for each scattered Compton photon, along with initial kinematics and theoretical scattering asymmetry for that particular event.

A signal-weighted analyzing power calculated using the Monte Carlo is,

$$\langle A_l \rangle = \frac{\Sigma_i E_i^W A_i^l}{\Sigma_i E_i^W}, \tag{111}$$

where E_i^W is the simulated energy deposited in the GSO for each Compton scattered photon and A_i^l is the associated longitudinal scattering asymmetry for that photon.

Figure 88 shows the energy deposited in the GSO crystal for the CREX beam energy, blue curve is experimental energy deposition and red curve is energy deposited with out considering any detector response (scattered photon energy). We saw there is huge discrepancy between these two in high energy region. To understand this behaviour we looked at energy deposited after each component to see any geometrical effect cutting the rate. We saw some photons are escaping the crystal without depositing and that is the cause for the discrepancy in the high energy end.

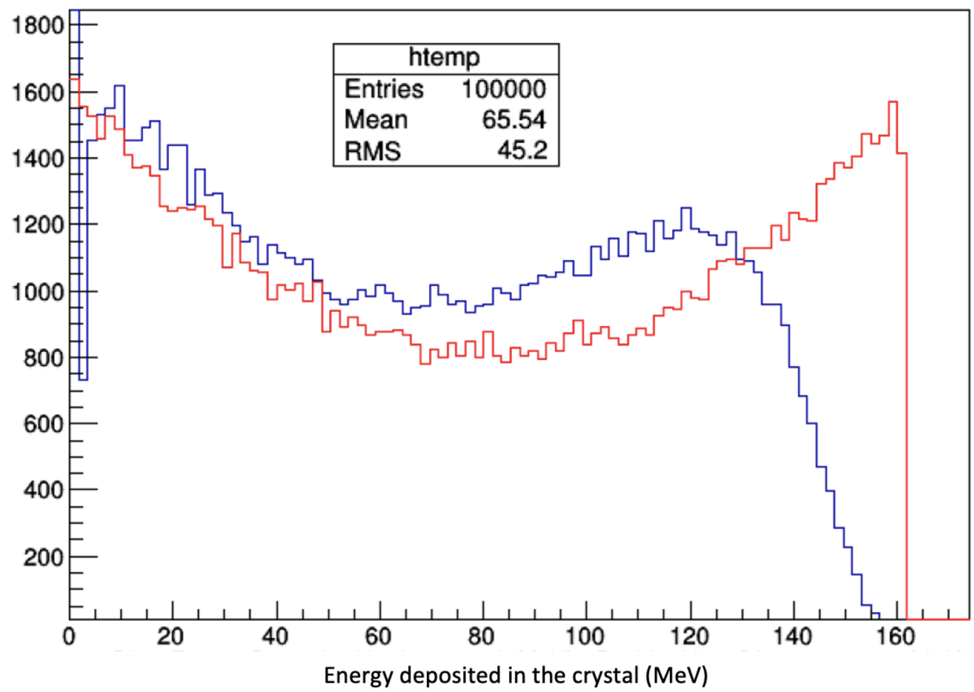

FIG. 88: A simulation of the energy deposited in the GSO crystal for CREX energy. Blue: simulated energy deposited in the crystal, Red: the scattered photon energy

CHAPTER 5

COMPTON POLARIMETRY DATA ANALYSIS

This chapter highlights the analysis of the data collected to extract the electron beam polarization from the accumulator data. This requires making cuts to the data, Monte Carlo simulation of the analyzing power and statistical and systematic error analysis.

During PREX-2, the Compton polarimeter only ran during the final half of the experiment, due to problems with the laser system. For CREX, the Compton polarimeter ran consistently for almost the entire experiment.

5.1 COMPTON ANALYZER

We have a separate analyzer for Compton data and it's called CompMon (Compton Monitor). The raw data collected by CODA system is translated into root tree format by CompMon. The output data file is formatted as a series of CODA "events" which contain ROC readout information for each MPS. The format of the CompMon output has several recorded data tables and all follow a data structure called "tree" in the ROOT software library [58].

"mpswise", records accumulator and scaler data per MPS. "multipletwise", records accumulators summed separately for positive and negative helicity states in each helicity pattern. "triggerwise", records the sums and pedestals for each accepted Compton pulse, maps them to their constituent MPS and multiplet. The Compton asymmetries were calculated from data in the multiplet tree.

5.2 MEASURING THE EXPERIMENTAL ASYMMETRY

When measuring Compton integrating mode asymmetry, it is important that we correct for the backgrounds produced by the beam (non Compton processes that is not electron-photon scattering from the laser). Running electron beam without laser will give a good measurement of the background, but this background signal potentially changes over a small time scale (minutes). Therefore, to get this correctly, Compton laser is cycled on-off-on with an appropriate interval. But turning off the laser is not possible, therefore, we lock and unlock the the laser to the cavity.

For PREX-2 and CREX we used 60s laser locked to the cavity and 30s laser unlocked. But this time interval is not precise, sometimes laser will unlock itself before the 60s and sometimes it will take more than 30s for laser to lock, also sometimes the electron beam can shut down during a laser cycle. Because the laser locked-unlocked periods are not the same every time, it is necessary to cleanly identify these laser cycles in the analysis.

The photon data analysis includes a method to identify good cycles from the data stored in the MPS and multiplet trees [36]. First, iterate over all multiplets in the run to track multiplet laser state. When encountered a multiplet with a different laser state than the one before it, record the MPS number of the change and store it as a laser period with the starting and ending MPSs and the laser state. If there is a laser period that has less than 3 seconds worth of multiplets with electron beam on above threshold, remove it from the list. Then iterate over all remaining laser periods. If the laser periods before and after a removed laser period are the same laser state, then merge them into a single period as this represents a brief failure in the laser locking. If a period of laser-on is sandwiched between two laser-off periods, that's one laser cycle. Next verify, the laser cycle has an off-on-off pattern, has at least three seconds worth of beam-on data, the first laser-off period and the laser-on period are separated by no more than ten second, the laser-on period and the second laser-off period are separated by no more than ten seconds. If all the above are true, mark the laser cycle with its first and last MPS number of all the laser periods and record it [36].

The laser cycle is the fundamental unit of the Compton asymmetry measurement, and this is a good timescale to accurately determine backgrounds and correct for it.

The main experiment uses an Insertable Half Wave Plate (IHWP) as a slow helicity reversal during the experiment, as discussed in Section 2.2.2. This reverses the incident laser polarization by 90 degrees before entering the Pockels cell. This is needed to cancel out helicity correlated systematics. IHWP was flipped every ~ 8 hours and this reversal changes the beam polarization, and therefore the sign of the measured Compton asymmetry, relative to the helicity correlated signal. A technology is adopted for this analysis, in which IHWP state time periods are called a "snail", and Compton data in each IHWP state is averaged over a snail and from that calculate snaillwise polarization. After correcting for the sign, these snail polarizations are averaged to produce an average polarization for the experiment[1].

5.2.1 ASYMMETRY MEASUREMENT

The CompMon analyzer divide the measured yields from the photon detector by helicity,

[1] "snail" is nod to the "slug" in parity analysis

laser and beam state. Asymmetry analysis is done with electron beam-on data only. Using the multiplet tree we can compute helicity correlated differences and sums for each laser state. In the analysis below S^+_{ON} and S^-_{ON} are laser-on data for two helicity states, S^+_{OFF} and S^-_{OFF} are laser-off data for two helicity states, $D_{ON(OFF)}$ helicity correlated difference for laser-on(off) and $Y_{ON(OFF)}$ is helicity correlated sum for laser-ON(OFF).

$$D_{ON} = S^+_{ON} - S^-_{ON}, \tag{112}$$

$$D_{OFF} = S^+_{OFF} - S^-_{OFF}, \tag{113}$$

$$Y_{ON} = S^+_{ON} + S^-_{ON}, \tag{114}$$

$$Y_{OFF} = S^+_{OFF} + S^-_{OFF}. \tag{115}$$

Here, the values S^+_{OFF} and S^-_{OFF} are averaged over both laser-off periods in a cycle ($\langle Y_{OFF}\rangle$) Then we can compute the helicity correlated asymmetry as,

$$A_{ON} = \frac{D_{ON}}{Y_{ON} - \langle Y_{OFF}\rangle}, \tag{116}$$

$$A_{OFF} = \frac{D_{OFF}}{Y_{ON} - \langle Y_{OFF}\rangle}. \tag{117}$$

Figure. 89 shows the distributions of the quantities in Eq. 114 through Eq. 117 during a laser cycle.

Since there are no Compton scatters with laser off, in theory, the laser-off asymmetry (A_{OFF}) should be zero. But beam properties like helicity correlated beam halo can produce non zero laser-off asymmetries. This false asymmetry should be corrected to get the actual experimental asymmetry. Then, we can write the experimental asymmetry and the statistical uncertainty as,

$$A_{exp} = \langle A_{ON}\rangle - \langle A_{OFF}\rangle, \tag{118}$$

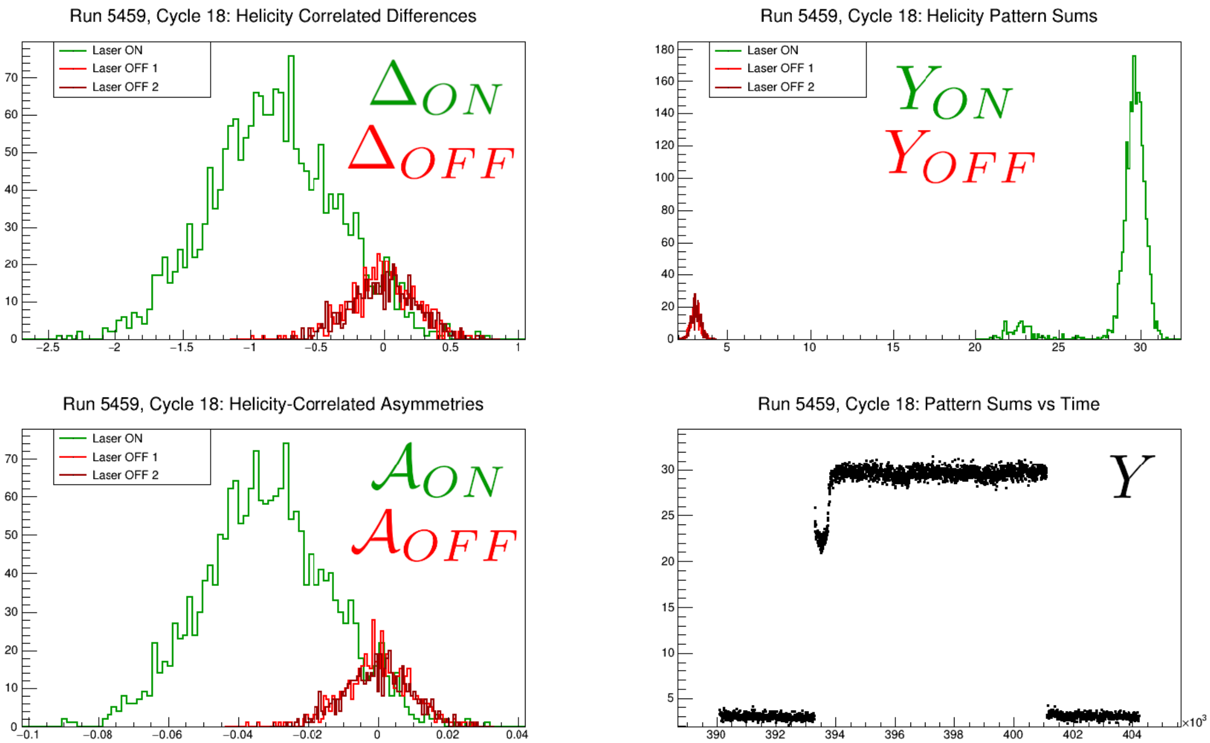

FIG. 89: Compton multiplet histograms for each quantity in Eq. 114 through Eq. 119. The top left is helicity correlated differences of photon detector signal, top left is the photon detector sums of each helicity sign, the bottom right is a histogram of computed asymmetries and the bottom left shows the timescale of the laser cycle, photon detector multiplet yield vs time.

$$\begin{aligned}\delta A_{exp} = \Bigg[\langle A_{ON}\rangle^2 \left(\frac{\delta D_{ON}}{\langle D_{ON}\rangle}\right)^2 + \langle A_{OFF}\rangle^2 \left(\frac{\delta D_{OFF}}{\langle D_{OFF}\rangle}\right)^2 + \\ [\langle A_{ON}\rangle^2 + \langle A_{OFF}\rangle^2] \frac{\delta Y_{ON}^2 + \delta Y_{OFF}^2}{[\langle Y_{ON}\rangle - \langle Y_{OFF}\rangle]^2} \Bigg]^{\frac{1}{2}},\end{aligned} \tag{119}$$

where δD_{ON}, δD_{OFF}, δY_{ON}, δY_{OFF} are the statistical uncertainties for each multiplet variable.

5.3 CALIBRATION OF BEAM MONITORS

In order to make quality cuts, we need to track different beam parameters such as beam current, beam position or laser power. The Compton DAQ track these signals through a series of V2F converters, where raw signals are converted into pulses with frequency proportional to the voltage of the original signal. Then these pulses are fed to an IP scaler module and signals are converted to counts. To get the actual beam positions, beam current or laser power, these counts should be calibrated to meaningful units. Each channel is calibrated against the same component data as reported in EPICS.

For beam current tracking, the polarimeter used Hall A BCM 4A. The Calibrated BCM value can be written as [36],

$$I_{beam} = \alpha_{BCM} f_{clock} \frac{n_{BCM}}{n_{clock}} - \beta_{BCM}, \tag{120}$$

where α_{BCM} is the pedestal value and β_{BCM} is the gain constant, $f_{clock} = 40$ MHz is the clock frequency, n_{BCM} is the number of BCM V2F pulses counted over the MPS and n_{clock} is the number of clock pulses counted in the MPS. α_{BCM} and β_{BCM} can be calculated from a current scan with several set points.

The laser power in the optical cavity is measured using the Compton laser transmitted photodiode (PDT)(see Fig. 72). The process for calibrating the laser cavity power vs. EPICS is the same as calibrating the BCM. In these calibrations only the pedestal matters for the asymmetry analysis ad the gain is approximated for operational purposes only.

To track the electron beam position and angle inside the cavity, and to keep the electron beam locked on to the laser at the CIP, we use two BPMs, BPM 2A and BPM 2B. The BPM coordinate position for each direction can be calculated for each BPM separately as (see Section 2.4.1),

$$x_{rot} = k \frac{(x_p - x_p^0) - \alpha_{BPM}(x_m - x_m^0)}{(x_p - x_p^0) + \alpha_{BPM}(x_m - x_m^0)}, \tag{121}$$

where x_p and x_m are the raw IP scaler counts for BPM wires x_p and x_m respectively, x_p^0 and x_m^0 are the pedestal values for the two wires respectively, α_{BPM} is the calibration constant, and k is the BPM sensitivity (a value known from the geometry of the BPMs).

Then these coordinates are rotated into lab coordinates as,

$$\begin{pmatrix} x \\ y \end{pmatrix} = \begin{pmatrix} \cos\theta & -\sin\theta \\ \sin\theta & \cos\theta \end{pmatrix} \begin{pmatrix} x_{rot} \\ y_{rot} \end{pmatrix} - \begin{pmatrix} \beta_x \\ \beta_y \end{pmatrix}, \tag{122}$$

where β_x and β_y are the zero position values for the x- and y-coordinate respectively, and $\theta = 45^\circ$. Then, the BPMs are calibrated vs the EPICS readback.

5.4 DATA QUALITY AND CUTS

5.4.1 PEDESTAL CORRECTION

In order to get a precise asymmetry measurement, pulse sums and Acc0 values should be properly calibrated. These are measured in raw ADC units, and measured relative to the fADC electronic pedestal. To correctly measure the Acc0 pedestal we look for electron beam off periods and average the fADC response during that period and then subtract that from each Acc0 value. Beam current corrections need the electron beam off pedestal because background also depends on the current.

During CREX we noticed some irregular pedestal shifts, as shown in Fig. 90. More investigations showed both experiments had this behaviour of fADC shifting the signal instantaneously by considerable amount. These shifts are not related to laser beam state or electron beam state changes, therefore it should be a change in the pedestal. During CREX experiment this problem was traced to a signal attenuator box connected between the 10x PMT amplifier and the fADC and box was removed, no shifts were observed after that in the fADC data. All of PREX-2 data and part off CREX data had this problem. To first order this affect $\langle Y_{OFF} \rangle$ and so directly the asymmetries with instability on the laser cycle timescale.

To solve the pedestal problem in the data, first, pedestal shifts should be identified. To do that, a threshold was defined, which cuts the cycle if the Acc0 RMS for any period in the cycle is too large.nSince Acc0 RMS depend on the beam quality, this cut threshold should be tuned for changing beam conditions.

5.4.2 CYCLE CUTS

In our data analysis we need to come up with a system to remove the cycles with poor data quality, high background data or fluctuating background data. A “CycleCut” function is introduced to the data to cut cycles in different criteria and cycles that have been cut are stored with an identifying flag. Here is a list of cycle cut criteria.

1. Background RMS cut

This is the cut that discussed in Section 5.4.1. We cut the cycles to correct for pedestal shifts [59]. A plot of PREX-2 laser-off Acc0 RMS is shown in Fig. 91. Here, we visually divide data into run ranges based on laser-off Acc0 RMS and put data into a histogram. Then for each run range, extract the central value of the most populated bin of the histogram (“mode”). Cut on any cycle whose Acc0 RMS for any laser period exceeds the mode of Acc0 RMS for that run range by at least 0.15 RAU.

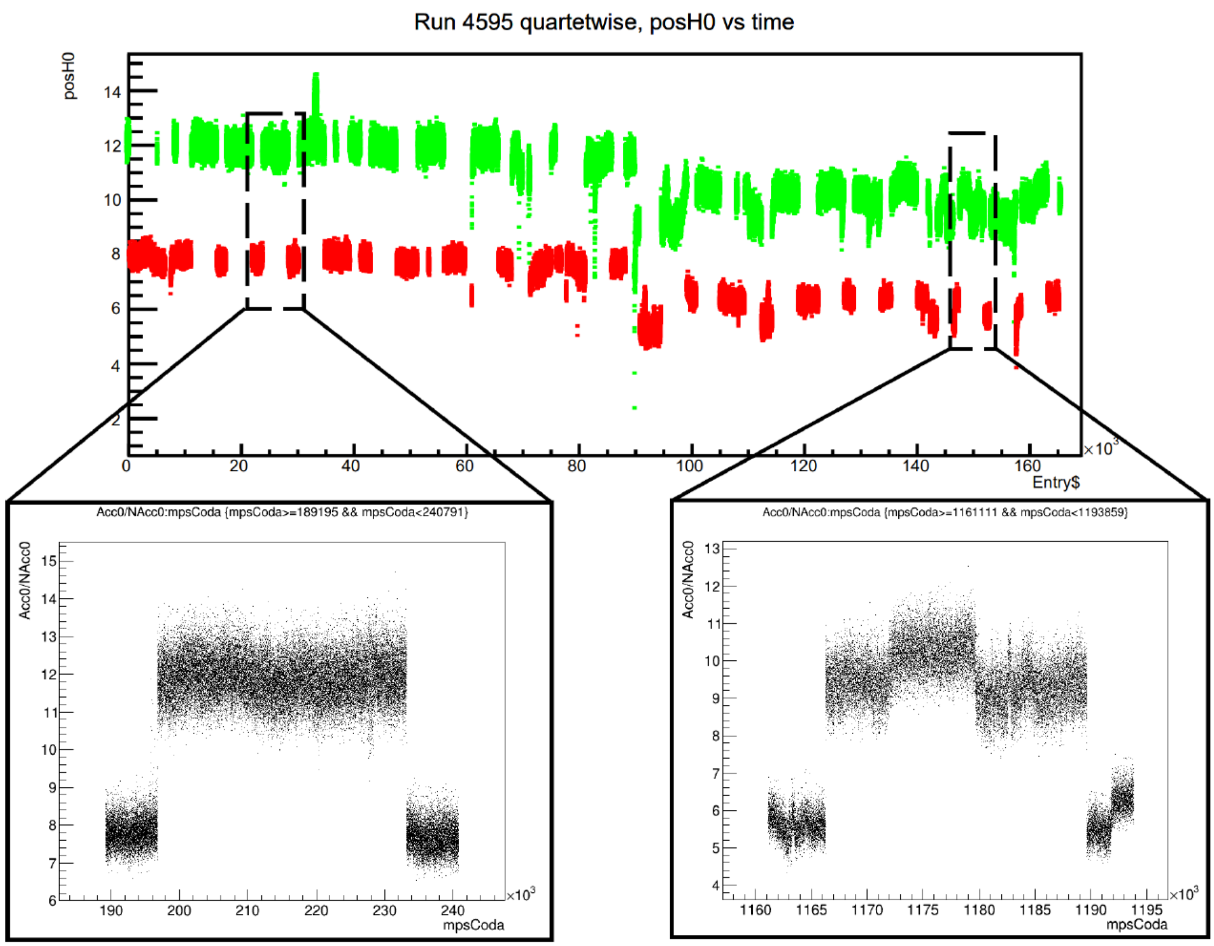

FIG. 90: Plot of a Compton run which had pedestal shifts. Left: signal is stable with no pedestal shifts, Right: multiple pedestal shifts.

2. Signal size cut

If the the photon detector signal and the backgrounds are comparable it can create poorly normalized data. Because asymmetry measurement use Acc0 laser-on periods minus Acc0 laser-off periods a small fractional shift on this can significantly skew results. To prevent this, all cycles with laser-on Acc0 less than 0.7 RAU greater than laser-off Acc0 are cut.

3. Double difference cut

To get the Compton asymmetry we use Eq. 120 and in that A_{OFF} is average of both laser off periods before and after the laser-on period in a cycle. To use average A_{OFF} for entire laser-on period, A_{OFF} must not vary. For this cut, the values of A_{OFF} for both periods in a cycle are subtracted to define a "double-difference" value, and then normalized to the

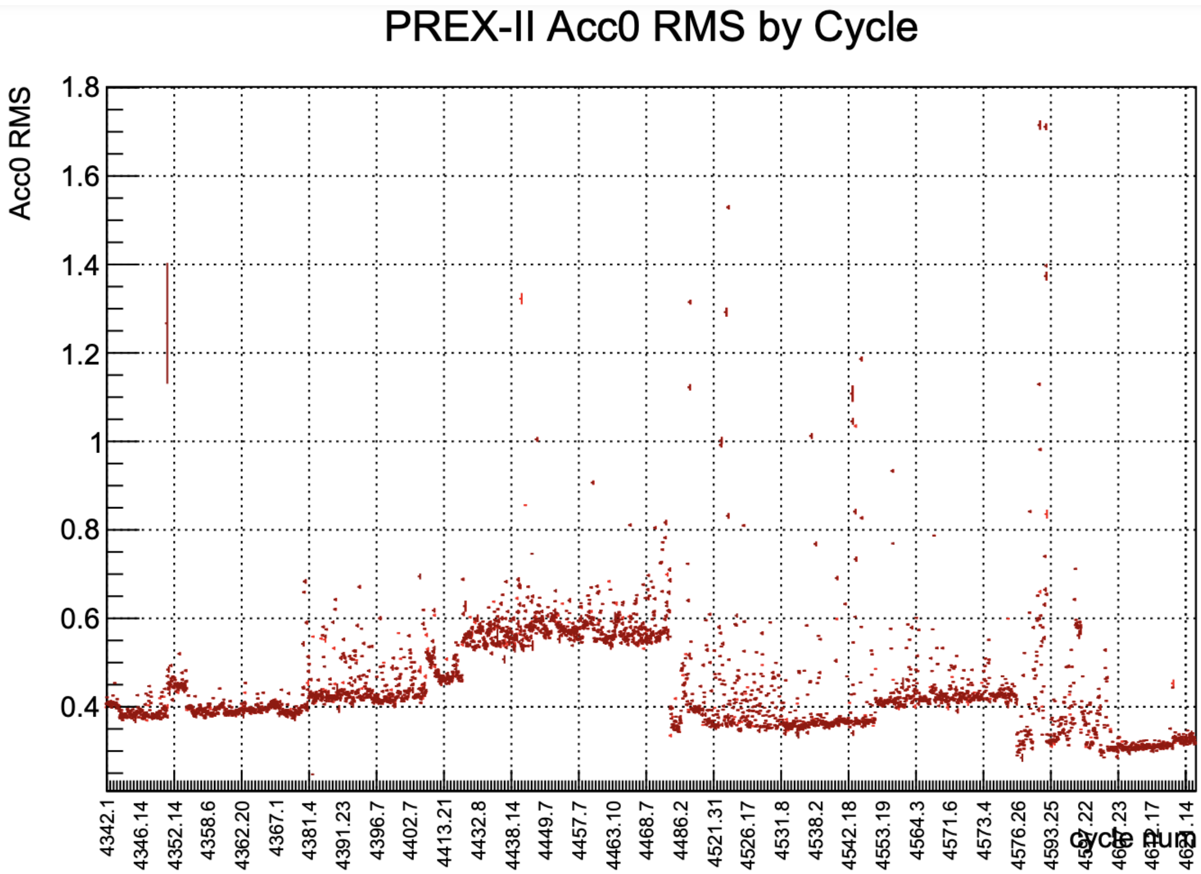

FIG. 91: A plot of laser-off Acc0 RMS by cycle for PREX-2.

propagated uncertainty of both asymmetry measurements as,

$$A_{DD} = \frac{A_{OFF}^{(1)} - A_{OFF}^{(2)}}{\sqrt{(\delta A_{OFF}^{(1)})^2 + (\delta A_{OFF}^{(2)})^2}}, \tag{123}$$

where, $A_{OFF}^{(1)}$ and $A_{OFF}^{(2)}$ is asymmetry for each laser-off period. A plot of A_{DD} for PREX-2 data is shown in Fig. 92. If the value of A_{DD} is greater than 3 for a cycle, then the cycle is cut.

4. Asymmetry uncertainty cut

For PREX-2, if the uncertainty of asymmetry for any cycle is greater than 5 parts per thousand and for CREX, 11 parts per thousand, the cycle is cut. Low statistical precision of the asymmetry uncertainty can be come from beam instability, beam misalignment with the laser target, or low cycle statistics, therefore we cut these cycles.

5. Background rate cut

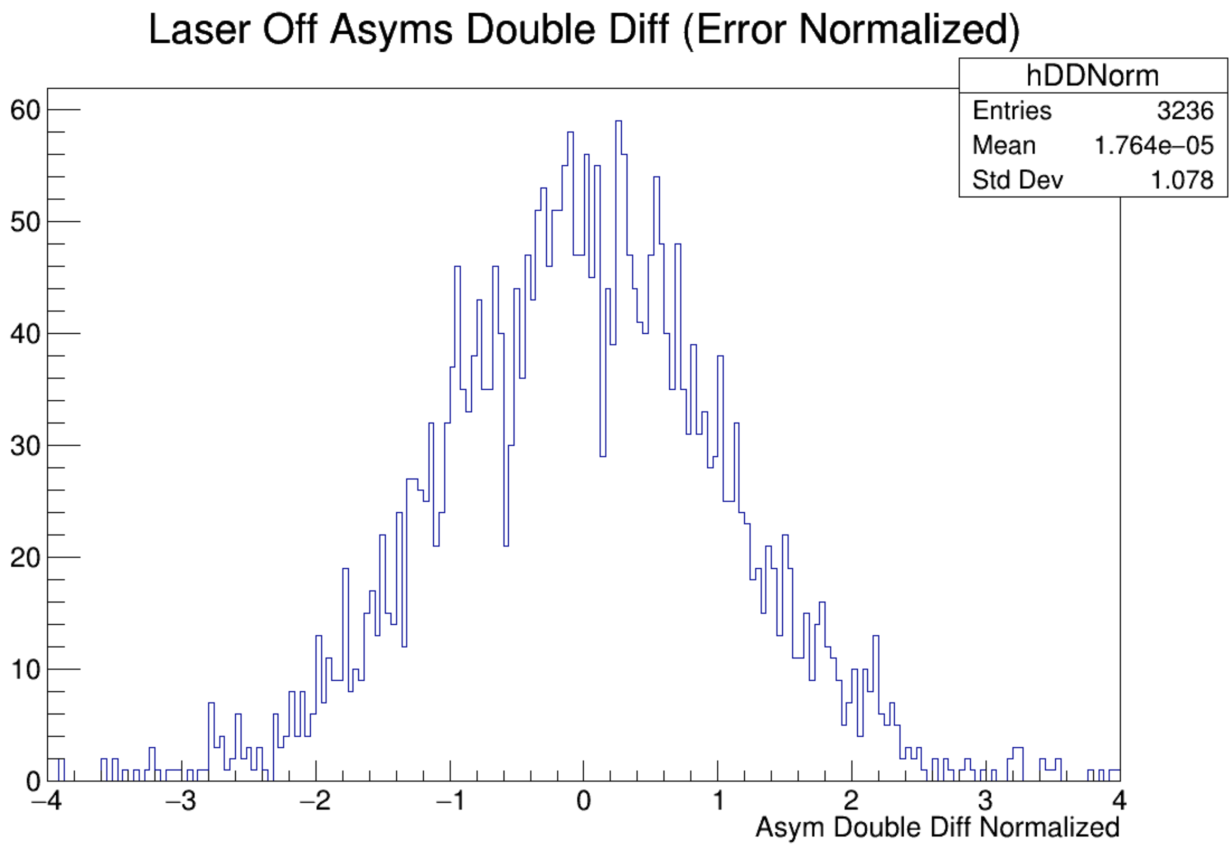

FIG. 92: A plot of asymmetry double difference for PREX-2.

There are four background detectors mounted on the laser table as described in Section 3.6.1. For PREX-2 a cycle is cut if the rate in upstream detector 1 (usbg1) is higher than 192 Hz, or if the rate in upstream detector 2 (usbg2) is greater than 672 Hz. This cut is not applied for CREX.

6. Charge asymmetry cut

To control helicity correlated beam asymmetries, PREX-2 and CREX use a continuous charge feedback system. Therefore, overall charge asymmetry for production running is well below what is required for the polarimetry analysis. But if there are brief periods of high charge asymmetry that could affect the polarimetry measurement. Therefore a cycle is cut if the average measured charge asymmetry in the photon DAQ for any period in a laser cycle is measurably nonzero, that is if $|A_{charge}|/\delta A_{charge} > 3$.

7. Background jitter cut

Here, a cut was made looking at the background jitter, that is the power difference between laser-off before and after in a cycle divided by the signal over background distribution.

$$\text{gitter} = \frac{Acc0^{(1)}_{OFF} - Acc0^{(2)}_{OFF}}{Acc0_{ON} - \frac{1}{2}(Acc0^{(1)}_{OFF} - Acc0^{(2)}_{OFF})}, \tag{124}$$

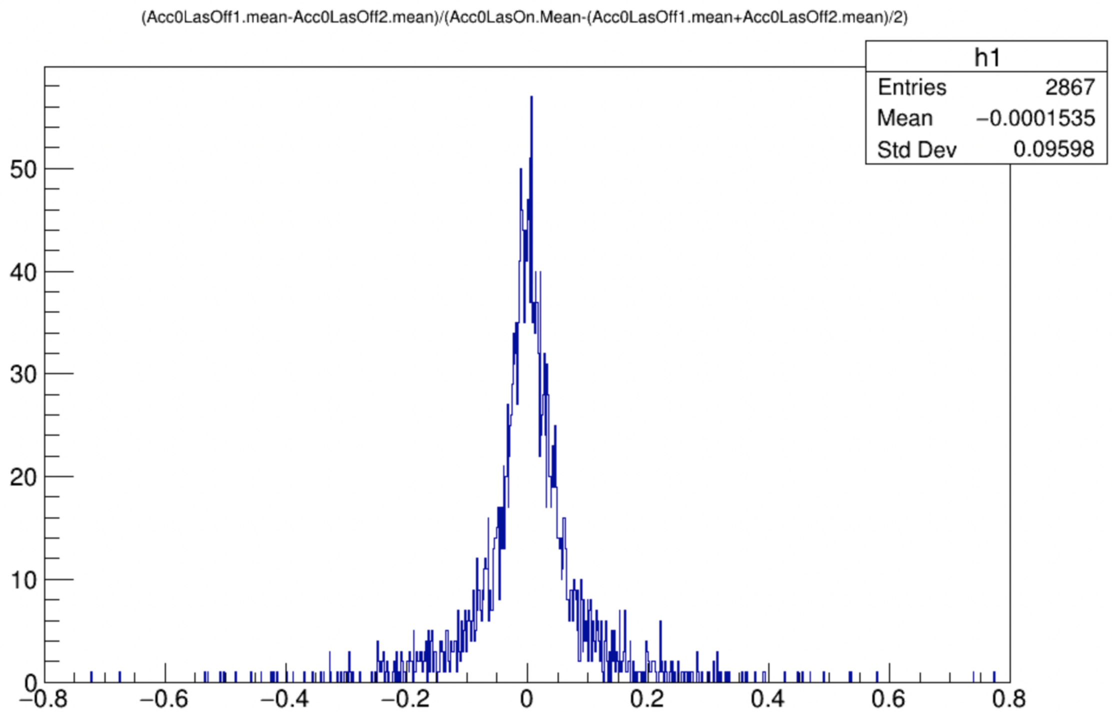

FIG. 93: A plot of background jitter for PREX-2.

If the jitter is greater than 20%, then the cycle is cut for PREX-2. For CREX cut threshold is 3%.

The results of cycle cut can be seen in Table. 5 for PREX-2 and CREX.

5.5 COMPTON ANALYZING POWER

The analyzing power calculation and Monte Carlo simulation is described in Section 4.8. Different GEANT4 simulations have been done to understand how different geometrical components are changing the experimental analyzing power (the different geometrical components are discussed in Section 4.5.1). In those simulations, beamline parameters such as collimator position in the GEANT4 Monte Carlo are varied over an experimentally possible range of values, and corresponding fractional change in the analyzing power is calculated.

Simulation studies showed closing the “jaws” collimator interrupted scattered photons and changed the effective analyzing power. For this reason the jaws were kept fully open

	PREX-2	**CREX**
Total cycles	**2867**	**15232**
RMS cut	236	354
Signal size cut	77	11
Double difference cut	65	78
Asymmetry uncertinity cut	11	34
Background rate cut	45	0
Charge asymmetry cut	31	257
Background gitter cut	84	0
Cycles left after cuts	**2318**	**14498**

TABLE 5: Number of laser cycles cut by each cut for PREX-2 and CREX. Cuts are applied in series.

throughout the PREX-2 and CREX. Results of another simulation study motivated the use of the thinnest synchrotron shield we had. Figure 94 shows how the analyzing power is changing with synchrotron shield thickness for PREX-2 experiment.

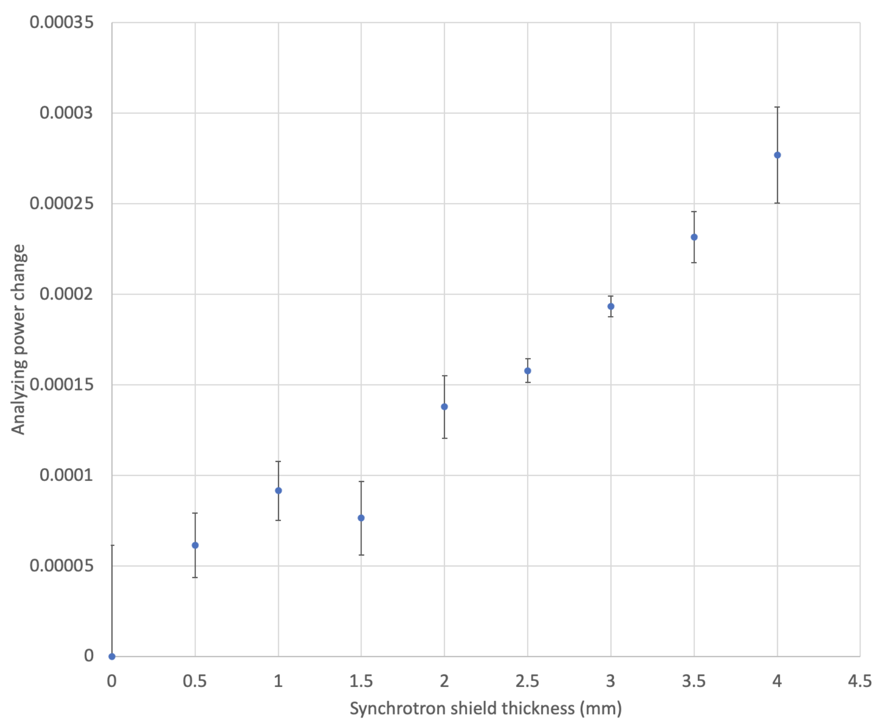

FIG. 94: The analyzing power change vs. the synchrotron shield thickness for PREX-2.

The most important scan is the Compton collimator axis change with respect to the photon beam. Here we saw a notable deviation of the analyzing power and since the collimator is fixed and unchangeable, we needed to quantify this collimator offset precisely. The scattered photon beam is in the shape of a cone with its vertex at the CIP. Intercepting that photon-cone offset affects the analyzing power by changing the distribution of Compton photon energy that reaches the photon detector. The effective offset of the collimator relative to the photon cone can change as the trajectory of the electron beam varies. Figure 95 and Fig. 96 shows the simulated analyzing power as a function of photon cone offset and the Compton spectrum with different energy ranges for PREX-2 and CREX. The collimator position affects the shape of the Compton energy spectrum, particularly at low energies, due to the specific kinematics of Compton scattering. In the Fig. 95 and Fig. 96 the effect of the offset can be seen at low energies, with increasing threshold for greater offsets.

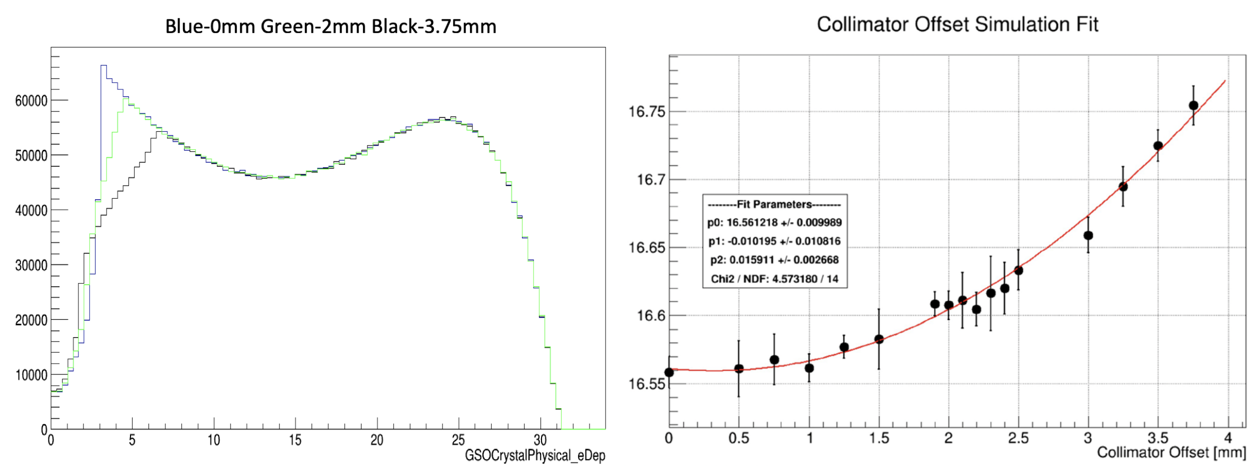

FIG. 95: Left: Simulated PREX-2 analyzing power as a function of photon cone offset. Right: Simulated PREX-2 spectra with offsets ranging between 0 mm and 3.75 mm.

5.6 SYSTEMATIC UNCERTAINTY

A systematic uncertainty is a correction to the measured asymmetry and its uncertainty due to limitations of the Compton setup and running conditions. Each systematic can arise from laser polarization, the experimental estimated analyzing power or the experimental asymmetry.

5.6.1 PHOTON CONE OFFSET

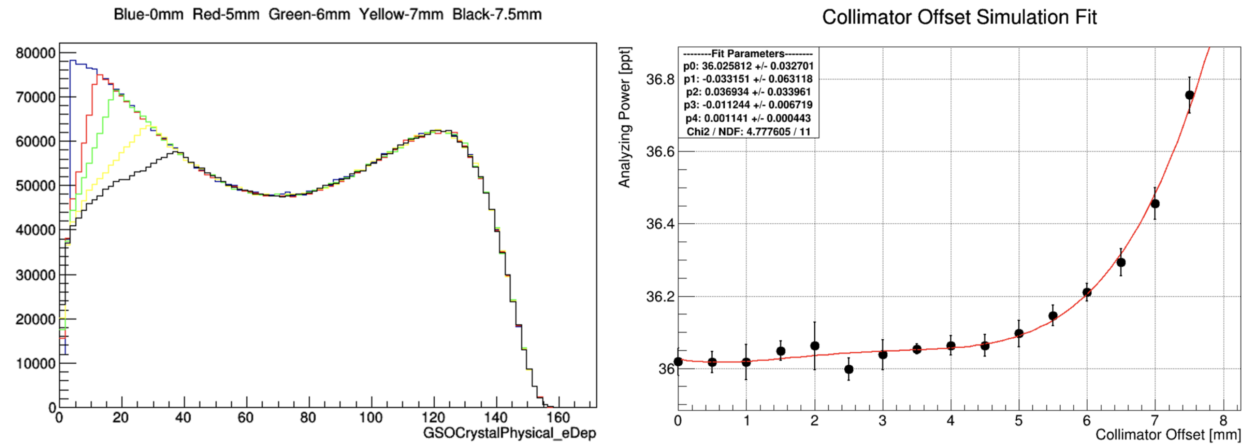

FIG. 96: Left: Simulated CREX analyzing power as a function of photon cone offset. Right: Simulated CREX spectra with offsets ranging between 0 mm and 7 mm.

As discussed in Section 5.5 the collimator position with respect to the photon beam effect the analyzing power and need to quantify that effect. The direction of the scattered photon propagation is mostly determined by the direction of the incoming electron beam, but the electron propagation inside the chicane is not fixed and this can change the center of the photon beam relative to the center of the collimator.

There are two BPMs in the Compton setup, BPM 2A and BPM 2B, when running the experiment, electron beam inside the Compton chicane is locked to these BPMs using a special lock, setup by the accelerator. Even though the electron beam is locked, sometime the positions drift due to different accelerator configurations. The calculation for the offset of the photon cone from the collimator axis in BPM coordinates is,

$$\Delta d = \sqrt{\left(6(X_{2B} - x_{2A}) + X_{2A}\right)^2 + \left(6(Y_{2A} - Y_{2B}) + Y_{2A}\right)^2}, \tag{125}$$

where X_{2A}, X_{2B}, Y_{2A}, and Y_{2B} are the x and y coordinates of BPM 2A and 2B, 6m is the distance between the CIP and the photon detector and distance between the two BPMs is 1m.

Since the electron beam position is drifting and changing the photon cone offset, the solution was to compare Compton spectrum for each run with the simulated Compton spectrum and determine which offset that run had and add a correction to analyzing power based on that. But the problem was getting the Compton spectrum for each run. The Compton photon detector captures neutron backgrounds coming from the target and the collimator,

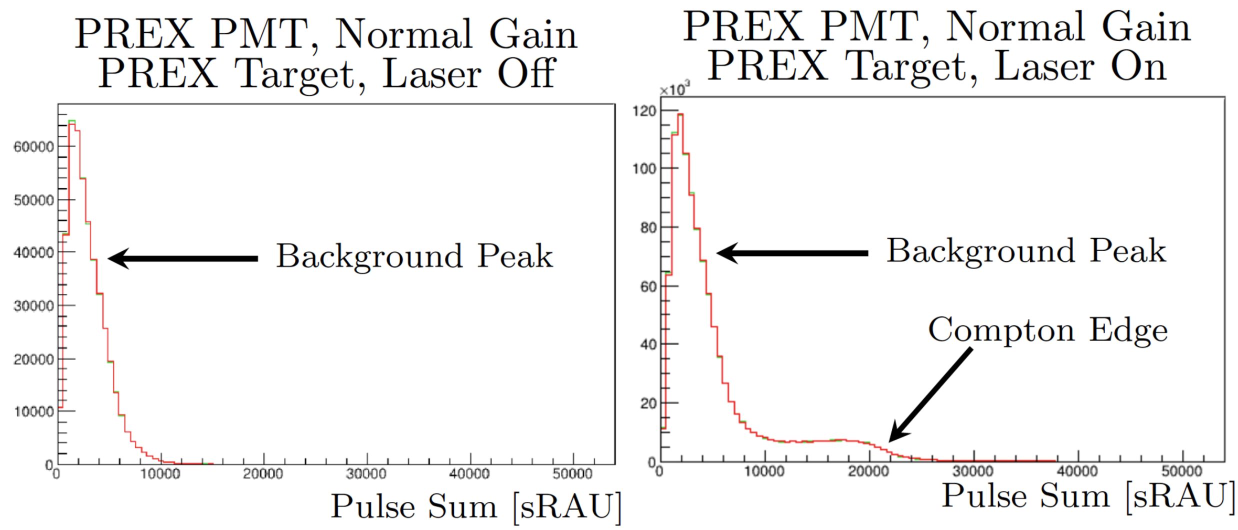

FIG. 97: PREX-2 Compton spectrum. Left: Compton spectrum with laser-off, Right: Compton spectrum with laser-on.

the neutron background spectrum dilutes any effect from photon cone offset during regular PREX-2 and CREX running. Figure 97 shows laser-off and laser-on Compton spectrum for PREX-2 running; the huge background peak is due to the neutrons scattering backwards from the target and collimator.

Getting an accurate background subtracted spectrum is hard here due to the large thermal neutron background. To resolve this issue, the Hall A Compton is run periodically for short periods with the target out where background subtraction is possible. Also, these spectrum runs are performed with the detector high voltage set to double the PMT gain of the regular experiment in order to increase detector resolution over threshold. Typically, a Compton spectrum run is about 15 minutes long and to minimize pile up issues these are run at low current level. Pileup effects occur due to multiple pulses occur during the window read out for a single trigger. Once a spectrum is obtained, the spectrum is fit by spectra from the Monte Carlo simulation with different photon cone offsets and the best fit is chosen as the one that had the lowest χ^2-test value. Figure 98 shows a background subtracted spectrum for one of the low current PREX-2 spectrum runs, with the the best fit from the simulation spectra.

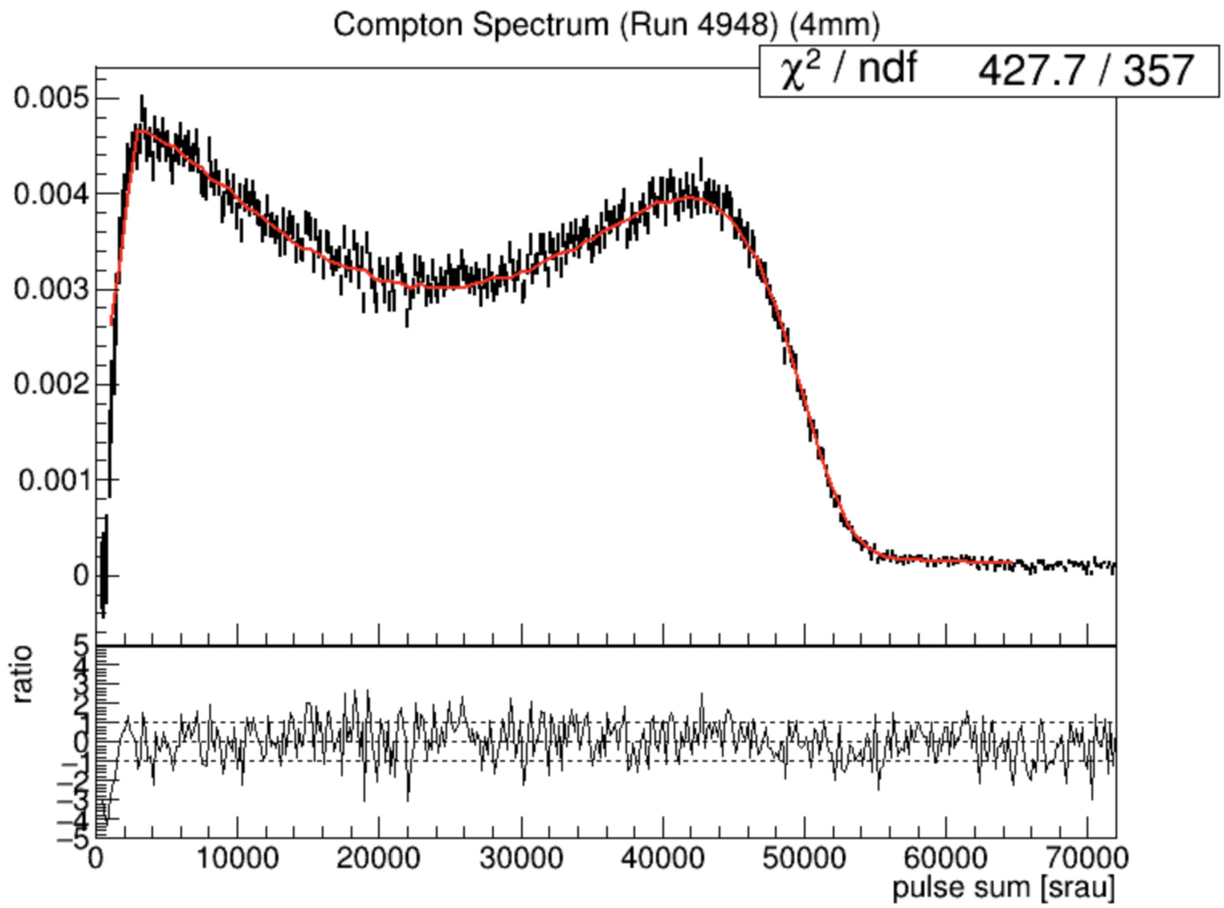

FIG. 98: PREX-2 background subtracted Compton spectrum.

PREX-2 collimator offset

During PREX-2 running, after every accelerator configuration change or after every BPM position change, a low current spectrum run was performed. Then these spectrum runs are compared with the simulated spectrum to determine the collimator offset. Next step is to find the overall relative offset between the BPM projection and the center of the collimator. The photon cone offsets and the projected positions of the photon beam should form a map of the collimator face, and the approximate collimator center should be where the offsets intersect. Then, a global average of the collimator offset circles are computed to find the average collimator center position. Figure 99 shows a circle plot of different spectrum runs with their offsets, here the centroid of each circle is the projected collimator position from the BPM data, the circle radii are the photon cone offset of each run matched to simulation and the color band in each circle is the estimated uncertainty of that offset. The color corresponds to an index identifying each individual calibration run.

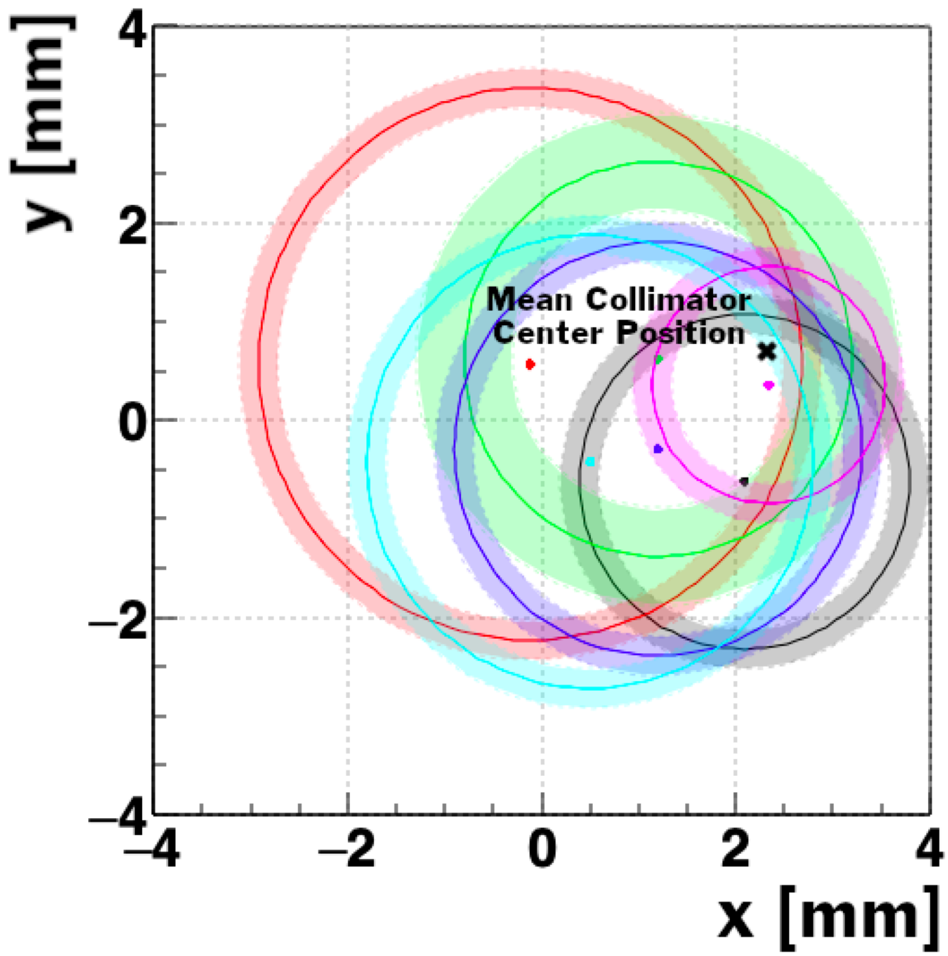

FIG. 99: A circle plot with PREX-2 spectrum runs. Centroid of each circle is the projected collimator position from the BPM data, the circle radii are the photon cone offset of each run matched to simulation and the color band in each circle is the estimated uncertainty of that offset.

The PREX-2 asymmetry data is then re-analyzed with the fitted collimator center position, from that the actual offset in BPM coordinates can be calculated. Then using the polynomial fit applied to the simulated analyzing powers vs. the collimator offset in Fig. 95, the analyzing power can be modify based on the offset for each run.

To estimate the uncertainty in the analyzing power measurement, first, the average analyzing power is calculated as a weighted average. Here, the weights are calculated from the Compton asymmetry uncertainty for each cycle.

$$w_i = \frac{1}{(\delta A_{exp})^2}. \tag{126}$$

Here w_i is the weight and δA_{exp} is the asymmetry uncertainty for cycle i. The weighted average is,

$$\langle A_l \rangle = \frac{\Sigma_1 w_i \langle A_l \rangle_i}{\Sigma_i w_i}, \tag{127}$$

where $\langle A_i \rangle$ is the analyzing power calculated from the offset for cycle i.

The analyzing power uncertainty is calculated from the analyzing power fit (Fig. 95). It is calculated as the difference between the analyzing power mean and the analyzing power calculated with one standard error added to that offset as,

$$\delta \langle A_l \rangle_i = (A_l)_i(\Delta c_i + \delta \Delta c_i) - (A_l)_i(\delta c_i). \tag{128}$$

Then, the overall analyzing power uncertainty from error propagation of the weighted average is,

$$\delta \langle A_l \rangle = \frac{\sqrt{\Sigma_i w_i^2 (\delta \langle A_l \rangle_i)^2}}{\Sigma_i w_i}. \tag{129}$$

After the collimator correction, the average analyzing power and uncertainty for PREX-2 is (16.649 $\pm$ 0.05) ppt, that is 0.3% relative uncertainty for the entire PREX-2 analyzing power measurement.

CREX collimator offset

The same procedure was carried out for CREX to understand the collimator offset systematic. For CREX there are more beam drifts and after every beam drift we don't have a low current spectrum run. Figure 100 shows the circle plot for CREX.

Here, there are some notable outlier runs which did not have the offset within 1 mm of the average collimator offset. Also, this suggested that some of the Compton data has about 7mm Collimator offset. At 7 mm photon cone offset analyzing power change is about 1.22% (see Fig. 96) and that would be immediately noticeable from the shape of the Compton spectrum and measured asymmetry, but we couldn't see evidence of high collimator offset in the spectrum or asymmetry data. This make us doubt about the accuracy of this method for CREX.

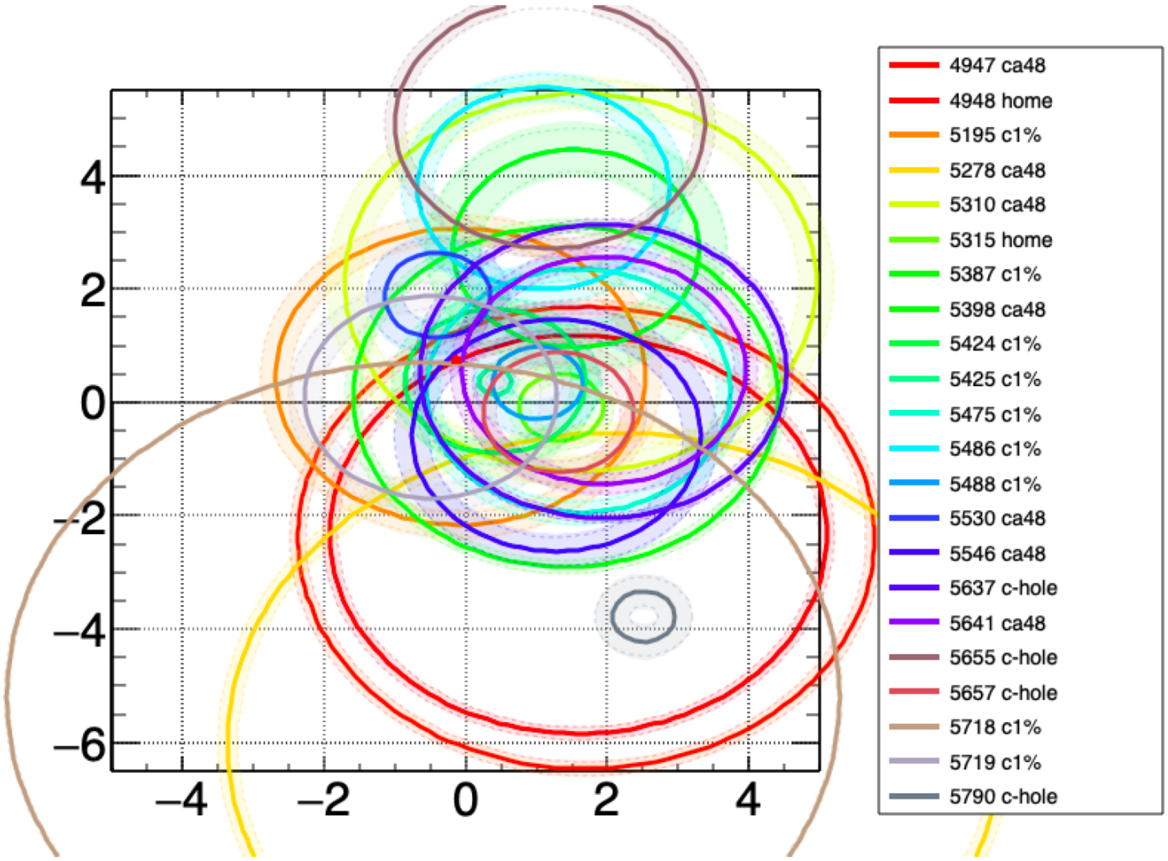

FIG. 100: A circle plot with CREX spectrum runs. Centroid of each circle is the projected collimator position from the BPM data, the circle radii are the photon cone offset of each run matched to simulation and the color band in each circle is the estimated uncertainty of that offset.

The first analysis of the CREX run without an analyzing power correction showed $\chi^2 = 1.3$ with individual snails having average χ^2 close to 1. If the larger χ^2 is coming from the noise from the analyzing power, it has a time dependence because the effect can be seen for the entire data set but not for short period of time.

A study was done to compare the average analyzing power correction with variations on the data set. This showed that if the average analyzing power correction was more than 0.2% , the statistical consistency of the data would have been significantly worse. Therefore 0.2% was taken as the uncertainty on the CREX analyzing power.

5.6.2 LASER POLARIZATION

As described in Section 4.5.3, the degree of circular polarization (DOCP) of the laser inside the cavity cannot be measured directly, therefore an optical model is used to accurately determine the DOCP.

For PREX-2 the uncertainty due to the various fit parameters ends up being 0.1% [60]. For CREX running this uncertainty formulation is complicated. The entrance function measured for CREX has two solutions, resulting in two possible solutions for optimum QWP/HWP setting. At the optimum running position used for CREX-II, solution 1 gives $0.9999 \pm 0.03\%$ and solution 2 gives $0.9974 \pm 0.26\%$. The problem is there is no clear way to distinguish between the validity of either solution, therefore both are incorporated into the DOCP calculation. Here, we combine uncertainty range from solution 1 and solution 2 for each QWP/HWP setting, and used the median value of that range as the cavity DOCP. The two solutions for CREX can be seen in Fig. 101. Curves represents the two entrance function solutions for the cavity DOCP model, and data points are normalized measured polarization for CREX, for different QWP/HWP configurations. For CREX the uncertainty due to the fit parameters is 0.26%.

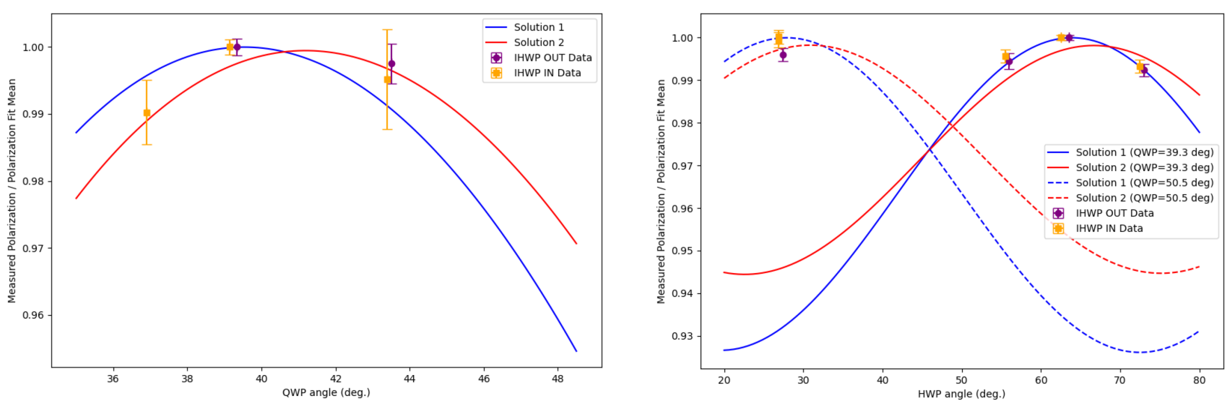

FIG. 101: Measured laser polarization vs QWP and HWP angles for CREX. Left: HWP angle is fixed at 63.5°, right: QWP angle fixed at either 39.3° or 50.5°. Curves represents the two entrance function solutions for the cavity DOCP model, and data points are average laser polarization measured at each wave plate setting for CREX [59].

Next we need to characterize the time dependence of the DOCP inside the cavity. The laser polarization in the exit line can be monitored non-invasively using the pair of exit line integrating spheres along with the Wollaston prism and quarter wave plate as discussed in Section 4.5.3. We saw some time dependence in this measurement.

But there is no one-to-one correlation between the DOCP in the cavity and the DOCP at the exit, therefore we need a model to link the exit line DOCP to cavity DOCP. To do this, we need a transfer function. From the cavity DOCP tests for some QWP/HWP configurations we have the cavity DOCP and the exit line DOCP, which we can use to constrain this transfer function. Exit line transfer function can be fitted using two polarization rotation angles θ_{exit} and η_{exit} and a phase retardance δ_{exit}, using the cavity DOCP and exit line DOCP. In addition to the DOCP at the cavity exit, we can also look at the light reflected back from the cavity (RRPD photodiode) while it's locked to gain some insight into possible time dependence of the cavity birefringence. By solving for both cavity DOCP and exit line DOCP as a function of QWP/HWP and reflected power, the exit line DOCP measurement can be used to directly track the cavity DOCP. The contribution to the uncertainty from time-dependent effects in PREX-2 is calculated be 0.12% at most.

For CREX, the exit line DOCP varied by about 0.1% throughout the experiment, which translates to an uncertainty contribution to of 0.05%.

Another source of uncertainty is the effect of birefringence of the cavity exit mirrors. Measurements of the cavity birefringence parameters relied on the assumption that the transmission of the stored light in the cavity through the exit mirror substrate results in no change to the laser polarization. It turns out, this was tested using an uncoated blank mirror substrate by Abdurahim Rakhman for the PREX-1 setup [61]. As in this paper we suggest a 0.1% uncertainty be assigned to be conservative.

The final uncertainty comes from using a cavity polarization model. Ideally, we could directly check the agreement of our model with the measured DOCP from the locked cavity, but this cannot be done for the cavity under vacuum, but can be checked for the cavity open to the air measurements. Residuals are calculated between the cavity polarization model and the measurements of DOCP taken with the cavity-open, and we saw as the cavity DOCP decreases, the deviation between the fit and measurements grow. Because of this behaviour, an uncertainty is applied for the polarization measurement. The residuals for the PREX-2 model are only considered with DOCP>0.98 because the majority of PREX-2 running was taken with DOCP above this threshold. For CREX running, the residuals threshold is DOCP>0.99. For PREX-2 and CREX the largest residuals of any open cavity measurement are about 0.3%

Table 6 shows the total DOCP uncertainty for PREX-2 and CREX.

5.6.3 DETECTOR CORRECTIONS

	PREX-2	CREX
Fit parameters	0.1%	0.26%
Time dependance	0.12%	0.05%
Substrate birefringence	0.1%	0.1%
Model residuels	0.33%	0.34%
Total	**0.38%**	**0.44%**

TABLE 6: Sources of systematic uncertainty for the laser DOCP.

PREX-2 and CREX ran with different PMTs and bases which are operated at different voltages. The two primary sources of uncertainty for the Compton photon detector is the PMT nonlinearity and the gain shift. Both of these are measured using LED pulser setup, discussed in Section 4.7.

Detector nonlinearity

The photon detector has a nonlinearity, where the detector yield as a function of photon light intensity (Y(I)), has small nonlinear terms. Modified measured yield can be written as,

$$Y(I) = I + c_1 I^2 + c_2 I^3 + - - - + c_I^{n+1}, \tag{130}$$

where $c_1 ... c_n$ are dimensionless coefficients for a polynomial of arbitrary degree n. If the system is perfectly linear, the coefficients are zero. As discussed in Section 4.7, to measure the coefficients we use two LEDs, "variable" and "delta," flashed for short intervals in sequence at 1 kHz. We then measure the difference between the variable + delta flash and the variable alone flash Y(x + δ) Y(x) and plot it vs the variable alone yield Y(x).

The nonlinearity function can be thought of as the deviation of the integral of a pulse of energy ρ from the expected proportional PMT response. To estimate the nonlinearity, we fit this function with an polynomial. Then we can modify the PMT response function to only represents non linear components as,

$$\epsilon(\rho) = \frac{Y(I)}{I} = 1 + c_1 I + c_2 I^2 + - - - + c_I^m. \tag{131}$$

For a perfectly linear system $\epsilon(\rho) = 1$. For PREX-2 and CREX nonlinearity studies, polynomial fits of degree m = 3 were sufficient for obtaining nonlinearity measurements. Then the non linearity function can be added to the Eq. 86 to get the corrected analyzing power as,

$$\langle A_l \rangle = \frac{\int_0^1 d\rho A_c(\rho)\rho(1 + c_1\rho + c_2\rho^2 + c_3\rho^3)\frac{d\sigma}{d\rho}}{\int_0^1 d\rho\rho(1 + c_1\rho + c_2\rho^2 + c_3\rho^3)\frac{d\sigma}{d\rho}}. \tag{132}$$

The nonlinearity corrected analyzing power is then calculated and compared to the analyzing power without nonlinearity correction. For PREX-2 PMT, this correction is 0.08% of the analyzing power and for CREX it is 0.02%.

Gain shift

Nonlinearity tests with the PREX-2 PMT showed that the PMT gain might be dependent on the incident light intensity of the PMT. When both pulser and beam were running, the delta LED appears to have a lower pulse integral while the laser is locked than while it is unlocked, suggesting there is a PMT gain shift. With average signal that might affect the background subtraction.

The primary parameter to describe gain shift is the relative change in pulse size α,

$$\alpha = \frac{\Delta_{ON} - \Delta_{OFF}}{\Delta_{ON}}, \tag{133}$$

where Δ_{ON} is the integrated pulse size of the delta LED with laser on, and Δ_{OFF} is for laser off. The corrected asymmetry can be written as,

$$\langle A_{corrr} \rangle = \frac{A_{exp} + \alpha f D_{OFF}}{1 + \alpha f Y_{OFF}}, \tag{134}$$

where,

$$f = \frac{1}{Y_{ON} - Y_{OFF}}. \tag{135}$$

A gain shift test was conducted on the PREX-2 tube after the PREX-2 experimental run, and measured 0.22% relative correction to the asymmetry.

For CREX, we were unable to directly measure the gain shift on the bench due to a malfunction in the pulser system after the CREX run. The gain shift calculation is determined from pulser running that was taken during the CREX experimental run. It was measured that the relative correction for the asymmetry is 0.15% for CREX.

5.6.4 BEAM KINEMATICS

The analyzing power is dependent on the beam energy, therefore the precision of the beam energy measurement should be added to the uncertainty on the analyzing power.

The experimental beam energy is measured by observing the beam position along the arc on the beamline heading into Hall A after the steering dipoles. For PREX-2, beam energy was E = 953.4 ± 1.0 MeV, while for CREX the beam energy was E = 2182.2 ± 1.1 MeV. For PREX-2 the relative correction on the analyzing power was 0.3% and for CREX it was 0.1%.

The simulation determined the analyzing power using an assumed beam energy and after getting the true beam energy, the analyzing power should be scaled accordingly. PREX-2 analyzing power was changed by 0.05% and CREX was changed by 0.03%.

5.6.5 RADIATIVE CORRECTION

A radiative correction due to virtual one-loop Compton scattering diagrams, as calculated by Denner and Dittmaier [62] is included as a analyzing power correction. For first order, the correction is,

$$A_l = A_{Born}(1 + \Delta A), \tag{136}$$

$$\Delta A = \frac{\alpha}{\pi}\frac{3\cos\theta_\gamma^{CM} - 1}{4(\beta + \cos\theta_\gamma^{CM})}, \tag{137}$$

where $\beta = k^{'CM}/E^{'CM}$ and θ_γ^{CM} is the photon scattering angle measured in the center of mass.

This correction is well defined and the the systematic uncertainty contribution from this corrections is negligible. Both PREX-2 and CREX measured asymmetries should be corrected by a factor 0f 0.997 (0.997 × $A_{measured}$).

5.7 PREX-2 COMPTON RESULTS

As discussed in Section 4.2.1 the photon asymmetries are calculated for each laser cycle and these laser cycles are grouped into snail, which have the same IHWP state, to calculate snail laser polarization. The asymmetries and polarizations are calculated for each cycle, then every cycle in a snail is averaged to produce a snail polarization value, weighted by the inverse square of each cycle asymmetry uncertainty as,

$$\langle A_{exp}^{(snail)}\rangle = \frac{\Sigma_i w_i \langle A_{exp}^{(cycle)}\rangle_i}{\Sigma_i w_i}, \tag{138}$$

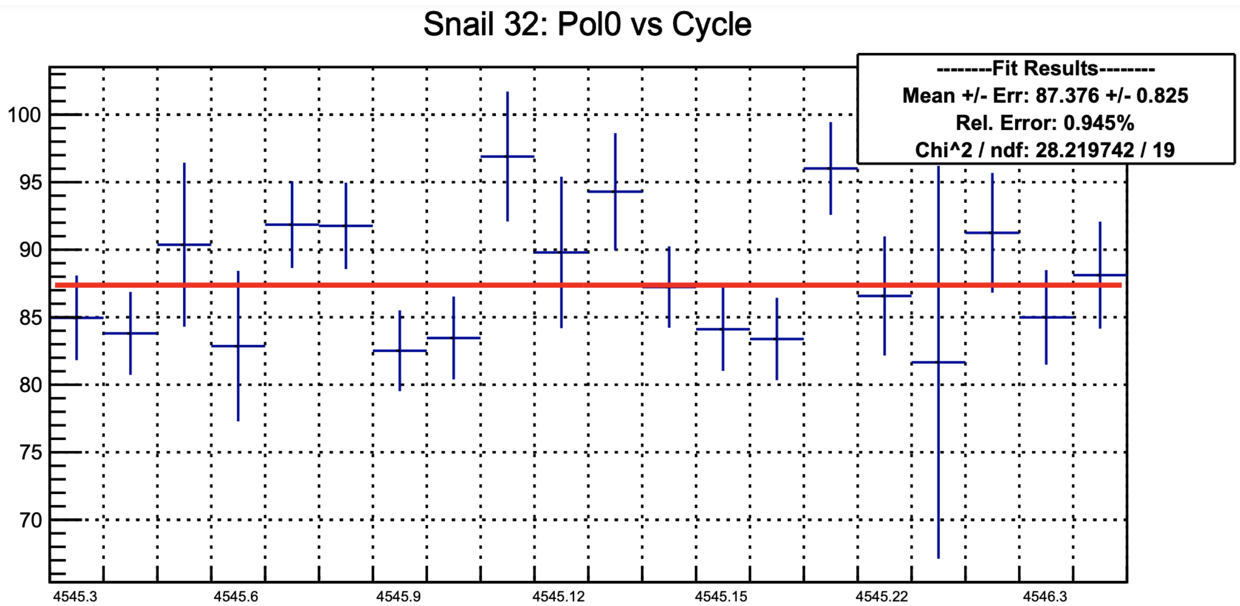

FIG. 102: Snail plot for PREX-2 experiment. X-axis is the cycles in the snail, Y-axis is the polarization for each cycle.

where,

$$w_i = \frac{1}{(\delta A_{exp}^{(cycle)})_i^2} \tag{139}$$

The combined statistical uncertainty can be written as the inverse sum of the weights,

$$(\delta A_{exp}^{(snail)})^2 = \frac{1}{\Sigma_i \frac{1}{(\delta A_{exp}^{(cycle)})^2}}. \tag{140}$$

A snail plot for PREX-2 is shown in Fig. 102.

After all the corrections, these snail polarization averages revealed non-statistical behavior in the measured polarization in the PREX-2 data set. To understand this behaviour, a deeper investigation was done looking at possible systematics, but none of those made a difference to the statistical noise.

We calculated background jitter for PREX-2 (discussed in Section 5.4.2) and the plot of background jitter is shown in Fig. 103. We saw a change in background jitter for different snails. The background is slowly varying but unstable at the timescale of the laser cycle "non-statistical" noise (jitter) since we use a short timescale (MPS) to determine statistical noise. That is the origin of the additional uncertinity we added here. From this we calculated a piecewise RMS for different snail groups and then add that RMS to each cycle polarization mean error. This reduced chi^2 by a little amount but still see a non statistical behaviour. We looked for BPM drifts, Pockels cell voltage changes, background detector changes, but statistical behavior cannot be correlated with any known variables in the Compton system. PREX-2 snail polarization plot is shown in Fig. 104.

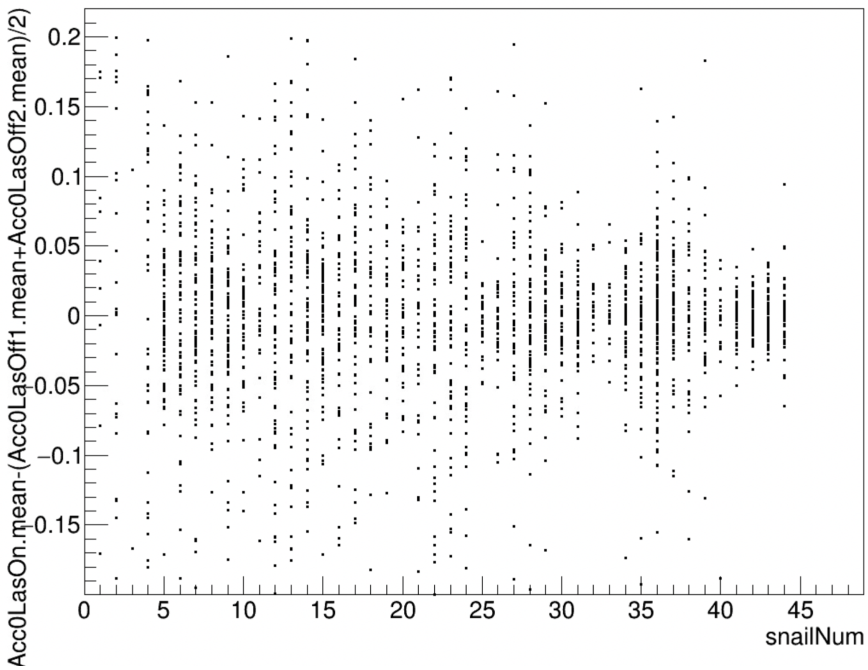

FIG. 103: Background gitter in PREX-2 experiment.

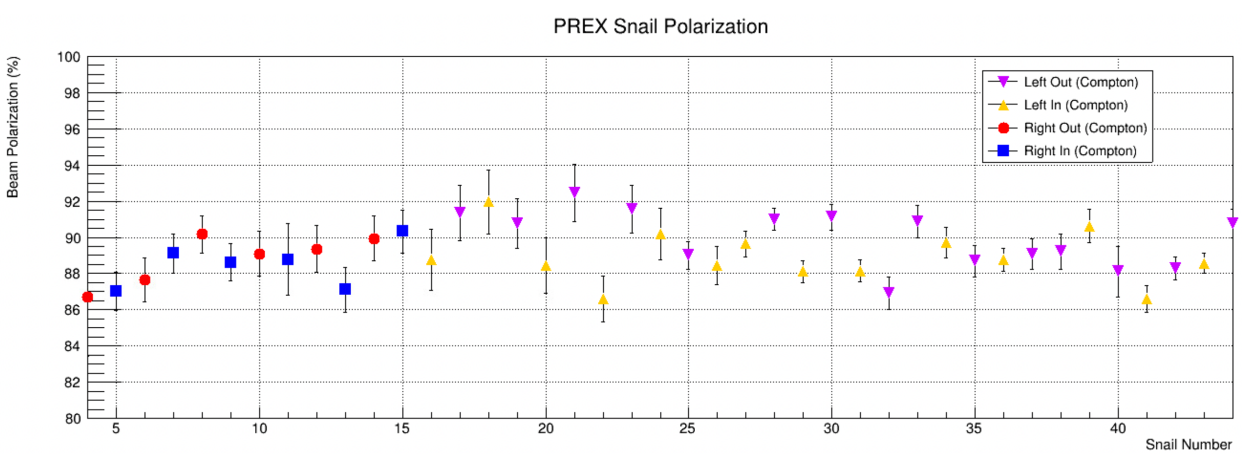

FIG. 104: PREX-2 snail polarization.

When averaging the PREX-2 data, the snail polarizations is weighted by the statistical precision of the main experiment data taken during the same time as each Compton data point.

$$w_i = \frac{1}{(\delta A_{PV})_i^2}, \tag{141}$$

where, δA_{PV} is parity violating asymmetry uncertainty for each snail period. In addition, to find the polarization average a time-dependence is accounted. The Compton data is divided into three "pieces". First piece is wien right and the second and third pieces are wien left. The wien left period is divided into two pieces by looking at the change in the polarization (see Fig. 105). Different IHWP states are fit separately. Each piece is fit and the average polarization is calculated by taking a weighted average of each piece.

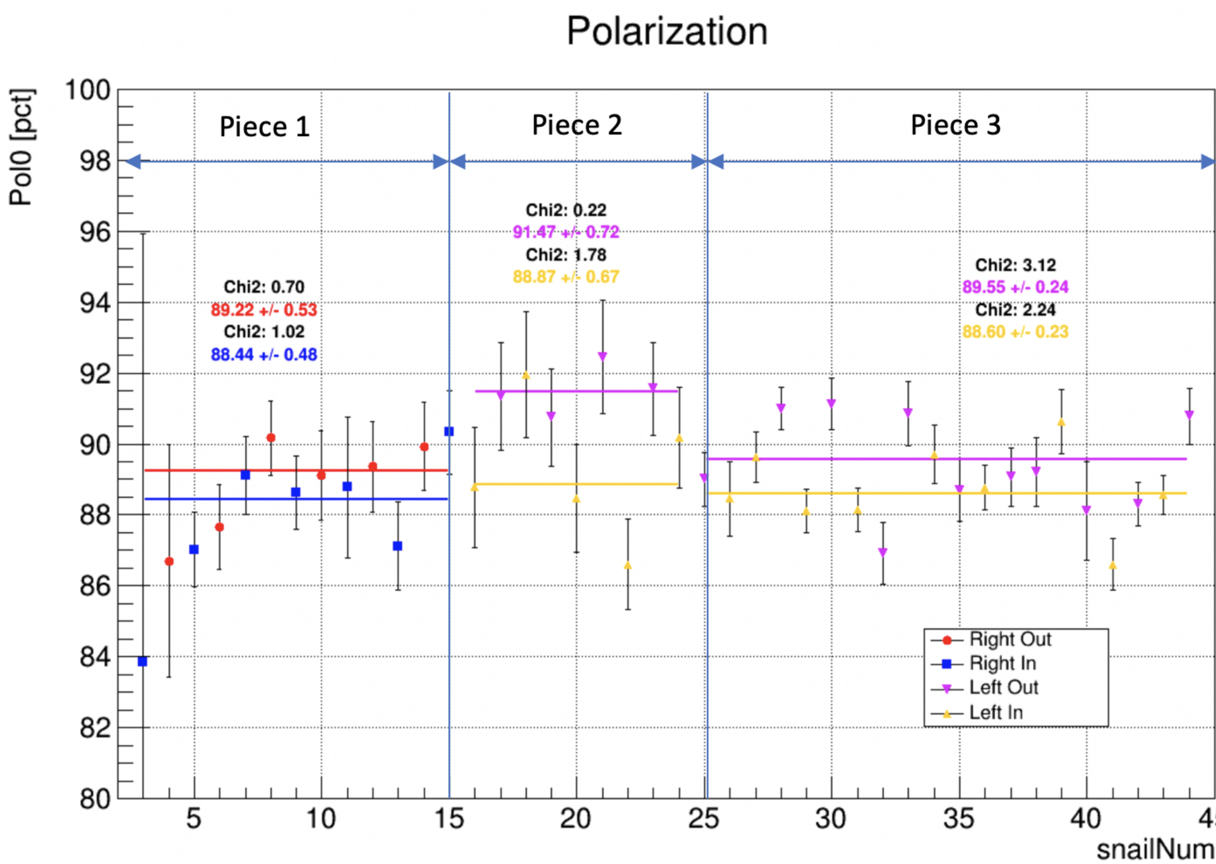

FIG. 105: PREX-2 piecewise snail polarization.

In the Fig. 105 we can see the magnitude of polarization is lower for IHWP in data than it was for IHWP out data. For PREX-2 and CREX running we had different PITA set points for IHWP in and out. The vacuum window birefringence was corrected with Pockels cell PITA voltage and improved the polarization for one IHWP state and not for the other, hence a difference in polarization for two states. This was identified and corrected prior to running CREX.

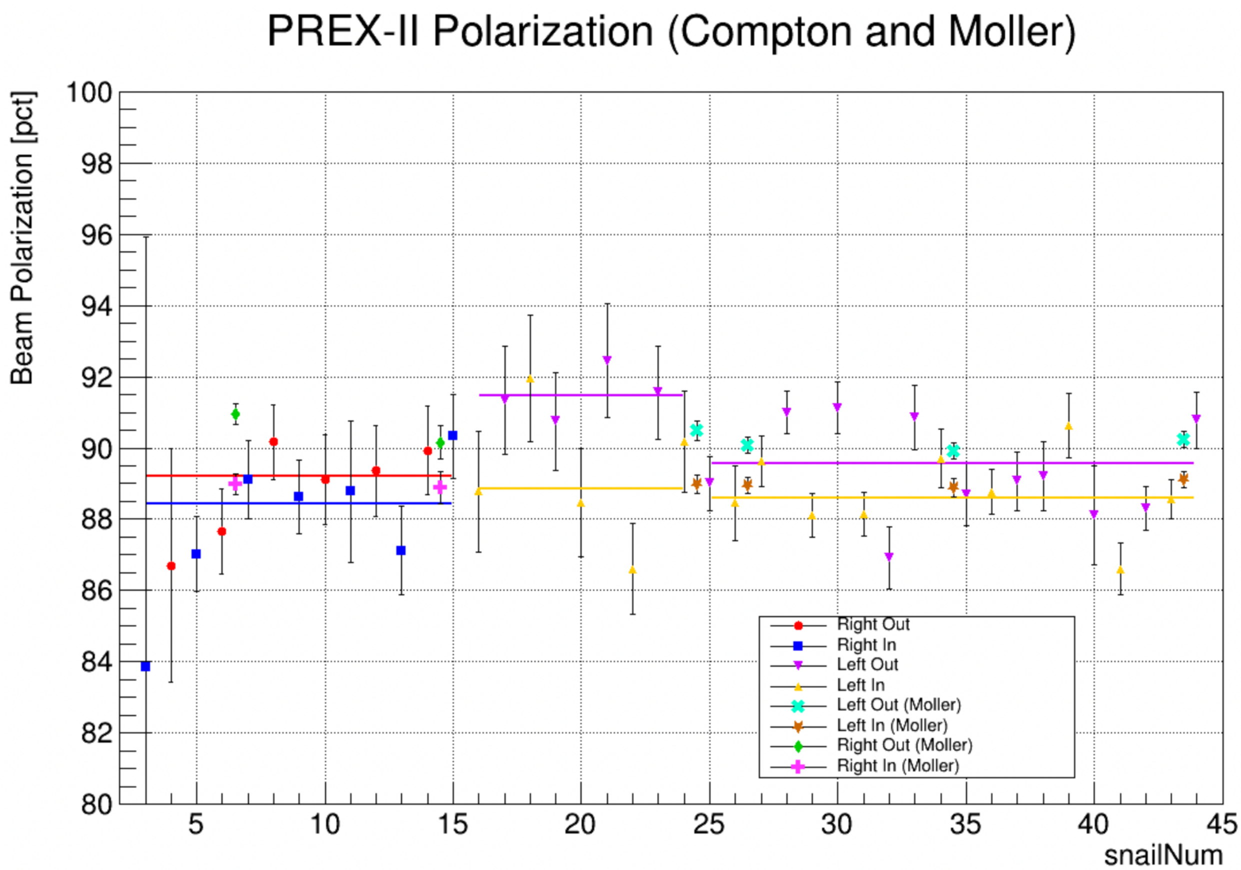

FIG. 106: PREX-2 Compton snail polarization averages and Moller polarization measurements plotted by time of measurement

For PREX-2, the weighted average mean polarization comes out to be 89.24% with a statistical uncertainty of 0.52%.

The systematic uncertainties for the PREX-2 measurement can be seen in Table 7. The corrections for asymmetries are applied for laser polarization, the beam energy correction to the analyzing power, and the radiative corrections to the measured asymmetries.

Source	Relative Correction	Uncertainty contribution
Laser DOCP	0.26%	0.38%
Photon cone offset	0.53%	0.30%
Gain shift	-	0.22%
Non linearity	-	0.08%
Beam Energy	0.3%	0.10%
Radiative correction	0.3%	-
Statistics	-	0.52%
Total	-	**0.73%**

TABLE 7: Uncertainty table for PREX-2 Compton measurement

With the statistical and systematic error, the PREX-2 Compton polarimeter measurement is $P_e^{Compton} = (89.24 \pm 0.65)\%$ with 0.73% relative uncertainty. For PREX-2, Moller polarimeter measured, $P_e^{Moller} = (89.67 \pm 0.81)\%$ with 0.90% relative uncertainty [63]. Figure 106 shows Compton PREX-2 results and Moller results.

Even though there is a good agreement between Compton and Moller polarimeter results, due to non-statistical behavior in the measured polarization in the Compton data set, it was decided not to use that for the beam polarization results. Therefore, only Moller polarimeter data was used for PREX-2. The Compton data used as a cross check for Moller polarimeter data to add confidence in control of systematic uncertainties in Moller analysis, but no improvement in uncertainty was ascribed to this cross check

5.8 CREX COMPTON RESULTS

For CREX when we look at the snail polarization we saw that the beam polarization was slowly decreasing and later found out this is highly correlated with the decreasing quantum efficiency[2]of the polarized source (see Fig. 107). This effect had been observed in polarized beam experiments at JLab before. When quantum efficiency decreases, the laser spot location on the photocathode is moved to another position and it can gain some quantum efficiency. In the Fig.107 we can see when we change the laser spot position, beam polarization is also increasing and with decreasing quantum efficiency, beam polarization is decreasing.

To get the CREX Compton polarization average three methods were used. Also, for

[2]quantum efficiency (QE), is the ratio of emitted electrons per incident photon.

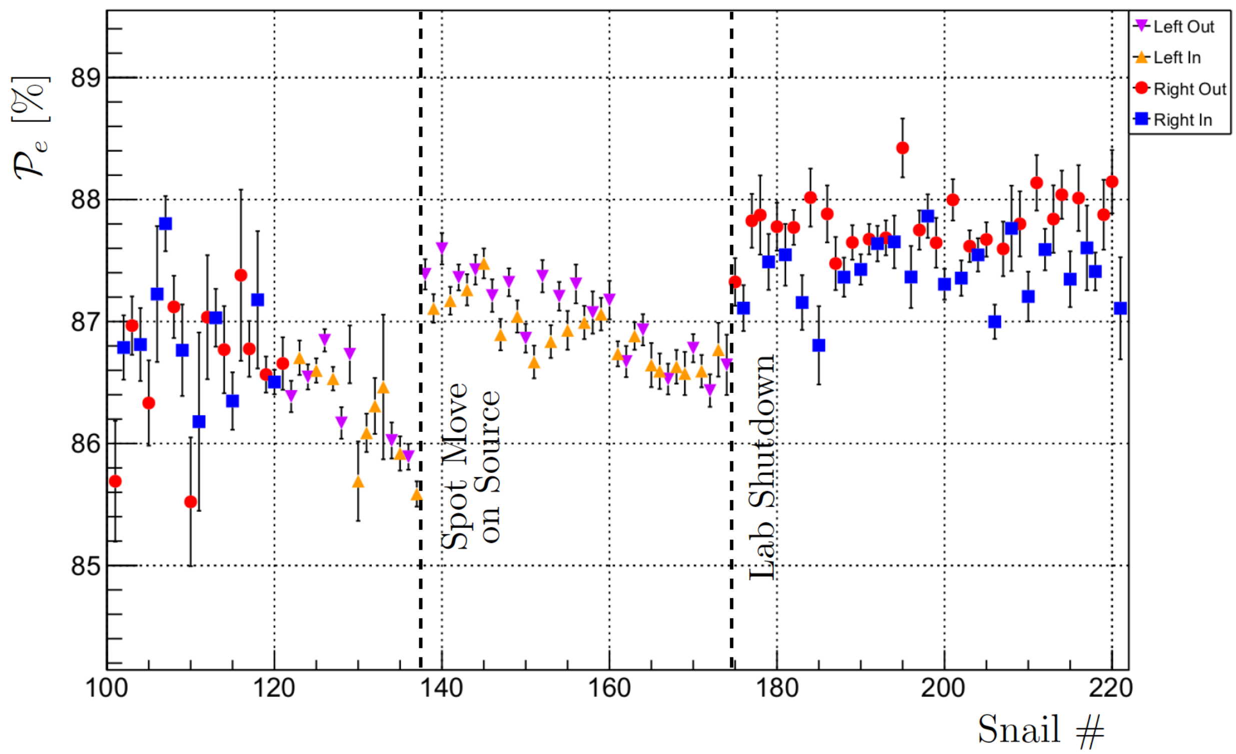

FIG. 107: Polarization measurement for each of the CREX snails.

CREX data another method of aggregation was used. Snails are grouped together into periods called "escargatoires". Escargatoires are constructed such that each escargatoire should have approximately equal statistical precision, must have a start time and an end time such that the periods from the main experiment data and the Compton data can be matched exactly, only have data from each IHWP and matching wien state, and the data must be taken within three days of each other [36].

Method	**Polarization Mean**	**Relative Uncertainity**
Escargatoire Average	87.118%	0.021%
Piecewise Fits	87.119%	0.018%
Mini-Escargatoire Average	87.104%	0.022%
Total Average	**87.115%**	**0.020%**

TABLE 8: Average and uncertainty of the CREX polarization for all three methods [64].

First, escargatoire average was calculated for the entire Compton run. Just like the PREX-2 analysis, the paity violating asymmetry uncertainties were used as a weight. Secondly, piecewise fit was calculated. The CREX data was divided into five pieces. The average polarization is calculated by evaluating the fit for each piece, and taking a weighted average of each piece. Lastly, a mini-escargatoire average was calculated for CREX data set. Mini-escargatoire is small in time scale than a regular escargatoires and only requirement is to match the start and stop times of parity data sets taken at the same time.

Table 8 shows the mean polarization and statistical uncertainty for each model. Table 9 shows systematic uncertainties incorporated with the CREX measurements.

Source	**Uncertainty contribution**
Laser DOCP	0.45%
Photon cone offset	0.2%
Gain shift	0.15%
Non linearity	0.02%
Beam Energy	0.05%
Model	0.02%
Radiative correction	-
Statistics	0.02%
Total	**0.52%**

TABLE 9: Uncertainty table for CREX Compton measurement [65].

For CREX, the Compton polarimeter measurement found that $P_e^{Compton} = (87.115 \pm 0.453)\%$ which is 0.52% relative uncertainty. This measurement is one of the most accurate Compton polarimetry measurements of an electron beam ever made. The Moller polarimeter measured $P_e^{Moller} = (87.06 \pm 0.74)\%$ which comes out to 0.85% relative uncertainty.

We can further increase the precision on the CREX beam polarization by combining these two measurements. Figure 108 shows the Moller data points added to Compton fits. The average difference between the Moller measurements and the Compton fits is small and has a good agreement between Compton and Moller measurements well within the overall uncertainty of both measurements. Because the sources of Moller systematic uncertainty are not correlated to the sources of Compton systematic uncertainty, the average polarizations of both Moller and Compton polarimetry can be combined using an inverse-variance weighted mean. With $P_e^{Compton} = (87.115 \pm 0.453)\%$ and $P_e^{Moller} = (87.06 \pm 0.74)\%$ the overall beam polarization is $P_e = (87.10 \pm 0.386)\%$ with 0.44% relative uncertainty. This is the most accurate beam polarization measurement for an experiment at JLab.

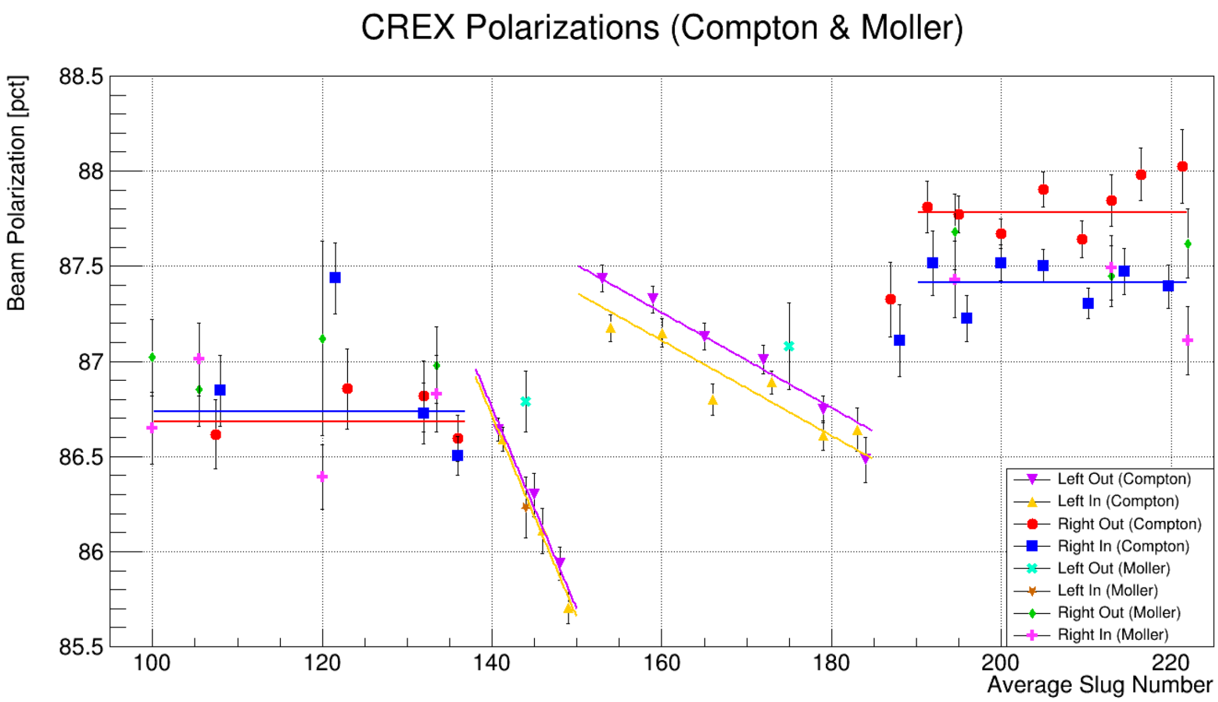

FIG. 108: Compton escargatoire polarization averages and Moller polarization measurements plotted by time of measurement [65].

CHAPTER 6

PREX-2 AND CREX ANALYSIS

PREX-2 experiment ran for 85 days at an average of 70 μA current and accumulated 114 C of beam charge after cuts defined for analysis during running. For CREX, the run period was 120 days at an average of 150 μA and 383 C passed the cuts. Since we are measuring a tiny asymmetry it is important to understand and control all sources of systematic error and backgrounds.

6.1 ASYMMETRY ANALYSIS

It is useful to consider a segmentation of the collected in time. Each "run" consisted of a single data tab from the data acquisition, and were typically but not always about one hour long. A "minirun" was composed of about five minutes, worth of "good" data (or 9000 good multiplet patterns). "Good" data means events which pass all the event cuts. PREX-2 collected a total of 5084 miniruns and CREX collected 8527 miniruns. The IHWP state is changed every 6 - 8 hours of good data. The runs for each IHWP state are then grouped into larger data set intervals called "slugs", corresponds to about 12 hours of data. PREX-2 collected a total of 96 slugs and CREX collected 123 slugs. The wien state was changed after several weeks of good data. By the end of PREX-2, we had changed the wien setting three times, and for CREX it was changed two times. Then slugs are grouped into "Pitts" which consist of four neighboring slugs with approximately equal statistics in each IHWP state. The use of these various groupings allowed for the comparison of average values, balancing precision with resolution in time.

6.1.1 CUTS

Distribution which include each and every MPS window (described in Section 2.7.1) and multiplet have been thoroughly studied to develop cuts which reject unacceptably large beam fluctuations or obvious hardware failuers.

Beam fluctuation cuts such as, beam current threshold cut, beam position excursion cut, beam current stability cut, and beam energy excursion cut, are used for both PREX-2 and CREX. Hardware failures in the fast feedback system or in beam current or position were also monitored and cut by the analyzer. Data taken while the beam modulation system (Section 2.4.3) was active was flagged, and analyzed separately.

Sometimes other run specific, special cuts are applied in the event of DAQ failure, magnet failure, or when any other anomalies are observed. None of these cuts are directly applied based on detector data, or asymmetries.

6.1.2 PEDESTAL CALIBRATION

Beamline monitors (BPMs, BCMs) and the quartz detectors should be calibrated properly to get a precise measurements of parity violating asymmetry.specifically, the signals are used to measure an asymmetry, which requires only that the response is linear with respect to the detected input. This linearity can only be used if the pedestal is known accurately. The pedestal is defined as the response corresponding to zero input signal. It includes electronic baseline and any dark current. It also includes a possible non-linearity at low signal levels, so it must be evaluated by linear extrapolation by calibrated inputs. If the pedestal is S_{ped}, the signal recorded by the ADC can be written as,

$$S_{R(L)}^{measured} = S_{R(L)}^{phys} + S_{ped}, \tag{142}$$

Therefore, the measured detector asymmetry is given by,

$$A_M = \frac{S_R^{phys} - S_L^{phys}}{S_R^{phys} + S_L^{phys} + 2S_{ped}} \sim A - \frac{S_{ped}}{\langle S^{phys} \rangle}. \tag{143}$$

BPM, BCM, and detector pedetals are calibrated on a weekly timescale. Also, whenever there is any change in the detector configuration, pedestal calibration is preformed. We first calibrate the UNSER (discussed in Section 2.4.2) pedestal. UNSER provides a linear response at short time scale but it is noisy and unstable on a few minute timescale. For this reason the beam is turned on and off repeatedly during a calibration scan with the UNSER. After correct the UNSER for its pedestal drifts this signal can be used as the reference to calibrate the RF BCMs.

The calibration of an RF BCM versus UNSER was done using a beam-offand beam-on current ramp ($\sim$ 10 μA step from 20-70 μA), as shown in Fig. 109. To extract the pedestal, a first order polynomial linear fit was performed between the BCM and the UNSER. The UNSER signal is corrected for each current based on the predestal measured in ithe neighboring no-beam data. An example of the BCM pedestal calibrations relative to the UNSER is shown in Fig. 110. All of the other monitors are then calibrated with respect to

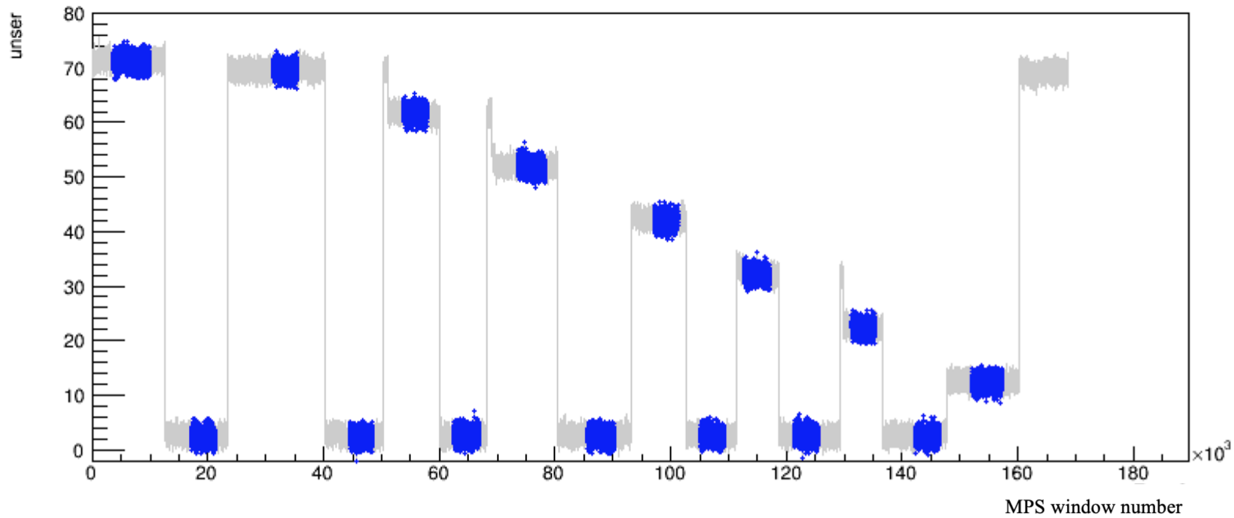

FIG. 109: An example of the UNSER BCM signal during a beam current scan.

this normalizing RF BCM.

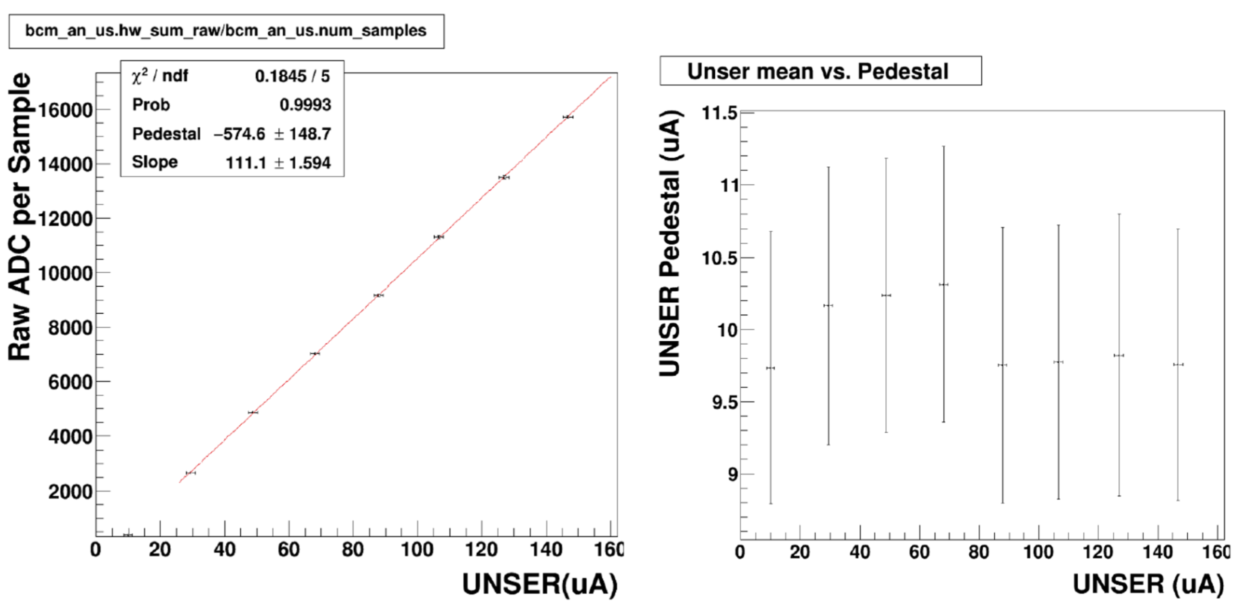

FIG. 110: Left: Example of UNSER relative calibration of the BCM AN US for CREX. Right: beam-offpedestal values for the Unser.

		Mean(ppb)	Error(ppb)
PREX-2	$\boldsymbol{A_{raw}}$	431.64	44.01
	$\boldsymbol{A_q}$	20.68	25.80
CREX	$\boldsymbol{A_{raw}}$	2026.81	189.88
	$\boldsymbol{A_q}$	-88.8	26.22

TABLE 10: Average raw asymmetries(blinded) and charge asymmetry during PREX-2 and CREX [37] [66].

6.1.3 ASYMMETRIES

The raw detector asymmetry contains noise contributions from the beam intensity fluctuations. Therefore, we normalize the detector signal by the beam current. The raw asymmetry measured by each detector can be written as,

$$A_{raw} = \frac{\frac{F_R}{I_R} - \frac{F_L}{I_L}}{\frac{F_R}{I_R} + \frac{F_L}{I_L}}, \tag{144}$$

where F_R and F_L is the flux measured by the detector during a consecutive pair of right and left helicity window states, and I_R and I_L are the corresponding beam intensities. To first order A_{raw} can be written as,

$$A_{raw} = A_{det} - A_q, \tag{145}$$

where, $A_{det} = \frac{F_R - F_L}{F_R + F_L}$ is the asymmetry measured by the detector, and $A_q = \frac{I_R - I_L}{I_R + I_L}$ is the charge asymmetry measured by the BCM.

The blinded (see Section 6.5) raw asymmetry (A_{raw}) averaged between the two HRSs, are given in Table 10 with charge asymmetry (A_q).

6.1.4 HELICITY CORRELATED POSITION DIFFERENCE

Beam position and energy difference between pairs of opposite helicity states give rise to a potential false asymmetry background. The trajectory fluctuations are determined using two BPMs, separated by 4m referred to as BPM4a and BPM4e. For the energy fluctuation correction, PREX-2 used a linear combination of the x-position measured by the two energy monitors BPM11 and BPM12, and for CREX only the BPM12 is used. These BPMs are in the dispersive arc, and the combination used during PREX-2 maximized the sensitivity to the energy relative to the trajectory.

If $X_{L(R)}$ is the beam position for the left(right) helicity states in a multiplet pattern, then the position difference, ΔX, can be written as,

$$\Delta X = \frac{X_R - X_L}{2}, \tag{146}$$

The differences are then weighted by the statistical precision of the main detectors in each minirun. The weighted, slug-average position difference can be written as,

$$\langle \Delta X \rangle = \frac{\Sigma_i w_i \Delta X_i}{\Sigma_i w_i}, \tag{147}$$

where, $w_i = \frac{1}{\sigma^2_{A_i}}$, σ_{A_i} is the statistical precision of the main detectors for a minirun i. ΔX_i is the ΔX averaged over the multiplets in the minirun i. The weighted slug average position difference error is given by,

$$\langle \sigma_{\Delta X} \rangle = \sqrt{\frac{\Sigma_i w_i^2 \sigma^2_{X_i}}{(\Sigma_i w_i)^2}}, \tag{148}$$

where σ_{X_i} is the RMS distribution of ΔX for multiplets in each minirun.

We don't have a direct measurement of the beam position and angle difference at the target, this can be inferred from BPM4a and BPM4e.

$$\Delta X_{targ} = \frac{\Delta BPM4eX - \Delta BPM4aX}{D/L} + \Delta BPM4aX, \tag{149}$$

$$\Delta Y_{targ} = \frac{\Delta BPM4eY - \Delta BPM4aY}{D/L} + \Delta BPM4aY, \tag{150}$$

$$\Delta \theta_X = \frac{\Delta BPM4eX - \Delta BPM4aX}{D}, \tag{151}$$

$$\Delta \theta_X = \frac{\Delta BPM4eY - \Delta BPM4aY}{D}, \tag{152}$$

where D = 4.083 m is the distance along the beamline between BPM4e and BPM4a BPMs and L = 5.725 m is the distance between the target and bpm4a.

Average Position and angle difference at the target for PREX-2 and CREX are given in Table 11.

6.1.5 FALSE ASYMMETRY CORRECTION

	PREX-2		CREX	
	Mean	**Error**	**Mean**	**Error**
$\boldsymbol{\Delta X_{targ}}$	-1.3 nm	2 nm	-2.59 nm	1.81 nm
$\boldsymbol{\Delta Y_{targ}}$	1.1 nm	0.5 nm	-0.37 nm	0.88 nm
$\boldsymbol{\Delta \theta_X}$	-0.28 nrad	0.32 nrad	-0.03 nrad	0.05 nrad
$\boldsymbol{\Delta \theta_Y}$	-0.14 nrad	0.09 nrad	-0.13 nrad	0.08 nrad

TABLE 11: Helicity correlated beam position and angle differences at the target for PREX-2 and CREX [67] [68].

The false asymmetries from the beam arise from helicity dependent effects of the beam at the target. Any systematic change in the beam, such as charge, position, energy, and angle caused by helicity reversal, accounts for a potential helicity correlated false asymmetry. This false asymmetry should be removed from the measured detector asymmetry. The asymmetry after beam correction can be written as,

$$A_{corr} = A_{raw} - A_{false}, \tag{153}$$

where,

$$A_{false} = \sum_{i}^{5} \alpha_i \Delta B_i, \tag{154}$$

where, $\vec{B} = (X, Y, \theta_X, \theta_Y, E_{beam})$ are beam positions X and Y, angles θ_X and θ_Y and beam energy E_{beam} on the target. $\Delta B_i = (B_i^+ - B_i^-)/2$ is the helicity correlated beam parameter difference. Here, α_i is the sensitivity of the measured asymmetry to the fluctuation in beam parameter ΔB_i.

$$\alpha_i = \frac{\partial A_{raw}}{\partial \Delta_{Bi}}. \tag{155}$$

We used three different methods to make this correction, which allows for consistency cross checks between the different methods. The techniques are: linear regression, dithering, and Lagrange multiplier method. These corrections helped to cancel the beam jitter and lower the statistical width of the asymmetry. The correction for a typical CREX run can be found in Fig. 111.

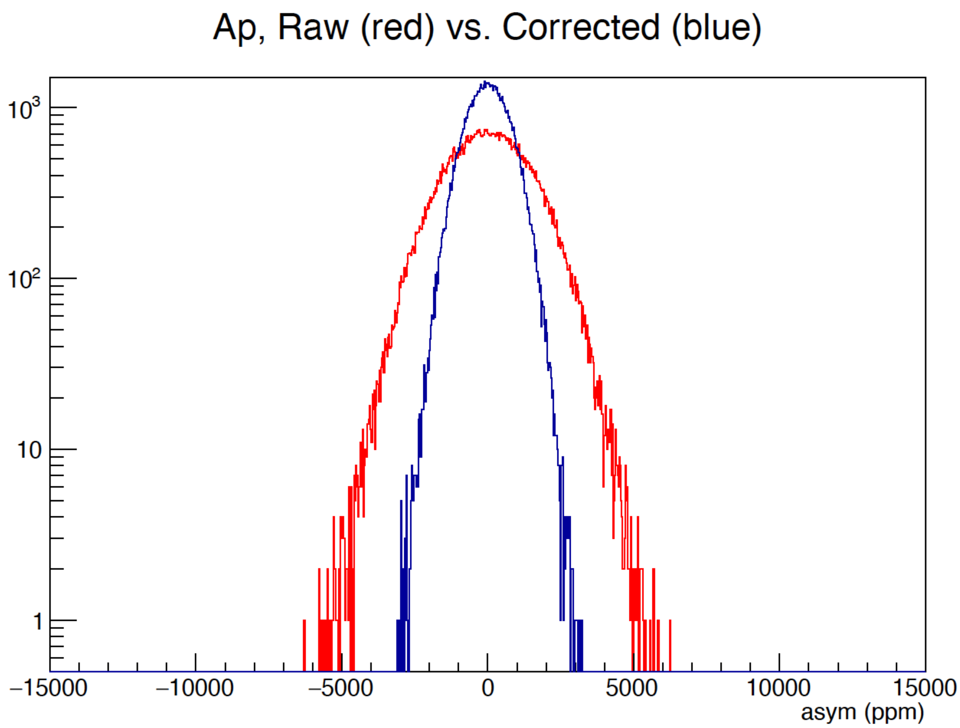

FIG. 111: Example of the power of beam corrections to remove random noise due to beam jitter for a typical CREX run. Red: raw detector asymmetry, Blue: detector asymmetry after beam corrections.

Linear regression

The linear regression technique is used to measure the correction slopes of the raw asymmetries versus position, angle, and energy differences due to natural beam motion during production data taking.

The correlation slopes α_i, in the Eq. 160, represent the effect of helicity correlated beam properties at the target but the measurement of correlation slopes is taken at each position monitor, using 12 BPMs. The phase space of five beam parameters can be spanned by the 12 position monitors with the linear transformation,

$$\Delta\vec{B} = \mathbf{R}\Delta\vec{M}. \tag{156}$$

where, $\Delta\vec{M}$ are the beam monitor differences. The transformation R must be diagonalized to calculate an independent correction for each of 12 degrees of freedom in the phase space covered by the beam monitors. It is expected that there are only 5 degrees of freedom corresponding to the beam, so the over determined eigenvectors also account for instrumental noise [66].

Then, Eq. 159 can be changed as,

$$A_{corr} = A_{raw} - \sum_i \beta_i \Delta M_i, \tag{157}$$

where, β_i is the beam monitor correlation slopes. To get the regression slopes, the raw asymmetries A_{raw} are plotted against the position differences ΔM_i, and the slopes are extracted. The slope of each beam parameter is determined using a least-squares fit, which minimizes the χ^2. In the multivariate regression equation, detector raw asymmetries are the dependent variables, and the position differences measured by the twelve position monitors (BPM11X, BPM11Y, BPM12X, BPM12Y, BPM16X, BPM16Y, BPM1X, BPM1Y, BPM4aX, BPM4aY, BPM4eX, and BPM4eY) are the independent variables. Then minimized the value of χ^2 as,

$$\chi^2 = \sum_j \left[A_{raw_j} - \sum_i \beta_i (\Delta M_i)_j \right]^2, \tag{158}$$

where, $(\Delta M_i)_j$ is the j^{th} measurement of the i^{th} independent variable. The χ^2 is minimized for each $\frac{\partial \chi^2}{\partial \beta_i} = 0$. This equation is then solved for β_i by applying an inverse linear transform. Example correlation plots between the upstream main detector asymmetries and position differences of bpm4eX, bpm4eY, and bpm12X for a PREX-2 run are shown in Fig. 112.

Beam Modulation (Dithering)

Another way of doing false asymmetry correction is the beam modulation. This technique uses controlled excursions of the beam position, angle, and energy on target to determine the responses of the detectors. After every dithering cycle, the response in both the beam monitors and the detectors are calculated. In the beam modulation system we have iron-free dipole coils to deflect the beam. The beam is harmonically drive through multiple periods for each modulation coil at 15 Hz frequency with ~ 100 μm amplitude position swings. An RF cavity is also actuated in a similar manner with the resulting energy shift creating a similar magnitude of position deflection in the dispersion region of the beamline.

The sensitivity to each beam monitor M_i is calculated as $\frac{\partial D}{\partial M_i}$, D represents the detector responses. Beam modulation directly measures the sensitivity of the detector to each coil C_k, as $\frac{\partial D}{\partial C_k}$, and the sensitivity of the beam monitors to the coils $\frac{\partial M_i}{\partial C_k}$. The normalized detector sensitivity to the k_{th} modulation coil, can be written as,

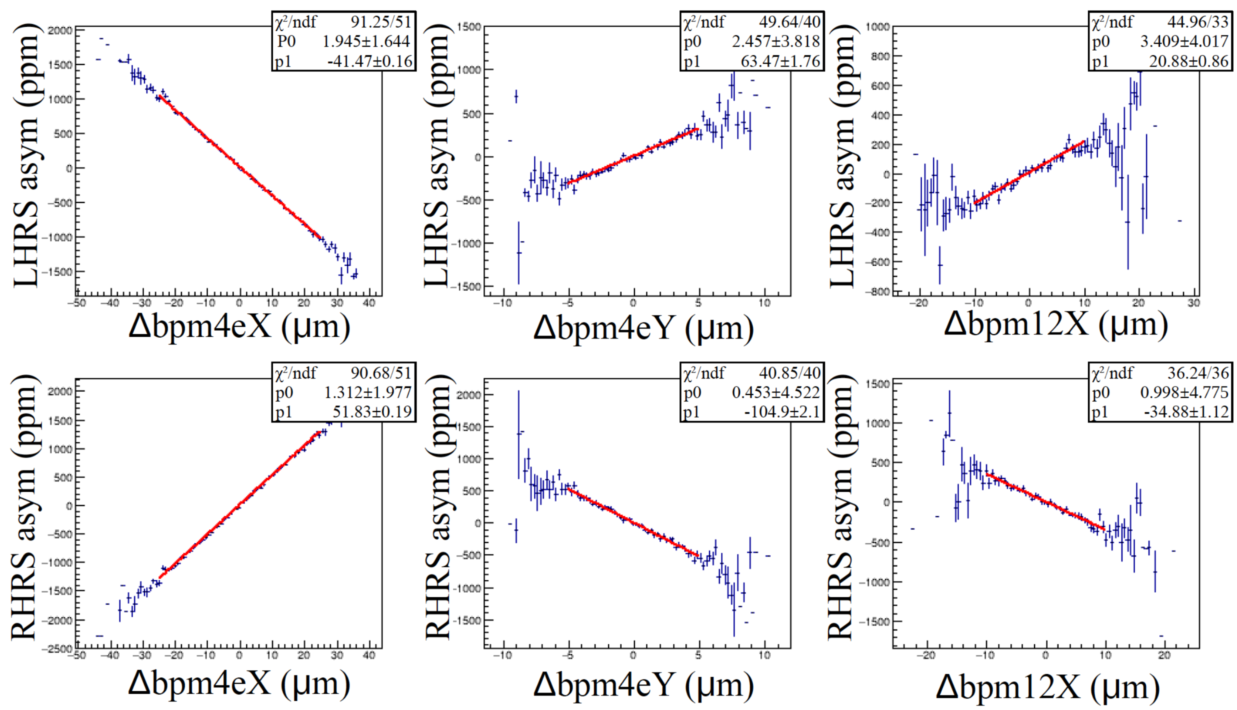

FIG. 112: Example correlation plots between the upstream main detector raw asymmetries and position differences of BPM4eX, BPM4eY, and BPM12X for a PREX-2 run.

$$\frac{\partial D}{\partial C_k} = \sigma_i \frac{\partial D}{\partial M_i}\frac{\partial M_i}{\partial C_k}. \tag{159}$$

The equation then can be rewritten in matrix form, from which the normalized detectors slopes to the i_{th} position monitor, $\alpha_i = \frac{\partial D}{\partial M_i}$, is extracted using the inversion matrix method [66]. The coil sensitivities for a single beam modulation cycle can be seen in Fig. 113.

Lagrange Multipliers

This is a combination of the regression and beam modulation techniques, which calculates a correlation slopes and a χ^2 minimization of the Lagrangian. The Lagrangian function can be written as,

$$\mathbf{L} = \chi^2 + \sum_k \lambda_k \left(\frac{\partial D}{\partial C_k} - \sum_i \alpha_i \frac{\partial M_i}{\partial C_k} \right), \tag{160}$$

where λ_k is the Lagrange multiplier for modulation coil k and the χ^2 is defined in Eq. 164. Constraints on the Lagrangian are,

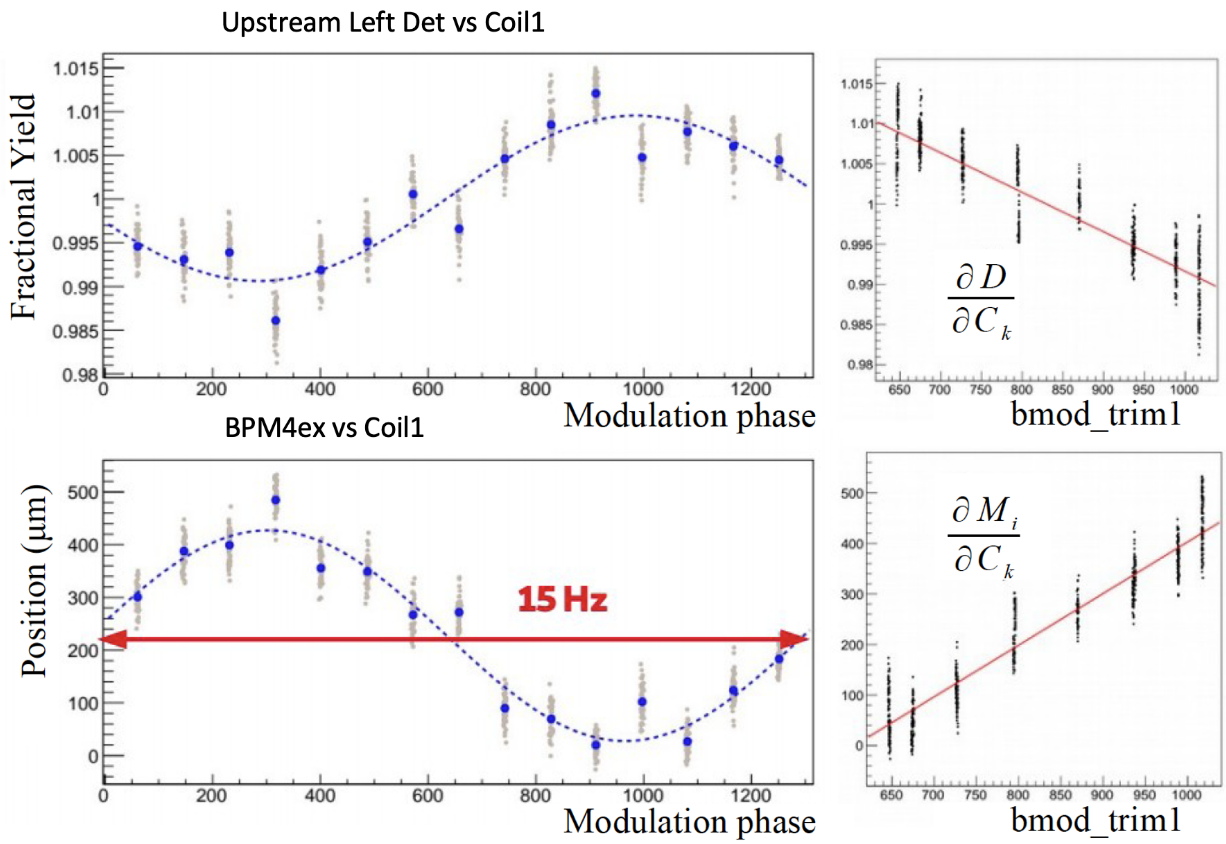

FIG. 113: Left: plot of response of the main detector and BPM to a dithering cycle modulation phase, Right: linear correlation between the monitor response and the magnitude of the driving signal [69].

$$\frac{\partial L}{\partial \lambda_k} = 0, \qquad \frac{\partial L}{\partial \alpha_i} = 0. \tag{161}$$

For the Lagrange multiplier analysis, the BPM configuration includes all 12 available BPMs in the Hall A beamline. With this analysis, correcting beam fluctuations is more flexible and precise than for modulation alone. The corrections are also restricted to conform to the constraints of the modulation calibration, protecting against inaccuracies in a regression only analysis which can be be disturbed by the noise. An extensive set of consistency checks over time and between monitors was performed leading to a robust estimate of the possible uncertainty in this correction [66]. The total correction to the asymmetry due to helicity correlated beam properties is,

$$A_{\text{false}}^{(\text{PREX-2})} = -60.38 \pm 2.50 \text{ ppb}, \tag{162}$$

$$A_{\text{false}}^{(\text{CREX})} = 53.45 \pm 5.44 \text{ ppb}. \tag{163}$$

6.2 COUNTING MODE MEASUREMENTS

Counting mode measurements are mainly used for main detector alignment and Q^2 measurements. Before the start of PREX-2 and CREX experimental running optics calibrations are done to align the main detectors. The main detector alignment is important to maximize the acceptance of elastically scattered electrons into the detector, while rejecting the inelastic electrons. .

6.2.1 INELASTIC BACKGROUND

A careful detector alignment could exclude most of the inelastic events from the detectors but not all. Therefore inelastic background contamination should be calculated for each experiment.

For PREX-2, low lying inelastic states had a relatively low cross-section, so inelastic contribution were very small. For CREX this correction is more significant. Even though ^{48}Ca first excited state and ground state is relatively separated, the kinematics of the CREX measurement, and natural fluctuations in the beam energy, make it difficult to reject inelastic electrons [70].

The primary excited states of ^{48}Ca contributing to the CREX parity violation measurement are the spin-parity 2^+ and two 3^- states. To make a correction for each of these states, a theoretical estimate of asymmetry contribution is calculated with the uncertainty. Inelastic background produce an overall relative uncertainty of 0.82% on CREX A_{PV}.

Q^2 Measurement

The square of the four-momentum transferred by a scattered electron to the target is given by,

$$Q^2 = 2EE'(1 - \cos\theta), \tag{164}$$

where, E is the electron's incoming energy, E' is the outgoing energy of the electron, and θ is the scattering angle.

The incident energy(E) can be measured from the beam trajectory using the magnetic field integral of the dipole magnets that bend the electron beam from the LINAC to Hall A. Using the beam bending angle we can get an estimate of electron beam energy [71]. The average beam energy measured during PREX-2 is 953.4 ± 1 MeV and for CREX 2182.2 ± 1.1 MeV. The energy of the outgoing, scattered electron is measured by the HRSs.

The scattering angle can be determined by the HRS relative to the central ray θ_0. θ_0 measurement is obtained from the "pointing" measurement using the standard Hall A water cell target. Using the energy difference between the two peaks of ^1H and ^{16}O nuclei in the water cell target, θ_0 can be calculated.

To determine the stability of Q^2 measurements are taken regularly for both PREX-2 and CREX with dedicated low beam current runs, by measuring the Q^2 distribution accepted by the quartz detector. For PREX-2 measured, $Q^2 = 0.00616 \pm 0.00004$ (GeV/c)^2 and for CREX $Q^2 = 0.0297 \pm 0.0002$ (GeV/c)^2

6.3 SPECTROMETER ACCEPTANCE

The spectrometer acceptance is primarily defined by the Q1 collimator, and different points within this acceptance may have different detection efficiencies and different asymmetries. The actual asymmetry we measure is an average over the acceptance. Therefore to make a theoretical interpretation of the measured asymmetry, effect of this finite acceptance must be understood clearly. The acceptance function can be written as [72],

$$\langle A \rangle = \frac{\int d\theta A(\theta) \frac{d\sigma}{\mathrm{d}\Omega} \epsilon(\theta)}{\int d\theta \frac{d\sigma}{d\Omega} \epsilon(\theta)}, \tag{165}$$

where $A(\theta)$ is the asymmetry within the acceptance as a function of θ, $\frac{d\sigma}{d\Omega}$ is the differential scattering cross section, and $\epsilon(\theta)$ is the acceptance function.

The acceptance function can be derived by comparing the measured magnetic transport kinematic distributions at the target with a tuned parameter Monte Carlo simulation. Insertable sieve collimator with a distinct pattern of holes is used during optics studies to reconstruct scattering geometry at the target. Acceptance function for CREX experiment is shown in the Fig. 114.

6.4 TRANSVERSE ASYMMETRY MEASUREMENT

The transverse asymmetry (A_T), comes from a non zero component of beam polarization in a direction transverse to the beam direction. This is a potentially important systematic

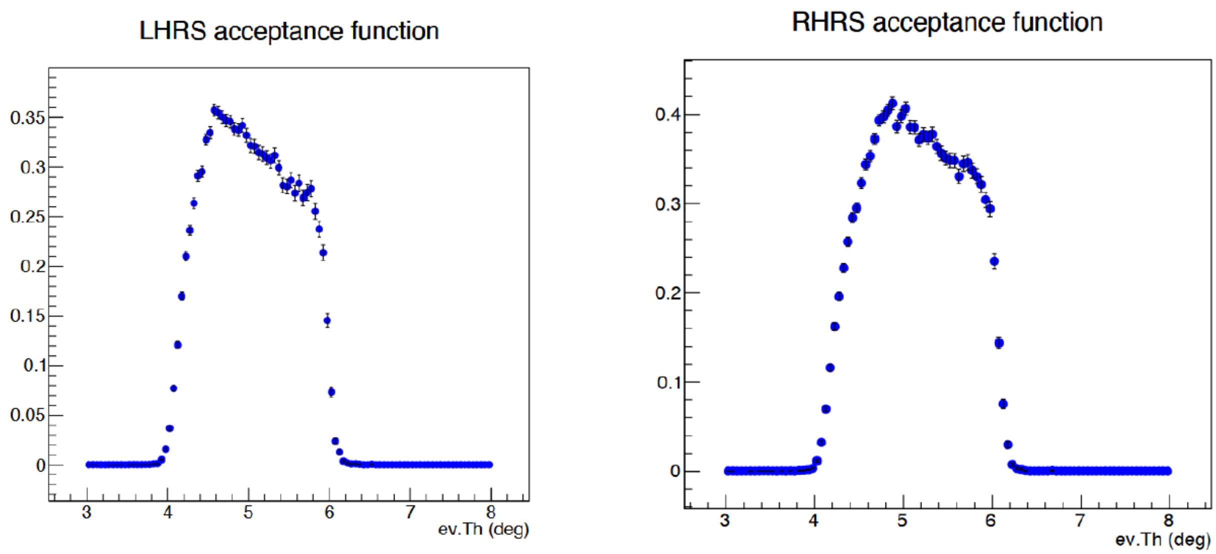

FIG. 114: CREX acceptance function versus lab scattering angle for both HRSs.

uncertainty to the A_{PV} measurement, because there is some residual transverse polarization in the electron beam.

Using a fully transverse polarized electron beam, we conducted several days of dedicated measurements of the transverse asymmetries for all physics related targets during PREX-2 and CREX. The measurement is made for ^{208}Pb, ^{40}Ca, and ^{12}C targets during PREX-2. During CREX ^{48}Ca and the same three targets measured during PREX-2 was measured.

There are two components to A_T. A_{TH} is the horizontal transverse asymmetry and A_{TV} is the vertical transverse asymmetry. A_{TV} creates an asymmetry in the horizontal detector direction and therefore it can be measured using the main detectors. A_{TH} cannot be measured using the main detectors. Auxiliary detector, called "A_T" detectors, were used during production running for both PREX-2 and CREX. These "A_T" detectors are placed vertically above and below the main detectors, where they had increased sensitivity to a potential in-plane residual transverse polarization [73].

For both PREX-2 and CREX, transverse asymmetry did not contribute a correction to the parity violating asymmetry, but an uncertainty was added for this correction (see Table 12 13).

6.5 PARITY VIOLATING ASYMMETRY

The corrected asymmetry, A_{corr} can be written as,

$$A_{corr} = A_{raw} - A_{false} - A_{nonLin} - A_{A_T} - A_{blind}, \tag{166}$$

where, A_{raw} is the A_q corrected detector asymmetry, A_{false} is the asymmetry corrections due to beam fluctuations, A_{nonLin} is the detector non linearity, A_{A_T} is the transverse asymmetry, and A_{blind} is the blinding term. A_{blind} offset is used to to avoid human bias on the measured asymmetry. A constant offset is added to the measured asymmetry and it is chosen by an arbitrary text sentence which is hashed to a numerical offset before each experiment began. Note that no correction for non linearity and transverse polarization were required, for PREX-2 and CREX, although estimates are made for the systematic uncertainty due to these terms.

The physics A_{PV}, after all corrections and normalization, is given by,

$$A_{PV} = \frac{A_{corr} - P_e \sum_i f_i A_i}{P_e(1 - \sum_i f_i)} R_{radcorr} R_{Q^2} R_{acc}, \tag{167}$$

where, P_e is the electron beam polarization. A_i and f_i refer to the asymmetry and rate fraction of a background processes. R_{Q^2} is a correction obtained from the Q^2 measurement, R_{acc} is the correction from the acceptance function and $R_{radcorr}$ is from radiative corrections.

The purity of the target material plays an essential role in the interpretation of the measured asymmetry. As we discussed in Section 2.4.7, ^{208}Pb target foil is sandwiched by thin foils of diamond to help protect it from melting while running at high beam currents. The parity violating asymmetry of ^{12}C and the contamination to the measured asymmetry can be easily corrected. The corrected asymmetry of ^{208}Pb, A_{PV}, is calculated using,

$$A_{PV} = \frac{A_{corr} - P_e f_c A_c}{P_b(1 - f_c)}, \tag{168}$$

where f_C is the carbon dilution fraction (calculated using an optical simulation), and A_C is the parity-violating asymmetry of carbon (see Table 12 for this correction).

As discussed in Section 2.4.7, following the ^{48}Ca target accident, the original target is replaced with a ^{48}Ca composite target with 8% ^{40}Ca composition. Using a theoretically computed parity violating asymmetry of ^{40}Ca, the A_{PV} contribution from the ^{40}Ca target fraction was calculated (see Table 13 for this correction).

The average beam polarization for PREX-2 is (89.7 ± 0.8)% (only Moller results were used). The combined Moller and Compton beam polarization for CREX is (87.10 ± 0.39)%.

The asymmetry blinding factor A_{blind} is only revealed after analysis work is completed. The list of various corrections to the final result are shown in Table. 12 for PREX-2, and

Correction	Absolute (ppb)	Relative (%)
Beam trajectory and energy	-60.4 $\pm$ 3.0	11.0 $\pm$ 0.5
Charge correction	20.7 $\pm$ 0.2	3.8 $\pm$ 0.0
Beam polarization	56.8 $\pm$ 5.2	10.3 $\pm$ 1.0
Target diamond foils	0.7 $\pm$ 1.4	0.1 $\pm$ 0.3
Spectrometer rescattering	0.0 $\pm$ 0.1	0.0 $\pm$ 0.0
Inelastic contributions	0.0 $\pm$ 0.1	0.0 $\pm$ 0.0
Transverse asymmetry	0.0 $\pm$ 0.3	0.0 $\pm$ 0.1
Detector nonlinearity	0.0 $\pm$ 2.7	0.0 $\pm$ 0.5
Angle determination	0.0 $\pm$ 3.5	0.0 $\pm$ 0.6
Acceptance function	0.0 $\pm$ 2.9	0.0 $\pm$ 0.5
Total correction	**17.7 $\pm$ 8.2**	**3.2 $\pm$ 1.5**
Statistical uncertainty	**16**	**2.9**

TABLE 12: Corrections and corresponding systematic uncertainties to PREX-2 A_{PV} [74].

in Table. 13 for CREX. The experimental asymmetries with all the corrections applied can be seen in Table. 14. After all background and beam fluctuation corrections, the physics asymmetry measured by PREX-2 is A_{PV} = 550 $\pm$ 16 (stat) $\pm$8 (syst) ppb (3.3% overall precision). For CREX, A_{PV} = 2668 $\pm$ 106 (stat) $\pm$ 39 ppb (4.2% overall precision).

6.6 WEAK CHARGE RADIUS

As discussed in Chapter 1 A_{PV} can be written as,

$$A_{PV} = \frac{G_F Q^2}{4\pi\alpha\sqrt{2}} \frac{|Q_W|}{Z} \frac{F_W(Q^2)}{F_{ch}(Q^2)}. \tag{169}$$

With the experimental A_{PV} the weak form factor measured using PREX-2, at $Q^2 = 0.00616$ GeV^2 is [74],

$$F_W(^{208}\mathrm{Pb}) = 0.368 \pm 0.013(\mathrm{exp}) \pm 0.001(\mathrm{model}), \tag{170}$$

where the experimental uncertainty includes both statistical and systematic contributions and the second uncertainty is associated with theoretical corrections, including Coulomb corrections.

Correction	Absolute (ppb)	Relative (%)
Beam trajectory and energy	-68 ± 7.0	2.5 ± 0.3
Charge correction	112 ± 1	4.2 ± 0.0
Beam polarization	382 ± 13	14.3 ± 0.5
Isotopic purity	19 ± 3	0.7 ± 0.1
3.831 MeV (2^+) inelastic	-35 ± 19	-1.3 ± 0.7
4.507 MeV (3^-) inelastic	0 ± 10	0.0 ± 0.4
5.370 MeV (3^-) inelastic	-2 ± 4	-0.1 ± 0.1
Transverse asymmetry	0 ± 13	0.0 ± 0.5
Detector nonlinearity	0 ± 7	0.0 ± 0.3
Acceptance	0 ± 24	0.0 ± 0.9
Radiative corrections	0 ± 10	0.0 ± 0.4
Total correction	**40**	**1.5**
Statistical uncertainty	**106**	**4.0**

TABLE 13: Corrections and corresponding systematic uncertainties to CREX A_{PV} [75].

Asymmetry	PREX-2	CREX
A_{raw}	431.64 ± 44.01 (stat)	2106 ± 178.9 (stat)
A_{corr}	492.02 ± 13.52 (stat)	2080.3 ± 83.8 (stat)
Blinded A_{PV}	549.4 ± 16.1 (stat) ± 8.1 (syst)	2412.3 ± 106.1 (stat) ± 40 (syst)
A_{blind}	-0.5	-255.7
Unblinded A_{PV}	550 ± 16 (stat) ± 8 (syst)	2668 ± 106 (stat) ± 40 (syst)

TABLE 14: The path to experimental A_{PV} for PREX-2 and CREX. All values are in units of ppb.

$F_W(Q^2)$ can be written as a Fourier transformation of the charge density distribution ($\rho_W(r)$) [76],

$$F_W(Q^2) = \frac{1}{Q_W}\int d^3r \frac{\sin(qr)}{qr}\rho_W(r). \tag{171}$$

To get correlation between A_{PV} and the ^{208}Pb weak radius, $\rho_W(r)$ predictions from non-relativistic and relativistic density functional models were fitted to a two parameter Fermi function [77].

$$\rho_W(r) = \rho_W^0 \frac{\sinh(c/a)}{\cosh(r/a) + \cosh(c/a)}, \tag{172}$$

$$\rho_W^0 = \frac{3Q_W}{r\pi(c^2 + \pi^2 a^2)}, \tag{173}$$

where r is the radial coordinate, c is the radius parameter, a is the surface thickness. Then one can express the weak charge radius (R_W) as [77],

$$R_W^2 = \frac{1}{Q_W}\int r^2 \rho_W(r) \mathrm{d}^3 r = \frac{3}{5}c^2 + \frac{7}{5}\pi^2 a^2, \tag{174}$$

R_W of ^{208}Pb as a function of A_{PV} for various theoretical models as shown in Fig. 115. The weak charge radius of ^{208}Pb is extracted to be,

$$R_W(^{208}\mathrm{PB}) = 5.795 \pm 0.082(\mathrm{exp}) \pm 0.013(\mathrm{model})\ \mathrm{fm}. \tag{175}$$

After extracting the weak charge radius from the measured A_{PV}, to get the weak charge skin, we need to subtract the charge radius (R_{ch}) of the target nucleus. R_{ch} has been experimentally determined to be 5.503 fm [78].

$$R_{skin}^W = R_W - R_{ch} = 0.292 \pm 0.082(\mathrm{exp}) \pm 0.013(\mathrm{model})\ \mathrm{fm}. \tag{176}$$

The neutron skin thickness is defined as the difference between the point neutron radius and the point proton radius. The R_{skin} is given by [79],

$$R_{skin} = R_n - R_p = \left(1 + \frac{Zq_p}{Nq_n}\right)(R_W - R_{ch}), \tag{177}$$

where Z is the nuclear charge number, N is the neutron number of the nucleus, $q_p = 0.0721$ is the radiatively corrected weak charge of a proton, and q_n = -0.9878 is the radiatively corrected weak charge of a neutron. The ^{208}Pb neutron skin as a function of A_{PV} is obtained

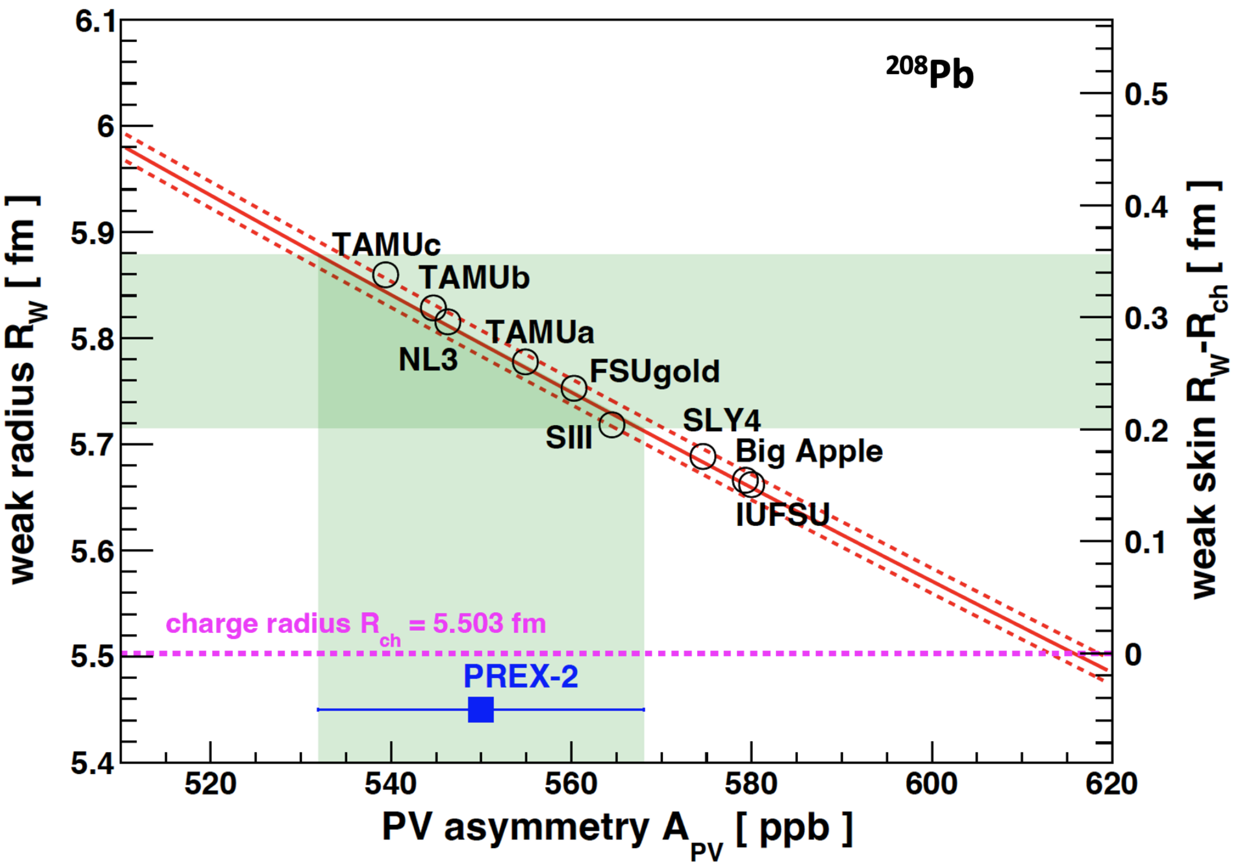

FIG. 115: Weak charge radius (R_W) and neutron skin (R_{skin}) of 208Pb as a function of A_{PV} for various theoretical models. The vertical green band highlights the PREX-2 measured A_{PV} with its $1-\sigma$ experimental uncertainty. The dotted red lines give the model uncertainty [74].

from various theoretical models for PREX-2 is shown in Fig. 115. This gives the neutron skin for ^{208}Pb to be [74],

$$R_{skin}(^{208}Pb) = R_W - R_{ch} = 0.278 \pm 0.078(\text{exp}) \pm 0.012(\text{model}) \text{ fm}. \tag{178}$$

Combining PREX-1 and PREX-2 results, the weak radius and the neutron skin are,

$$R_W(^{208}Pb) = 5.800 \pm 0.075 \text{ fm}, \tag{179}$$

$$R_{skin}(^{208}Pb) = 0.283 \pm 0.71 \text{ fm}. \tag{180}$$

The same analysis was applied for the CREX data to derive the physical properties of ^{48}Ca. For the smaller ^{48}Ca nucleus, the weak charge density is not well represented by the 2 parameter Fermi function, and more significant model uncertainty is introduced in translating from F_W to R_W. As in the case of ^{208}Pb, the extraction of F_W for A_{PV} is theoretically straightforward, and provides a theoretically clean point of comparison for any nuclear structure model. Summary of both PREX-2 and CREX physical properties are shown in Table. 15.

	PREX-2	**CREX**
Target	^{208}Pb	^{48}Ca
$Q^2(GeV^2)$	0.00616 ± 0.00005	0.0297 ± 0.0002
A_{PV} (ppb)	550 ± 16(stat) ± 8 (syst)	2668 ± 106(stat) ± 40 (syst)
F_W	0.368 ± 0.013(exp) ± 0.001 (model)	0.1304 ± 0.0052(exp) ± 0.0020 (model)
R_W (fm)	5.795 ± 0.082(exp) ± 0.013 (model)	3.640 ± 0.026(exp) ± 0.023 (model)
R_{skin} (fm)	0.278 ± 0.078(exp) ± 0.012 (model)	0.121 ± 0.026(exp) ± 0.024 (model)

TABLE 15: Summary of physical results extracted from PREX-2 and CREX [74][75].

CHAPTER 7

SUMMARY AND CONCLUSIONS

The PREX-2 and CREX experiments were run in Hall A at JLab from Summer 2019 to Fall 2020. These experimental results have significant implications for the theory of nuclear structure. The PREX-2 result has implication on neutron star structure and CREX results will provide bridge between different theoretical nuclear modelling methods.

7.1 PARITY VIOLATING ASYMMETRY A_{PV}

The parity violating asymmetry for PREX-2 and CREX is,

$$A_{PV}^{PREX-2} = 550 \pm 16(\text{stat.}) \pm 8(\text{syst.})\ \text{ppb}, \tag{181}$$

$$A_{PV}^{CREX} = 2668 \pm 106(\text{stat.}) \pm 40(\text{syst.})\ \text{ppb}. \tag{182}$$

7.2 NEUTRON SKIN (R_{SKIN})

PREX-2 measured the weak charge radius (R_W) of ^{208}Pb to be,

$$R_W(^{208}Pb) = 5.795 \pm 0.082(\text{exp.}) \pm 0.013(\text{model})\ \text{fm}. \tag{183}$$

Subtracting the known experimental R_{ch} from this R_W, R_{skin} in ^{208}Pb is calculated to be,

$$R_{skin}(^{208}Pb) = 0.278 \pm 0.078(\text{exp.}) \pm 0.012(\text{model})\ \text{fm}. \tag{184}$$

With PREX-1 and PREX-2, the combined ^{208}Pb neutron skin measurement is,

$$R_{skin}^{comb.}(^{208}Pb) = 0.283 \pm 0.071\ \text{fm}. \tag{185}$$

For CREX experiment R_W and R_{skin} found to be,

$$R_W(^{48}Ca) = 3.640 \pm 0.026(\text{exp.}) \pm 0.023(\text{model})\ \text{fm}, \tag{186}$$

$$R_{skin}(^{48}Ca) = 0.121 \pm 0.026(\text{exp.}) \pm 0.024(\text{model})\ \text{fm}. \tag{187}$$

7.3 IMPLICATIONS OF PREX-2 RESULTS

As discussed in Section 1.2, there is a strong correlation between the slope of the symmetry energy (L) and the neutron skin measurement. Figure 116 shows L as a function of R_{skin} for ^{208}Pb, at nuclear saturation density ρ_0 and $\frac{2}{3}\rho_0$, for a range of nuclear structure models. The combined PREX result implies a relatively large slope with L(ρ_0) = (106 ± 37) MeV [74]. This result is in tension with predictions made using different empirical and calculated constraints. The astrophysical implication of this result suggest a large pressure (Eq. 33) and stiffer equation of state in neutron stars which would be consistent with a common equation of state. If observation of neutron stars conflicts with these bounds, this may imply onset of new phase of nuclear matter.

As we discussed in Chapter 1 the size of R_{skin} in neutron rich matter, can be used to infer the size of neutron stars. The pressure in the core of neutron rich matter determines the thickness of the neutron skin in an atomic nucleus, and the radius of a neutron star [80]. Therefore, the measurement of R_{skin} can be used to set bounds on the astrophysical properties of neutron stars.

Combining the PREX result with constraints from NICER (Neutron Star Interior Composition Explorer), for a 1.4 solar mass neutron star, sets upper and lower bound on R_{skin}, for ^{208}Pb to be $0.21 \leq R_{skin}(fm) \leq 0.31$, and upper and lower bound on a neutron star radius to be $13.25 \leq R_*^{1.4}(fm) \leq 14.26$ [80]. The Fig. 117 shows the dimensionless tidal deformability[1] of a 1.4 solar mass neutron star as a function of both the stellar radius $R_*^{1.4}$ and R_{skin}. The combination of NICER and PREX-2 limits deformability as $642 \leq \Lambda_*^{1.4} \leq 955$ [80]. We see that the PREX measurement is consistent with the NICER result. Tidal deformability can be probed by detection of the gravitational waves produced by the binary system. LIGO observation of GW170817 sets an upper limit on deformability as $\Lambda_*^{1.4} \leq 580$[81] which conflicts with the PREX-2 result.

The combined PREX neutron skin result corresponds to a ^{208}Pb interior weak charge density of[74],

$$\rho_W^0 = -0.0796 \pm 0.0038 \text{ fm}^{-3}. \tag{188}$$

With the well measured interior electromagnetic charge density and interior weak charge density, the ^{208}Pb interior baryon density is[74],

$$\rho_0^b = 0.1480 \pm 0.0038 \text{ fm}^{-3}. \tag{189}$$

[1] In a binary system, neutron star deforms due to the tidal force from the other body, this property is described by the tidal deformability

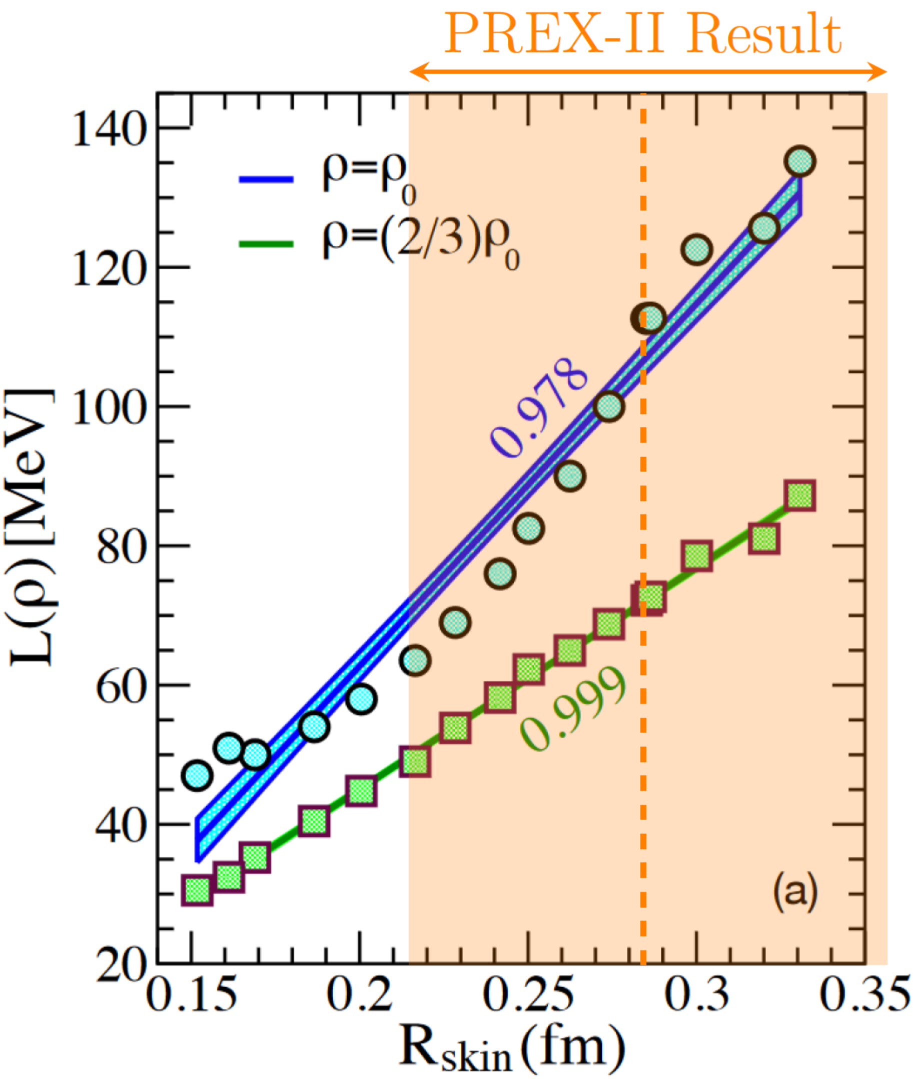

FIG. 116: Slope of the symmetry energy (L(ρ)) as a function of R_{skin} for ^{208}Pb at nuclear saturation density ρ_0 and $\frac{2}{3}\rho_0$ [80].

Figure 118 shows the inferred radial dependence of the ^{208}Pb charge, weak and total baryon densities with their uncertainty bands.

7.4 IMPLICATION OF CREX RESULTS

The difference between form factors, $F_{ch} - F_W$ is calculated to be 0.0277 ± 0.0055 for CREX. The Fig. 119 shows form factor difference plotted with a range of nuclear structure models.

The Fig. 120 shows a comparison between the experimental results and theoretical

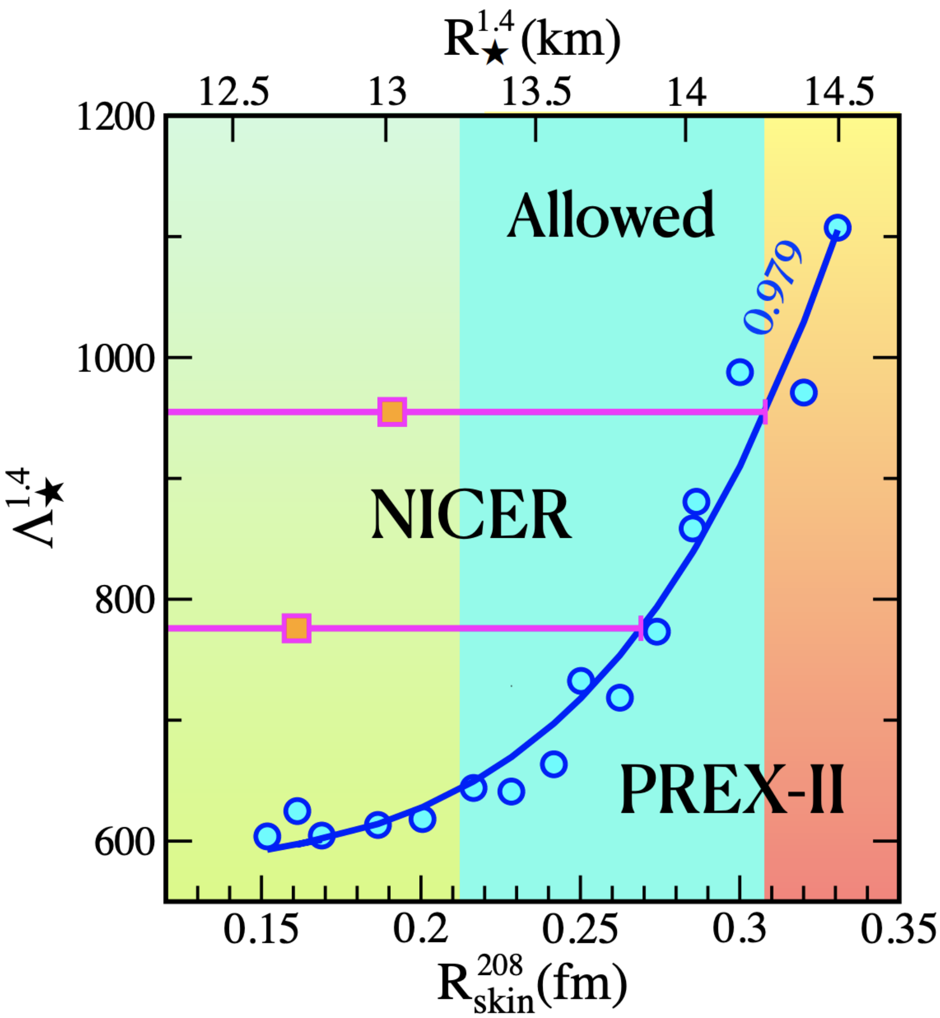

FIG. 117: Tidal deformability of a 1.4 solar neutron star versus its radius (upper X-axis) and the neutron skin thickness of ^{208}Pb (lower X-axis). Blue dots show theoretical predictions from set of energy density functionals, the blue line is a fit to these dots. The light blue region corresponds to the radius range allowed by both NICER and PREX-2 [80].

predictions of the neutron skin thickness and form factor differences of ^{208}Pb and ^{48}Ca. Among all the models, only a few of them can predict the neutron skin thicknesses and weak FFs of ^{208}Pb and ^{48}Ca simultaneously. The extracted neutron skin of ^{48}Ca (CREX) is relatively thin compared to the predictions and that of ^{208}Pb (PREX) is thick. The constraints provide by this measurement will help to guide the development of DFT and ab-initio calculations.

7.5 FUTURE EXPERIMENTS

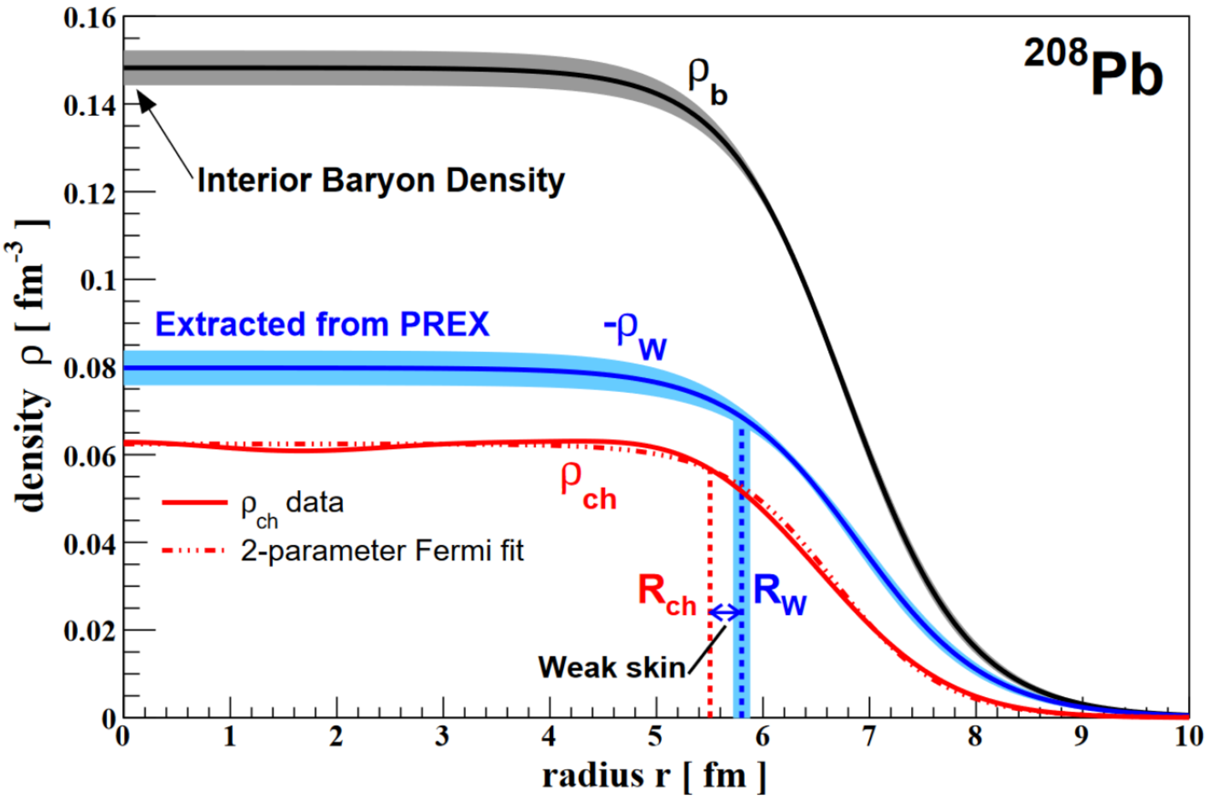

FIG. 118: ^{208}Pb weak and baryon densities from the combined PREX datasets, with uncertainties shaded. EM charge (red), weak charge (blue) and baryon (black) [74].

Future parity violating electron scattering experiments are being developed and the improved techniques of past experiments will be used for these experiments. Several PVES experiments have been proposed including MOLLER [82] and SoLID at JLab, as well as P2[83] and MREX at Mainz.

7.5.1 MOLLER (MEASUREMENT OF LEPTON LEPTON ELECTROWEAK REACTION

The weak mixing angle has a great importance as a test of standard model and this needed to obtained empirically. CERN made measurements of $\sin^2\theta_W$ at q $\approx$ 100 GeV using electron-positron collisions [84] and at low q we have measurements like Qweak [85]. But it is important to do a higher precision measurements of $\sin^2\theta_W$. Figure 121 shows the running of the weak mixing angle along the energy scale with different (proposed) measurements.

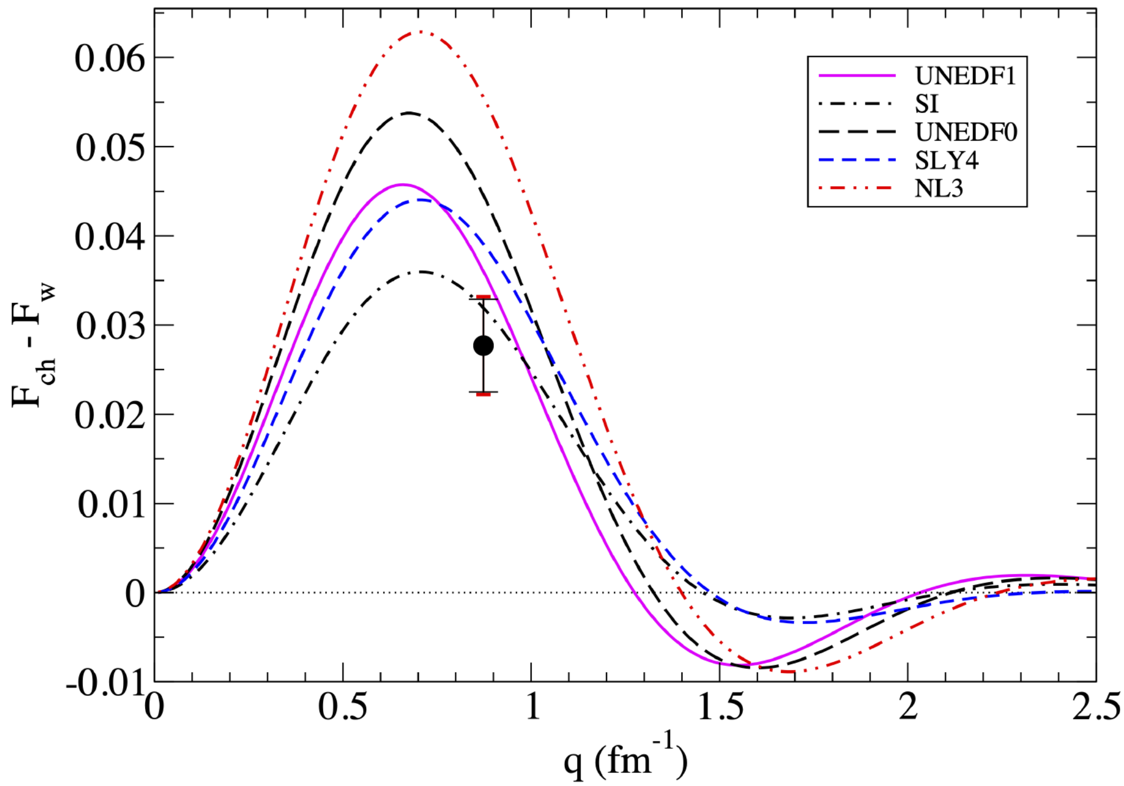

FIG. 119: The difference between the charge and weak form factors for ^{48}Ca as a function of momentum transfer q $= \sqrt{Q^2}$. The curves are the results for non-relativistic and relativistic density functional models. The CREX measurement is the black circle with statistical uncertainty in black error bar and total uncertainty in red error bar[75].

The MOLLER Experiment at JLab Hall A will make a precise measurement of the weak mixing angle at $Q^2 = 0.0056$ (GeV/c)^2. The MOLLER proposes a measurement of $A_{PV} \approx$ (35.6 $\pm$ 0.73) ppb. PREX-2 and CREX have shown significant progress, in experimental techniques towards meeting the goals for MOLLER.

7.5.2 SOLID (SOLENOIDAL LARGE INTENSITY DETECTOR)

SoLID is a new spectrometer with large angular and momentum acceptance, high luminosity detector package which includes GEM tracking detectors, electron and hadron Cerenkov detectors, and a calorimeter for particle identification.

One of the experiments in SoLID proposes to probe the parity violating effect in deep inelastic scattering (PVDIS) with a 0.6% precision measurement on A_{PV}. The goal of this experiment is to precisely measure the weak couplings of quarks C_2q. This measurement

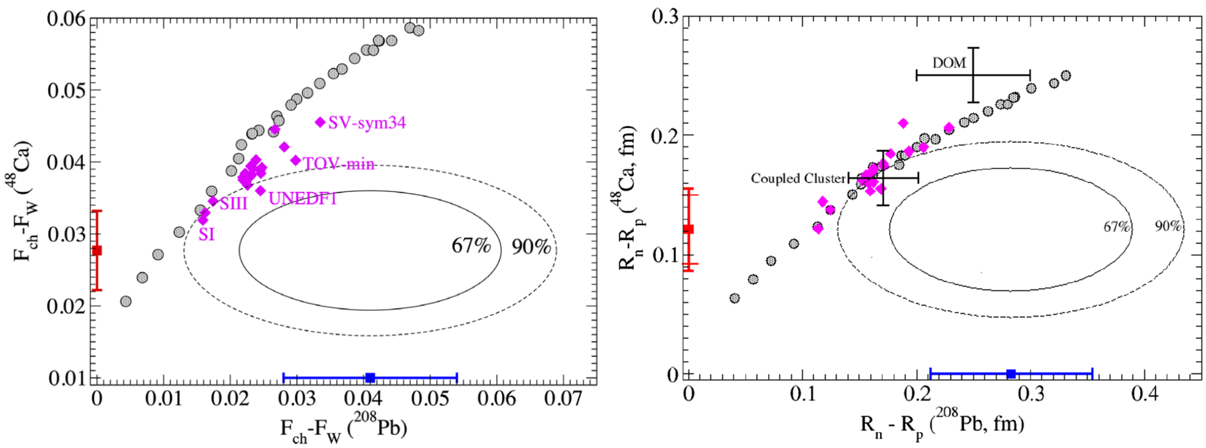

FIG. 120: Experimental and theoretical calculations of the FF difference (left) and the neutron skin thickness (right) of ^{208}Pb and ^{48}Ca. Two ellipses show the 1 σ and 90% probability contours of the overlap region for the two experiment results. The gray circles (magenta diamonds) are a range of relativistic (non-relativistic) density functionals [75].

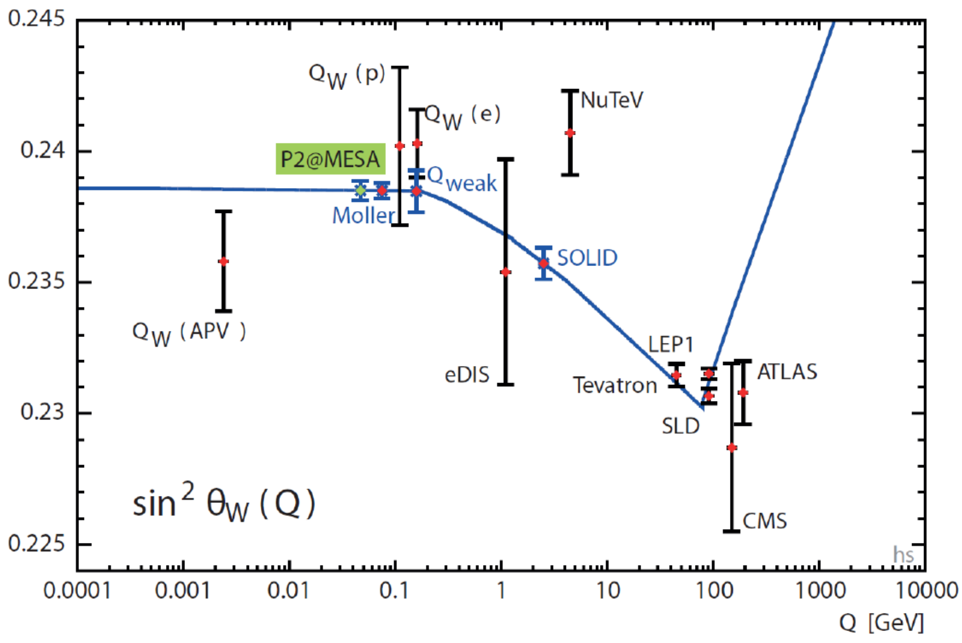

FIG. 121: Running weak mixing angle along the energy scale with different (proposed) measurements.

relies on polarimetry precision of 0.4%. Although at a lower beam energy, CREX provided an important determination of techniques for high precision Compton polarimetry.

7.5.3 P2 AND MREX

P2 aims for a high precision determination of the weak mixing angle $\sin^2\theta_W$ to a precision of 0.14% at a four-momentum transfer of $Q^2 = 4.5 \times 10^3$ GeV^2. This will run at upcoming MESA accelerator in Mainz [83]. Compared to Qweak, P2 will improve the measurement precision by a factor of three.

The Mainz Radius Experiment (MREX) proposes to measure the neutron skin thickness of ^{208}Pb with a precision approximately double that of PREX-2.

Overall, improvements to the experimental method motivate the next generation ultra precise PVES experiments. These experiments will search for novel physics outside the boundaries of the standard model and seek even more precise bounds on the neutron skin of heavy, neutron rich nucleus.

BIBLIOGRAPHY

[1] E. Rutherford, "LXXIX. ithe scattering of and particles by matter and the structure of the atom/i," The London, Edinburgh, and Dublin Philosophical Magazine and Journal of Science **21**, 669–688 (1911).

[2] J. Chadwick, "Possible existence of a neutron," Nature **129**, 312–312 (1932).

[3] `https://en.wikipedia.org/wiki/Gauge_boson#/media/File:Standard_Model_of_Elementary_Particles.svg`.

[4] David Griffiths, *Introduction to Elementary Particles* (Wiley, 1987).

[5] `https://physics.aps.org/articles/v6/111`.

[6] G. Aad et al., "Observation of a new particle in the search for the standard model higgs boson with the atlas detector at the lhc," Physics Letters B **716**, 1–29 (2012).

[7] Devi Lal Adhikari, "Neutron Skin Measurements of 208Pb Using Parity-Violating Electron Scattering," PhD thesis .

[8] Nina Byers, "The life and times of emmy noether; contributions of e. noether to particle physics," (1994).

[9] T. D. Lee and C. N. Yang, "Question of parity conservation in weak interactions," Phys. Rev. **104**, 254–258 (1956).

[10] C. S. Wu, E. Ambler, R. W. Hayward, D. D. Hoppes, and R. P. Hudson, "Experimental test of parity conservation in beta decay," Phys. Rev. **105**, 1413–1415 (1957).

[11] C. J. Horowitz, "Parity violating elastic electron scattering and coulomb distortions," Phys. Rev. C **57**, 3430–3436 (1998).

[12] Caryn Palatchi, "Laser and Electron Beam Technology for Parity Violating Electron Scattering Measurements," PhD thesis .

[13] T.W. Donnelly, J. Dubach, and Ingo Sick, "Isospin dependences in parity-violating electron scattering," Nuclear Physics A **503**, 589–631 (1989).

[14] Samuel S. M. Wong, *Introductory Nuclear Physics* (Wiley, 1998).

[15] M. Thiel, C. Sfienti, J. Piekarewicz, C. J. Horowitz, and M. Vanderhaeghen, "Neutron skins of atomic nuclei: per aspera ad astra," Journal of Physics G Nuclear Physics **46**, 093003 (2019), arXiv:1904.12269 [nucl-ex] .

[16] X. Roca-Maza, M. Centelles, X. Viñas, and M. Warda, "Neutron skin of 208pb, nuclear symmetry energy, and the parity radius experiment," (2011), 10.48550/ARXIV.1103.1762.

[17] X. Roca-Maza and N. Paar, "Nuclear equation of state from ground and collective excited state properties of nuclei," (2018), 10.48550/ARXIV.1804.06256.

[18] Wei-Chia Chen and J. Piekarewicz, "Building relativistic mean field models for finite nuclei and neutron stars," Phys. Rev. C **90**, 044305 (2014).

[19] Brendan T. Reed, F. J. Fattoyev, C. J. Horowitz, and J. Piekarewicz, "Implications of prex-2 on the equation of state of neutron-rich matter," Phys. Rev. Lett. **126**, 172503 (2021).

[20] Michael Bender, Paul-Henri Heenen, and Paul-Gerhard Reinhard, "Self-consistent mean-field models for nuclear structure," Rev. Mod. Phys. **75**, 121–180 (2003).

[21] G. Hagen, A. Ekström, C. Forssén, G. R. Jansen, W. Nazarewicz, T. Papenbrock, K. A. Wendt, S. Bacca, N. Barnea, B. Carlsson, C. Drischler, K. Hebeler, M. Hjorth-Jensen, M. Miorelli, G. Orlandini, A. Schwenk, and J. Simonis, "Neutron and weak-charge distributions of the 48ca nucleus," Nature Physics **12**, 186–190 (2015).

[22] `https://hallaweb.jlab.org/parity/prex/c-rex2013_v7.pdf`.

[23] Brendan T. Reed, Z. Jaffe, C. J. Horowitz, and C. Sfienti, "Measuring the surface thickness of the weak charge density of nuclei," Phys. Rev. C **102**, 064308 (2020).

[24] `https://hallaweb.jlab.org/parity/prex/prex-II.pdf` ().

[25] C. J. Horowitz, Z. Ahmed, C.-M. Jen, A. Rakhman, P. A. Souder, M. M. Dalton, N. Liyanage, K. D. Paschke, K. Saenboonruang, R. Silwal, G. B. Franklin, M. Friend, B. Quinn, K. S. Kumar, D. McNulty, L. Mercado, S. Riordan, J. Wexler, R. W. Michaels, and G. M. Urciuoli, "Weak charge form factor and radius of ^{208}pb through parity violation in electron scattering," Phys. Rev. C **85**, 032501 (2012).

[26] `http://www.flickr.com/photos/jeffersonlab/12599705145` ().

[27] http://en.wikipedia.org/wiki/Thomas_Jefferson_National_Accelerator_Facility ().

[28] Rupesh Silwal, "Probing the Strangeness Content of the Proton and the Neutron Radius of 208Pb using Parity-Violating Electron Scattering," PhD thesis .

[29] Emmanouil Kargiantoulakis, "A Precision Test of the Standard Model viaParity-Violating Electron Scattering in the Qweak Experiment," PhD thesis .

[30] D.W. Higinbotham and T. Keppel, "2017 version: Jefferson lab hall a standard equipment manual," https://hallaweb.jlab.org/github/halla-osp/version/Standard-Equipment-Manual.pdf.

[31] M. Steigerwald, "Mev mott polarimetry at jefferson lab," AIP Conference Proceedings **570**, 935–942 (2001), https://aip.scitation.org/doi/pdf/10.1063/1.1384229 .

[32] J. M. Grames, C. K. Sinclair, J. Mitchell, E. Chudakov, H. Fenker, A. Freyberger, D. W. Higinbotham, M. Poelker, M. Steigerwald, M. Tiefenback, C. Cavata, S. Escoffier, F. Marie, T. Pussieux, P. Vernin, S. Danagoulian, V. Dharmawardane, R. Fatemi, K. Joo, M. Zeier, V. Gorbenko, R. Nasseripour, B. Raue, R. Suleiman, and B. Zihlmann, "Unique electron polarimeter analyzing power comparison and precision spin-based energy measurement," Phys. Rev. ST Accel. Beams **7**, 042802 (2004).

[33] William Henry, "PRECISION MØLLER POLARIMETRY AND APPLICATIONS AT JEFFERSON LABORATORY," PhD thesis .

[34] D.E. King, D.C. Jones, C. Gal, D. Gaskell, W. Henry, A.D. Kaplan, J. Napolitano, S. Park, K.D. Paschke, R. Pomatsalyuk, and P.A. Souder, "Precision møller polarimetry for PREX-2 and CREX," Nuclear Instruments and Methods in Physics Research Section A: Accelerators, Spectrometers, Detectors and Associated Equipment **1045**, 167506 (2023).

[35] https://prex.jlab.org/DocDB/0000/000025/003/PREX2target_covrig_oct2017.pdf.

[36] Allison Jane Zec, "Compton Polarimetry for Neutral Weak Form Factor Measurements in 208Pb and 48Ca," PhD thesis .

[37] Cameron Clarke, "Measurement of Parity Violating Asymmetry in Elastic Electron Scattering off 48Ca," PhD thesis .

[38] Caryn Palatchi and Kent Paschke, "Rtp pockels cell with nanometer-level position control," (2021).

[39] T.B. Humensky, R. Alley, A. Brachmann, M.J. Browne, G.D. Cates, J. Clendenin, J. deLamare, J. Frisch, T. Galetto, E.W. Hughes, K.S. Kumar, P. Mastromarino, J. Sodja, P.A. Souder, J. Turner, and M. Woods, "SLAC's polarized electron source laser system and minimization of electron beam helicity correlations for the e-158 parity violation experiment," Nuclear Instruments and Methods in Physics Research Section A: Accelerators, Spectrometers, Detectors and Associated Equipment **521**, 261–298 (2004).

[40] Thomas Brian Humensky, "Probing the standard model and nucleon structure via parity-violating electron scattering," PhD thesis .

[41] `https://raicol.com/rtp/rtp-for-eo`.

[42] `https://prex.jlab.org/cgi-bin/DocDB/private/ShowDocument?docid=322`.

[43] `http://ace.phys.virginia.edu/Lab26/858`.

[44] `http://ace.phys.virginia.edu/Lab26/860`.

[45] `https://logbooks.jlab.org/entry/3641908`.

[46] `http://ace.phys.virginia.edu/Lab26/828`.

[47] Arthur Holly Compton, "A quantum theory of the scattering of x-rays by light elements," Physical Review **21**, 483–502.

[48] F. W. Lipps and Hendrik Anton Tolhoek, "Polarization phenomena of electrons and photons. i: General method and application to compton scattering," Physica D: Nonlinear Phenomena **20**, 85–98 (1954).

[49] Abdurahim Rakhman, "THE DESIGN AND CONSTRUCTION OF A GREEN LASER AND FABRY-PEROT CAVITY SYSTEM FOR JEFFERSON LAB'S HALL A COMPTON POLARIMETER," PhD thesis .

[50] D. Neyret et al. G. Bardin, C. Cavata, "Conceptual design report of a compton polarimeter for cebaf hall a," Technical Report 96-14 (DAPNIA-SPhN (1996)).

[51] C. Y. Prescott, "Spin dependent compton scattering for use in analyzing electron beam polarizations," (SLAC-TN-73-1, (1973)).

[52] Megan Friend, "THE DESIGN AND CONSTRUCTION OF A GREEN LASER AND FABRY-PEROT CAVITY SYSTEM FOR JEFFERSON LAB'S HALL A COMPTON POLARIMETER," PhD thesis .

[53] Donald Charles Jones, "Measuring the Weak Charge of the Proton via Elastic Electron-Proton Scattering," PhD thesis .

[54] A. Rakhman, M. Hafez, S. Nanda, F. Benmokhtar, A. Camsonne, G.D. Cates, M.M. Dalton, G.B. Franklin, M. Friend, R.W. Michaels, V. Nelyubin, D.S. Parno, K.D. Paschke, B.P. Quinn, P.A. Souder, and W.A. Tobias, "A high-finesse fabry–perot cavity with a frequency-doubled green laser for precision compton polarimetry at jefferson lab," Nuclear Instruments and Methods in Physics Research Section A: Accelerators, Spectrometers, Detectors and Associated Equipment **822**, 82–96 (2016).

[55] Dennis H. Goldstein, *Polarized Light* (CRC Press, 2017).

[56] N. Vansteenkiste, P. Vignolo, and A. Aspect, "Optical reversibility theorems for polarization: application to remote control of polarization," J. Opt. Soc. Am. A **10**, 2240–2245 (1993).

[57] Beth Schaefer, Edward Collett, Robert Smyth, Daniel Barrett, and Beth Fraher, "Measuring the stokes polarization parameters," American Journal of Physics **75**, 163–168 (2007).

[58] `https://root.cern/`.

[59] `https://hallcweb.jlab.org/elogs/Hall+A+Compton/668` ().

[60] `https://hallcweb.jlab.org/elogs/Hall+A+Compton/697` ().

[61] A. Rakhman, M. Hafez, S. Nanda, F. Benmokhtar, A. Camsonne, G.D. Cates, M.M. Dalton, G.B. Franklin, M. Friend, R.W. Michaels, V. Nelyubin, D.S. Parno, K.D. Paschke, B.P. Quinn, P.A. Souder, and W.A. Tobias, "A high-finesse fabry–perot cavity with a frequency-doubled green laser for precision compton polarimetry at jefferson lab," Nuclear Instruments and Methods in Physics Research Section A: Accelerators, Spectrometers, Detectors and Associated Equipment **822**, 82–96 (2016).

[62] A. Denner and S. Dittmaier, "Complete $o(\alpha)$ QED corrections to polarized compton scattering," Nuclear Physics B **540**, 58–86 (1999).

[63] David Eric King, "Utilizing Parity Violating Electron Scattering As a Probe to Measure the Neutron Radius of 208-pb," PhD thesis .

[64] https://hallcweb.jlab.org/elogs/Hall+A+Compton/836 ().

[65] https://hallcweb.jlab.org/elogs/Hall+A+Compton/842 ().

[66] Tao Ye, "Precision measurement of the parity violating asymmetry in elastic electron scattering of 208pb," PhD thesis .

[67] http://ace.phys.virginia.edu/HAPPEX/4451 ().

[68] http://ace.phys.virginia.edu/HAPPEX/4644 ().

[69] https://drive.google.com/file/d/1JSC5DyuGlOOQgTMs__-_gm7qnHudbxOq/view.

[70] http://ace.phys.virginia.edu/HAPPEX/4595.

[71] S. N. Santiesteban, L. Tracy, D. Flay, D. W. Higinbotham, D. Marchand, P. Vernin, and A Saha, "Precise beam energy determination for hall a after the cebaf 12 gev upgrade," (2021).

[72] S. Abrahamyan et al. (PREX Collaboration), "Measurement of the neutron radius of ^{208}Pb through parity violation in electron scattering," Phys. Rev. Lett. **108**, 112502 (2012).

[73] Ryan Richards, "Measurements of the beam normal asymmetry using polarized elastic electron scattering off various spin-0 nuclei at 1 gev," PhD thesis .

[74] D. Adhikari et al. (PREX Collaboration), "Accurate determination of the neutron skin thickness of ^{208}Pb through parity-violation in electron scattering," Phys. Rev. Lett. **126**, 172502 (2021).

[75] D. Adhikari et al., "Precision determination of the neutral weak form factor of ^{48}ca," (2022), 10.48550/ARXIV.2205.11593.

[76] C. J. Horowitz, Z. Ahmed, C.-M. Jen, A. Rakhman, P. A. Souder, M. M. Dalton, N. Liyanage, K. D. Paschke, K. Saenboonruang, R. Silwal, G. B. Franklin, M. Friend, B. Quinn, K. S. Kumar, D. McNulty, L. Mercado, S. Riordan, J. Wexler, R. W. Michaels, and G. M. Urciuoli, "Weak charge form factor and radius of ^{208}pb through parity violation in electron scattering," Phys. Rev. C **85**, 032501 (2012).

[77] Brendan T. Reed, Z. Jaffe, C. J. Horowitz, and C. Sfienti, "Measuring the surface thickness of the weak charge density of nuclei," Phys. Rev. C **102**, 064308 (2020).

[78] B. Frois, J. B. Bellicard, J. M. Cavedon, M. Huet, P. Leconte, P. Ludeau, A. Nakada, Phan Zuan Hô, and I. Sick, "High-momentum-transfer electron scattering from ^{208}Pb." Phys. Rev. Lett. **38**, 576–576 (1977).

[79] https://prex.jlab.org/DocDB/0004/000467/001/Horowitz_PREXII.pdf.

[80] J. Piekarewicz, A. R. Linero, P. Giuliani, and E. Chicken, "Power of two: Assessing the impact of a second measurement of the weak-charge form factor of ^{208}Pb," Phys. Rev. C **94**, 034316 (2016).

[81] B. P. Abbott et al. (The LIGO Scientific Collaboration and the Virgo Collaboration), "Gw170817: Measurements of neutron star radii and equation of state," Phys. Rev. Lett. **121**, 161101 (2018).

[82] J. Benesch et al., "The moller experiment: An ultra-precise measurement of the weak mixing angle using møller scattering," (2014).

[83] Dominik Becker, Razvan Bucoveanu, Carsten Grzesik, Kathrin Imai, Ruth Kempf, Matthias Molitor, Alexey Tyukin, Marco Zimmermann, David Armstrong, Kurt Aulenbacher, Sebastian Baunack, Rakitha Beminiwattha, Niklaus Berger, Peter Bernhard, Andrea Brogna, Luigi Capozza, Silviu Covrig Dusa, Wouter Deconinck, Jürgen Diefenbach, James Dunne, Jens Erler, Ciprian Gal, Michael Gericke, Boris Gläser, Mikhail Gorchtein, Boxing Gou, Wolfgang Gradl, Yoshio Imai, Krishna S. Kumar, Frank Maas, Juliette Mammei, Jie Pan, Preeti Pandey, Kent Paschke, Ivan Perić, Mark Pitt, Sakib Rahman, Seamus Riordan, David Rodríguez Piñeiro, Concettina Sfienti, Iurii Sorokin, Paul Souder, Hubert Spiesberger, Michaela Thiel, Valery Tyukin, and Quirin Weitzel, "The p2 experiment," The European Physical Journal A **54** (2018), 10.1140/epja/i2018-12611-6.

[84] https://inis.iaea.org/collection/NCLCollectionStore/_Public/27/032/27032888.pdf?r=1&r=1.

[85] "Precision measurement of the weak charge of the proton," Nature **557**, 207–211 (2018).